COMITÉ NATIONAL FRANÇAIS DE RADIOÉLECTRICITÉ SCIENTIFIQUE
UNION RADIO SCIENTIFIQUE INTERNATIONALE
SIÈGE SOCIAL : ACADÉMIE DES SCIENCES, 23 QUAI DE CONTI, PARIS 6ÈME

URSI FRANCE JS 19

JOURNÉES SCIENTIFIQUES, *WORKSHOP*

APPROCHER LES DEUX INFINIS PAR LES ONDES ELECTROMAGNÉTIQUES
APPROCHING BOTH INFINITIES THROUGH ELECTROMAGNETIC WAVES WAVES

26 / 27 MARS, 2019
OBSERVATOIRE DE VERSAILLES SAINT-QUENTIN-EN-YVELINES

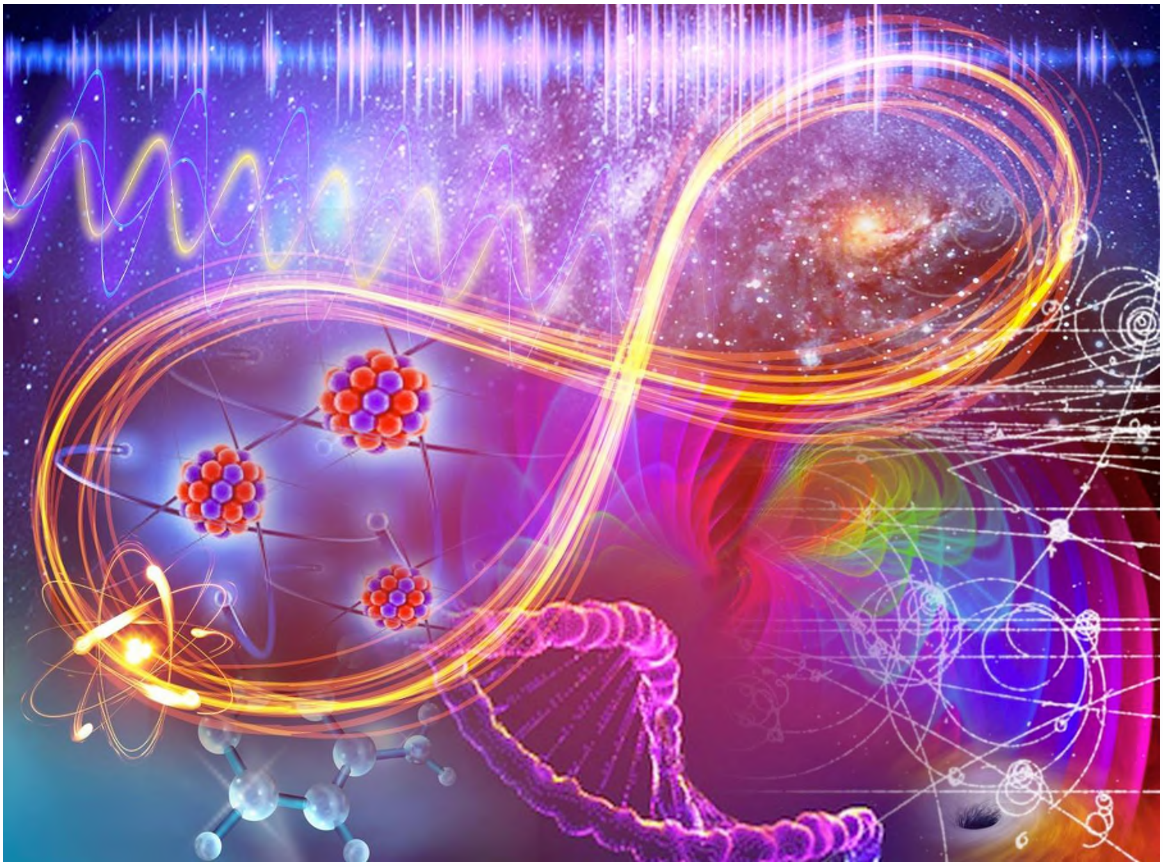

ACTES *PROCEEDINGS*

Crédit illustration de couverture : Atelier Isatis – Dijon
Cover image Credit: Atelier Isatis - Dijon

Table of contents

Electromagnetism and interaction with the cell; **75**

Electromagnetism and interaction with the cell (Posters) 95

Ultra hot plasmas 98

Antennas, propagation and information 113

Space observation

Efficient Full Wave Simulation of SKA-low Stations
Simulation ondes pleines efficace pour les stations SKA basses fréquences

Jean Cavillot[1]***, Eloy de Lera Acedo***[2]***, Nima Razavi-Ghods***[2]***, and Christophe Craeye***[1]

[1]*ICTEAM, Université Catholique de Louvain, {jean.cavillot@uclouvain.be, christophe.craeye@uclouvain.be}*
[2]*Department of Physics, University of Cambridge, {eloy@mrao.cam.ac.uk, nima@mrao.cam.ac.uk }*

Keywords: SKA, Method of Moments, Macro Basis Functions (MBF), Finite ground plane
Mots-clefs: SKA, Méthode des Moments, Macro fonctions de base (MBF), Plan de masse fini

Abstract:

Fast and accurate methods to compute the mutual coupling between elements and with a finite ground plane are presented in this paper. The initial formulation is based on the Method of Moments (MoM). The HARP software presented here accelerates the MoM solution by using a combination of the Macro Basis Function (MBF) approach with an interpolatory technique. After that, those MBFs, which correspond to an infinite ground plane solution, are used to describe the interactions of the array with a finite ground plane lying on a semi-infinite soil. The methods are validated here for the SKA Log Periodic antenna (SKALA), under study for the Square Kilometer Array (SKA). The patterns are compared here with results obtained with the commercial software FEKO.

Résumé:

Cet article présente deux méthodes permettant de tenir compte du couplage mutuel inter-éléments ainsi qu'avec le plan de masse fini dans les réseaux d'antennes. La formulation initiale est basée sur la Méthode des Moments. Celle-ci est accélérée grâce à une combinaison de la méthode des Macro fonctions de base (MBF) avec une technique interpolatoire dans le software baptisé HARP. Ces MBFs, calculées sous la condition d'un plan de masse infini, sont utilisées pour caractériser les interactions avec un plan de masse fini lui-même posé sur un sol infini. Les méthodes sont ensuite appliquées à l'antenne SKALA (SKA Log Periodic antenna) du radiotélescope Square Kilometer Array (SKA). Les diagrammes de rayonnement sont ensuite validés à l'aide des résultats obtenus avec le software commercial FEKO.

1 Introduction

The SKA (Square Kilometer Array) [1] represents the next generation of radio telescopes. It aims to survey the sky much faster and in a more accurate way than any other previous system. Therefore, the SKA will collect information over more than a square kilometer area. This project, in which more than 100 companies and research institutions from different countries cooperate, represents a true challenge for engineers in many areas such as digital hardware, signal processing, antenna design and array simulation. This radio telescope aims to achieve an unprecedented sensitivity by using thousands of dishes and up to a million of low-frequency antennas. The latter will form many base stations appearing as a collection of radio telescopes. The main targeted cosmology experiments are the Epoch of Reionization (EoR) and the Cosmic Dawn (CD) [2]. The SKA low-frequency array is composed of base stations containing each 256 SKA Log-periodic Antennas (SKALA [3]). The frequency band of this array lies between 50 MHz and 350MHz. A base station using the fourth version of the SKALA antenna has already been deployed in Australia and is currently under test. The deserts of South Africa and Australia have been designated for the SKA location in order to benefit from a minimum radio interference.

In order to perform the best calibration, radio-astronomers need accurate Embedded Element Patterns (EEP), i.e. the radiation pattern of each individual element assuming the other antennas are passively terminated. Indeed, since SKA-low is a phased array and given that the embedded element patterns are not the same, the shape of the beam changes rapidly as the array is scanned. Small changes in the shape of the beam are not necessarily an issue, since some imaging algorithms can cater for different patterns at the level of different stations. Though, since high dynamic range is targeted, those small differences in array patterns need to be known very accurately. Regarding the sidelobes, things are even more crucial because non-regular arrays produce relatively high sidelobes and the impact of mutual coupling (i.e. of varying embedded element patterns) is actually much higher in the sidelobes. Hence, if one wants to perform nulling of far-out interferrers [4], the accurate knowledge of embedded element patterns is even more crucial.

The mutual coupling and the ground plane finiteness strongly impact the EEPs. In order to accurately predict these patterns, full wave simulations such as those obtained with the Method of Moments [5] need to be carried out. When considering large irregular arrays, full wave simulations using commercial software is time consuming and requires a lot of memory. This issue has been tackled for decades and two categories of methods appear. The first category represents the iterative methods based on Multipoles [6]. In those methods, a new simulation is needed every time the excitation port changes and for every change of the antennas positions. Moreover, condition number issues can appear due to fine-mesh details. The other category contains the non-iterative solvers. These methods are based on the assumption that the current distribution on the antennas can be decomposed into a limited number of current distributions. In this category, the Macro Basis Function [7] technique allows to solve smaller systems of equations. Besides, fast methods have been developed to compute the interactions between MBFs [8], [9], [10]. However, when considering a finite ground plane, the interaction of the MBFs with the latter become prohibitive. The inhomogeneous plane wave algorithm can be used to efficiently perform the interactions between scatterers [12]. In this spectral approach, the number of plane waves required to compute the interactions greatly decreases with increasing distance between the scatterers.

In this paper, a software named HARP [13] which efficiently handles the mutual coupling is presented. It is based on a combination of the MBF method with an interpolatory technique [10]. The set of MBFs is built assuming an infinite ground plane. The finite ground plane is then taken into account by computing the interaction with the MBFs using the inhomogeneous plane waves algorithm.

The remainder of the paper is organized as follows: Section 2 briefly describes the main design parameters of the SKALA antenna. Section 3 describes the HARP software and compares it in terms of performance to the commercial software CST [11]. Section 4 describes how the finite ground plane is taken into account using inhomogeneous plane waves and Section 5 concludes the paper.

2 SKALA

The SKALA [3] shown in Figure 1 has been designed according to the observation of those predetermined cosmology experiments: the Epoch of Reionization (EoR) and the Cosmic Dawn (CD). Based on these experiments, the SKALA should present a smooth frequency response in order to detect faint signals. The antenna has been designed to maximize the sensitivity of the SKA-low array on a 7:1 frequency band by optimizing the effective area, minimizing the footprint and the receiver noise. In order to measure the foregrounds of the EoR, the antenna also requires a low relative cross-polarization. An evaluation of the SKALA performance with respect to the EoR and CD experiments is presented in [14]. According to the planned number of deployed antennas (more than 3 million), the cost per element and the durability are also important parameters. Indeed, the antenna should be able to last more then 30 years in the desert.

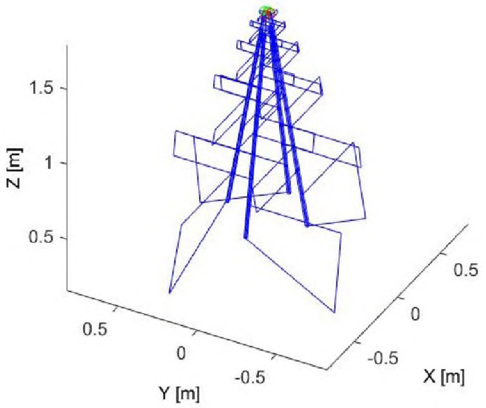

Figure 1 – Verison 2 of SKALA

3 HARP

The traditional Method of Moments (MoM) gives the current distribution on the antennas as the solution of the following system of equations:

$$Zi = v \tag{1}$$

where Z is the MoM impedance matrix, v is a vector of excitation and i is the current distribution. Considering N_a antennas meshed with N_e basis functions, the solution has a complexity $O((N_a N_e)^3)$.
In the MBF formulation, one considers a Q matrix where each column corresponds to a MBF. Thanks to that consideration, the solution, approximated as $i^r \simeq Q\ i$, can be obtained by solving a reduced system of equations [15]:

$$Z^r i^r = v^r \tag{2}$$

where $Z^r = Q^H Z Q$ and $v^r = Q^H v$. Thanks to that formulation, the solution complexity is reduced to $O((N_a N_m)^3)$ where N_m is the number of MBFs which is considerably smaller than the number of basis functions N_e. As an example, the SKA-low stations can be simulated with $N_m = 20$ MBFs whereas every antenna needs to be meshed with $N_e = 1218$ basis functions.
The blocks of the matrix Z^r contain the interactions between MBFs. The far-field interaction between a MBF S placed at the origin and a MBF T positionned at $(r_{mn}, \hat{\alpha})$ can be approximated as:

$$Z_{TS}^{app}(r_{mn}, \hat{\alpha}) \simeq -j\omega\mu\ \overrightarrow{F}_{T,m}^{\hat{\alpha},*} \cdot \overrightarrow{F}_{S,n}^{\hat{\alpha}} \frac{e^{-jkr_{mn}}}{4\pi r_{mn}} \tag{3}$$

where $\overrightarrow{F}_{T,m}^{\hat{\alpha},*}$, and $\overrightarrow{F}_{S,n}^{\hat{\alpha}}$ are the radiation patterns of the testing and source MBFs respectively, $*$ stands for the complex conjugate, j is the wavenumber, ω is the angular frequency and μ is the free-space permeability.

The interpolatory method used in HARP was proposed in [10]. In this method, the blocks of the matrix Z^r are obtained as a combination of the far-field interaction in (3) and a matrix B represented by a harmonic-polynomial model.
This matrix B can be obtained in three steps:

- Subtraction of the far-field expression for the interactions.
- Phase extraction
- Harmonic polynomial representation

Applying the two first steps gives:

$$B_{TS}(r_{mn}, \hat{\alpha}) = \frac{Z_{TS}^{r}(r_{mn}, \hat{\alpha}) - Z_{TS}^{app}(r_{mn}, \hat{\alpha})}{e^{-jkr_{mn}}} \tag{4}$$

The subtraction in the numerator represents the far-field subtraction and the division indicates the phase correction step. Note that the method requires to compute the exact interactions on a limited number of points positioned on a pre-defined polar-radial grid.
After applying the change of variable $d = \frac{1}{r^2}$, (5) can be fitted with the following harmonic polynomial model:

$$B_{TS}(r_{mn}, \hat{\alpha}) = \sum_{p=-P}^{P} e^{jp\alpha} \sum_{q=0}^{Q} c_{pq}\ d^q \tag{5}$$

where, c_{pq} are the coefficients calculated in the least-squares sense, P is the Fourier Series order and Q is the polynomial order.

Thanks to this interpolatory method, the interaction between MBFs can be fast computed as:

$$Z_{TS}^{r}(r_{mn}, \hat{\alpha}) = Z_{TS}^{app}(r_{mn}, \hat{\alpha}) + B_{TS}(r_{mn}, \hat{\alpha})\ e^{-jkr_{mn}} \tag{6}$$

Let us consider an array of 16 SKALA antennas on an infinite ground plane. The radiation patterns obtained with FEKO [20] and HARP are compared in Figure 3 considering a frequency of 145 MHz.
Some differences may appear in the sidelobes due to the different modelling of the antenna in HARP and FEKO. Moreover, the simulations are done using the fourth version of the SKALA antenna which is more complicated than the previous versions. Considering now a SKA station composed of 256 version 2 SKALAs, the commercial software needs more than 90 hours to simulate the station [13]. Moreover, a new simulation is required every time the excitation port changes. The software HARP, however needs 3 hours of pre-processing per frequency. Once the pre-processing is done, HARP only needs 0.5 min to simulate the station. If the antennas positions are modified, the simulation only takes another 0.5 min.

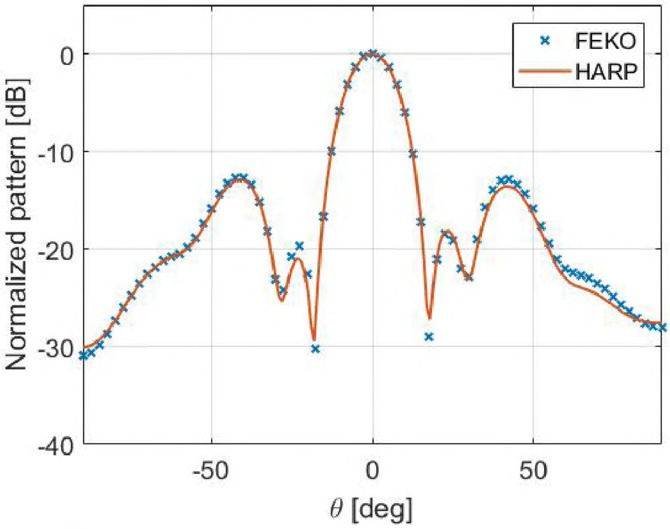

Figure 2 – E-plane normalized radiation patterns of HARP vs FEKO

4 Finite ground plane

As stated before, not only the mutual coupling impacts the embedded element patterns but also the finite ground plane as shown in [16]. In this section, the inhomogeneous plane waves algorithm is used to describe the interactions between the MBFs calculated thanks to the HARP software and the finite ground plane. Using a MoM formulation, the finite ground plane is meshed with RWG basis functions [19]. It should be pointed out that the MBFs are calculated assuming an infinite ground plane. However, as will be shown in the results, this assumption is consistent.

Let us consider a SKALA above a finite ground lying itself upon a semi-infinite soil. Using the mathematical definitions and derivations in [17]. The field radiated by the antenna and tested by the finite ground plane can be written as:

$$\overrightarrow{E}(x,y,z) = \frac{-jk\eta}{(2\pi)^2}\iint F_p(k_x,k_y)\cdot\hat{e}_p\ (1+\Gamma_p)\ \frac{e^{-j(k_x x+k_y y-k_z z)}}{2jk_z}\ Q\ dk_{xR}\ dk_{yR} \tag{7}$$

where p is the polarization (TE or TM), η is the free space impedance, k is the wavenumber which is also the norm of the wavevector $\overrightarrow{k} = (k_x, k_y, k_z)$, Γ_p is the reflection coefficient due to the presence of the soil [18], Q is a term allowing the integration only on real parts of k_x and k_y and $F_p(k_x,k_y)$ is the radiation pattern of the MBF expressed as:

$$F_p(k_x,k_y) = \sum_{m=0}^{M}\epsilon_m \iiint_V \overrightarrow{J_m}(\overrightarrow{r}')\cdot\hat{e}_p\ e^{j(k_x x'+k_y y'-k_z z')}\ dV \tag{8}$$

where M is the number of elementary basis functions per MBF, ϵ_m is the weight of the mth basis functions and $\overrightarrow{J_m}(\overrightarrow{r}')$ is the mth basis function of the MBF situated in $r' = (x', y', z')$. Once the tested field in (7) has been computed, the current distribution on the ground plane is obtained by solving the following system of equations:

$$Z_{gg}\ i_g = v \tag{9}$$

where Z_{gg} is the MoM impedance matrix of the ground, i_g represents the equivalent currents of the ground plane and v is the excitation vector resulting from the projection of (7) on the finite ground basis functions.

Let us consider ρ the radial distance from the antenna. It should be pointed that computing the interactions with the finite ground plane is very efficient when ρ is lower than the wavelength. However, the required number of inhomogeneous plane waves becomes too high when ρ is increasing above a few wavelengths and the methods looses its efficiency. In a nutshell, it appears that the inhomogeneous plane wave algorithm is efficient only when considering a relatively low field of view defined as ρ/z' where z' is the distance between the antenna MBF and the ground plane [21].

As a validation, let us consider a SKALA-2 antenna lying above a 8 m diameter finite ground plane. The frequency considered is 80 MHz. The results are consistent with those of FEKO and confirm the antenna infinite ground plane currents assumption.

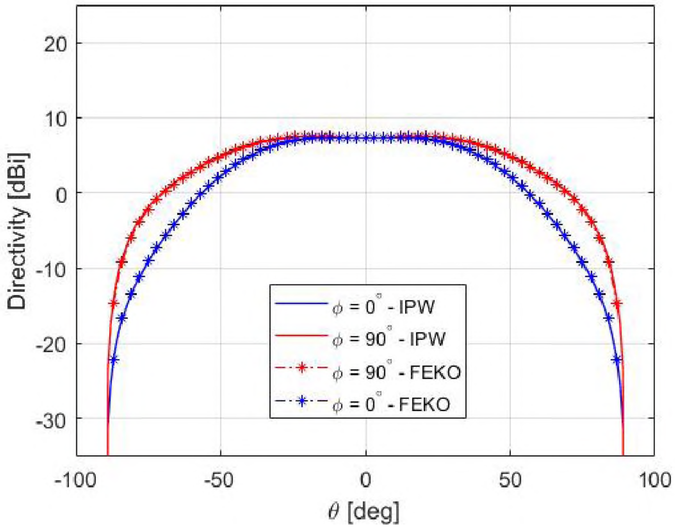

Figure 3 – Radiation patterns of HARP vs FEKO considering one SKALA on a 8 m diameter ground plane

5 Conclusion

In this paper, we have described efficient methods to compute the coupling between elements as well as with the finite ground plane. The results have been then validated thanks to the commercial software FEKO. However, the inhomogeneous plane waves methods do not perform efficiently when the finite ground plane becomes electrically large. Thus, the door is open to new methods handling large ground planes.

6 References

[1] www.skatelescope.org

[2] Koopmans L., et al., "The Cosmic Dawn and Epoch of Reionization with the Square Kilometer Array," Available at https://arxiv.org/abs/1505.07568.

[3] E. de Lera Acedo, et al., "SKALA, a log-periodic array antenna for the SKA-low instrument: design, simulation, tests and system considerations," *Proc. Int. Conf. Electromag. in Ad. App. (ICEAA),* Sept. 2012.

[4] H. Bui-Van, et al., "Direct Deterministic Nulling Techniques for Large Random Arrays Including Mutual Coupling". *IEEE Tran. Antennas Propag.,*

[5] R. F. Harrington, "Field Computations by Moment Method in Electromagnetics," Melbourne, FL: Krieger, 1982.

[6] R. Coifman, et al., "The fast multipole method for the wave equation: a pedestrian prescription," *IEEE Tran. Antennas Propag.,* vol. 35, no. 3, pp. 7-12, June 1993.

[7] E. Suter and J. R.Mosig, "A subdomain multilevel approach for the efficient MoM analysis of large planar antennas," *Microw. Opt. Technol. Lett.*, vol. 26, no. 4, pp. 270–277, Aug. 2000.

[8] C. Craeye, "A fast impedance and pattern computation scheme for finite antenna arrays," *IEEE Trans. Antennas Propag.,* vol. 54, no. 10, pp. 3030–3034, Oct. 2006.

[9] D. Gonzalez-Ovejero, F. Mesa and C. Craeye, "Accelerated macro basis functions analysis of finite printed antenna arrays through 2D and 3D fast multipoles," *IEEE Trans. Antennas Propag.,* vol. 61, no. 2, pp. 707-717, Feb. 2013.

[10] D. Gonzalez-Ovejero and C. Craeye, "Interpolatory macro basis functions analysis of non-periodic arrays," *IEEE Trans. Antenna Propag.,* vol. 59, no. 8, pp. 3117 – 3122, Aug. 2011.

[11] https://www.cst.com/

[12] B. Hu, et al., ”Fast inhomogeneous plane wave algorithm for the fast analysis of two-dimensional scattering problems,” *Radio Science*, vol. 34, no. 4, pp. 759 - 772, 1999

[13] H. Bui-Van, et al., "Fast and Accurate Simulation Technique for Large Irregular Arrays," *submitted to IEEE Trans. Antennas Propag.,*. Also available at https://arxiv.org/abs/1702.03781.

[14] E. de Lera Acedo, et al.,"Spectral Performance of SKA Log-periodic Antenna I: Mitigating spectral artefacts in SKA1-LOW 21-cm cosmology experiment," Available at https://arxiv.org/abs/1702.05126v2.

[15] O. A. Iupikov, et al.,"Domain-Decomposition Approach to Krylov Subspace Iteration," *IEEE Antennas and Wireless Prop. Letters*, vol. 15, pp. 1414-1417, December 2015.

[16] J. Cavillot, et al., "Efficient analysis of a 3D antenna installed on a finite ground plane," *Proc. 12th Eur. COnf. Antennas Prop.*, London, April 2018.

[17] K. Alkhalifeh, et al.,"Efficient MoM Simulation of 3-D Antennas in the Vicinity of the Ground," *IEEE Trans. Antennas Propag.,* vol. 64, pp. 5335 - 5344, Dec. 2016.

[18] K.A. Michalski and J.R. Mosig, "Multilayered media Green’s functions in integral equation formulations," *IEEE Tran. Antennas Prop.*, vol. 45, Mars 1997.

[19] S. M. Rao, et al, "Electromagnetic scattering by surfaces of arbitrary shape ," *IEEE Tran. Antennas Prop.*, vol. 30, pp. 409-418, 1982.

[20] www.feko.info

[21] Q. Gueuning et al., "Sampling Rules for an Inhomogeneous Plane-wave Representation of Scattered Fields," Accepted for publication in *IEEE Tran. Antennas Propag.,* December 2018.

Gravitational wave searches using radio pulsar timing
Recherche des ondes gravitationnelles par la chronométrie des pulsars

Lucas Guillemot[1,2]

[1]*Laboratoire de Physique et Chimie de l'Environnement et de l'Espace – Université d'Orléans / CNRS, F-45071 Orléans Cedex 02, France, lucas.guillemot@cnrs-orleans.fr*
[2]*Station de radioastronomie de Nançay, Observatoire de Paris, CNRS/INSU, F-18330 Nançay, France*

Keywords: Pulsars, Radio Astronomy, Nançay Radio Telescope, Gravitational Waves
Mots-clefs: Pulsars, Radioastronomie, Nançay Radio Telescope, Ondes Gravitationnelles

Abstract:
Pulsars are rapidly-rotating, highly-magnetized neutron stars both in supernova explosions of massive stars. They produce beams of radio emission that are swept across the sky as they rotate, so that pulsars appear to us as "cosmic lighthouses". The fastest-spinning pulsars, the so-called "millisecond pulsars" (MSPs), have spin periods as short as a few milliseconds and are extremely stable rotators so that the weak radio pulses of an MSP are analogous to the ticks of an ultra-stable clock located at a very large distance. By combining such ticks from an ensemble of MSPs distributed across the sky, it is possible to search for very low-frequency (nHz) gravitational waves (GWs), e.g. emitted by supermassive black hole binaries at cosmological distances. I will present a review of pulsars observations in radio, in the context of GW searches with pulsar timing.

Résumé:
Les pulsars sont des étoiles à neutrons fortement magnétisées et en rotation rapide, nés lors de l'explosion d'étoiles massives en supernovae. Ils produisent des faisceaux d'émission qui balaient le ciel au fil de la rotation de l'étoile, si bien qu'ils nous apparaissent comme des "phares cosmiques". Ceux dont la rotation est la plus rapide, les pulsars milliseconde (MSPs), ont des périodes de rotation de quelques millisecondes seulement. Leur rotation est si stable que les faibles impulsions radio émises par un MSP sont analogues aux battements d'une horloge ultra-stable située à une très grande distance. En combinant les battements d'un ensemble de MSPs bien répartis sur le ciel, il est possible de chercher des ondes gravitationnelles (OGs) de très basses fréquences (nHz), émises par exemple par des systèmes binaires de trous noirs supermassifs, à des distances cosmologiques. Je vais présenter une revue des observations de pulsars en radio, dans le contexte des recherches d'OGs par la chronométrie des pulsars.

1 Introduction: Pulsar Timing

A few years ago, the first detection of gravitational waves (GWs) emitted by coalescing binary black holes by the LIGO-VIRGO interferometers opened the era of GW astrophysics [1]. These ground based detectors are sensitive to GWs with frequencies ranging from a few Hz to several kHz or more. LISA, the GW space observatory, will be launched around 2034 and will be sensitive to GWs in the $10^{-6} - 10^{-1}$ Hz range [2]. At even lower frequencies ($10^{-9} - 10^{-5}$ Hz), Pulsar Timing Arrays (PTAs) use sets of ultra-stable pulsars distributed across the sky to search for GWs emitted, for instance, by supermassive black hole binaries at cosmological distances. In this review we first present the principles of the "pulsar timing" technique, and then give an overview of low-frequency GW searches using PTAs. We finally discuss the current limitations of PTAs and avenues for overcoming these limitations.

Pulsars are rapidly rotating, highly magnetized neutron stars born in supernova explosions of massive stars at the end of their lives. They emit beams of electromagnetic radiation which are swept across the sky as they rotate, in the same way lighthouse beams sweep across an observer, so that they appear to pulse to a distant observer. Since the first discovery of a pulsar in 1967 [3], over 2600 pulsars have now been detected, mainly from radio observations[1]. Most known pulsars are in the Galactic disk, and a fraction reside in globular clusters or in the Magellanic clouds. The majority of known pulsars are split into two categories: "Normal pulsars", which have rotational periods P ranging from 0.1 s to ~10 s, and the so-called "millisecond pulsars" (MSPs) which have periods between 1.4 ms to a few tens of ms and are thought to have been spun-up by the accretion of matter and angular momentum from a companion in a binary system [4]. In practice, most known MSPs are indeed observed to be in binary systems. Radio observations of MSPs have demonstrated that they are extremely stable rotators, that can be used for a large variety of astrophysical applications. Timing observations of the binary pulsar PSR B1913+16 provided the first observational evidence for GWs [5]. Observations of the millisecond pulsar B1257+12 enabled the very first discovery of exoplanets [6]. The long-term timing of the pulsars in the double pulsar system PSR J0737−3039A/B provides stringent tests of theories of gravity in

---

[1] See ATNF Pulsar Catalogue, `http://www.atnf.csiro.au/research/pulsar/psrcat/expert.html`

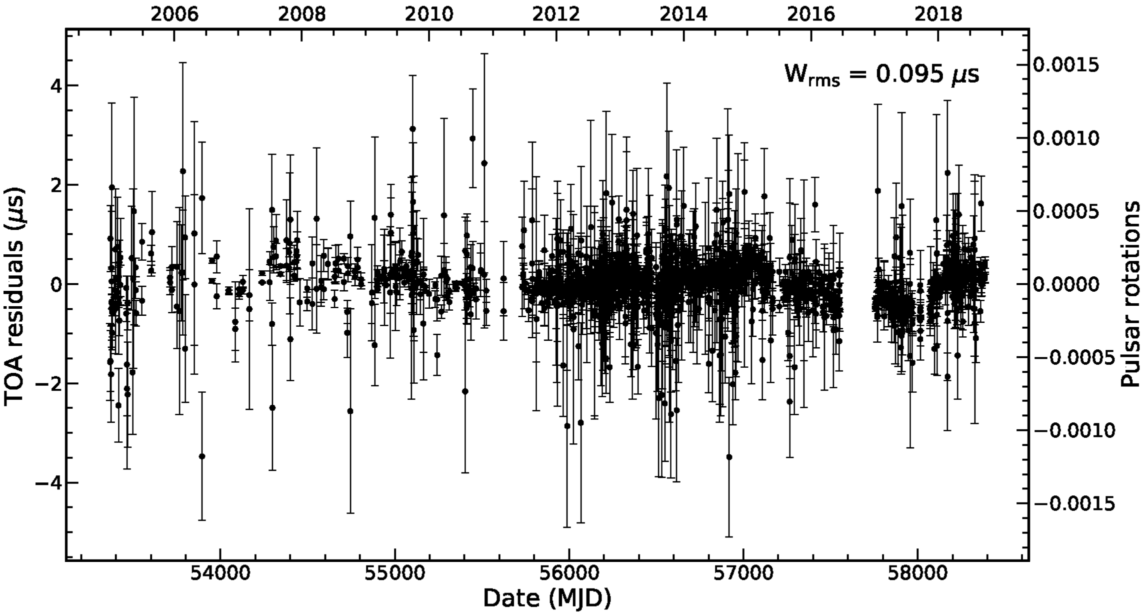

Figure 1 – Nançay Radio Telescope timing residuals for the millisecond pulsar J1909−3744, between 2005 and early 2018. The bulk of the observations were conducted at a frequency of 1.4 GHz, with a bandwidth of 128 MHz for observations made before mid-2011, and a bandwidth of 512 MHz for those made after that date. The RMS of the timing residuals is $\sim$ 95 *ns, i.e., our timing model for PSR J1909−3744 enables us to predict TOAs with a typical accuracy below 100 ns.*

the strong-field regime [7], and the recently-discovery MSP in a triple system, PSR J0337+1715, is a unique laboratory for testing the strong equivalence principle of General Relativity [8].

Pulsar Timing consists in measuring the times of arrival (TOAs) of the pulses of a pulsar at a telescope, and comparing these TOAs with those predicted by a "timing model". Since individual pulses are generally too weak to be detected, pulse profiles are typically formed by averaging up minutes to hours of observation, and the profiles are then compared to a "standard profile" for the pulsar to extract the TOAs. These topocentric TOAs are then transferred to an inertial reference frame, the solar system barycenter, to eliminate effects caused by the motion of the Earth with respect to the pulsar. The timing data are also "dedispersed", *i.e.*, they are corrected for the frequency-dependent dispersion delays caused by the presence of ionized gas between the pulsar and the telescope. For pulsars residing in binary systems, the barycentric TOAs are then corrected for the orbital motion. Finally, the TOAs transferred to the pulsar frame and the pulsar's rotational parameters (rotational period P and subsequent time derivatives, $\dot{P}$, $\ddot{P}$, etc.) are used to calculate rotational phases $\Phi(t)$ as a function of time, which are compared with the predictions of the timing model to form "timing residuals", $R(t)$, calculated as:

$$R(t_i) = P(t_i) \times [\Phi(t_i) - N(t_i)]\,, \tag{1}$$

where t_i denotes the i-th TOA, $P(t_i)$ is the rotational period at t_i, $\Phi(t_i)$ the rotational phase at t_i, and $N(t_i)$ is the nearest integer to $\Phi(t_i)$. Figure 1 shows Nançay Radio Telescope timing residuals over several years for the MSP J1909−3744 (rotational period $P \sim 2.947$ ms, orbital period $P_{\mathrm{orb}} \sim 1.533$ d), the latter MSP being the most stable pulsar visible from Nançay. As can be seen from the above expression, what makes pulsar timing powerful is that it makes it possible to unambiguously account for every single rotation of a given pulsar over long periods of time. Timing models include the pulsar's rotational parameters mentioned above, its astrometric parameters (sky coordinates, proper motion parameters, etc.), dispersion parameters (dispersion measure DM and time derivatives), and the orbital parameters for pulsars in binary systems. The timing residuals are minimized in a least-square fitting procedure to estimate the parameters of the timing model and their uncertainties, using dedicated pulsar timing software such as TEMPO2[2] [9]. Unmodelled, systematic variations in the timing residuals can indicate the existence of errors in the model, or the presence of effects affecting the timing, that need to be accounted for. The latter effects can for instance include unmodelled noise in the pulsar timing, post-Newtonian perturbations to the pulsar's orbital motion, or the signature of gravitational waves.

---

[2] `https://sourceforge.net/projects/tempo2/`

2 Gravitational wave searches with PTAs

As mentioned above, MSPs are extremely stable rotators, and they are thus similar to clocks located at large (typically, galactic) distances that can be used for a number of astrophysical applications. Nevertheless, since the timing of a given MSP can still be affected by unmodelled intrinsic effects, timing noise due to changes of the interstellar medium or other sources of noise (discussed later in this article), increased sensitivity to timing perturbations caused by the passage of GWs can be achieved by observing an array of stable MSPs, widely distributed across the sky and over as long a time period as possible, and by searching for correlations in the timing residuals of these pulsars. In these PTA experiments, the pulsars are test masses, and each pulsar-Earth baseline acts as the arm of giant, Galactic-scale interferometer. In practice, the passage of a GW signal will cause the observed pulse frequency ν of a given pulsar to fluctuate, by:

$$\frac{\partial\nu}{\nu} = -H^{ij}\left[h_{ij}(t_e, x_e^i) - h_{ij}(t_e - D/c, x_p^i)\right], \tag{2}$$

where D is the distance to the pulsar, c is the speed of light, h_{ij} denotes the GW strain evaluated at the Earth at time t_e and position x_e, and at the pulsar, and H^{ij} is a geometrical term that depends on the positions of the GW source, of the Earth and of the pulsar. This rotational frequency will in turn induce fluctuations in the timing, *i.e.*, timing residuals. For example, the amplitude of the timing residuals caused by a distant binary system can be estimated to be [10]:

$$\Delta R(t) = 10\ \text{ns}\left(\frac{1\text{Gpc}}{d}\right)\left(\frac{M}{10^9 M_\odot}\right)^{5/3}\left(\frac{10^{-7}\ \text{Hz}}{f}\right)^{1/3}. \tag{3}$$

In the above expression, d is the distance to the system, f is the GW frequency and $M/(1+z)$ (where z is the redshift) is the total mass of the system.

PTA observations are typically conducted with a sampling interval of days or weeks over $T = 10$ yrs or more, implying that they are sensitive to GWs with frequencies in the order of $1/T \sim 1 - 100$ nHz. In this GW frequency range, potentially detectable sources could be: individual supermassive black hole binary systems, a stochastic background emitted by a population of supermassive black hole binaries distributed throughout the Universe, GW signals from cosmic strings [11] and inflation [12], bursts with memory caused by black hole mergers [13], or other sources of GW bursts. In the case of an isotropic, stochastic background of GWs from a population of supermassive black hole binaries, the timing residuals for pairs of pulsars will be correlated as [14]:

$$\chi(\zeta) = \frac{3}{2}x\ln x - \frac{x}{4} + \frac{1+\delta(x)}{2} \tag{4}$$

with $x = \dfrac{1-\cos(\zeta)}{2}$. Here, ζ is the sky separation between the two pulsars and δ is the Dirac delta function. This correlation function, which is displayed in Figure 2, is known as the Hellings-and-Downs curve.

Three major PTAs are currently actively searching for low-frequency gravitational waves. The Parkes PTA (PPTA, [16]) uses pulsar timing data from the Parkes radio telescope in Australia. The North American Nanohertz Observatory for Gravitational Waves (NANOGrav, [17]) uses pulsar observations made with the Green Bank telescope in the US and with Arecibo telescope in Puerto Rico. Finally, the European PTA (EPTA, [18]) uses pulsar timing data recorded with the Jodrell Bank (UK), Westerbork (Netherlands), Effelsberg (Germany), Sardinia (Italy) and Nançay (France) radio telescopes. Each PTA typically has timing data on a few tens of MSPs over time periods of a few years to several decades. The three PTAs have recently joined forces and combined data to form an International PTA (IPTA, [19]), whose sensitivity is higher than those of individual PTAs. Data from the five European telescopes are also combined coherently, to simulate pulsar observations with a much higher effective aperture, equivalent to a 195-m diameter telescope (the Large European Array for Pulsars, LEAP, see [18]). In the future, it is expected that radio telescopes located in other countries or regions will join the IPTA and contribute to GW searches. Examples include the Chinese Five Hundred Metre Aperture Spherical Telescope (FAST) that recently started operating, the future 110-m diameter fully-steerable single-dish radio telescope QTT, also in China, MeerKAT in South Africa and the planned Square Kilometre Array (SKA). Telescopes that are currently in the IPTA and those that are expected to join in the future are shown in Figure 3.

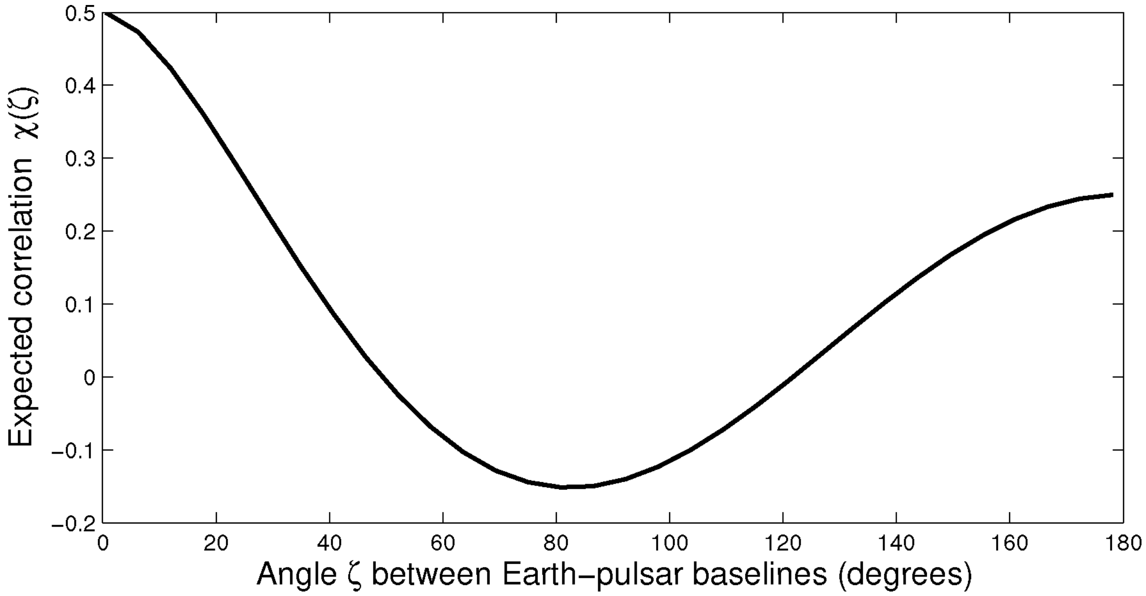

Figure 2 – The Hellings-and-Downs curve, which corresponds to the expected correlation between the timing residuals of pairs of pulsars due to an isotropic stochastic background of GWs, as a function of the angular separation between the pulsars in the pairs. Figure taken from [15].

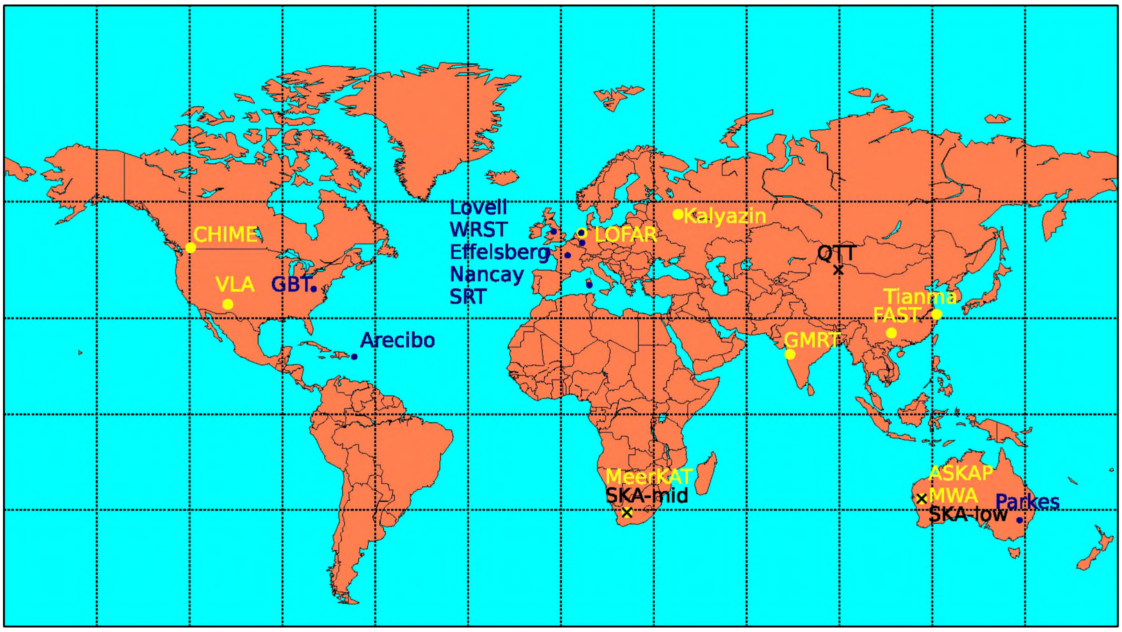

Figure 3 – Map showing the locations of the radio telescopes that are currently part of the International Pulsar Timing Array (IPTA), and those that are expected to join in the future. Telescopes that are already in the IPTA are labelled in blue. Figure adapted from [20].

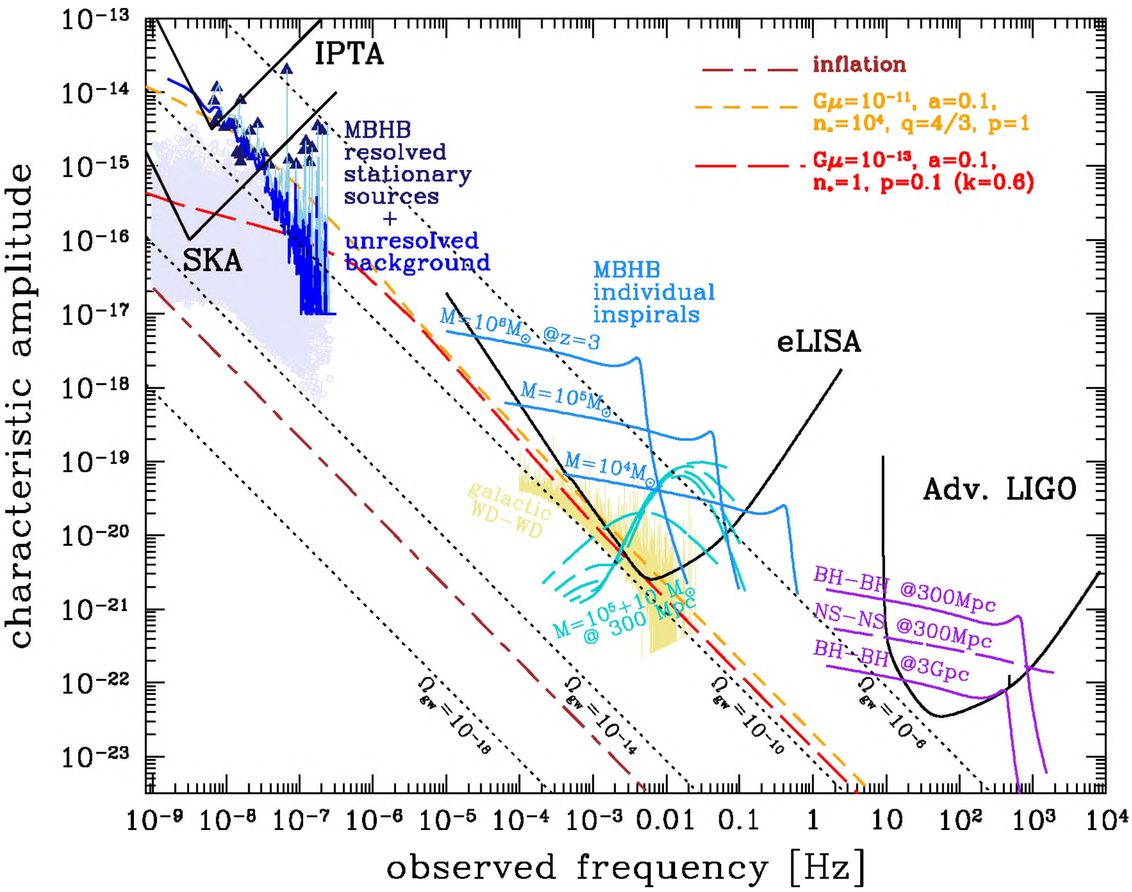

Figure 4 – Characteristic strain h_c of gravitational waves as a function of frequency. The expected sensitivities of the IPTA and of the SKA are plotted, along with realizations of the expected GW signal from the cosmological population of supermassive black hole binaries. The brown, red and orange lines correspond to expected cosmological backgrounds from standard inflation and selected string models, with the parameters displayed at the top right. Also shown are the eLISA sensitivity curve and the expected sensitivity curve of Advanced LIGO. See [26] for full details.

The continental and international PTAs have, until now, not been able to detect any low-frequency GW signal in the pulsar timing data. A number of upper limits on the amplitude of a gravitational wave background have been published (see e.g. [21, 22, 23]). One of the most stringent upper limits placed to date is that published by the IPTA, of 1.7×10^{-15} [24]. IPTA limits on a stochastic background of gravitational waves are plotted in Figure 4, along with the expected sensitivity curves for the SKA, eLISA and Advanced LIGO. Numerous other upper limits have been placed on GW emission from individual supermassive black hole binary systems, or GW bursts with memory. As can be seen from Figure 4, it is expected that future radio telescopes, such as the SKA, will increase our sensitivity of low-frequency GWs significantly. New generation instruments will indeed enable us to monitor known stable MSPs with much increased sensitivity and thus extract more precise and more numerous TOAs. Additionally, they will allow us to probe the Galactic population of MSPs much more deeply, thereby increasing the number of ultra-stable MSPs that PTAs could monitor. It is expected [25] that 5 to 10 years of timing of at least 20 MSPs with an accuracy better than 100 ns would be needed to make a first detection of the GW background. At present, this level of accuracy is achieved on a handful of MSPs only; hence the need to discover many new stable MSPs. However, current PTA experiments also need to address a number of limitations to increase their sensitivity to gravitational waves. In the following section we discuss some of the main known limitations of GW searches with PTAs.

3 Current limitations

As mentioned in the previous section, currently-existing PTAs have not yet been able to detect significant GW emission in the $\sim 1 - 100$ nHz frequency range. One obvious limitation in current searches for GWs by PTAs is that the number of MSPs that can be timed with very high accuracy (typically, with an RMS timing residual < 100 ns over a decade or more) is limited to a handful of objects at present. Future pulsar searches with new generation radio telescopes such as FAST, MeerKAT or SKA will likely expand the known population of ultra-stable MSPs. With their increased collective area and frequency bandwidths, future instruments will also measure pulsar TOAs much more accurately. Denoting σ the uncertainty on a given TOA, we have:

$$\sigma \propto \frac{w}{S_{\mathrm{PSR}}} \times \frac{T_{\mathrm{sys}}}{A} \times \frac{1}{\sqrt{B \times t_{\mathrm{obs}}}}. \tag{5}$$

In the above expression, w is the pulse width of the considered pulsar, S_{PSR} is its flux density, T_{sys} is the telescope's system temperature, A its collecting area, B is the frequency bandwidth and t_{obs} denotes the duration of the observation.

Interestingly, for some bright MSPs the sensitivity of current telescopes is not a limiting factor for timing precision. One key assumption of current pulsar timing techniques is that pulsar pulse profiles are stable when averaged over a large enough number of rotations. Under this assumption, pulsar profiles are averaged and compared to a standard profile for extracting TOAs, which then refer to a common phase in the pulse profile. For a small number of MSPs such as PSR J1713+0747, intrinsic fluctuations in the phase and amplitude of the pulse components are observed, a phenomenon known as "pulse jitter" (see e.g. [27]). Pulse jitter is a source of white noise that limits timing accuracy for the brightest MSPs only. However, with their much increased sensitivity compared to current instruments, future telescopes are expected to be very affected by jitter noise. A way to limit the effect of jitter is to increase the duration of observations, so that phase and amplitude fluctuations get averaged.

In addition to this source of noise acting on short timescales, MSPs are also affected by long-term timing perturbations referred to as "timing noise". These perturbations are currently not well understood and are most prominent in pulsars with long data spans and high-enough instantaneous timing accuracy. Various methods exist for whitening the white noise and the red noise introduced by those long-term intrinsic instabilities.

Other sources of noise affecting pulsar timing on both short and long timescales are those caused by changes in the interstellar plasma, between pulsars and the Earth. Radio waves are dispersed by the free electrons along the line-of-sight between the observed pulsar and the telescope. This dispersion effect induces a time delay given by:

$$\Delta t_{\mathrm{DM}} = D \times \frac{\mathrm{DM}}{f^2}, \tag{6}$$

where f is the observing frequency, $D = 4.148808 \times 10^3$ MHz^2 pc^{-1} cm^3 s is the dispersion constant and DM, the "dispersion measure", is the integrated column density of free electrons: $\mathrm{DM} = \int_0^d n_e \, dl$. The latter quantity is observed to vary as the Earth and the pulsars move with respect to the interstellar medium. As a consequence of this DM variation, the timing residuals of MSPs are affected by frequency-dependent delays that can be mitigated by observing pulsars at different radio frequencies, or by using wide-band frequency receivers. Pulsar observations at low radio frequencies (*i.e.*, 100 – 400 MHz or below) by instruments such as LOFAR or NenuFAR are particularly useful in this regard, since they are strongly affected by dispersive effects and can thus be used to monitor and study turbulences in the interstellar medium. Additionally, multi-path propagation in the inhomogeneous interstellar plasma can cause radio pulses from pulsars to get broadened. The time-varying delays introduced by this pulse broadening are another source of noise that need to be mitigated when analyzing PTA data.

Unlike the above sources of noise, which are generally uncorrelated between pulsars, some other processes can introduce correlated noise in the timing data. Understanding and mitigating correlated noise is of prime importance, since, as mentioned above, PTAs search for low-frequency gravitational wave signals by analyzing correlations in the timing residuals of arrays of pulsars. Sources of correlated noise are, for example:

- Errors in terrestrial clocks, which are expected to affect TOA measurements of all pulsars identically.
- Inaccuracies in solar system ephemerides, which are used to convert topocentric TOAs to the solar system barycenter.
- Variations in the solar wind, which induce frequency-dependent timing residuals.

The Nançay Radio Telescope plays a key role in the search for GWs with PTAs, by recording large volumes of high-quality pulsar timing data which are shared and analyzed in the context of the EPTA and of the IPTA.

The current pulsar instrumentation in place at the Nançay Radio Telescope is the "NUPPI" backend, which has been used as the main pulsar instrument since mid-2011. Nançay observations of pulsars are mainly done at 1.4 GHz, with observations also done at higher frequencies of 2.1 or 2.5 GHz, to be sensitive to the short and long-term DM variations mentioned above. The NUPPI backend coherently dedisperses the radio signal over a total instantaneous frequency bandwidth of 512 MHz. The pulsar team in Orléans is currently involved in the construction of a new backend, that will enable pulsar observations over a total frequency bandwidth of ~ 2 GHz. Such large instantaneous frequency coverage will be particularly useful for mitigating several of the above-listed sources of noise.

The list of noise processes given above is non exhaustive. Current PTAs are actively working on understanding these sources of noise and defining analysis or observation strategies for mitigating them as much as possible. Despite these limitations, PTAs have already obtained stringent limits on GW emission from the population of supermassive black hole binaries, and have started to put some strong constraints on the properties of this population. With their much increased sensitivity compared to current telescopes, future large radio telescopes such as the SKA will make it possible to monitor pulsars with very high timing accuracy and will also discover many new stable MSPs. Although challenging, PTA-type GW searches with future instruments will undoubtedly open a new window on the study of GWs at low frequencies.

4 References

[1] B. P. Abbott, R. Abbott, T. D. Abbott, *et al.*, "Observation of Gravitational Waves from a Binary Black Hole Merger," *Physical Review Letters*, vol. 116, p. 061102, Feb. 2016.

[2] P. Amaro-Seoane, H. Audley, S. Babak, *et al.*, "Laser Interferometer Space Antenna," *arXiv e-prints*, Feb. 2017.

[3] A. Hewish, S. J. Bell, J. D. H. Pilkington, P. F. Scott, and R. A. Collins, "Observation of a Rapidly Pulsating Radio Source," *Nature*, vol. 217, pp. 709–713, Feb. 1968.

[4] M. A. Alpar, A. F. Cheng, M. A. Ruderman, and J. Shaham, "A new class of radio pulsars," *Nature*, vol. 300, pp. 728–730, Dec. 1982.

[5] J. H. Taylor and J. M. Weisberg, "A new test of general relativity - Gravitational radiation and the binary pulsar PSR 1913+16," *ApJ*, vol. 253, pp. 908–920, Feb. 1982.

[6] A. Wolszczan and D. A. Frail, "A planetary system around the millisecond pulsar PSR1257 + 12," *Nature*, vol. 355, pp. 145–147, Jan. 1992.

[7] M. Kramer, I. H. Stairs, R. N. Manchester, *et al.*, "Tests of General Relativity from Timing the Double Pulsar," *Science*, vol. 314, pp. 97–102, Oct. 2006.

[8] A. M. Archibald, N. V. Gusinskaia, J. W. T. Hessels, *et al.*, "Universality of free fall from the orbital motion of a pulsar in a stellar triple system," *Nature*, vol. 559, pp. 73–76, July 2018.

[9] G. B. Hobbs, R. T. Edwards, and R. N. Manchester, "TEMPO2, a new pulsar-timing package - I. An overview," *MNRAS*, vol. 369, pp. 655–672, June 2006.

[10] F. Jenet, L. S. Finn, J. Lazio, *et al.*, "The North American Nanohertz Observatory for Gravitational Waves," *arXiv e-prints*, Sept. 2009.

[11] S. A. Sanidas, R. A. Battye, and B. W. Stappers, "Constraints on cosmic string tension imposed by the limit on the stochastic gravitational wave background from the European Pulsar Timing Array," *Phys. Rev. D*, vol. 85, p. 122003, June 2012.

[12] M. L. Tong, Y. Zhang, W. Zhao, J. Z. Liu, C. S. Zhao, and T. G. Yang, "Using pulsar timing arrays and the quantum normalization condition to constrain relic gravitational waves," *Classical and Quantum Gravity*, vol. 31, p. 035001, Feb. 2014.

[13] J. M. Cordes and F. A. Jenet, "Detecting Gravitational Wave Memory with Pulsar Timing," *ApJ*, vol. 752, p. 54, June 2012.

[14] R. W. Hellings and G. S. Downs, "Upper limits on the isotropic gravitational radiation background from pulsar timing analysis," *ApJ*, vol. 265, pp. L39–L42, Feb. 1983.

[15] F. A. Jenet and J. D. Romano, “Understanding the gravitational-wave Hellings and Downs curve for pulsar timing arrays in terms of sound and electromagnetic waves,” *American Journal of Physics*, vol. 83, pp. 635–645, July 2015.

[16] G. Hobbs, “The Parkes Pulsar Timing Array,” *Classical and Quantum Gravity*, vol. 30, p. 224007, Nov. 2013.

[17] M. A. McLaughlin, “The North American Nanohertz Observatory for Gravitational Waves,” *Classical and Quantum Gravity*, vol. 30, p. 224008, Nov. 2013.

[18] M. Kramer and D. J. Champion, “The European Pulsar Timing Array and the Large European Array for Pulsars,” *Classical and Quantum Gravity*, vol. 30, p. 224009, Nov. 2013.

[19] R. N. Manchester and IPTA, “The International Pulsar Timing Array,” *Classical and Quantum Gravity*, vol. 30, p. 224010, Nov. 2013.

[20] G. Hobbs and S. Dai, “A review of pulsar timing array gravitational wave research,” *arXiv e-prints*, July 2017.

[21] L. Lentati, S. R. Taylor, C. M. F. Mingarelli, *et al.*, “European Pulsar Timing Array limits on an isotropic stochastic gravitational-wave background,” *MNRAS*, vol. 453, pp. 2576–2598, Nov. 2015.

[22] R. M. Shannon, V. Ravi, L. T. Lentati, *et al.*, “Gravitational waves from binary supermassive black holes missing in pulsar observations,” *Science*, vol. 349, pp. 1522–1525, Sept. 2015.

[23] Z. Arzoumanian, A. Brazier, S. Burke-Spolaor, *et al.*, “The NANOGrav Nine-year Data Set: Limits on the Isotropic Stochastic Gravitational Wave Background,” *ApJ*, vol. 821, p. 13, Apr. 2016.

[24] J. P. W. Verbiest, L. Lentati, G. Hobbs, *et al.*, “The International Pulsar Timing Array: First data release,” *MNRAS*, vol. 458, pp. 1267–1288, May 2016.

[25] F. A. Jenet, G. B. Hobbs, K. J. Lee, and R. N. Manchester, “Detecting the Stochastic Gravitational Wave Background Using Pulsar Timing,” *ApJ*, vol. 625, pp. L123–L126, June 2005.

[26] G. Janssen, G. Hobbs, M. McLaughlin, *et al.*, “Gravitational Wave Astronomy with the SKA,” *Advancing Astrophysics with the Square Kilometre Array (AASKA14)*, p. 37, Apr. 2015.

[27] K. Liu, C. G. Bassa, G. H. Janssen, *et al.*, “Variability, polarimetry, and timing properties of single pulses from PSR J1713+0747 using the Large European Array for Pulsars,” *MNRAS*, vol. 463, pp. 3239–3248, Dec. 2016.

L'émission radio du fond du ciel au-dessous de 10 MHz
On Galactic background radiation at frequencies below 10 MHz

***Alain Lecacheux*[1], *Milan Maksimovic*[2]**

[1]*LESIA-Observatoire de Paris, alain.lecacheux@obspm.fr*
[2]*LESIA-Observatoire de Paris, milan.maksimovic@obspm.fr*

Mots clés: radioastronomie ; galaxie ; milieu interstellaire.
Keywords : radio astronomy ; galaxy ; interstellar medium.

Résumé/Abstract

Aux grandes longueurs d'onde, le signal radio venant du fond du ciel est la résultante des émissions et absorptions des rayonnements thermiques et non thermiques du gaz ionisé interstellaire et des radiosources discrètes galactiques et extra galactiques. Au-dessus de la fréquence de coupure ionosphérique (10-15 MHz), la distribution de brillance, maintenant bien cartographiée, est essentiellement celle d'une émission concentrée le long de l'équateur galactique, avec un maximum en direction du Centre Galactique, et d'un halo plus diffus qui décroit en intensité vers les pôles. Au-dessous de 10 MHz, faute de résolution spatiale de la part des radiomètres embarqués sur satellite, la distribution de brillance du ciel en radio reste très mal connue. Quelques rares observations depuis le sol, dans des conditions extrêmes, et les prédictions théoriques, suggèrent une situation inverse: l'équateur galactique en absorption et l'émission plutôt concentrée vers les hautes latitudes. En utilisant les données d'expériences de radioastronomie spatiale récentes (Cassini/RPWS par exemple), équipées de corrélateurs analysant plusieurs antennes filaires en rotation avec le satellite, nous montrons en effet qu'entre 10 et 1 MHz la distribution de brillance évolue graduellement d'une situation à l'autre. Nous décrivons la méthode, ses limitations, et les implications astrophysiques du résultat.

The brightness distribution of the radio sky is nowadays well documented in the part of the radio spectrum above Earth's ionosphere cut-off. As the result of emissions and absorptions of thermal and non-thermal radiations from interstellar ionized gas and discrete radio sources, the brightness is concentrated along the Galactic Equator, mainly towards the Galactic Centre. In the frequency range not available from the ground and lacking of instrumentation with spatial resolution capability (typically below 10 MHz), theoretical predictions and a few observations indicated that the maximum sky brightness would be rather located at much higher galactic latitudes. By analysing data from a radio spectrometer using a spinning, tri-axial antenna system (e.g. Cassini/RPWS), we confirm that the overall galactic brightness distribution gradually evolves from equatorial to polar, when frequency is decreasing. We describe our method of analysis, its limitations and discuss astrophysical implications of the result.

1 Introduction

Among the wealth of contributions to the knowledge of the Universe brought to us by the Radio Astronomy, a basic one is the appearance of the whole (radio) sky as a function of the frequency. Its description has well progressed in the two last decades thanks to the development of powerful radio imaging techniques and also because of the necessity to clean the newly obtained Cosmic Microwave Background maps from all foreground contaminations.

In the frequency range available from the ground (say from about 30 MHz to 100 GHz and above), the overall picture is now well described and understood [1]: it is dominated by an anisotropic diffuse component, concentrated along the Galactic Equator (the plane of our Galaxy), mainly in direction of the Galactic Centre (Sgr A), The observed brightness is a combination of thermal emission and absorption by the galactic warm ionized gas (mainly HII) and of non-thermal emission by the galactic relativistic electrons. A second weaker component, likely to be isotropic, is due to the large (infinite ?) amount of emitting extragalactic radio sources lying in every direction. Since the free-free optical depth of such a medium varies with the frequency (as $\nu^{-2.1}$), the relative contrast of the various visible structures is changing with the frequency, but the large scale features remain similar over the whole spectrum [1]. An example of such a sky radio map, which was recently obtained at the frequency of 45 MHz [2], is shown in Fig. 2a.

In the frequency range blocked by Earth's ionosphere (from about 30 MHz or below), the appearance of the radio sky is much less documented. In space, techniques are not yet available to directly make maps with angular resolution comparable to what can be done from the ground. However, a few observations from the ground, made in special conditions, indicate that the sky appearance, regarding its brightness distribution, might be very different in the lowest frequency range. For instance, taking good advantage of an ionospheric hole over Tasmania, Reber [3], then Ellis [4] were able to observe sky at frequencies as low as 2 MHz, measuring a much higher brightness at the South Galactic Pole than at the Equator.

Even more convincing, - and this time by using a space borne experiment -, Manning and Dulk [5] were using radio data from the WIND spinning spacecraft and suggested that the sky brightness maximum location moves from the Galactic Centre to the Poles when the observing frequency varies from 10 down to 1 MHz. They were using the modulated antenna response due to the spacecraft spin, but in a somewhat qualitative way. As stated in their paper: “as the antenna rotates, the received intensity varies from a maximum approximately when the antenna is broadside to the regions of lowest brightness”. The aim of the present paper is to investigate what can be ultimately done with such a space experiment, - say, a wideband spectrometer fed to a system of wire antennas aboard a spinning spacecraft -. In section 2, we present a quantitative formulation of the problem. In section 3 we show an example of application obtained by using the Cassini/RPWS instrument en route to Saturn. The results are briefly discussed in section 4.

2 What can be actually obtained by using a radiometer on a single spacecraft ?

In the fields of solar and planetary space radio astronomy, there is an abundant literature on spinning radio antennas (for instance [6], [7], [8]). The method was mostly used for studying small size radio sources, so that only the simplest point source case was deeply analysed. Applying those simple analyses to the extended case of the galactic radiation is clearly not satisfying. However, it is known for a long time ([3], [4]) that the galactic background can modulate the antenna output at a significant level, only depending on the sensitivity of the receiving system.

Our method of analysis starts with the basic relationship between the incident electric field and the antenna output voltage, here written in the (frequency) Fourier domain as a scalar product of complex quantities:

$$V(\omega) = H^{\dagger}E(\omega) \qquad (1)$$

The factor H is the impulse response of the antenna, considered as a linear (filtering) device. It is otherwise known as the antenna *effective length* vector. The latter can also be modelled as the Fourier transform of the (steady) current established on the antenna body. In the case of a system of several antennas, the equation (1) still hold: H becomes a matrix and V is the vector of the corresponding antenna output voltages. Effective lengths are most often considered in projection onto the plane perpendicular to the wave vector (which contains the incident electric field for a source at infinite distance). Here we will rather characterize the antenna(s) by their effective lengths expressed in some working reference frame (for instance the spacecraft XYZ reference frame) and consider the matrix R of the transformation from this frame to the wave reference frame. The basic equation read now as:

$$V = (RH)^{\dagger}E$$

The covariance matrix of the measured voltages, - the final output of the system -, follows as:

$$\Gamma_A = \langle VV^{\dagger}\rangle = H^{\dagger}\,(R^T\Gamma R)\,H \qquad (2)$$

where $\Gamma = \langle EE^{\dagger}\rangle$ is the coherence matrix of the incident electric field. Brackets mean integration over time. In the following, since observing frequencies are lower than 10 MHz and antenna lengths shorter than a few meters, the antennas can be considered as short with respect to the wavelength: H does not depend on the wave direction (but can depend on the frequency) and is a real vector, at least within a reasonable approximation. The matrix $C_0 = R^T\Gamma R$ contains most of the information available from the observed electromagnetic wave (namely its direction, intensity and polarisation).

Let consider the brightness $B_\nu(\theta,\varphi)$ of the whole radio sky as made of individual, uncorrelated, unpolarised point sources located in each direction (θ,φ). The overall radiation from the whole sky is then characterized by:

$$C_{4\pi} = \iint C_0(\theta,\varphi)\sin\theta\, d\theta\, d\varphi = \iint B_\nu(\theta,\varphi)\, M(\theta,\varphi)\sin\theta\, d\theta\, d\varphi$$

in which $M(\theta,\varphi)$ is some matrix (not shown here for saving space) containing sine and cosine combinations up to the power of 2.

Now the $B_\nu(\theta,\varphi)$ function, defined on the 2-sphere S_2, can be developed in a series of orthogonal spherical harmonics Y_l^m, as:

$$B_\nu(\theta,\varphi) = \sum_{l} \sum_{|m|\le l} b_{l,m} Y_l^m(\theta,\varphi) \tag{3}$$

together with the reciprocal formula: $b_{l,m} = \iint B_\nu(\theta,\varphi)\, \bar{Y}_l^m(\theta,\varphi) \sin\theta \, d\theta \, d\varphi$. The $b_{l,m}$ are complex numbers, often described as the Fourier coefficients of the expansion (3) on the sphere S_2. Substituting in the above integral, one obtains:

$$C_{4\pi} = \sum_{l} \sum_{|m|\le l} b_{l,m} \iint Y_l^m(\theta,\varphi)\, M(\theta,\varphi) \sin\theta \, d\theta \, d\varphi$$

One can easily check that all the integrals in previous formula vanish, except those for $l = 0$ and $l = 2$, so that one get:

$$C_{4\pi} = \sqrt{\frac{2\pi}{15}} \begin{bmatrix} \frac{2\sqrt{5}\, b_{0,0} + b_{2,0}}{\sqrt{6}} - \mathrm{Re}(b_{2,2}) & \mathrm{Im}(b_{2,2}) & \mathrm{Re}(b_{2,1}) \\ \mathrm{Im}(b_{2,2}) & \frac{2\sqrt{5}\, b_{0,0} + b_{2,0}}{\sqrt{6}} + \mathrm{Re}(b_{2,2}) & -\mathrm{Im}(b_{2,1}) \\ \mathrm{Re}(b_{2,1}) & -\mathrm{Im}(b_{2,1}) & 2\frac{\sqrt{5}\, b_{0,0} - b_{2,0}}{\sqrt{6}} \end{bmatrix} \tag{4}$$

Given a particular antenna system described by the H matrix, the output of the correlator (formula (2)), corresponding to the “all sky” emission, finally read as:

$$\Gamma_A = H^\dagger\, C_{4\pi}\, H \tag{5}$$

While the actual sky map would in principle be defined by a large number of $b_{l,m}$ coefficients, the observed radio map appears to be strongly filtered into only six independent measurable quantities, namely: the real parts of $b_{0,0}$ and $b_{2,0}$, and the real and imaginary parts of $b_{2,1}$ and $b_{2,2}$ (taking into account that $b_{2,-1} = -\bar{b}_{2,1}$ and $b_{2,-2} = \bar{b}_{2,2}$ since B_ν is a real function).

A consistency check can be done by substituting in (4) the coefficients for the point source in direction (θ_0, φ_0)

$$b_{l,m}^{(0)} = \iint \delta(\theta - \theta_0, \varphi - \varphi_0)\, \bar{Y}_l^m(\theta,\varphi) \sin\theta \, d\theta \, d\varphi$$

and verifying that (4) reduces to $C_0(\theta_0, \varphi_0)$.

When the spacecraft spins and the antenna boom rotates, the signal (formula 5) is modulated at both the fundamental and first harmonics of the spin frequency [6]. The resulting Fourier series is made of three complex components, corresponding to five independent real quantities, which can be easily fitted to the data. One can show that there is a one-to-one correspondence between those spin modulation Fourier components and the $\{b_{0,0}, b_{2,m}\}$ components described above.

A single antenna on a spinning spacecraft is not enough for retrieving all the six quantities ($b_{0,0}$ and $b_{2,0}$ cannot be resolved). At least two antennas are needed, with different tilt angles with respect to the spin axis. The “ideal” configuration [11] would involve three no coplanar antennas in full correlation: all the six involved quantities can then be determined with some redundancy, what can be useful for a maximum accuracy.

Changing the working reference frame, i.e. the orientation of the spacecraft spin axis, if any, does not bring any new information. Indeed, it is well known [12] that, under a rotation, each spherical harmonic Y_l^m of degree l is transformed into a linear combination of the Y_l^m with same l degree, namely:

$$R\left(Y_l^{m'}\right)(\theta,\varphi) = \sum_{|m|\le l} Y_l^m(\theta,\varphi)\, \mathcal{D}_{m,m'}^{(l)}(R)$$

leading to the component transformation:

$$R(b_{l,m'}) = \sum_{|m|\leq l} \overline{\mathcal{D}}^{(l)}_{m,m'}(R)\, b_{l,m} \tag{6}$$

whose calculation involves the so-called Wigner-D matrices, well studied and used in quantum mechanics and particle physics [10]. From the latter result, a powerful method for precise, in flight calibration of any space borne low frequency radio astronomy instrument could be derived, based on the determination of the amplitudes and phases of the $b_{2,m}$ coefficients at each frequency.

3 An application by using data from the Cassini/RPWS instrument :

The Radio and Plasma Wave Science investigation on board of the *Cassini* Saturn's orbiter is fully described in [11]. The HFR part of the instrument mainly dedicated to radio astronomy, was designed and developed in the Space Department of the Paris Observatory in the 1990s. It is based on digital, real time, spectral correlation of several pass band filters, analyzing a set of three 10 meter long, wire antennas. The analyzed frequency range extends from about 1 kHz to 16 MHz.

While *Cassini* orbiter was originally designed as a 3-D stabilized spacecraft, rolling the whole spacecraft about various axes was a thoroughly used method to move on board scientific instruments on their target, as well as for calibrating and doing general housekeeping. Many thousands of such roll manoeuvres are available throughout the life of *Cassini*.

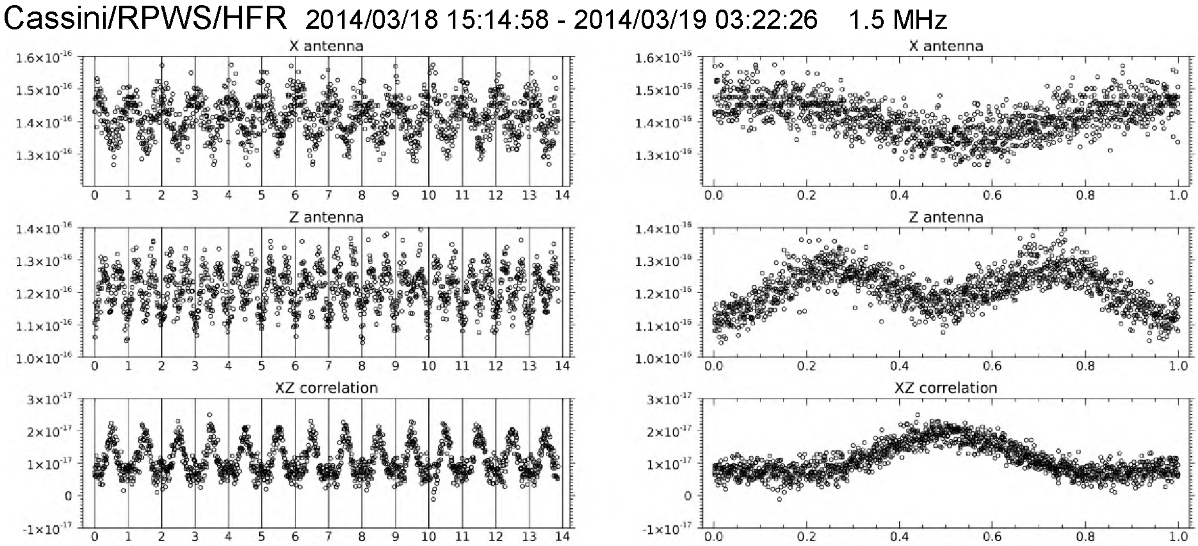

Figure 1 : Example of a Cassini roll maneuver, lasting about 12 hours on 2014, March 18. The left panel shows full time waveforms of the available output at 1.6 MHz from one pair of RPWS monopole antennas (X and Z). The horizontal axis is graduated in number of rotations at the rate of 2 milliRad/sec. The vertical axis is expressed in V^2Hz^{-1} at the receiver input. In the right panel, the same data are displayed, but after folding the rotation phase. The modulation amplitude, of the order of 20% of the DC level, is well measurable in spite of the instrumental noise due to the spectral analysis.

Fig.1 shows an example of a long lasting roll manoeuvre, dedicated to in flight calibration of another on board scientific instrument. The right panel displays the waveforms, at the frequency of 1.5 MHz, of the $\langle XX^*\rangle, \langle ZZ^*\rangle, \mathrm{Re}\langle XZ^*\rangle$ correlator output, computed by the digital receiver in real-time. Another pair of antennas (YZ) was analyzed in the same time, allowing for an accurate measurement of the coefficients of the $C_{4\pi}$ matrix given by formula (4)).

Fig.2 summarizes our final result. All six displayed maps are radio maps of the whole sky (shown in Mollweide projection, as described in the legend of the figure). The four first maps ((a) to (d)) are drawn from a reference map taken at the 45 MHz radio frequency and extracted from the low frequency sky survey by the LWA1 radio telescope [2]: the map is drawn in galactic coordinates, with an angular resolution of 3.6°. Map (b) is drawn from the same data as map (a), but in coordinates of the spacecraft reference frame corresponding to the orientation of *Cassini* at the starting time of the manoeuvre displayed in Fig.1 and computed from the archived *Cassini* spacecraft attitude data. Map (c), still in this reference frame, was built by using formula (3) and spherical harmonics components obtained from map (b). Then, formula (6) was used to back transform map (c) into galactic reference frame, as in map (a).

Comparison of map (c) with map (b), or map (d) with map (a), illustrates the huge angular resolution loss of the method, as discussed in previous section. The comparison of map (d) with map (a) shows also that the large scale brightness distribution is not too much distorted: the maximum brightness is well found at the centre of the map, the poles have much lower intensities, as expected. Replication at 180° of the bright central patch is an artefact due to the absence of $b_{1,m}$ harmonics (or, equivalently, due to the dipolar antenna beam symmetry between any direction and its anti-direction).

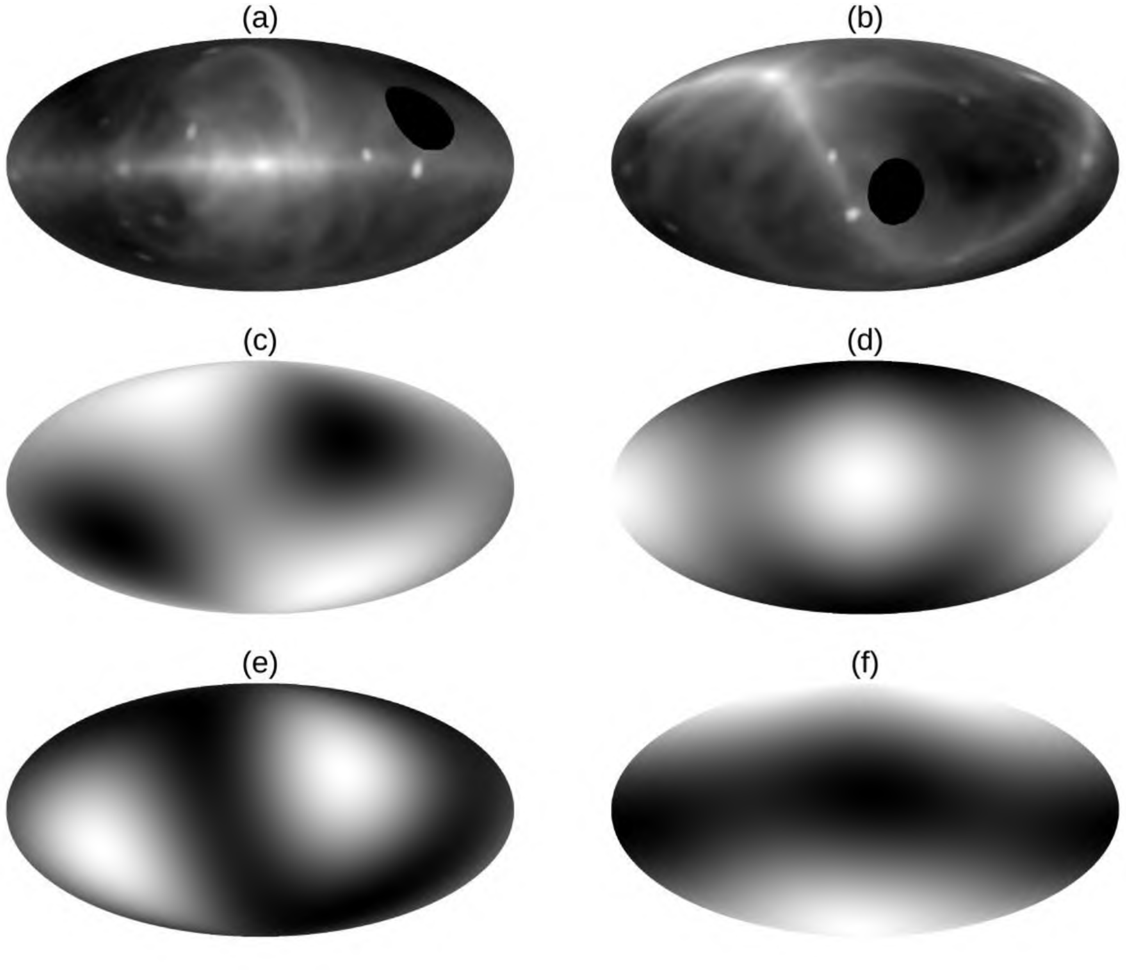

Figure 2 : six radio maps of the whole sky, drawn in Mollweide projection (North pole at the top; increasing longitudes from left (-180°) to right(+180°)). (a) reference map (45 MHz) in galactic coordinates; (b) same map but; (c) same as (b), but after antenna "filtering"; (d) back to galactic reference frame, to be compared to (a); (e) real measurement in the S/C reference frame, done at 1.5 MHz, by using Cassini/RPWS/HFR data; (f) back to galactic reference frame, to be compared to (a). See text for details.

The two last maps ((e) and (f)) are built by using the data (Fig.1) actually measured at much lower radio frequency, namely 1.5 MHz. Map (e) results from applying formula (3) as in case of map (c). Map (f) is the transformation into galactic coordinates by applying formula (6).

Clearly, passing from map (a) (or (d)) to map (f), that is from frequency range lying above to below 10 MHz, exchanges bright and dark regions. At 1.5 MHz, the galactic poles unambiguously appear to be much more brighter than the equator with, maybe, an excess of brightness at the South pole over the North one.

4 Discussion

Our result is not completely surprising: it is the confirmation of previous observations, as stated in the introduction. But for the first time, at our knowledge, one can get a clear evidence that the radio sky appearance is drastically changing when the observing frequency is decreasing from above to below 10 MHz.

The main reason is the presence within the galactic interstellar medium of a large amount of warm ionized gas (the so called Warm Ionized Medium), which has been inferred from other observations also. It is now believed that the WIM is responsible for producing, for instance, the diffuse optical H_α emission, the dispersion of pulsar radio signals, and the Faraday rotation observed in every direction in our Galaxy [15]. From all these observations, a general, quantitative picture of the WIM was deduced: with an average electron density of 0.025 cm^{-1} and an average temperature of 10^4 K, this is a quite irregular medium made of blobs (filling factor of ~0.1) of density 0.1-0.5 cm^{-1} and scale height of 1 kpc. Taking into account those physical properties, one can expect that the WIM optical depth is close to zero in all directions at 100 MHz and above, progressively increases with decreasing frequency in dense regions, then that the medium becomes optically thick to any radio emissions at some very low frequency (estimated to be around 4 MHz by using above numbers). For a far observer located in the periphery of the Galaxy (the case of the Solar System), the consequence is a strong extinction, from this frequency downward, of the synchrotron emission produced by the far galactic relativistic electrons, leaving only place to the emission from the local ones, within a radius of a few kpc. This absorption being likely more pronounced towards the equator than towards the poles.

If this scenario is correct, an increase of the angular resolution would show the irregularities that exist in the interstellar medium, e.g. the distribution of HII regions and dense clouds. A little bit more remains to be extracted from the existing single spacecraft radio observations. This is under study, now.

In the future, hopefully not too far, the final answer will become available when antenna arrays will be deployed on spacecraft clusters and will provide, by using interferometric technique, true detailed images of the sky background.

5 References

[1] A. de Oliveira-Costa, M. Tegmark, B. Gaensler, J. Jonas, T. Landecker et P. Reich, *MNRAS,* vol. 388, pp. 247-260, 2008.

[2] J. Dowell, G. Taylor, F. Schinzel, N. Kassim et K. Stovall, *MNRAS,* vol. 469, n° %14, pp. 4537-4550, 2017.

[3] G. Reber, *J.Franklin.Inst.,* vol. 285, pp. 1-12, 1968.

[4] G. Ellis, *Aust. J. Phys.,* vol. 35, p. 91ff, 1982.

[5] R. Manning et G. Dulk, *Astron.Astrophys.,* vol. 372, pp. 663-666, 2001.

[6] R. Manning et J. Fainberg, *Sp. Sci. Instr.,* vol. 5, p. 161ff, 1980.

[7] A. Lecacheux, *Astron. Astroph.,* vol. 70, pp. 701-706, 1978.

[8] B. Cecconi et P. Zarka, *Radio Science,* vol. 40, p. 3ff, 2005.

[9] L. Brown, *Ap.J.,* vol. 180, p. 359, 1973.

[10] J. Alexander, L. Brown, T. Clark, R. Stone et R. Weber, *Ap.J.,* vol. 157, n° %1L163, 1975.

[11] A. Lecacheux, C. Harvey et A. Boischot, *Ann. Telecomm.,* vol. 34, pp. 253-265, 1979.

[12] J. Driscoll et D. Healy, *Adv. Applied Math.,* vol. 15, pp. 202-250, 1994.

[13] M. Blanco, M. Florrez et M. Bermejo, *J. Molecular Structure,* vol. 419, pp. 19-27, 1997.

[14] D. Gurnett et e. al., «The Cassini Radio and Plasma Wave,» *Sp. Sci. rev.,* vol. 114, pp. 395-463, 2004.

[15] K. Dwarakanath, AGU Geophysical Monograph 119, R.G. Stone, K.W. Weiler, M.L. Goldstein and J.L Bougeret , 2000.

Les grandes structures et les grands radiotélescopes
Large Structures and large radio telescopes

Wim van Driel

[1]GEPI, Observatoire de Paris, wim.vandriel@obspm.fr

large structures ; dark matter ; SKA

Résumé/Abstract

De par des relevés faites en raie HI à 21 cm la radioastronomie joue un rôle important dans la mise en relation de nos connaissances de l'Univers à ses plus grandes et plus petites échelles. Ces relevés montrent la présence de matière noire, dont la nature précise reste inconnue. Des nouveaux grands relevés vont être mise en route avec une nouvelle génération de radiotélescopes, les "Pathfinders" vers le Square Kilometre Array. L'un des objectifs de ces relevés est la détection d'hydrogène neutre dans es structures de la "toile cosmique".

Through surveys made in the 21cm HI line, radio astronomy plays an important role in connecting our knowledge of the Universe on its largest and smallest scales. These surveys have shown the presence of Dark Matter, whose precise nature remains unknown. New large surveys are about to start with a new generation of radio telescopes, the so-called Pathfinders towards the Square Kilometre Array. One of the goals is the detection of neutral hydrogen inside "cosmic web" structures.

1 Proposition de communications

La radioastronomie joue un rôle important dans la mise en relation des études de l'Univers à ses plus grandes et plus petites échelles - des nombreuses études faites en raie HI à 21cm de galaxies et d'amas de galaxies ont montré la présence à toutes échelles de matière noire, dont la nature précise reste inconnue, et qui domine la masse dans l'Univers.

La communauté mondiale en radioastronomie s'emploie à construire un instrument géant: le Square Kilometre Array, SKA. Sur le chemin menant au SKA, des instruments appelés "Pathfinders" sont en train d'être mis en service, tels que ASKAP en Australie et MeerKAT en Afrique du Sud. Bien qu'ils aient la même sensibilité que les instruments existants, ils ont un champ de vue (beaucoup) plus large, et la décision stratégique a été prise de réaliser principalement un nombre limité de relevés de très grande taille avec ces instruments.

Certaines de ces grands relevés visent à cartographier des structures en HI à des très basses densités de colonne dans des amas de galaxies et autour des galaxies proches. L'un des objectifs est la détection de l'hydrogène neutre dans les structures de la toile cosmique, qui, selon les modèles, devrait être omniprésentes dans l'univers.

Un revu sera présenté des études antérieures des grandes structures dans l'Univers en raie HI à 21cm ainsi que des nouveaux relevés avec les instruments Pathfinder de SKA, en préparation de SKA Phase 1.

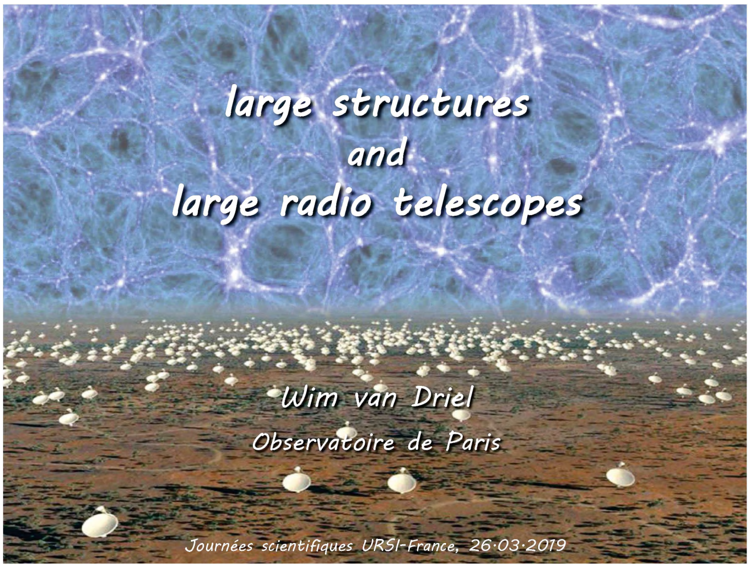

large structures
and
large radio telescopes

Wim van Driel

Observatoire de Paris

Journées scientifiques URSI-France, 26·03·2019

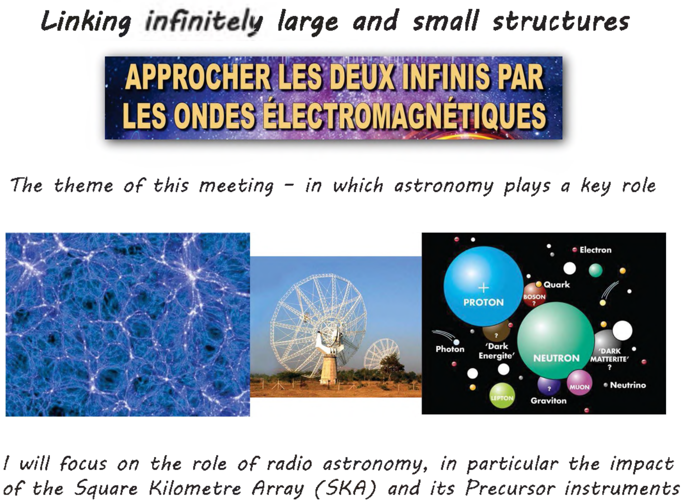

Linking infinitely large and small structures

APPROCHER LES DEUX INFINIS PAR LES ONDES ÉLECTROMAGNÉTIQUES

The theme of this meeting – in which astronomy plays a key role

I will focus on the role of radio astronomy, in particular the impact of the Square Kilometre Array (SKA) and its Precursor instruments

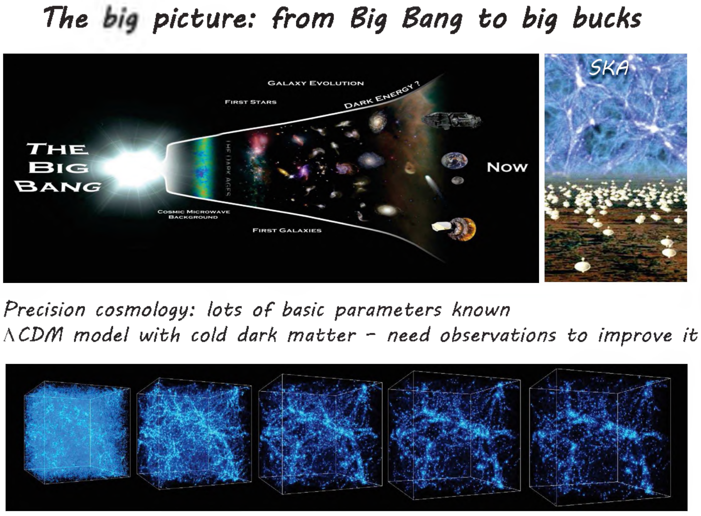

The big picture: from Big Bang to big bucks

Precision cosmology: lots of basic parameters known
ΛCDM model with cold dark matter – need observations to improve it

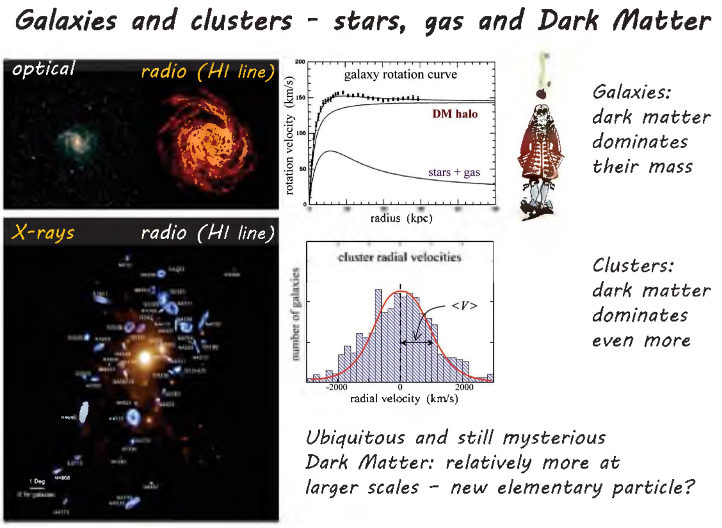

Galaxies and clusters – stars, gas and Dark Matter

Galaxies:
dark matter
dominates
their mass

Clusters:
dark matter
dominates
even more

Ubiquitous and still mysterious
Dark Matter: relatively more at
larger scales – new elementary particle?

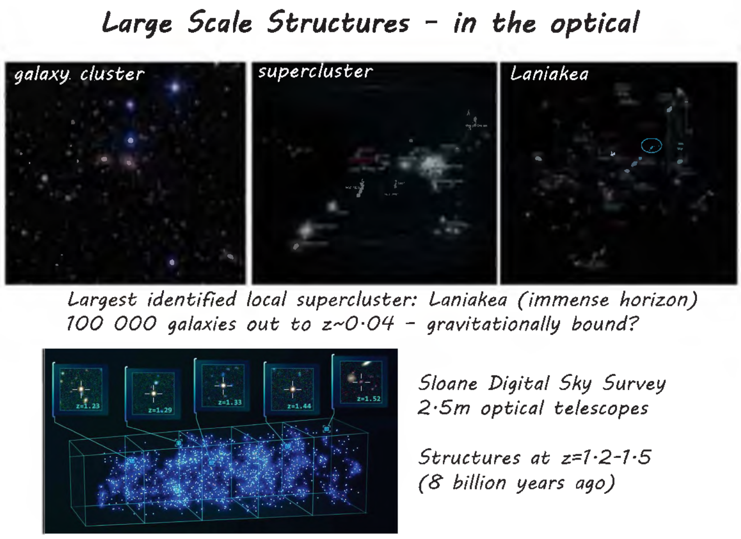

Large Scale Structures – in the optical

Largest identified local supercluster: Laniakea (immense horizon)
100 000 galaxies out to z~0·04 – gravitationally bound?

Sloane Digital Sky Survey
2·5m optical telescopes

Structures at z=1·2-1·5
(8 billion years ago)

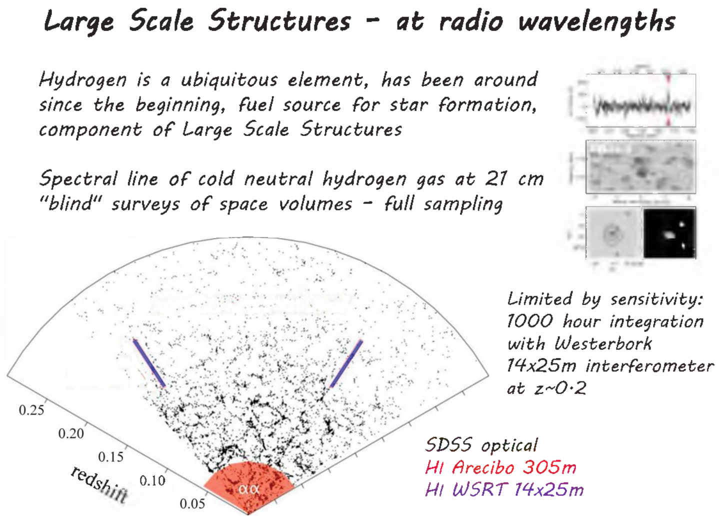

Large Scale Structures – at radio wavelengths

Hydrogen is a ubiquitous element, has been around since the beginning, fuel source for star formation, component of Large Scale Structures

Spectral line of cold neutral hydrogen gas at 21 cm "blind" surveys of space volumes – full sampling

Limited by sensitivity:
1000 hour integration
with Westerbork
14x25m interferometer
at z~0·2

SDSS optical
HI Arecibo 305m
HI WSRT 14x25m

What next? - on the backs of envelopes

For a paradigm shift: measure HI in galaxies when the Universe was really different - at z~1 (~8 billion years ago)

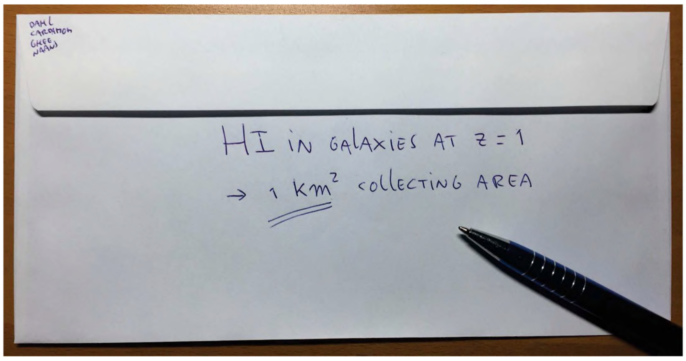

[1990]

Square Kilometre Array: basic parameters

Huge collecting area (= sensitivity) +
very large field(s)-of-view

1 billion galaxies in HI line, out to z~2
10 billion radio continuum sources

- **collecting area: one square kilometre** (equiv. 5500 15m dishes)

• radio line observations:	100 × more sensitive	
• frequency range:	0.1 - 10 GHz	(λ 1 cm - 1 m)
• field of view:	50 (degrees)^2	@ λ 21 cm
• multiple fields of view		
• angular resolution:	0.01 arcsec	@ λ 21 cm
interferometer, baselines up to ~3000 km		

Versatile instrument – for discovering unknown unknowns

[2005]

Towards the SKA

Pathfinders - operational; e.g.:

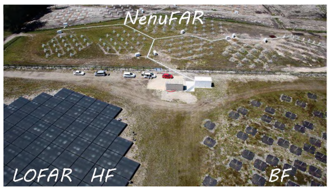

LOFAR: international telescope,
station at Nançay Radio Facility
NenuFAR: at Nançay Radio Facility
Phased arrays, at 10-240 MHz

Precursors - completed
Size of existing radio telescopes, large field-of-view, 1-10 GHz
Australia, South Africa (+ Netherlands)

SKA1 - construction will start in a few years
10% of SKA2 ; budget-limited (650 MEUR construction costs)

SKA2 - full monty square kilometre size radio telescope
science-limited ; > 2030?

SKA Precursors: HI surveys - complementarity

Large Programmes, for first 5 years of operations

ASKAP

36 x 12 m parabolas, 0.6-14 GHz, FoV 30 deg^2, resolution 30"

WALLABY 21cm HI line survey of 75% of entire sky
mJy rms, 500 000 galaxies, mean z~0.05

MeerKAT

64 x 13 m parabolas, 0.6-14 GHz, FoV 1 deg^2, resolution 8"

MHONGOOSE	deep HI, selected nearby galaxies
Fornax cluster	deeper HI in nearby cluster - cosmic web
LADUMA	ultra-deep HI field

SKA Precursors: HI surveys II.

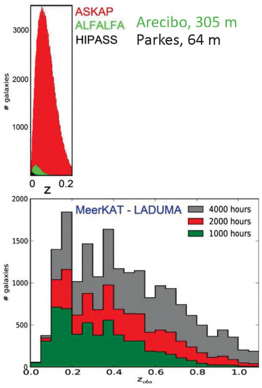

ASKAP + APERTIF: all-sky, shallowish

detection of a million galaxies
imaging of thousands of galaxies:
HI distributions and velocity fields
mean redshift ~0.05

MeerKAT: targeted, deeper

LADUMA: 1 deg^2 field, ultra-deep
detection of 20,000 galaxies
mean redshift ~0.3

Fornax cluster: detection of cosmic web

SKA1

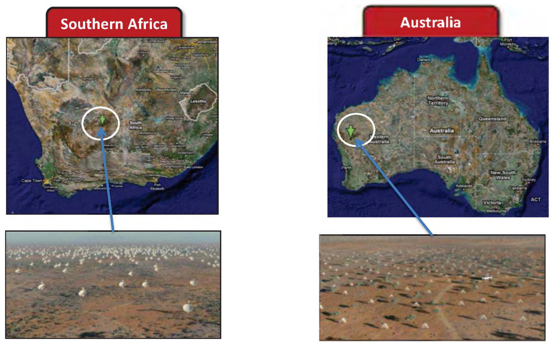

SKA1-mid
200 15 m dishes
(0.03 km^2)
freq. 0.35-14 GHz
1 deg^2 FoV
baselines 150 km

SKA1-low
130 000 phased array antennas
(0.4 km^2)
freq. 0.05-0.35 GHz
30 deg^2 FoV
baselines 65 km

Da capo: the radio astronomy HI revolution

The SKA is designed for gigantic surveys

Example: extragalactic HI surveys

2019: 40,000 detections, out to z~0·05
2028: 1,000,000 detections, out to z~0·5
2038: 1,000,000,000 detections, out to z~2

Telescope time to be shared with other key projects

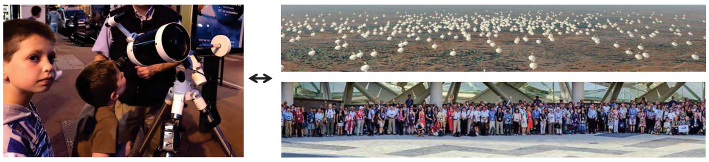

quietly, or we will all be sent to our rooms...

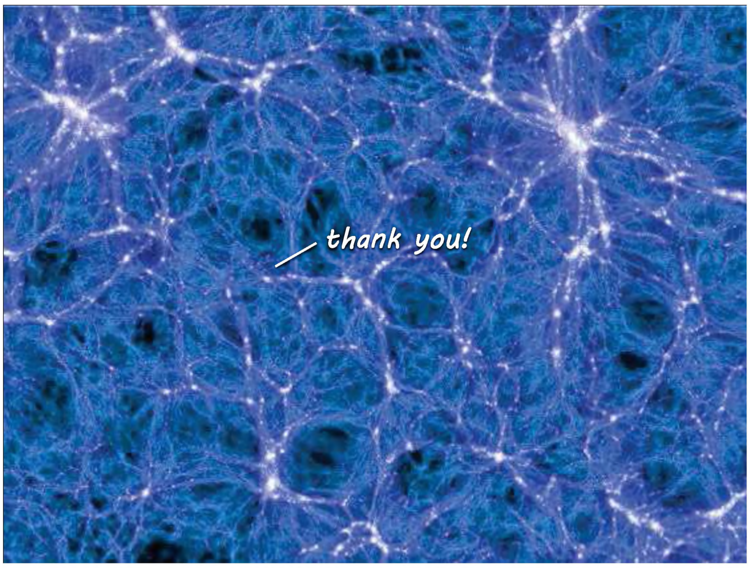

Low frequency pulsar observations with NenuFAR
Observation de pulsars à basse fréquence avec NenuFAR

L. Bondonneau[1]***, J.-M. Grießmeier***[1,2]***, G. Theureau***[1,2,3]***, I. Cognard***[1,2]***, and the NenuFAR-France collaboration***[1,2,3]

[1]*LPC2E - Université d'Orléans / CNRS, France*
[2]*Station de Radioastronomie de Nançay, Observatoire de Paris - CNRS/INSU, USR 704 - Univ. Orléans, OSUC, route de Souesmes, 18330 Nançay, France*
[3]*Laboratoire Univers et Théories LUTh, Observatoire de Paris, CNRS/INSU, Université Paris Diderot, 5 place Jules Janssen, 92190 Meudon, France*

Keywords: NenuFAR, Pulsar, Low frequency
Mots-clefs: NenuFAR, Pulsar, Basses fréquences

Abstract:

NenuFAR (New Extension in Nançay Upgrading loFAR) is the new radiotelescope developed and built in Nançay. Designed to observe the largely unexplored frequency window from 10 to 85 MHz, it has a high sensitivity across the bandpass. Still in the construction phase today, it already has more than 1000 antennas and is better suitable for large band observation than the European low frequency network LOFAR. The scientific exploitation is about to start.
Pulsar observations require a real-time pipeline able to cope with a high data rate in order to significantly reduce the required dedicated storage. The data are reduced by taking care of the interstellar medium through coherent dedispersion and by folding the data to the apparent rotation period of the neutron star. We will end by presenting the first results obtained using the pulsar instrumentation of NenuFAR.

Résumé:

NenuFAR (New Extension in Nançay Upgrading loFAR) est le nouveau radiotélescope développé et en cours de construction sur le site de Nançay. Conçu pour observer dans une fenêtre radio encore très peu étudiée de 10 à 85 MHz il est très sensible sur toute sa bande passante. Encore en phase de construction aujourd'hui il dépasse déjà les 1000 antennes et est plus adapté pour les observations large bande que le réseau basse fréquence européen de LOFAR. L'exploitation scientifique est sur le point de commencer.
L'observation des pulsars demande un traitement des données très haut débit en temps réel afin de considérablement diminuer le stockage nécessaire aux observations. Les données sont réduites en prenant soin de corriger de façon cohérente la dispersion du milieu interstellaire et par le repliement des données à la période de rotation apparente de l'étoile à neutron. Nous présenterons les premiers résultats de l'instrumentation pulsar de NenuFAR.

Figure 1 – Left picture: Satellite picture of NenuFAR. Green points are mini-arrays of 19 antennas. White points are future mini-arrays. Right picture: Picture of NenuFAR antennas (see [1]).

1 NenuFAR

NenuFAR is officially labelled as SKA pathfinder. In its present state NenuFAR-1, it is composed of 56 mini-arrays of 19 antennas (see left picture in Figure 1). The final NenuFAR will be composed of 96 such mini-arrays.

Because NenuFAR has a high gain across the full band, the sensitivity relative to the LOFAR core is especially high at low frequencies. For example, at 20 MHz, NenuFAR-1 is 5 times as sensitive as the LOFAR core. This is mainly due to the new design of NenuFAR antennas, optimized preamplifiers and the antenna spacing. Observations shown in this paper were made in commissioning mode, without proper coherent summation between mini-arrays. When the calibration phase will be completed with a proper coherent summation and pointing correction table the sensitivity of NenuFAR-1 will reach that of the LOFAR core. The final version will exceed the sensitivity of the LOFAR core by a factor 1.7.

2 Pulsar Backend

A pulsar backend is fed by the beamformer with waveform data through a User Datagram Protocol (UDP) connection corresponding to 300 MB/s. To be able to process this data stream in real time on a single machine all calculations have to be performed on Graphical Processing Units (GPUs) to optimise the parallelization. The backend has two main objectives: correct for the dispersion of the interstellar medium in the Fourier domain (coherent dedispersion [2]) and fold the observation at the period of the neutron star. Finally the output of the backend is saved as a Flexible Image Transport System (FITS) file a thousand time smaller than the original waveform data.

2.1 Low frequency Pulsar Backend

Low frequency coherent dedispersion in real time is a challenge due to the long time delay within the lowest frequency channel. For example, with a single channel of 195 kHz and for an observation at 20 MHz, B0329+54 (at a dispersion measure of 26.7 pc.cm^{-3}) has a intrachannel dispersive delay of 5 seconds, which corresponds to several times the pulse period. In the pulsar pipeline we need to double this dispersive delay to get an overlap. In consequence, for each channel and complex polarization we need an FFT (Fast Fourier Transform) on 2^{21} complex values of 5.12 microseconds, corresponding to more than 10.7 seconds of waveform data in a single FFT. For the total bandwidth (384 channels) we need 8 GB of memory in a single GPU.
If we look at the frequency resolved pulse profile of Figure 2 the difference is clearly visible between a dispersed profile (left plot) and a coherently dedispersed profile of B0950+08 (right plot). Note that the dispersion of this pulsar is low only 2.97 pc.cm^{-3}, which is the firth lowest DM value of 2659 known pulsars.

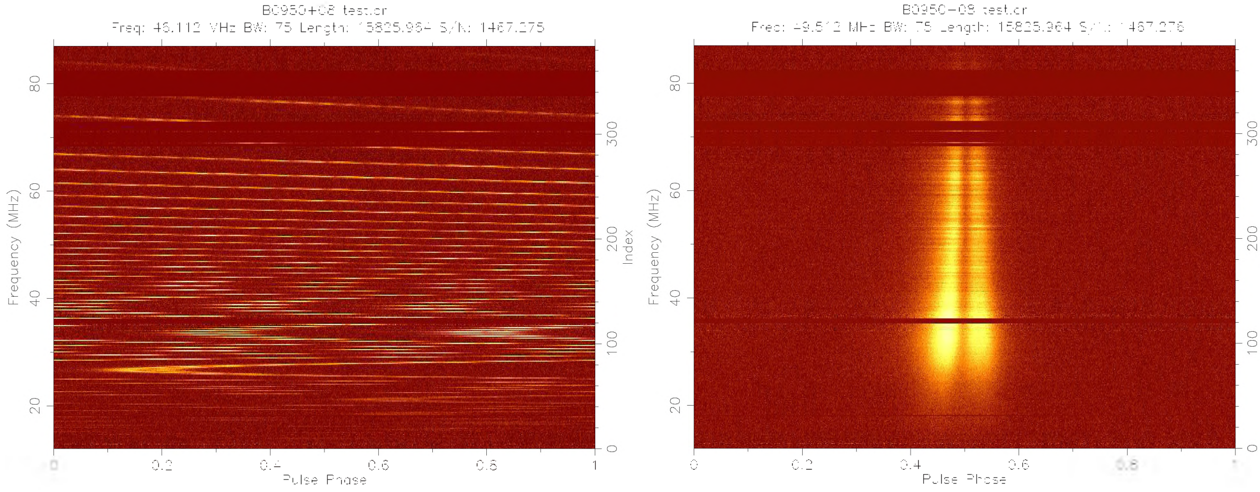

Figure 2 – Frequency resolved pulse profile for an observation of B0950+08 with 56 mini-arrays of NenuFAR. Left plot: The dispersed pulsar as observed by the radiotelescope. Right plot: The same observation coherently dedispersed.

UnDySPuTeD is the beamformed high rate backend of Nenufar on which the software LUPPI (Low frequency Ultimate Pulsar Processing Instrument) is installed. LUPPI is installed on two machines with in total 4 GPUs (GTX 1080 8 GB). It has been designed coherently dedisperse and fold up to 4 numerical beams of 37.5 MHz of bandwidth simultaneously (192 channels per beam).

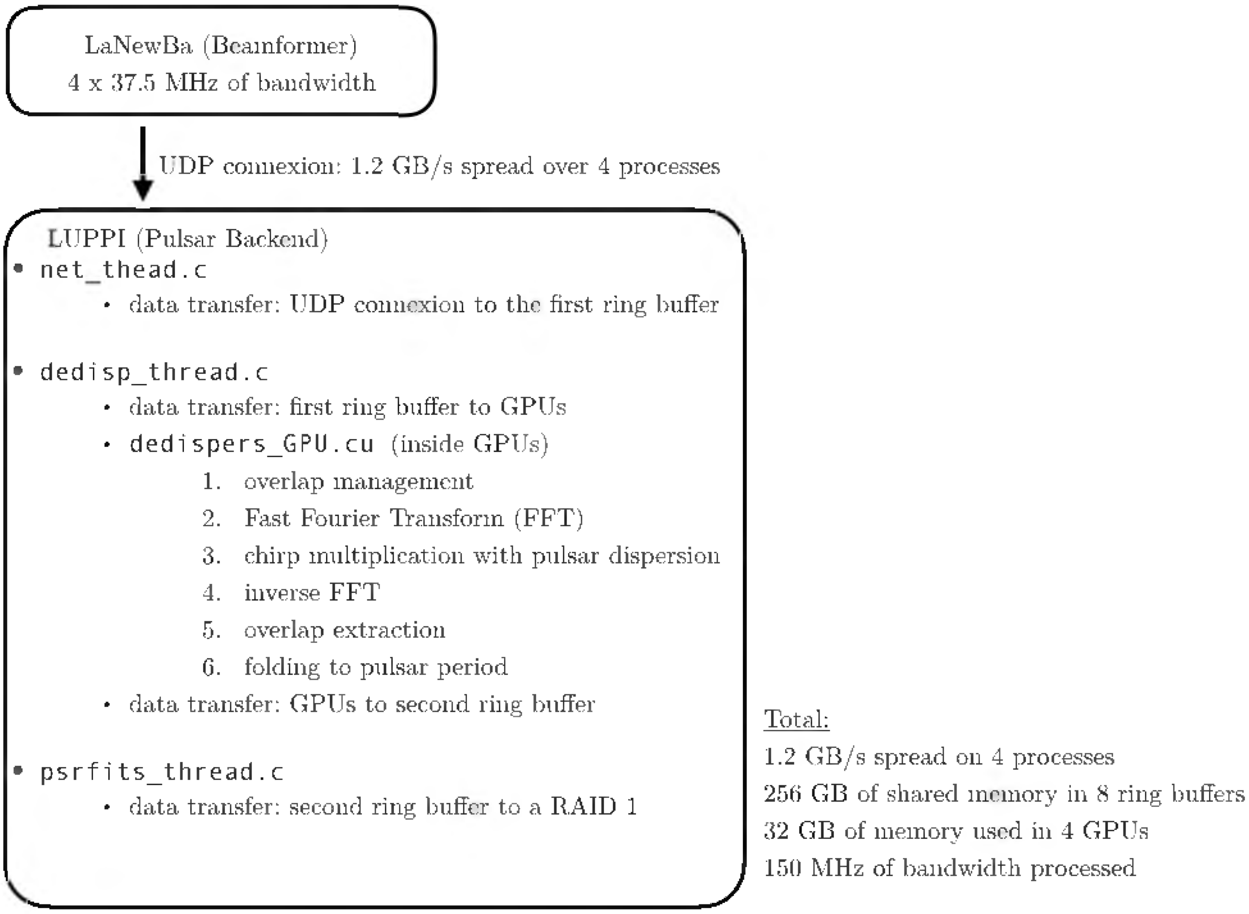

Figure 3 – Sketch of the Low frequency Pulsar Processing Instrument (LUPPI) describing how the data are processed from the beamformer to the final Flexible Image Transport System (FITS) file through the three main threads: net_ thread, dedisp_ thread and psrfits_ thread.

2.2 LUPPI

This section will detail the data processing applied by the Low frequency Ultimate Pulsar Processing Instrument (LUPPI) (see Figure 3). LUPPI is a dedispersing and folding algorithm working with GPU parallelization. This software is a low frequency adaptation of NUPPI[1] (Nançay Ultimate Pulsar Proccesing Instrument) which is the software used on the decimeter Radio Telescope of Nançay (NRT). NUPPI is directly inspired by GUPPI (Green Bank Ultimate Pulsar Processing Instrument, [3]).

The NenuFAR beamformer LaNewBa, uses Field-Programmable Gate Array (FPGA) boards and is able to broadcast 4x37.5 MHz of bandwidth in 768 channels of 195 kHz to Undysputed and LUPPI via four UDP links. LUPPI works with three main threads: The net_thread is bound to the UDP port and writes waveform packets for all channels to a first ring buffer. Secondly, dedisp_thread is the heart of the program, in which the waveform data is transmitted to the GPUs where most of calculations are done (FFT, management of the overlap, coherent dedispersion by multiplication of the waveform with the chirp function in the Fourier domain, inverse FFT, overlap extraction and folding of the subintegration by the pulsar period). Finally, the folded data stream is send in a second ring-buffer to be written to a RAID (Redundant Array of Independent Disks) in FITS format by psrfits_thread.

3 Observations

In this section we present the folding mode where the pulsar signal is integrated in time to increase the signal to noise ratio and show the frequency variations of the profiles. The total bandwidth is 75 MHz for all observations. The observation length is variable: from 32 minutes for B0809+74 to 5 hours for B1133+16.

---

[1] G. Desvignes, https://github.com/gdesvignes/NUPPI

The aim of this section is to illustrate the low frequency pulsar population by showing iconic low frequency pulsars (see on Figure 4 and 5).
These observations show high variations of pulsars profiles due to the interstellar medium and intrinsic magnetospheric properties of the pulsar.

3.1 B0809+74

This pulsar was already observed and studied with LOFAR [4], [5], [6] and with UTR-2 [7]. Two pulsations are apparent in Figure 4. It is particularly interesting for two reason: it exhibits impressive drifting subpulses (see [4]) and the ratio between the amplitudes of both pulsations reverses at 50 MHz as can be seen in Figure 4.

3.2 B0834+06

Observed by LOFAR [6] and UTR-2 [7]. This pulsar shows an exponential tail in the lowest part of the band below 29 MHz, which is the signature of the multi-path propagation in the interstellar medium [2].

3.3 B0950+08

This pulsar was observed with LOFAR [5] and with the MWA [8]. Defined as one of the least scattered pulsar in [9] there is no scattering tail visible in Figure 4.

3.4 B1133+16

Observed with UTR-2 [7], LOFAR [5], [6] and the MWA [8]. This pulsar is well know in low frequency for the increasing of the separation between both pulsations, which is the signature of the emission height in a bipolar model see [10] and [11], [2].

3.5 B1237+25

Observed with UTR-2 [7], the LWA [12] and LOFAR [5], [6]. B1237+25 is the first pulsar for which mode-changing behaviour was detected [13].

3.6 B1508+55

Studied with LOFAR [10] it is well know to have a low rotation measure (see [2]). Osłowski et al. (in prep.) as in [14] observed a profile variation in time interpreted as an echo of the main pulsation on a plasma bubble in the interstellar medium. This echo can be seen in Figure 5 just after the main pulse.

3.7 B1919+21

B1919+21 is the first pulsar discovered by Jocelyn Bell in 1967 [15]. Below 100 MHz it is the strongest pulsar in the north sky. In Figure 5 we can observe its three main components easily distinguishable at 40 MHz. It is interesting to observe that only the central component is visible below 30 MHz see in Figure 5. This could be a signature of a modification in the emission mechanism.

3.8 B2217+47

This pulsar is observed by LOFAR and discussed in [14], it is the best example of scattering tail for the low band (see Figure 5).

4 Conclusion

In this paper we go through the first real-time low-frequency pulsar backend working on Graphical Processing Units (LUPPI). We described the challenge of low frequency coherent dedispersion due the high dispersive delay. Finally we presented the first observations of iconic pulsars with NenuFAR.
Today with NenuFAR and Undysputed with LUPPI we have started to observe, coherently dedisperse and fold pulsars of the north sky (with limits of -10 degrees in declination and a maximum DM of 100 $pc.cm^{-3}$) to characterized the low frequency pulsar population. This will also be used to provide targets for future observations.
This new instrumentation allows us to deeply study the low-frequency variabilities of the flux density, the polarizations, the evolution of the profile in time and frequency which allows to constrain models of the emission mechanism and probing the interstellar medium via measurements of the DM and scattering.

5 References

[1] https://www.obs-nancay.fr/ NenuFAR-45-.html, “observatoir de nancay.”

[2] D. Lorimer and M. Kramer, “Handbook Of Pulsar Astronomy,” Dec. 2004.

[3] R. DuPlain, S. Ransom, P. Demorest, P. Brandt, J. Ford, and A. L. Shelton, “Launching GUPPI: the Green Bank Ultimate Pulsar Processing Instrument,” (Marseille, France), p. 70191D, Aug. 2008.

[4] T. E. Hassall, B. W. Stappers, P. Weltevrede, J. W. T. Hessels, A. Alexov, T. Coenen, A. Karastergiou, M. Kramer, E. F. Keane, V. I. Kondratiev, J. van Leeuwen, A. Noutsos, M. Pilia, M. Serylak, C. Sobey, K. Zagkouris, R. Fender, M. E. Bell, J. Broderick, J. Eisloffel, H. Falcke, J.-M. Griessmeier, M. Kuniyoshi, J. C. A. Miller-Jones, M. W. Wise, O. Wucknitz, P. Zarka, A. Asgekar, F. Batejat, M. J. Bentum, G. Bernardi, P. Best, A. Bonafede, F. Breitling, M. Bruggen, H. R. Butcher, B. Ciardi, F. de Gasperin, J.-P. de Reijer, S. Duscha, R. A. Fallows, C. Ferrari, W. Frieswijk, M. A. Garrett, A. W. Gunst, G. Heald, M. Hoeft, E. Juette, P. Maat, J. P. McKean, M. J. Norden, M. Pandey-Pommier, R. Pizzo, A. G. Polatidis, W. Reich, H. Rottgering, J. Sluman, Y. Tang, C. Tasse, R. Vermeulen, R. J. van Weeren, S. J. Wijnholds, and S. Yatawatta, “Differential Frequency-dependent Delay from the Pulsar Magnetosphere,” *Astronomy & Astrophysics*, vol. 552, p. A61, Apr. 2013. arXiv: 1302.2321.

[5] A. Bilous, V. Kondratiev, M. Kramer, E. Keane, J. Hessels, B. Stappers, V. Malofeev, C. Sobey, R. Breton, S. Cooper, H. Falcke, A. Karastergiou, D. Michilli, S. Osłowski, S. Sanidas, S. ter Veen, J. van Leeuwen, J. Verbiest, P. Weltevrede, P. Zarka, J.-M. Grießmeier, M. Serylak, M. Bell, J. Broderick, J. Eislöffel, S. Markoff, and A. Rowlinson, “A LOFAR census of non-recycled pulsars: average profiles, dispersion measures, flux densities, and spectra,” *Astronomy & Astrophysics*, vol. 591, p. A134, July 2016. arXiv: 1511.01767.

[6] M. Pilia, J. W. T. Hessels, B. W. Stappers, V. I. Kondratiev, M. Kramer, J. van Leeuwen, P. Weltevrede, A. G. Lyne, K. Zagkouris, T. E. Hassall, A. V. Bilous, R. P. Breton, H. Falcke, J.-M. Grießmeier, E. Keane, A. Karastergiou, M. Kuniyoshi, A. Noutsos, S. Osłowski, M. Serylak, C. Sobey, S. ter Veen, A. Alexov, J. Anderson, A. Asgekar, I. M. Avruch, M. E. Bell, M. J. Bentum, G. Bernardi, L. Bîrzan, A. Bonafede, F. Breitling, J. W. Broderick, M. Brüggen, B. Ciardi, S. Corbel, E. de Geus, A. de Jong, A. Deller, S. Duscha, J. Eislöffel, R. A. Fallows, R. Fender, C. Ferrari, W. Frieswijk, M. A. Garrett, A. W. Gunst, J. P. Hamaker, G. Heald, A. Horneffer, P. Jonker, E. Juette, G. Kuper, P. Maat, G. Mann, S. Markoff, R. McFadden, D. McKay-Bukowski, J. C. A. Miller-Jones, A. Nelles, H. Paas, M. Pandey-Pommier, M. Pietka, R. Pizzo, A. G. Polatidis, W. Reich, H. Röttgering, A. Rowlinson, D. Schwarz, O. Smirnov, M. Steinmetz, A. Stewart, J. D. Swinbank, M. Tagger, Y. Tang, C. Tasse, S. Thoudam, M. C. Toribio, A. J. van der Horst, R. Vermeulen, C. Vocks, R. J. van Weeren, R. A. M. J. Wijers, R. Wijnands, S. J. Wijnholds, O. Wucknitz, and P. Zarka, “Wide-band, low-frequency pulse profiles of 100 radio pulsars with LOFAR,” *Astronomy & Astrophysics*, vol. 586, p. A92, Feb. 2016.

[7] V. V. Zakharenko, I. Y. Vasylieva, A. A. Konovalenko, O. M. Ulyanov, M. Serylak, P. Zarka, J.-M. Grießmeier, I. Cognard, and V. S. Nikolaenko, “Detection of decametre-wavelength pulsed radio emission of 40 known pulsars,” *Monthly Notices of the Royal Astronomical Society*, vol. 431, pp. 3624–3641, June 2013.

[8] T. Murphy, D. L. Kaplan, M. E. Bell, J. R. Callingham, S. Croft, S. Johnston, D. Dobie, A. Zic, J. Hughes, C. Lynch, P. Hancock, N. Hurley-Walker, E. Lenc, K. S. Dwarakanath, B.-Q. For, B. M. Gaensler, L. Hindson, M. Johnston-Hollitt, A. D. Kapińska, B. McKinley, J. Morgan, A. R. Offringa, P. Procopio, L. Staveley-Smith, R. Wayth, C. Wu, and Q. Zheng, “Low-Frequency Spectral Energy Distributions of Radio Pulsars Detected with the Murchison Widefield Array,” *Publications of the Astronomical Society of Australia*, vol. 34, 2017.

[9] J. A. Phillips and A. W. Clegg, “Electron density fluctuations in the local interstellar bubble,” *Nature*, vol. 360, pp. 137–139, Nov. 1992.

[10] A. Noutsos, C. Sobey, V. I. Kondratiev, P. Weltevrede, J. P. W. Verbiest, A. Karastergiou, M. Kramer, M. Kuniyoshi, A. Alexov, R. P. Breton, A. V. Bilous, S. Cooper, H. Falcke, J.-M. Grießmeier, T. E. Hassall, J. W. T. Hessels, E. F. Keane, S. Osłowski, M. Pilia, M. Serylak, B. W. Stappers, S. ter Veen, J. van Leeuwen, K. Zagkouris, K. Anderson, L. Bähren, M. Bell, J. Broderick, D. Carbone, Y. Cendes, T. Coenen, S. Corbel, J. Eislöffel, R. Fender, H. Garsden, P. Jonker, C. Law, S. Markoff, J. Masters, J. Miller-Jones, G. Molenaar, R. Osten, M. Pietka, E. Rol, A. Rowlinson, B. Scheers, H. Spreeuw, T. Staley, A. Stewart, J. Swinbank, R. Wijers, R. Wijnands, M. Wise, P. Zarka, and A. van der Horst, “Pulsar polarisation below 200 MHz: Average profiles and propagation effects,” *Astronomy & Astrophysics*, vol. 576, p. A62, Apr. 2015.

[11] T. E. Hassall, B. W. Stappers, J. W. T. Hessels, M. Kramer, A. Alexov, K. Anderson, T. Coenen, A. Karastergiou, E. F. Keane, V. I. Kondratiev, K. Lazaridis, J. van Leeuwen, A. Noutsos, M. Serylak, C. Sobey, J. P. W. Verbiest, P. Weltevrede, K. Zagkouris, R. Fender, R. A. M. J. Wijers, L. Bähren, M. E. Bell, J. W. Broderick, S. Corbel, E. J. Daw, V. S. Dhillon, J. Eislöffel, H. Falcke, J.-M. Grießmeier, P. Jonker, C. Law, S. Markoff, J. C. A. Miller-Jones, R. Osten, E. Rol, A. M. M. Scaife, B. Scheers, P. Schellart, H. Spreeuw, J. Swinbank, S. ter Veen, M. W. Wise, R. Wijnands, O. Wucknitz, P. Zarka, A. Asgekar, M. R. Bell, M. J. Bentum, G. Bernardi, P. Best, A. Bonafede, A. J. Boonstra, M. Brentjens, W. N. Brouw, M. Brüggen, H. R. Butcher, B. Ciardi, M. A. Garrett, M. Gerbers, A. W. Gunst, M. P. van Haarlem, G. Heald, M. Hoeft, H. Holties, A. de Jong, L. V. E. Koopmans, M. Kuniyoshi, G. Kuper, G. M. Loose, P. Maat, J. Masters, J. P. McKean, H. Meulman, M. Mevius, H. Munk, J. E. Noordam, E. Orrú, H. Paas, M. Pandey-Pommier, V. N. Pandey, R. Pizzo, A. Polatidis, W. Reich, H. Röttgering, J. Sluman, M. Steinmetz, C. G. M. Sterks, M. Tagger, Y. Tang, C. Tasse, R. Vermeulen, R. J. van Weeren, S. J. Wijnholds, and S. Yatawatta, "Wide-band simultaneous observations of pulsars: disentangling dispersion measure and profile variations," *Astronomy & Astrophysics*, vol. 543, p. A66, July 2012.

[12] K. Stovall, P. S. Ray, J. Blythe, J. Dowell, T. Eftekhari, A. Garcia, T. J. W. Lazio, M. McCrackan, F. K. Schinzel, and G. B. Taylor, "Pulsar observations using the first station of the long wavelength array and the LWA pulsar data archive," *The Astrophysical Journal*, vol. 808, p. 156, July 2015.

[13] D. C. Backer, "Pulsar Nulling Phenomena," *Nature*, vol. 228, p. 42, Oct. 1970.

[14] D. Michilli, J. W. T. Hessels, J. Y. Donner, J.-M. Grießmeier, M. Serylak, B. Shaw, B. W. Stappers, J. P. W. Verbiest, A. T. Deller, L. N. Driessen, D. R. Stinebring, L. Bondonneau, M. Geyer, M. Hoeft, A. Karastergiou, M. Kramer, S. Osłowski, M. Pilia, S. Sanidas, and P. Weltevrede, "Low-frequency pulse profile variation in PSR B2217+47: evidence for echoes from the interstellar medium," *Monthly Notices of the Royal Astronomical Society*, vol. 476, pp. 2704–2716, May 2018. arXiv: 1802.03473.

[15] A. Hewish, S. J. Bell, J. D. H. Pilkington, P. F. Scott, and R. A. Collins, "Observation of a Rapidly Pulsating Radio Source," *Nature*, vol. 217, pp. 709–713, Feb. 1968.

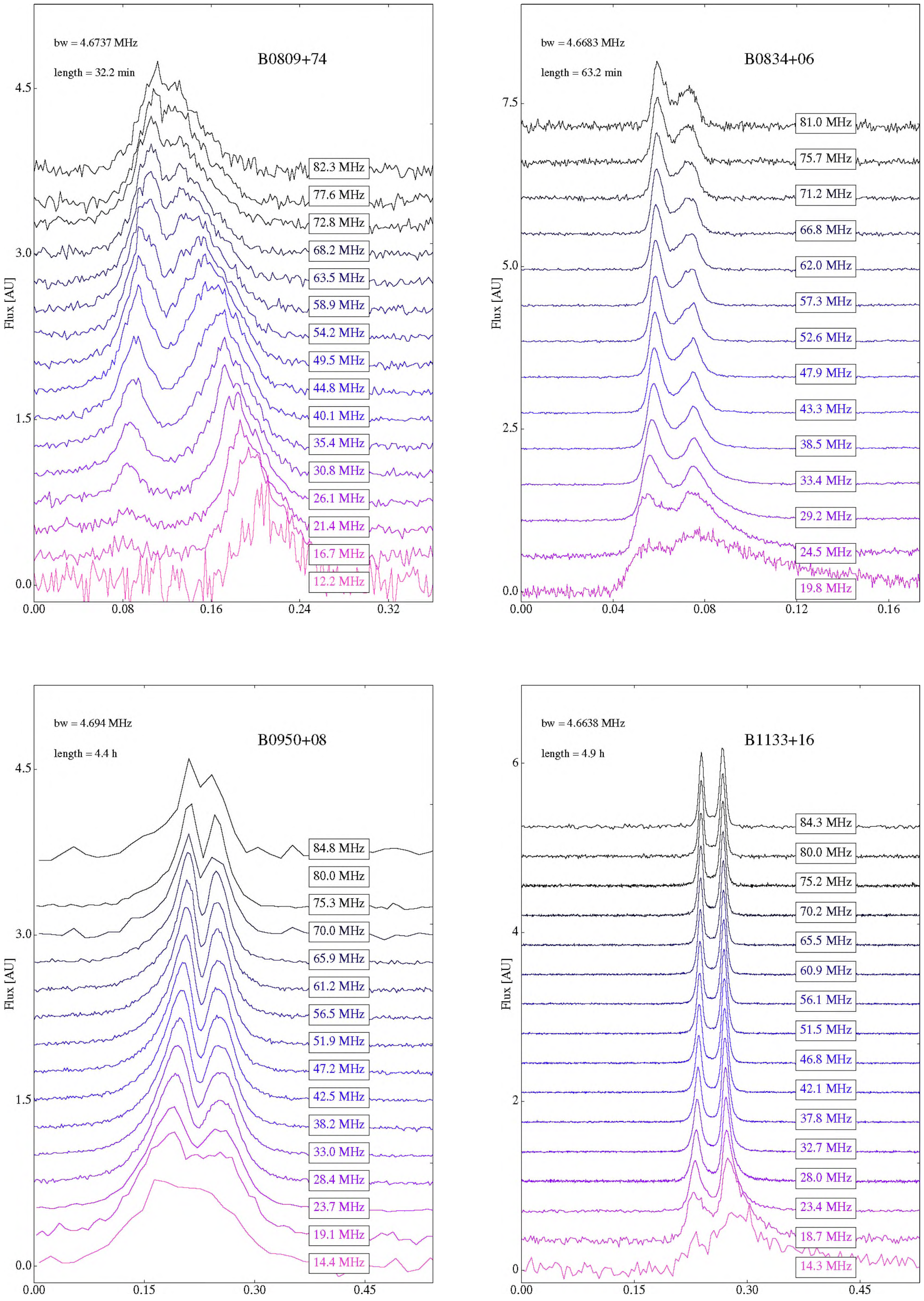

Figure 4 – Frequency stacked profiles for four pulsars: B0809+74, B0834+06, B0950+08 and B1133+16.

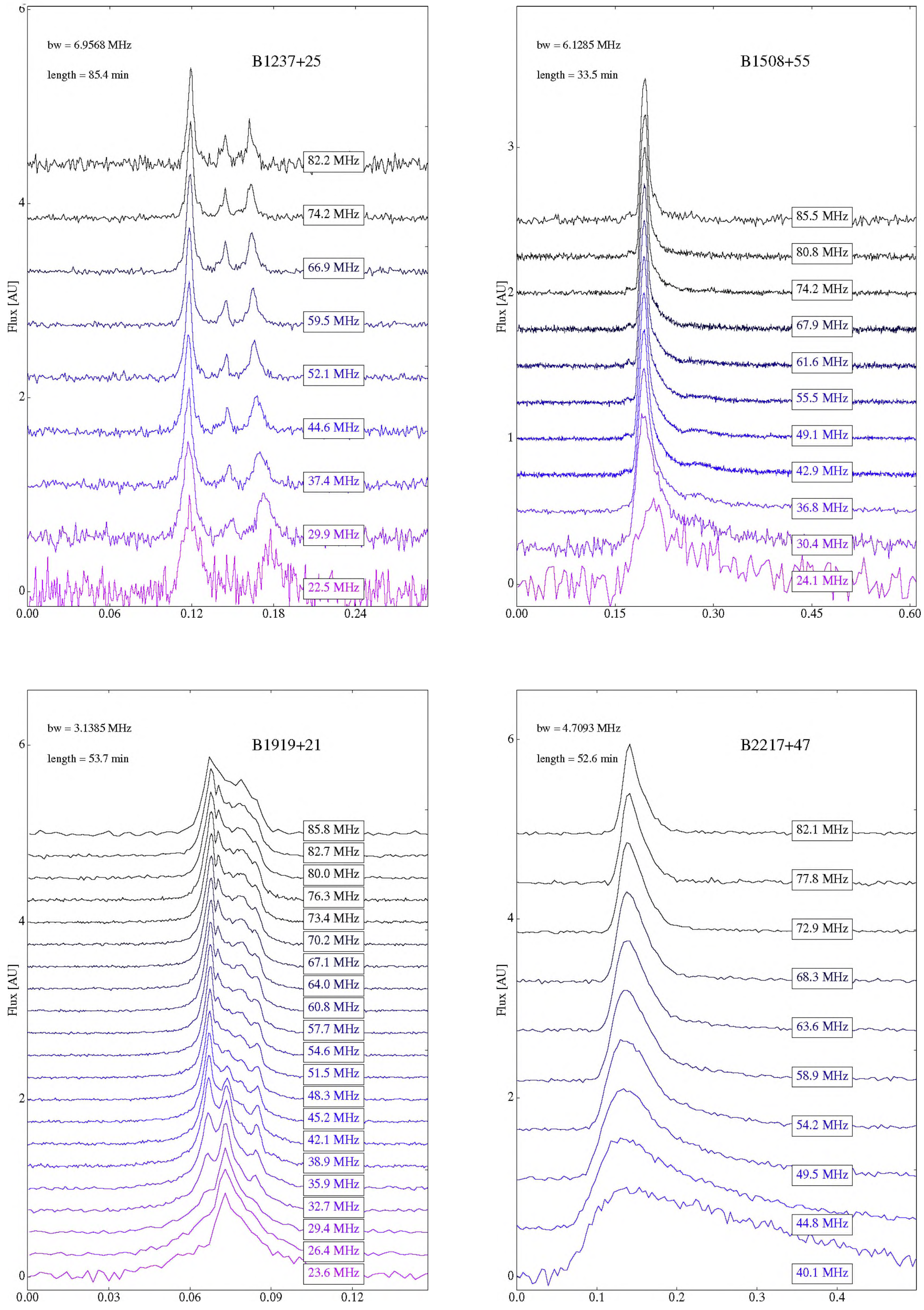

Figure 5 – Frequency stacked profiles for four pulsars: B1237+25, B1508+55, B1919+21 and B2217+47.

QUBIC - The Q & U Bolometric Interferometer for Cosmology

QUBIC - The Q & U Bolometric Interferometer for Cosmology

***S.A. Torchinsky*[1], *Peter Ade*[6], *Giorgio Amico*[7], *Didier Auguste*[8], *Jonathan Aumont*[7], *Stefano Banfi*[7], *Gustavo Barbaràn*[7], *Paola Battaglia*[7], *Elia Battistelli*[7,23], *Alessandro Baù*[7], *Benoit Bélier*[7], *David G. Bennett*[7], *Laurent Bergé*[8], *Jean Philippe Bernard*[7], *Marco Bersanelli*[7], *Marie Anne Bigot Sazy*[1], *Nathat Bleurvacq*[1], *Juan Bonaparte*[7], *Julien Bonis*[7], *Emory F. Bunn*[7], *David Burke*[5], *Daniele Buzi*[7], *Alessandro Buzzelli*[7], *Francesco Cavaliere*[7], *Pierre Chanial*[1], *Claude Chapron*[1], *Romain Charlassier*[1], *Fabio Columbro*[7], *Gabriele Coppi*[7], *Alessandro Coppolecchia*[7,23], *Giuseppe D'Alessandro*[7,23], *Paolo De Bernardis*[7,23], *Giancarlo De Gasperis*[7], *Michele De Leo*[7], *Marco De Petris*[7], *Andres Di Donato*[7], *Louis Dumoulin*[7], *Alberto Etchegoyen*[13], *Adrián Fasciszewski*[13], *Cristian Franceschet*[9], *Martin Miguel Gamboa Lerena*[14], *Beatriz Garcia*[13], *Xavier Garrido*[8], *Michel Gaspard*[8], *Amanda Gault*[19], *Donnacha Gayer*[5], *Massimo Gervasi*[4], *Martin Giard*[10], *Yannick Giraud Héraud*[1], *Mariano Gómez Berisso*[7], *Manuel González*[2], *Marcin Gradziel*[7], *Laurent Grandsire*[1], *Eric Guerard*[7], *Diego Harari*[7], *Vic Haynes*[7], *Sophie Henrot Versillé*[8], *Duc Thuong Hoang*[1], *Federico Incardona*[7], *Eric Jules*[8], *Jean Christophe Hamilton*[1], *Nicolas Holtzer*[13], *Jean Kaplan*[1], *Andrei Korotkov*[7], *Christian Kristukat*[2], *Luca Lamagna*[7,23], *Soutiris Loucatos*[1], *Thibaut Louis*[8], *Raùl Horacio Luterstein*[13], *Bruno Maffei*[22], *Stefanos Marnieros*[21], *Silvia Masi*[7,23], *Angelo Mattei*[7], *Andrew May*[3], *Mark McCulloch*[3], *Maria C. Medina*[8], *Lorenzo Mele*[7], *Simon J. Melhuish*[3], *Aniello Mennella*[4], *Ludovic Montier*[21], *Louise Mousset*[1], *Luis Mariano Mundo*[12], *James Murphy*[5], *John Anthony Murphy*[5], *Emiliano Olivieri*[21], *Creidhe O'Sullivan*[5], *Alessandro Paiella*[7,23], *Francois Pajot*[10], *Andrea Passerini*[4], *Hernan Pastoriza*[2], *Alessandro Pelosi*[7], *Camille Perbost*[1], *Maurizio Perciballi*[7], *Federico Pezzotta*[7], *Francesco Piacentini*[7,23], *Michel Piat*[1], *Lucio Piccirillo*[3], *Giampaolo Pisano*[6], *Gianluca Polenta*[7], *Damien Prêle*[1], *Roberto Puddu*[7], *Damien Rambaud*[10], *Pablo Ringegni*[12], *Gustavo E. Romero*[16], *Maria Salatino*[1,24], *Alessandro Schillaci*[7], *Claudia G. Scóccola*[14], *Stephen P. Scully*[5], *Sebastiano Spinelli*[4], *Guillaume Stankowiak*[1], *Michail Stolpovskiy*[1], *Federico Suarez*[15], *Andrea Tartari*[1,23], *Jean Pierre Thermeau*[1], *Peter Timbie*[19], *Maurizio Tomasi*[9], *Mathieu Tristram*[8], *Gregory S. Tucker*[17], *Carole E. Tucker*[6], *Sylvain Vanneste*[8], *Daniele Viganò*[9], *Nicola Vittorio*[20], *Fabrice Voisin*[1], *Robert Watson*[3], *Francois Wicek*[8], *Mario Zannoni* [4], and *Antonio Zullo*[7]**

[1] *Astroparticle Physics & Cosmology, Observatoire de Paris, CNRS/IN2P3, Université Paris-Diderot, CEA, France*
[2] *Centro Atómico Bariloche and Instituto Balseiro, Argentina*
[3] *University of Manchester, UK*
[4] *Universita di Milano-Bicocca, Italy*
[5] *Maynooth University, Ireland*
[6] *Cardiff University, UK*
[7] *Universita La Sapienza, Roma, Italy*
[8] *Laboratoire de l'Accéllrateur Linéaire, (CNRS/IN2P3), France*
[9] *Universita degli studi di Milano, Italy*
[10] *Institut de Recherche en Astrophysique et Planétologie, Toulouse, France*
[11] *Centro Atómico Constituyentes, Argentina*
[12] *Grupo de Ensayos Mecànicos Aplicados, Argentina*
[13] *Comision Nacional de Energia Atomica, Argentina*
[14] *Facultad de Ciencias Astronómicas y Geofísicas, Argentina*
[15] *Instituto de Tecnologías en Detección y Astropartículas, Argentina*
[16] *Instituto Argentino de Radioastronomía, Argentina*
[17] *Brown University, USA*
[18] *Richmond University, USA*
[19] *University of Wisconsin, USA*
[20] *Università di Roma Tor Vergata, Italy*
[21] *Centre de Sciences Nucléaires et de Sciences de la Matière, CNRS, Paris, France*
[22] *Institut d'Astrophysique Spatiale, Paris, France*
[23] *Istituto Nazionale di Fisica Nucleare, Italy*
[24] *Kavli Institute for Particle Astrophysics and Cosmology, Stanford University, USA*

Keywords: Cosmology, Gravitational Waves, Inflation, Interferometry, self-calibration, aperture synthesis
Mots-clefs: Cosmologie, Ondes gravitationnelles, interérométrie, auto-étalonnage, synthèse d'ouverture

---

Abstract:

QUBIC is a millimetre wave telescope to measure the polarization B-modes in the Cosmic Microwave Background (CMB). Primordial B-modes polarization has yet to be detected, but it is are expected to be visible in the CMB as a result of Inflation in the fraction of a second after the Big Bang during which primordial gravitational waves are produced. The detection of B-modes in the CMB is fundamental to our understanding of the Universe and will help confirm the Standard Model of Cosmology, including Inflation. QUBIC uses a novel technique of bolometric interferometry, merging together the techniques of optical interferometry, in which the interference pattern is imaged on a detector array, and the radio interferometry technique of aperture synthesis, making a powerful wide band instrument capable of the radio technique of self calibration. This technique also permits QUBIC to use the frequency dependence of the synthesized beam to do spectral imaging of the CMB. As a result, QUBIC has a unique capability to reduce systematic and foreground effects from the measurement. QUBIC is currently integrated, and undergoing test at the facility at APC. A description of the instrument and characterization results will be presented.

Résumé:

QUBIC est un télescope d'ondes millimétriques pour mesurer le mode B de la polarisation du Fond Diffus Cosmologique (CMB). Jusqu'à présent, ce signal n'a pas été détecté, mais il est attendu d'après la théorie standard de la cosmologie qui prévoit une période d'inflation de l'Univers pendant la première fraction de seconde de son histoire. C'est à cette époque que des ondes gravitationnelles primordiales sont générées et qui doivent légèrement polariser le Fond Diffus en mode tensoriel. QUBIC est donc une expérience fondamentale pour notre connaissance de l'Univers et de la physique. QUBIC exploite une toute nouvelle technique d'observation, l'interférométrie bolométrique. On mélange la technique d'interférométrie optique qui crée une image d'interférogramme sur la matrice de détecteurs, et la technique radio de synthèse d'ouverture. La combinaison produit un instrument très puissant pour le filtrage des signaux non désirables venant de l'instrument et de l'avant plan en utilisant les techniques de l'imagerie spectrale et d'auto-étalonnage. QUBIC est actuellement en cours d'intégration dans le laboratoire APC et les tests de caractérisation sont en cours. Une description de l'instrument et de ses performances sera présentée.

1 Introduction

QUBIC is an experiment based on an idea proposed by Ali et al. [1, 2] for a millimetre wave bolometric interferometer. It is designed to measure the B-mode polarization anisotropies of the Cosmic Microwave Background (CMB). The QUBIC design combines the sensitivity of Transition Edge Sensors (TES), bolometric detectors with the systematic effects and foreground control provided by its interferometric design.

The control of astrophysical foregrounds, in particular, is a factor of increasing importance in CMB polarization experiments, and QUBIC allows us to disentangle sub-bands in each main frequency band thanks to its spectral imaging capability, which is deeply rooted in the interferometric nature of the instrument.

QUBIC will operate from the ground observing the sky in two main spectral bands centered at 150 and 220 GHz [3] and will be deployed in Argentina, at the Alto Chorrillos site. The team is currently finalizing the laboratory tests of the technical demonstrator, a simplified version of the instrument that will be installed at the site during 2019 and will demonstrate the technical and scientific potential of our approach. The final instrument will be deployed during 2020.

2 The Instrument

Figure 1 shows a schematic of QUBIC. The signal from the sky enters the cryostat through a High-Density Polyethylene (HDPE) window. Then, a rotating half-wave plate modulates the polarization, and a polarizing grid selects one of the two linear polarization components. An array of 400 back-to-back corrugated horns collects the radiation and re-images it onto a dual-mirror optical combiner that focuses the signal onto two orthogonal TES detector arrays. A dichroic filter placed between the optical combiner and the focal planes selects the two frequency bands, centred at 150 GHz and 220 GHz. The right panel of Figure 1 shows a 3D rendering of the inner part of the cryostat. A key part of the instrument is an array of movable shutters placed between the primary and secondary feed-horn arrays. Each shutter acts as an RF switch (a blade that can slide into a smooth circular waveguide), which is used to exclude particular baselines when the instrument operates in calibrating mode. This permits the exploitation of the calibration strategy called "self-calibration", which is a key feature of the QUBIC systematic effects control. A detailed description of the instrument is found in [4] and the theory of self-calibration for QUBIC is described in [5].

3 Measurement, Self-Calibration, and Spectral Imaging

3.1 Signal Model and Synthetic Beam

In QUBIC, the optical combiner focuses the radiation emitted by the secondary horns onto the two focal planes so that the image that forms on the detector arrays is the result of the interference arising from the sum of the

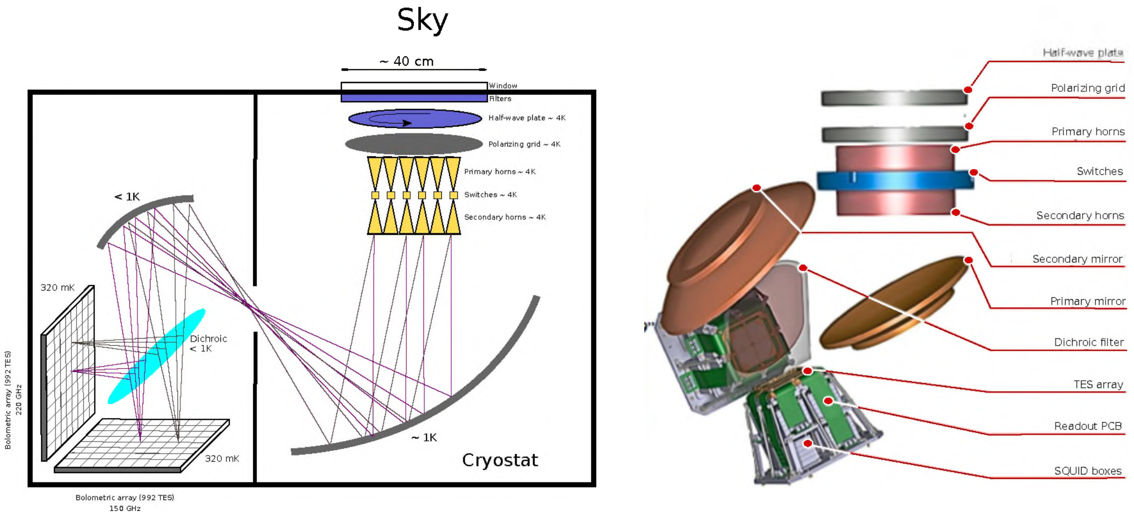

Figure 1 – (Left) Schematic of the **QUBIC** *instrument. The window aperture is about 40 cm; the cryostat is about 1.41 m in diameter and 1.51 m in height; (right) 3D rendering of the inner part of the cryostat. TES, Transition Edge Sensor.*

fields radiated from each of the 400 apertures.
Therefore, the signal measured at time t by a detector p on the focal plane is:

$$R(p,\nu,t) = K\left[S_I(p,\nu) + \cos(4\,\phi_{\mathrm{HWP}}(t))\,S_Q(p,\nu) + \sin(4\,\phi_{\mathrm{HWP}}(t))\,S_U(p,\nu)\right], \qquad (1)$$

where ν is the frequency, ϕ_{HWP} is the angle of the half-wave plate at time t, and K is an overall calibration constant that takes into account the efficiency of the optical chain. The three terms $S_{I,Q,U}$ in Equation (1) represent the sky signal in intensity and polarization convolved with the so-called synthetic beam.
Figure 2 shows the simulation of QUBIC observing a point source in the far field with all 400 antennas open to the sky. The image formed on each of the focal planes (right panel of Figure 2) is an interference pattern formed by peaks and lobes. This equivalent to the "dirty-image" produced in radio aperture synthesis (see for example [6]).
Therefore, if X is the signal from the sky (either in intensity, I, or polarization, Q, U), then the measured signal on the pixel p is $S_X(p) = \int X(\mathbf{n}) B^p_{\mathrm{synth}}(\mathbf{n}) d\mathbf{n}$. This means that QUBIC data can be analyzed similarly to the data obtained from a normal imager, provided that we build a window function of the synthetic pattern for each pixel.

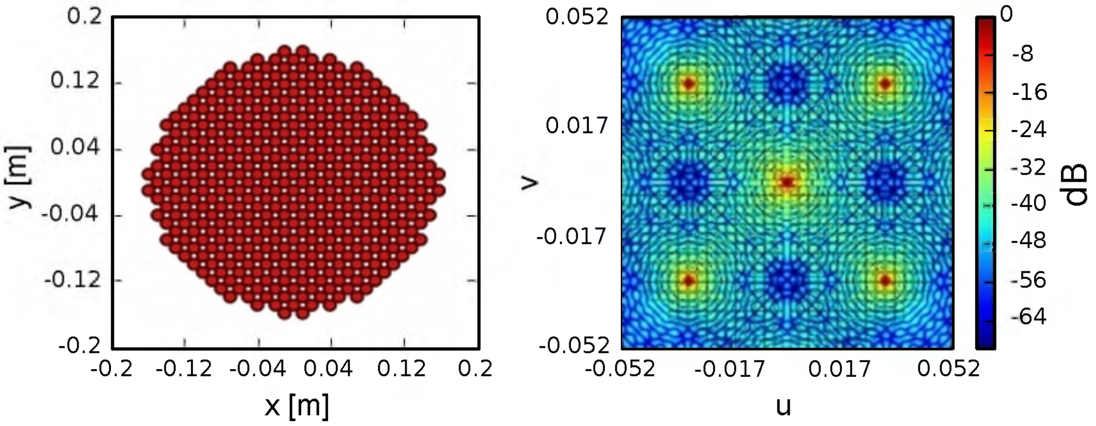

Figure 2 – (Left) QUBIC aperture plane showing all 400 antennas open to the sky; (right) the interference pattern formed on each of the focal planes when the instrument is observing a point source located in the far field vertically along the instrument line-of-sight. The u and v coordinates are defined as: $u = \sin\theta\cos\phi$ and $v = \sin\theta\sin\phi$, where θ and ϕ are the angles on the celestial sphere defining the synthetic beam.

3.2 Self-Calibration

QUBIC self-calibration is a technique derived from the technique in radio-interferometry. This technique evolved from the original idea in the 1970's of "phase-closure" [7, 8, 9] to become in the early 1980's "self-calibration" [10, 11]. In QUBIC, self-calibration exploits the redundant interferometric patterns obtained when we selectively close various combinations of the 400 apertures.

To understand the basic concept, see the four panels of Figure 3. The top-right plot shows the interference pattern arising from a horn configuration in which only two horns are open and all the others are closed (top-left). The panels in the bottom row show that if we open any other horn pair with the same baseline, we should ideally obtain exactly the same interference pattern. Furthermore, Bigot-Sazy et al. [5] showed that the configuration in which only two horns are open is equivalent to the complementary arrangement in which only two horns are closed.

We can now use the fact that, for an ideal instrument, the interferometric pattern depends only on the baseline. This allows us to characterize the instrumental parameters and non-idealities using an observation mode called self-calibration. In the self-calibration mode, pairs of horns are successively shut while QUBIC observes an artificial partially-polarized source (a microwave synthesizer or a Gunn oscillator) in the far field. Then, we reconstruct the signal measured by each individual pair of horns in the array and compare them.

The point now is that if the source is stable and carefully monitored, then redundant baselines correspond to the same mode of the observed field, so that a different signal between them can only be due to photon noise or instrumental systematic effects. Using a detailed parametric model of the instrument, we can fully recover the instrument parameters through a non-linear inversion process. The updated model of the instrument can then be used to reconstruct the synthetic beam and improve the map-making, reducing the leakage from E- to B-modes.

In Figure 4 (adapted from [5]), we show the improvement in the power spectrum estimation with self-calibration according to three schemes. Even with 1 s per baseline (corresponding to a full day dedicated to self-calibration), we can reduce significantly the $E \to B$ leakage. This leakage can be further reduced by spending more time in self-calibration. The three B-mode power spectra in black solid lines are the theoretically-expected spectra for three values of the parameter r, i.e., the ratio between the amplitudes of the tensor and scalar fluctuations during inflation.

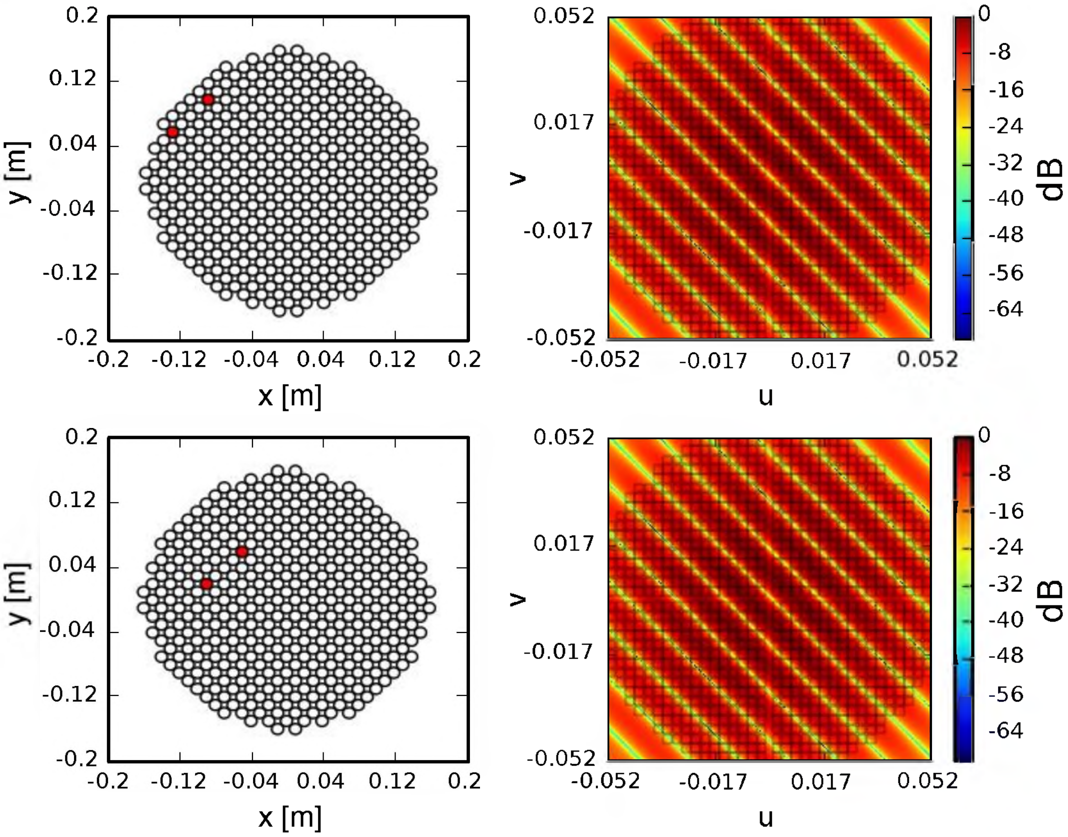

Figure 3 – Schematic of QUBIC self-calibration. The pictures in the two rows show that if we open any pair of horns with a given baseline, then in absence of systematic effects, we should measure exactly the same interference pattern.

3.3 Spectral Imaging

The interferometric nature of QUBIC provides us with another unique feature: the possibility to split the data of each main frequency band into sub-bands, thus considerably increasing the leverage in the control of astrophysical foregrounds.

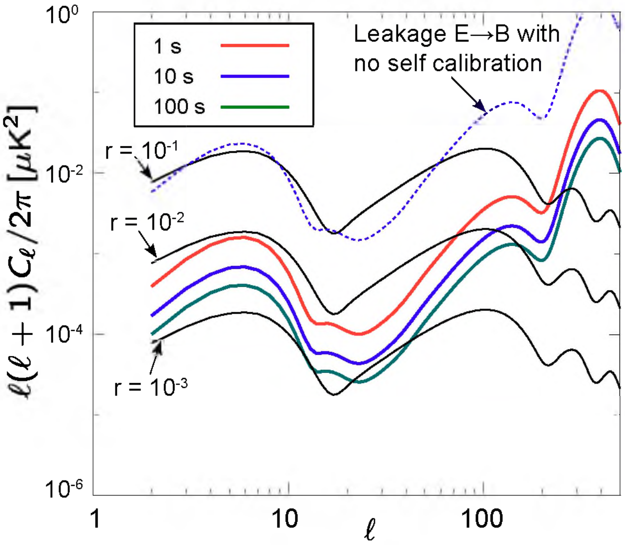

Figure 4 – Improvement in the recovery of the B-mode power spectrum as a function of the time spent in the self-calibration mode. The three curves drawn with black solid lines represent theoretical B-mode power spectra calculated for three different values of the tensor-to-scalar ratio, r. (adapted from [5])

This feature is called "spectral imaging", and its concept is explained schematically in Figure 5. The left panel of Figure 5 shows the synthetic beams (solid lines) and main feedhorn beams (dashed lines) at two monochromatic frequencies. The figure clearly shows that the sidelobe peaks are well separated, and this sensitivity of the synthetic beam to the frequency can be exploited to separate the various sub-bands in the input data.

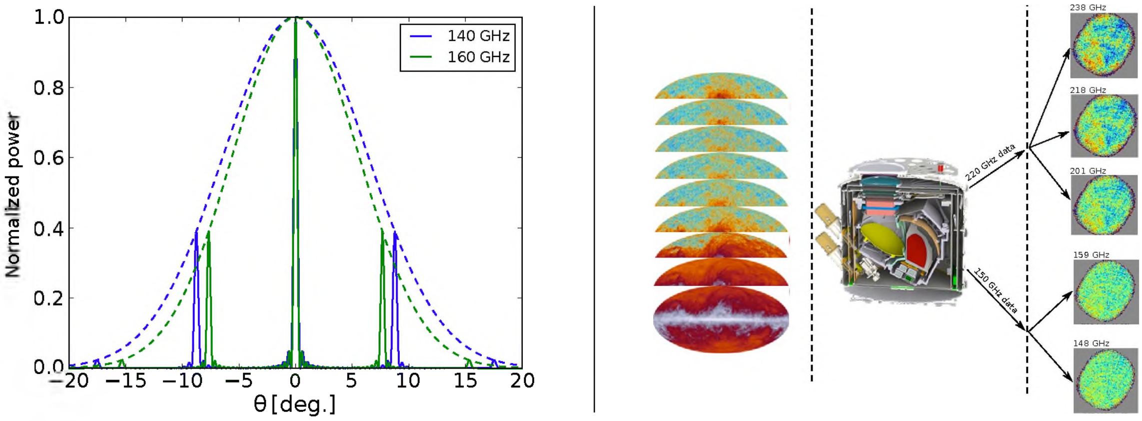

Figure 5 – (Left) Cut of the synthesized beam for two monochromatic signals. The main central peaks superimpose each other, but the first lobes are separated so that they can be resolved. The dashed lines represent the horn beams. (Right) Schematics representing the ability to resolve spectral sub-bands in each of the main QUBIC bands. The instrument first separates the wide-band sky signal into two main bands (150 and 220 GHz), then we further separate each band into sub-bands thanks to the spectral sensitivity of the synthesized beams. The Planck maps shown on the left have the only purpose of explaining the concept.

The right panel of Figure 5 shows schematically the process of sub-band separation in the data analysis. The instrument measures the wide-band sky signal and splits the two main frequency bands of 150 GHz and 220 GHz. Then, the main bands are further separated in the data analysis pipeline by exploiting the frequency sensitivity of the synthetic beam.

As spectral imaging opens new possibilities of foreground control, it also requires component separation codes that have been not been developed yet. We are currently working on a first detailed assessment of its potential and will soon submit a specific paper on spectral imaging.

4 The QUBIC Site

QUBIC will be deployed in Argentina, at the Alto Chorrillos mountain site (24°11′11.7″ S; 66°28′40.8″ W, altitude of 4869 m a.s.l.) near San Antonio de los Cobres, in the Salta province [12] (see the left panel of

Figure 6). The zenith optical depth measured at 210 GHz, τ_{210}, is <0.1 for 50% of the year and <0.2 for 85% of the year. Winds are usually mild (<6 m/s for 50% of the year), which suggests limited turbulence.

While the statistics for τ_{210} in Alto Chorrillos is worse than that of an Antarctic site (either South Pole or Dome C), the site access and logistics are easier. Our trade off is also justified by the following two facts: (i) the atmospheric emission is not polarized to first order, and (ii) a bolometric interferometer intrinsically rejects large-scale atmospheric gradients, which produce most of the atmospheric noise.

The right panel in Figure 6 (adapted from [4]) shows the overall site quality. In the plot, we see the uncertainty in the tensor-to-scalar ratio, r, as a function of the fraction of usable time for two years of operations. The circled point shows the estimate for the case in which zero or 12 h a day are spent in calibration mode. The plot shows that for a 30% usable time (a conservative estimate for our site), we can reach a sensitivity on r of 10^{-2} with two years of operations.

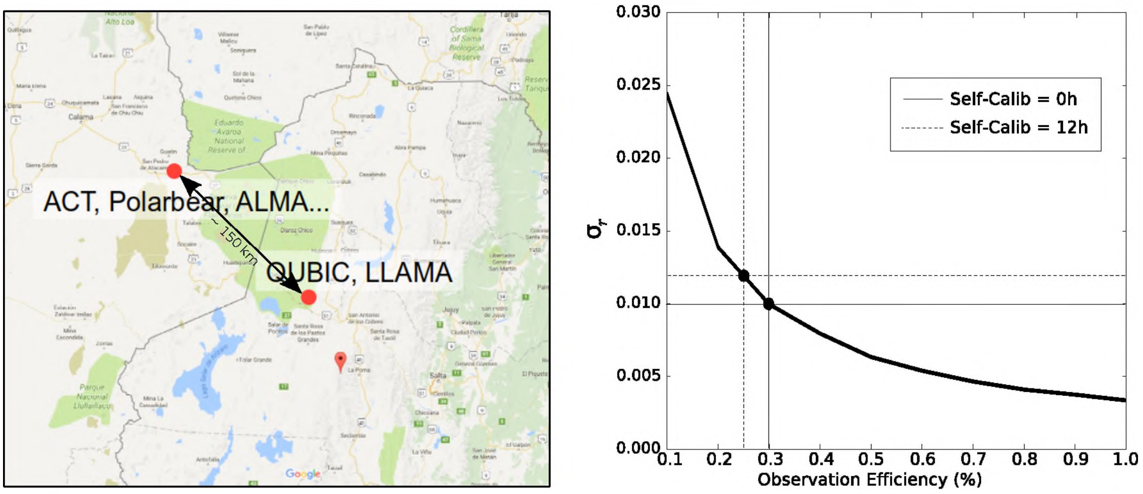

Figure 6 – (Left) Location of the QUBIC site compared to the Atacama plateau; (right) uncertainty in the tensor-to-scalar ratio, r, as a function of the fraction of usable time for two years of operations. The parameter r was computed considering noise-only simulations.

5 Current Status

QUBIC is currently in the phase of laboratory calibration of the so-called “Technological Demonstrator” (TD). The TD has a reduced focal plane and horn array with respect to the full instrument. In particular, the TD has only one-quarter of the 150-GHz TES focal plane, an array of 8 × 8 horns and switches, and a smaller optical combiner. The TD will demonstrate the feasibility of the bolometric interferometry both in the laboratory and in the field.

Figure 7 shows various QUBIC components. Panel (a) shows one of the two cryogenic detection chains. On top of the chain, one can see the TES focal plane. Panel (b) shows the array of the 8 × 8 back-to-back dual-band corrugated horns interfaced with the switch array. Panels (c) and (d) show the 1 K box before and during the integration into the QUBIC cryostat.

Figure 8 shows the setup in the laboratory at Astroparticle Physics and Cosmology (APC) in Paris. The calibration source reflects into the QUBIC cryostat window from a flat mirror. At a distance of over 11 m, the calibration source is well within t he far-field of QUBIC. The calibration source is a strong source easily detected by the detector array as seen in Figure 9. QUBIC was scanned in azimuth, and the beam mapped by one of the pixels is shown in Figure 10.

QUBIC TD is currently being calibrated at the Astroparticle Physics and Cosmology laboratory in Paris (APC). The testing phase will continue through Spring/Summer 2019 after which QUBIC will be shipped to Argentina and installed at the site for a first-light test foreseen within 2019. Components for the final instrument are being manufactured and tested in Europe, including the 20 × 20 horn array and switches, upgraded mirrors, and the two full TES detector arrays of 1024 detectors for each of the frequency bands (150 GHz and 220 GHz). The dual band QUBIC with complete detector arrays is expected to be operational on the Alto Chorrillos site in 2020.

6 Conclusions

QUBIC is a new way to measure the polarization of the CMB. It combines the sensitivity of TES bolometric arrays with the control of systematic effects that are typical of interferometers. This is a key asset in CMB

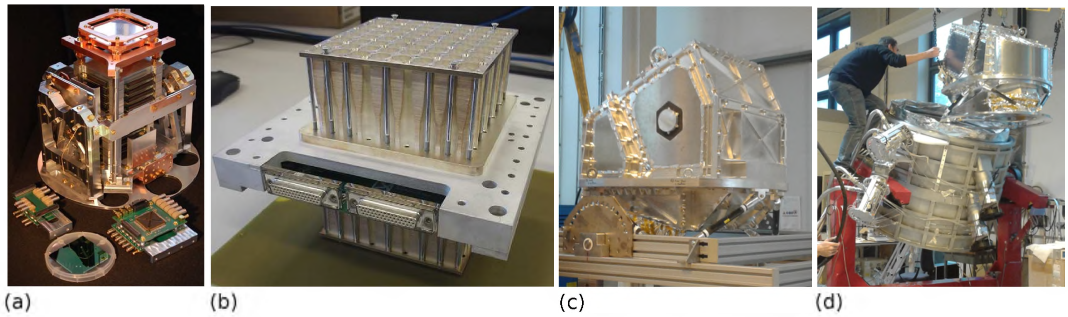

Figure 7 – Status of the current QUBIC development. ***(a)*** *The cryogenic section of the QUBIC detection chain;* ***(b)*** *the 8 × 8 back-to-back horns and switches array employed in the Technological Demonstrator (TD);* ***(c)*** *the integrated 1 K box;* ***(d)*** *integration of the 1K box in the cryostat shell.*

Figure 8 – (left) Photo of QUBIC in the foreground and the calibration source mounted on the wall at the far end of the room during the laser alignment procedure. (right) Photo of QUBIC looking along the line-of-sight from the calibration source. The reflection of the window is clearly visible in the flat mirror.

polarization experiments where high sensitivity must be combined with similarly low levels together with a high level of control of systematic and foreground effects. QUBIC responds to this challenge with the key features of self-calibration and spectral imaging, which are possible thanks to the interferometric nature of the instrument. A technological demonstrator is currently being tested in the laboratory and will soon be deployed in Argentina for a first-light test. We forecast the installation of the final instrument and the start of scientific operations during 2020, opening the way for a new generation of instruments in the field of Cosmic Microwave Background polarimetry.

QUBIC is funded by the following agencies. France: ANR (Agence Nationale de la Recherche) 2012 and 2014, DIM-ACAV (Domaine d'Interet Majeur—Astronomie et Conditions d'Apparition de la Vie), CNRS/IN2P3, CNRS/INSU. Italy: CNR-Programma Nazionale Ricerche in Antartide until 2016, Istituto Nazionale di Fisica Nucleare since 2017. Argentina: Secretaría de Gobierno de Ciencia, Tecnología e Innovación Productiva, Comisión Nacional de Energía Atómica, Consejo Nacional de Investigaciones Científicas y Técnicas. U.K.: the University of Manchester team acknowledges the support of STFCgrant ST/L000768/1. Ireland: James Murphy and David Burke acknowledge postgraduate scholarships from the Irish Research Council. Duc Hoang Thuong acknowledges the Vietnamese government for funding his scholarship at APC. Andrew May acknowledges the support of an STFCPhD Studentship.

7 References

[1] Ali, S.; Rossinot, P.; Piccirillo, L.; Gear, W. K.; Mauskopf, P.; Ade, P.; Haynes, V.; Timbie, P., MBI: Millimetre-wave bolometric interferometer, American Institute of Physics Conference Series, **2002** Vol 616, pp. 126-128, doi:10.1063/1.1475615

[2] Tucker, G.S. et al. New Astronomy Reviews 47 (2003) 11731176

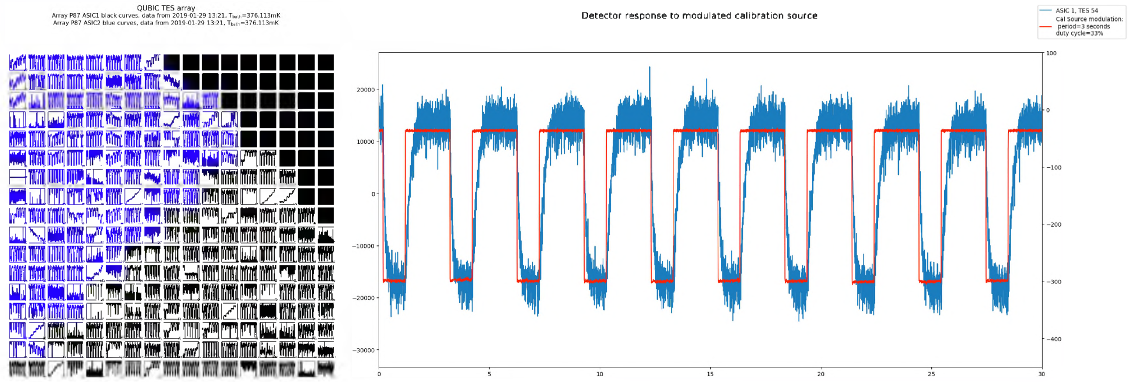

Figure 9 – Left: Detection of the modulated calibration source by the QUBIC detector array. The array shown here is for the Technological Demonstrator instrument and it covers one quarter of the full focal plane. Right: Comparison of the source modulation (red) with the detected signal (blue) for one of the TES detectors

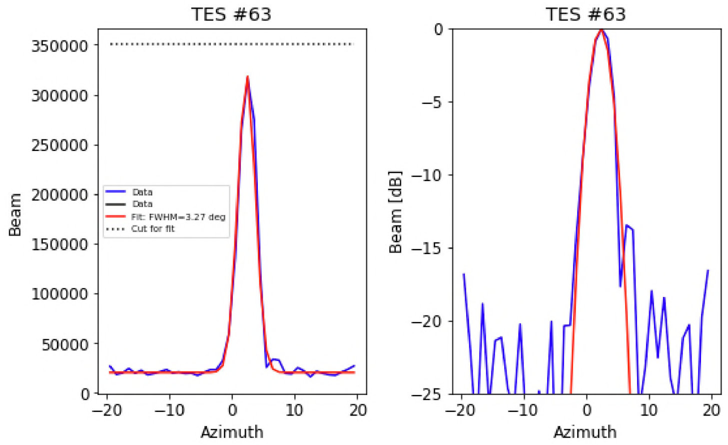

Figure 10 – An azimuth scan of the calibration source is shown here for one pixel. On the left, in linear intensity, and on the right on a dB scale.

[3] Tartari, A.; Aumont, J.; Banfi, S.; Battaglia, P.; Battistelli, E.S.; Baù, A.; Bélier, B.; Bennett, D.; Bergé, L.; Bernard, J.P.; et al. QUBIC: A Fizeau Interferometer Targeting Primordial B-Modes. *J. Low Temp. Phys.* **2015**, *181*, doi:10.1007/s10909-015-1398-3.

[4] Aumont, J.; Banfi, S.; Battaglia, P.; Battistelli, E.S.; Baù, A.; Bélier, B.; Bennett, D.; Bergé, L.; Bernard, J.P.; Bersanelli, M.; et al. QUBIC Technical Design Report. *arXiv* **2016**, arXiv:1609.04372.

[5] Bigot-Sazy, M.A.; Charlassier, R.; Hamilton, J.; Kaplan, J.; Zahariade, G. Self-calibration: An efficient method to control systematic effects in bolometric interferometry. *Astron. Astrophys.* **2013**, *550*, A59, doi:10.1051/0004-6361/201220429.

[6] Thompson, A. R.; Moran, J. M.; Swenson, Jr., G. W., Interferometry and Synthesis in Radio Astronomy, 3rd Edition, **2017**, doi:10.1007/978-3-319-44431-4

[7] Hogbom 1974, A&AS, 15, 417

[8] Fort & Yee 1976, A&A 50, 19

[9] Readhead & Wilkinson 1978, ApJ, 223, 25

[10] Cornwell & Wilkinson, 1981 MNRAS, 196, 1067

[11] Pearson, T. J., & Readhead, A. C. S. 1984, ARA&A, 22, 97

[12] De Bernardis, P.; Ade, P.; Amico, G.; Auguste, D.; Aumont, J.; Banfi, S.; Barbarán, G.; Battaglia, P.; Battistelli, E.; Baù, A.; et al. QUBIC: Measuring CMB polarization from Argentina. *Bol. Asoc. Argent. Astron. Plata Argent.* **2018**, *60*, 107–114.

SPICA:
Le futur grand observatoire spatial infrarouge de l'Europe et du Japon
The future ESA-JAXA large infrared space observatory

Giard M[1] et F. Herpin[2] et M. Sauvage[3] pour la collaboration SPICA

[1]IRAP, CNRS-UPS, Université de Toulouse, martin.giard@irap.omp.eu
[2]LAB, CNRS, Université de Bordeaux, fabrice.herpin@u-bordeaux.fr
[3]AIM, CEA-IRFU-DAp, Saclay, marc.sauvage@cea.fr

Mots clés (en français et en anglais) : astronomie spatiale infrarouge / infrared space astronomy

Résumé/Abstract

SPICA est le projet d'observatoire infrarouge spatial de nouvelle génération porté par l'Europe et le Japon, et qui pourrait voir sa première lumière au début de la décennie 2030. Il s'inscrit dans la lignée des observatoires spatiaux infrarouge de l'agence spatiale européenne: ISO et HERSCHEL. Equipé d'un miroir primaire de 2,5 mètre de diamètre, il sera le premier observatoire infrarouge disposant de systèmes de refroidissement 100% électriques, et sa durée de vie ne sera donc pas limitée comme pour ses prédécesseurs par la disponibilité de fluides cryogéniques embarqués. SPICA sera par ailleurs équipé d'une panoplie de détecteurs refroidis en dessous du degrés Kelvin, offrant des possibilités de mesures en spectroscopie, imagerie et polarisation, et qui offriront aux astronomes du monde entier des performances 100 à 1000 fois supérieures à ce qui aura été possible dans ce domaine de longueur d'onde (12 – 300 µm) aussi bien avec HERSCHEL, SOFIA que JWST. De cette façon, SPICA ouvrira une fenêtre d'étude totalement nouvelle sur la physico-chimie des régions obscurcies: systèmes planétaires en formation dans notre Galaxie et galaxies lointaines en formation.

SPICA is the future space infrared observatory discussed between the European (ESA) and Japanese (JAXA) space agencies to be in service in the beginning of the 2030's. On the European side, this will be the successor of ISO and HERSCHEL. With a primary mirror of 2,5 meter diameter, this will be the first infrared observatory equipped with fully electric cryogenic systems so that its lifetime will not be limited by cryogenic fluids reserves. The SPICA focal plane will be instrumented with sub-kelvin detectors, in spectroscopy, imagery and polarimetry, which will offer to the worldwide astronomy community performances 100 to 1000 times higher than what would have ever been achieved in this wavelength domain (12 – 300 µm) with HERSCHEL, SOFIA or JWST. SPICA will thus open a fully unexplored observing window on the physics of obscured regions in the Universe: planetary systems in formation within our Galaxy, and distant galaxies in the forming.

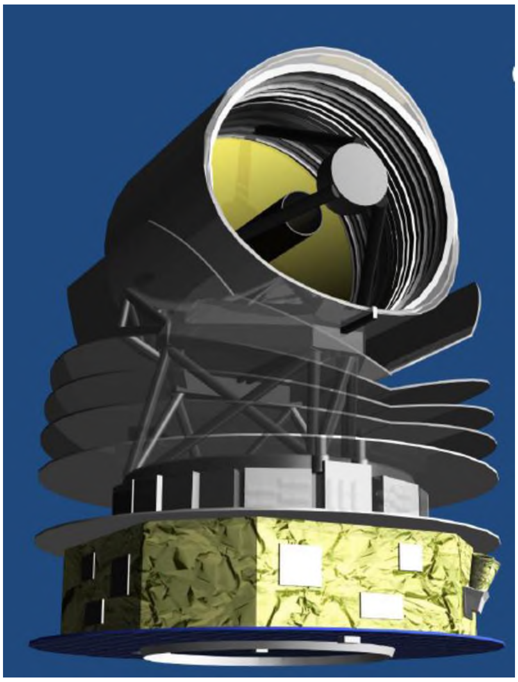

Figure 1 : l'observatoire spatial SPICA.

1 La mission SPICA

SPICA (the SPace Infrared telescope for Cosmology and Astrophysics) [1] sera un observatoire spatial infrarouge doté d'un télescope de 2,5 mètres de diamètre refroidi à 8 Kelvin par un système de refroidissement passif et des machines cryogéniques. Actuellement étudié par l'Agence Spatiale Européenne (ESA) pour un financement dans le cadre de la mission M5 du programme scientifique Cosmic Vision, SPICA sera réalisé en partenariat avec l'agence spatiale Japonaise (JAXA) en vue d'un lancement en 2032 par une fusée Japonaise pour une mise en service quelques mois plus tard au point de Lagrange L2 du système Soleil-Terre à environ 1 500 000 kilomètres de la Terre. SPICA sera équipé de trois instruments focaux (cf Tableau 1 ci dessous) lui permettant d'analyser les rayonnements infrarouge en spectroscopie, photométrie et polarimétrie de 12 à 300 µm : SMI sous responsabilité Japonaise, SAFARI sous responsabilité Hollandaise, et B-BOP sous responsabilité Française. Ces trois instruments utilisent des détecteurs inédits qui ont été spécifiquement développés au cours des dix dernières années au Japon [2], en Hollande [3] et en France [4].

Tableau 1 : Capacités instrumentales de SPICA

Spectroscopie		
SAFARI	34 – 230 µm	Résolution spectrale = 300 à 11000
SMI/MR	18 – 36 µm	Résolution spectrale ≈ 1000 à 2000
SMI/HR	12 – 18 µm	Résolution spectrale = 28000
SMI/LR	17 – 36 µm	Résolution spectrale ≈ 100
Imagerie		
SMI/CAM	30 – 37 µm	Champ de vue : 10'x12'
Polarimétrie		
B-BOP	110/220/350 µm	Champ de vue : 2,6'x2,6'

L'unicité de SPICA réside dans la combinaison d'un télescope refroidi à 8 Kelvin et d'instruments équipés de détecteurs refroidis en dessous de 0,1 Kelvin, de sorte que la sensibilité de cet observatoire spatial sera limitée uniquement par le bruit statistique du rayonnement de fond de ciel qui à ces longueurs d'onde provient de l'émission thermique des poussières diffuses dans le système solaire (lumière zodiacale) et dans la Voie Lactée (cirrus galactiques). De cette façon, SPICA ouvrira la fenêtre astronomique située entre celles des observatoires JWST (dans l'espace) et ALMA (au sol), avec une sensibilité 100 à 1000 fois supérieure à ce qu'a offert par le passé l'observatoire spatial HERSCHEL [5], ou ce qui est disponible actuellement à bord de l'observatoire stratosphérique SOFIA [6] (cf Figure 2).

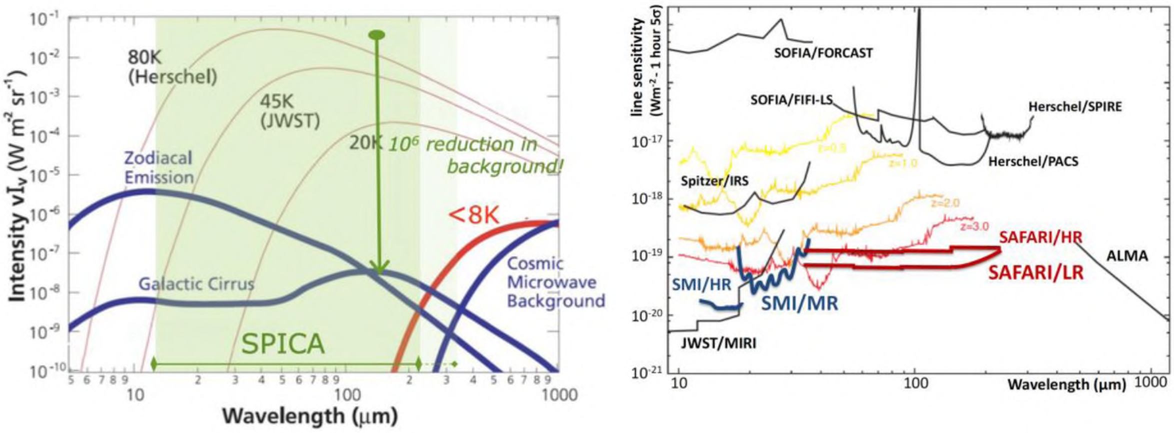

Figure 2 - gauche : niveaux comparés des fonds d'émission instrumentaux (HERSCHEL 80K, JWST 45K, SPICA <8K) et du ciel astronomique (émission zodiacale, émission galactique, rayonnement fossile). – droite : sensibilités spectroscopiques comparées de SPICA, JWST, HERSCHEL et ALMA.

Le refroidissement du télescope et de ses instruments est possible grâce à une combinaison de machines cryogéniques : réfrigérateurs Steerling coolers à 25K, 20K, et 15K, réfrigérateurs Joule-Thompson à 4K et 1K, réfrigérateur hybrides à sorption d'Hélium 3 (300 mK) et démagnétisation adiabatique (50mK).

Le développement de l'ensemble de la mission SPICA (ESA, JAXA) et de ses instruments (consortiums internationaux) est de l'ordre d'un milliard d'euros et atteint de fait l'ampleur d'une mission ESA de type L.

2 Objectifs scientifiques de SPICA.

L'unicité de SPICA sera dans sa capacité à caractériser physiquement, par la spectroscopie, l'imagerie et la polarimétrie, les régions obscurcies de notre Univers, celles qui renferment les clefs de la formation des étoiles, des éléments lourds et des planètes à partir du gaz primordial.

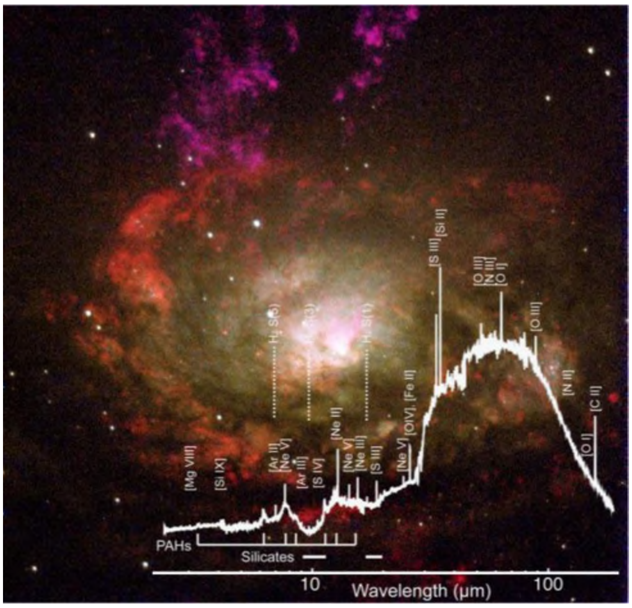

Figure 3 : spectre obtenu avec le satellite ISO sur la galaxie voisine Circinus, prototype d'une galaxie à flambée de formation d'étoiles [14]. SPICA pourra caractériser ainsi des milliers de galaxies dans l'univers lointain.

Dans le domaine de la formation des galaxies (cf Figure 3) et des trous noirs massifs qui leurs sont associés, ont sait qu'ils sont nés lors d'une flambée spectaculaire il y a 10 à 6 milliard d'années. SPICA sera le premier observatoire capable de construire avec ses instruments SAFARI et SMI une bibliothèque de spectres pour plus d'un millier de ces objets répartis sur toute la durée de cette flambée afin d'en élucider les mécanismes qui ont mené à l'Univers qui nous environne (cf [7], [8], [9], [10], [11], [12] et [13]). La spectroscopie des raies des ions, des atomes, de certaines molécules et des bandes des grains de poussière sont une observable absolument unique qui permettra de quantifier les processus physique à l'œuvre lors de cette période clef.

En ce qui concerne la formation des étoiles, B-BOP, l'imageur polarimétrique de SPICA, pourra mesurer les champs magnétiques au sein des nuages moléculaires proches, pouponnières d'étoiles nouvelles, aux échelles spatiales critiques pour comprendre les processus qui permettent au gaz moléculaire magnétisé de se condenser en étoiles et systèmes planétaires (cf la Figure 4 qui illustre le potentiel de B-BOP dans ce domaine par la superposition d'une image d'intensité réalisée avec HERSCHEL avec des lignes indiquant la direction du champ magnétique mesurée avec l'instrument polarimétrique PLANCK-HFI).

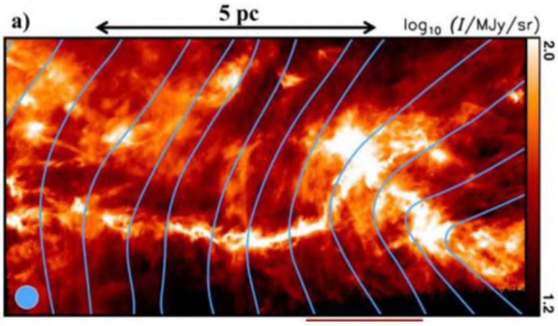

Figure 4 : couleurs : intensité de l'émission des poussières dans des filaments des nuages moléculaires proches cartographiée avec HERSCHEL, -lignes continues : direction du champ magnétique mesurée avec le satellite PLANCK.

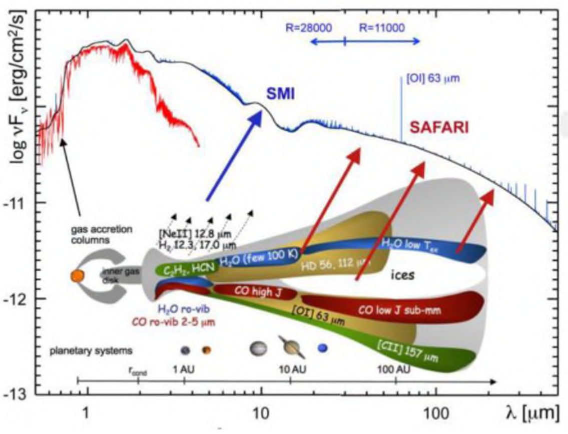

Figure 5 : séparation spectrale et caractérisation physique des gaz et poussières qui composent un disque de formation planétaire autour d'une très jeune étoile.

Dans le domaine de la formation des systèmes planétaires, c'est à nouveau la puissance spectrale de SAFARI et SMI qui permettra de caractériser l'état physique des disques de gaz et de poussières autour d'étoiles proches dans lesquels des planètes sont en train de se former. Grâce aux transitions de l'hydrogène moléculaire deutéré situées à 56 et 112 µm, SPICA sera le seul observatoire astronomique au monde capable d'évaluer directement la masse de ces disques gazeux, sans passer par des traceurs minoritaires comme le monoxyde de carbone utilisé communément par les grands observatoires sol comme ALMA.

Le gain en sensibilité de SPICA sera tel (un facteur 100 à 1000), que cette mission ouvrira à coup sur des chapitres complètement nouveaux de l'astrophysique. Par exemple, dans le domaine des champs magnétiques, de leur croissance à partir de mécanismes primordiaux et de leur rôle dans la formation des galaxies, B-BOP ouvrira très probablement des perspectives inconnues à ce jour.

Références bibliographiques

[1] Roelfsema, P., et al., 2018, Publications of the Astronomical Society of Australia, Volume 35, id.e030

[2] Khalap, V., & Hogue, H. 2012, Proc. SPIE, 8512, 85120O.

[3] Audley, M., et al. 2018, Proceedings of the SPIE, Volume 10708, id. 107080K.

[4] Goudon, V. et al., 2018, Proceedings of the SPIE, Volume 10708, id. 107083O.

[5] Pilbratt, G. et al., 2010, Astronomy and Astrophysics, Volume 518, id.L1.

[6] Temi, P., et al., 2014, The Astrophysical Journal Supplement Series, Volume 212, Issue 2, article id. 24.

[7] Spinoglio, L. et al., 2017, Publications of the Astronomical Society of Australia 34, pe057.

[8] Fernandez-Ontiveros, J.A. et al., 2017, Publications of the Astronomical Society of Australia 34, pe053.

[9] Gonz{\'a}lez-Alfonso, E. et al., 2017, Publications of the Astronomical Society of Australia 34, pe054.

[10] Gruppioni, C. et al., 2017, Publications of the Astronomical Society of Australia 34, pe055.

[11] van der Tak, F.~F.~S. et al., 2017, Publications of the Astronomical Society of Australia 35, pe002.

[12] Egami, E. et al. 2017, Publications of the Astronomical Society of Australia 35, p.

[13] Kaneda, H. et al., 2017, Publications of the Astronomical Society of Australia 34, pe059.

[14] Moorwood, A., 1999, Astrophysics with Infrared Surveys: A Prelude to SIRTF, ASP Conference Series, Vol. 177. ISBN: 1-58381-001-3 (1999), p.141

The renaissance of radio-astronomy with the Square Kilometre Array
La renaissance de la radio-astronomie avec le Square Kilometre Array

---

Marc-Antoine Miville-Deschênes[1]

[1]*Laboratoire AIM, Université Paris-Saclay, Orme-des-merisiers, 91191, Gif-sur-Yvette, marc-antoine.miville-deschenes@cnrs.fr*

Keywords: radiotelescope, astrophysics, cosmology, big data
Mots-clefs: raio-télescope, astrophysique, cosmologie, big data

---

Abstract:

The Square Kilometre Array is an international collaboration whose goal is the construction of the world's largest low-frequency (0.50 to 25 GHz) radio telescope. SKA will conduct groundbreaking research that will transform our understanding of the Universe and fundamental physics. It also represents a huge technological challenge, being in particular one of the main world-wide future Big Data projects.

In this talk I will be giving an overview of the scientific objectives and technological challenges of the SKA and the rapidly increasing progress towards the beginning of construction. I will present some first results from the precursor telescopes designed to paved the way to the full SKA. Finally I will describe how the SKA project has brought the french community to innovate and create a new structure, the « Maison SKA-France », to coordinate the activities of the scientific, technological and industrial partners involved in SKA.

Résumé:

Le Square Kilometre Array est une collaboration internationale dont l'objectif est la construction du plus grand radio-télescope basses fréquences (0.5 à 25 GHz) au monde. SKA permettra des explorations scientifiques inédites qui devraient transformer notre compréhension de l'Univers et de la physique fondamentale. Ce projet représente un défis technologique de taille, tout particulièrement en étant le plus grand projet Big Data des années à venir.

Dans cette présentation je présenterai sommairement les objectifs scientifiques de SKA, les défis technologiques spécifiques à ce projet et je ferai un point sur l'état d'avancement de la construction. Je présenterai les premiers résultats scientifiques des télescopes précurseurs de SKA. Finalement je décrirai comment la France a innové en créant une structure, la maison SKA-France, qui permet de coordonner les activités scientifiques, technologiques et industriels des partenaires impliqués dans SKA.

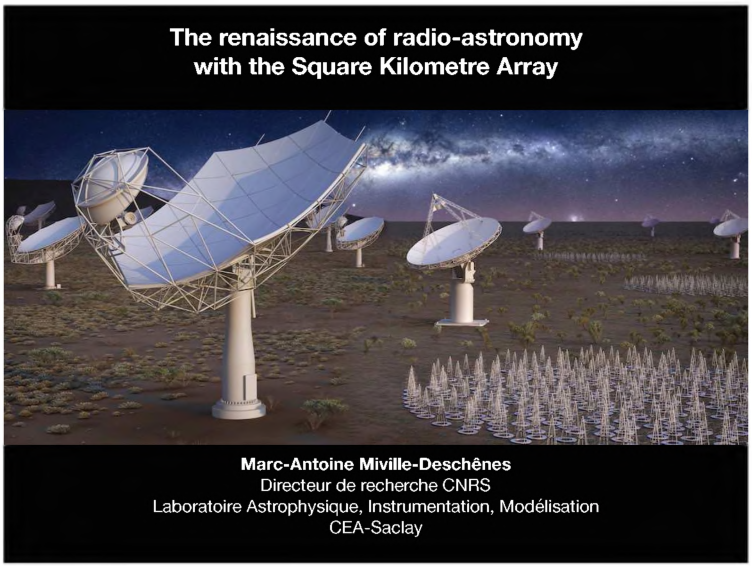

The renaissance of radio-astronomy with the Square Kilometre Array

Marc-Antoine Miville-Deschênes
Directeur de recherche CNRS
Laboratoire Astrophysique, Instrumentation, Modélisation
CEA-Saclay

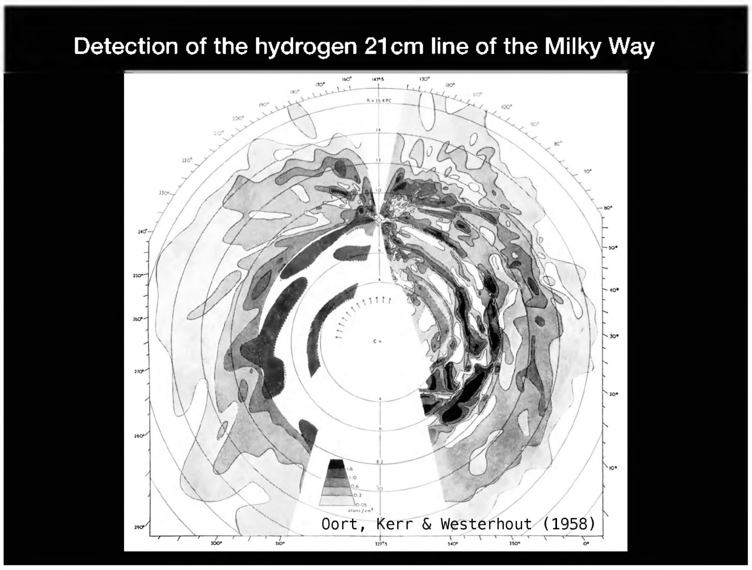

Detection of the hydrogen 21cm line of the Milky Way

Oort, Kerr & Westerhout (1958)

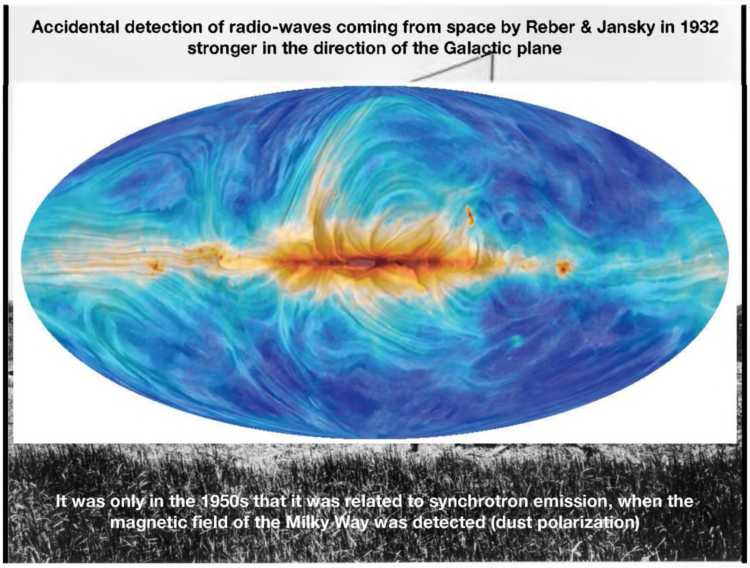

Accidental detection of radio-waves coming from space by Reber & Jansky in 1932 stronger in the direction of the Galactic plane

It was only in the 1950s that it was related to synchrotron emission, when the magnetic field of the Milky Way was detected (dust polarization)

THINGS

The HI Nearby Galaxy Survey

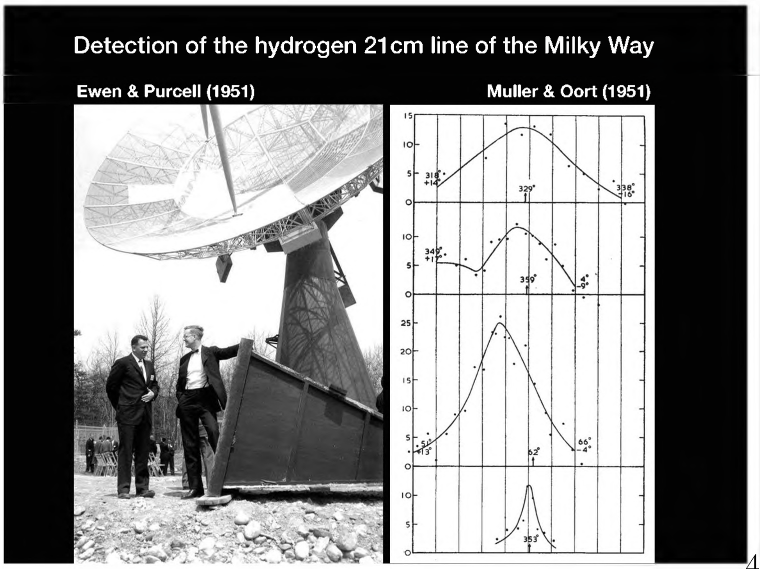

Detection of the hydrogen 21cm line of the Milky Way

Ewen & Purcell (1951)

Muller & Oort (1951)

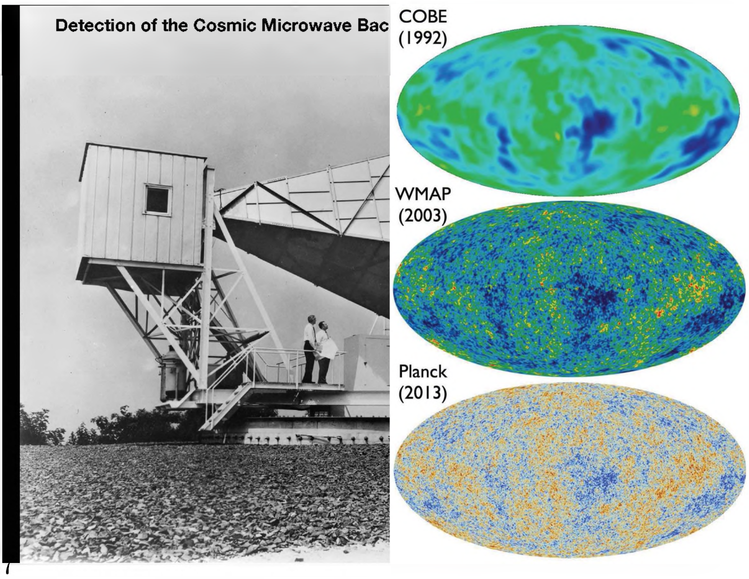

Detection of the Cosmic Microwave Bac

COBE (1992)

WMAP (2003)

Planck (2013)

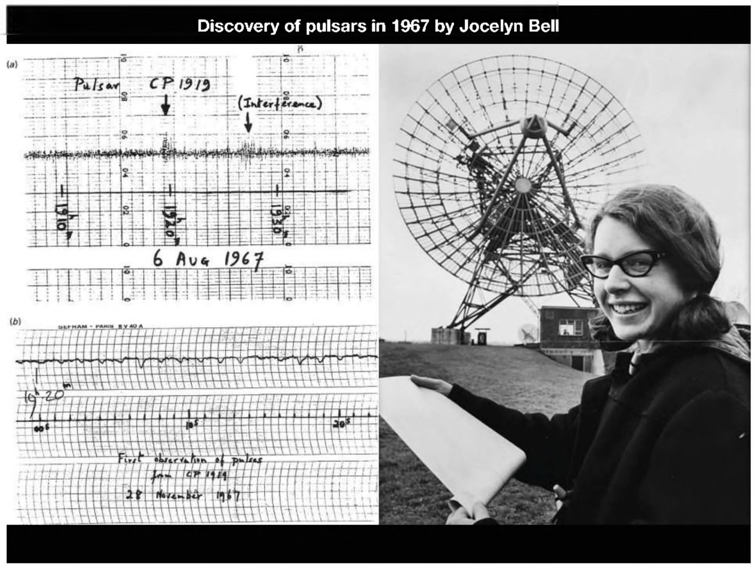

Discovery of pulsars in 1967 by Jocelyn Bell

Members
Host Countries: Australia, South Africa, United Kingdom

African partner countries

Potential futur members
Germany, Japan, Portugal, Switzerland, South Corea

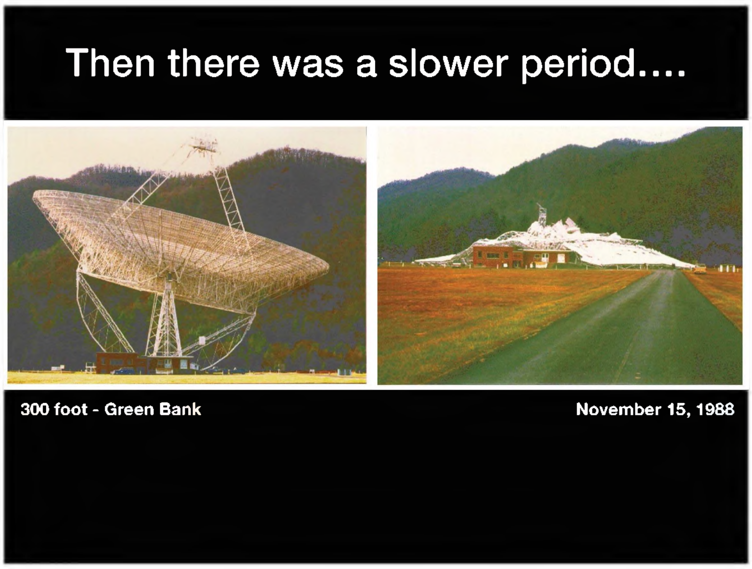

Then there was a slower period....

300 foot - Green Bank

November 15, 1988

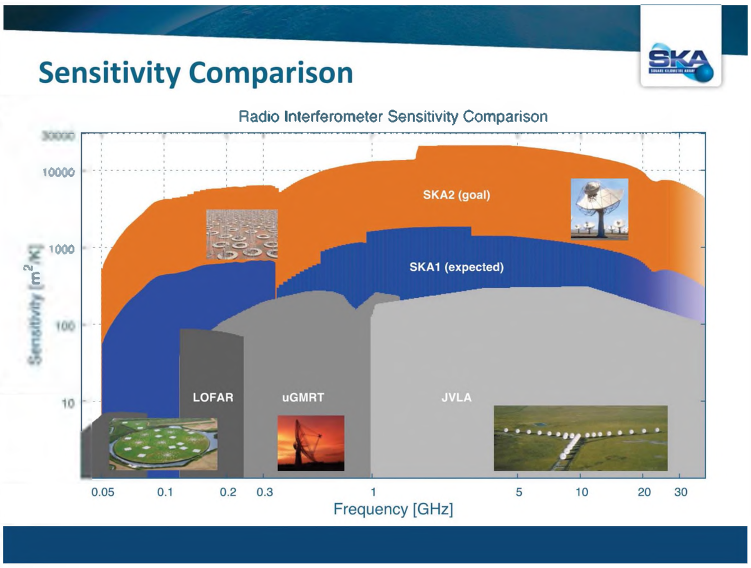

Sensitivity Comparison

Radio Interferometer Sensitivity Comparison

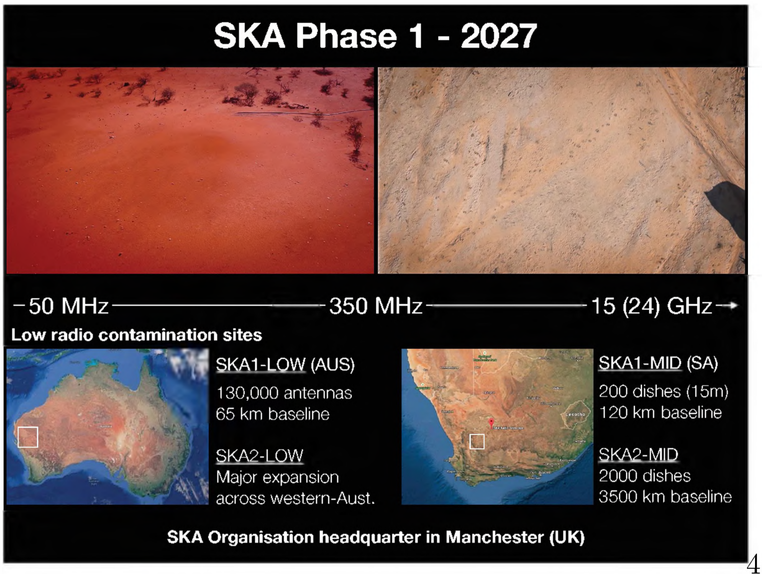

SKA Phase 1 - 2027

−50 MHz———350 MHz———15 (24) GHz→

Low radio contamination sites

SKA1-LOW (AUS)
130,000 antennas
65 km baseline

SKA2-LOW
Major expansion
across western-Aust.

SKA1-MID (SA)
200 dishes (15m)
120 km baseline

SKA2-MID
2000 dishes
3500 km baseline

SKA Organisation headquarter in Manchester (UK)

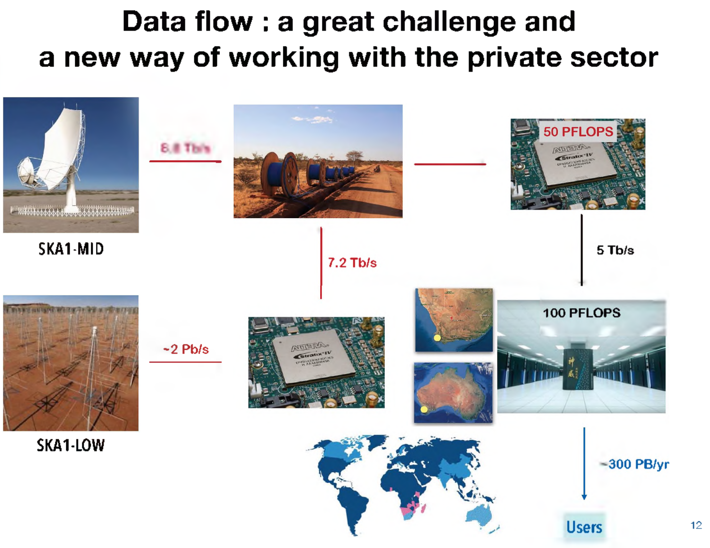

Data flow : a great challenge and a new way of working with the private sector

12

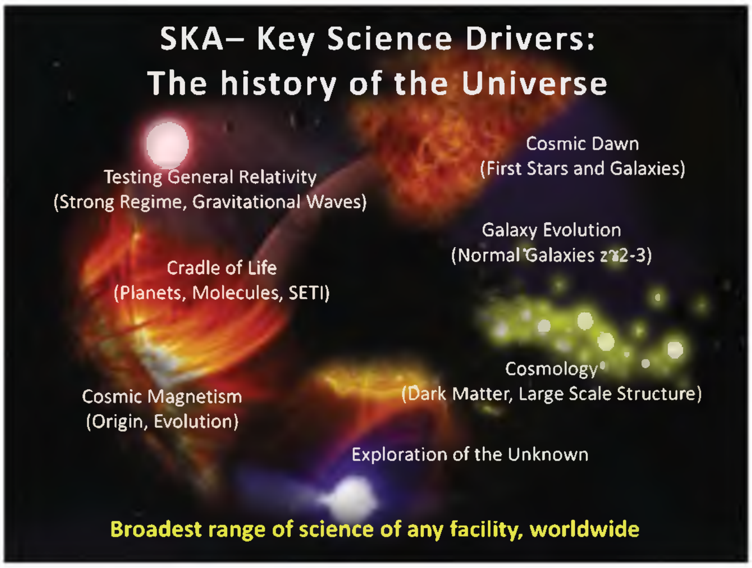

SKA– Key Science Drivers: The history of the Universe

Testing General Relativity
(Strong Regime, Gravitational Waves)

Cosmic Dawn
(First Stars and Galaxies)

Galaxy Evolution
(Normal Galaxies z~2-3)

Cradle of Life
(Planets, Molecules, SETI)

Cosmology
(Dark Matter, Large Scale Structure)

Cosmic Magnetism
(Origin, Evolution)

Exploration of the Unknown

Broadest range of science of any facility, worldwide

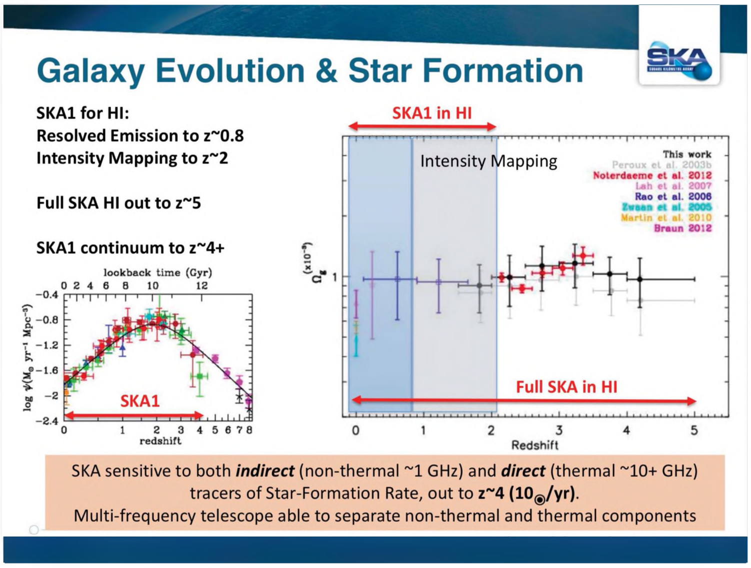

Galaxy Evolution & Star Formation

SKA1 for HI:
Resolved Emission to z~0.8
Intensity Mapping to z~2

Full SKA HI out to z~5

SKA1 continuum to z~4+

SKA sensitive to both ***indirect*** (non-thermal ~1 GHz) and ***direct*** (thermal ~10+ GHz) tracers of Star-Formation Rate, out to **z~4 (10$_{\odot}$/yr)**.
Multi-frequency telescope able to separate non-thermal and thermal components

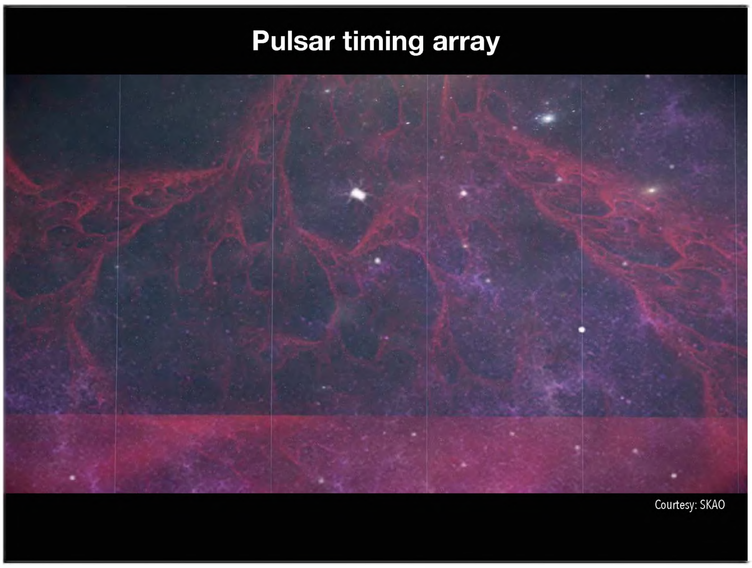

Pulsar timing array

Courtesy: SKAO

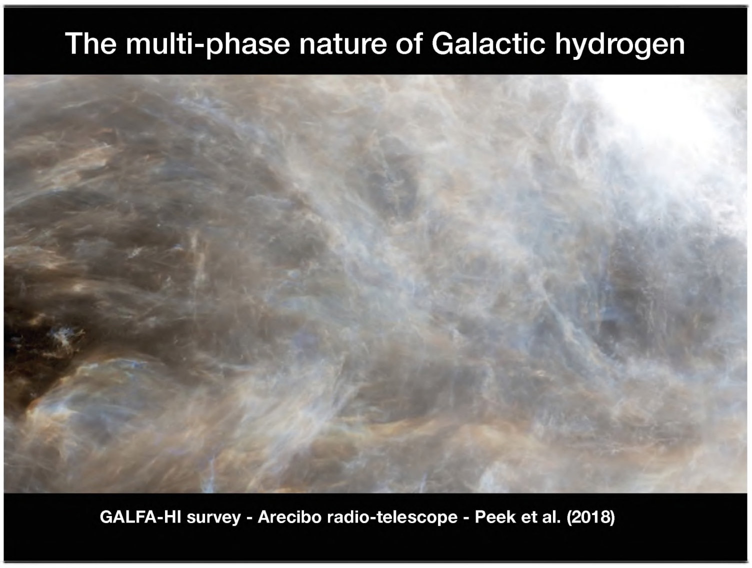

The multi-phase nature of Galactic hydrogen

GALFA-HI survey - Arecibo radio-telescope - Peek et al. (2018)

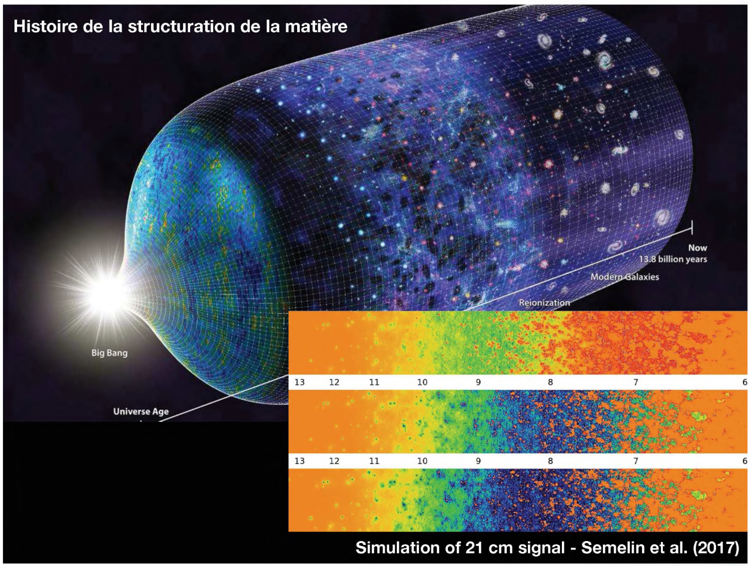

Histoire de la structuration de la matière

Simulation of 21 cm signal - Semelin et al. (2017)

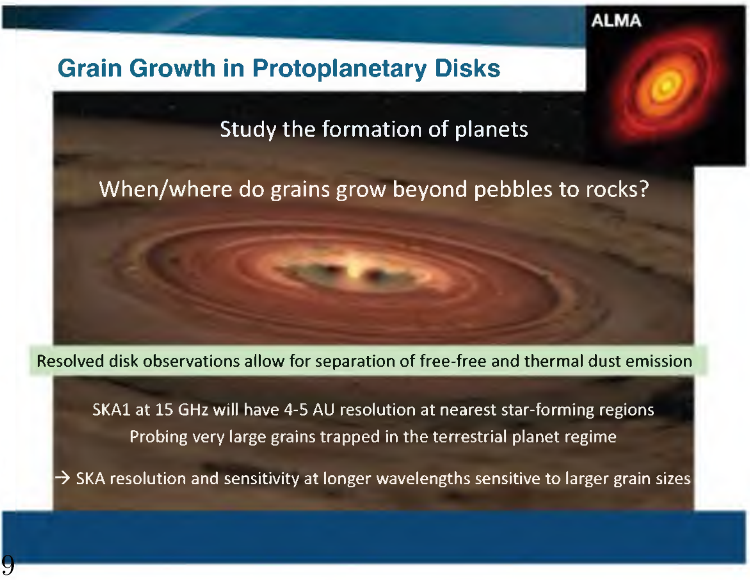

Grain Growth in Protoplanetary Disks

Study the formation of planets

When/where do grains grow beyond pebbles to rocks?

Resolved disk observations allow for separation of free-free and thermal dust emission

SKA1 at 15 GHz will have 4-5 AU resolution at nearest star-forming regions
Probing very large grains trapped in the terrestrial planet regime

→ SKA resolution and sensitivity at longer wavelengths sensitive to larger grain sizes

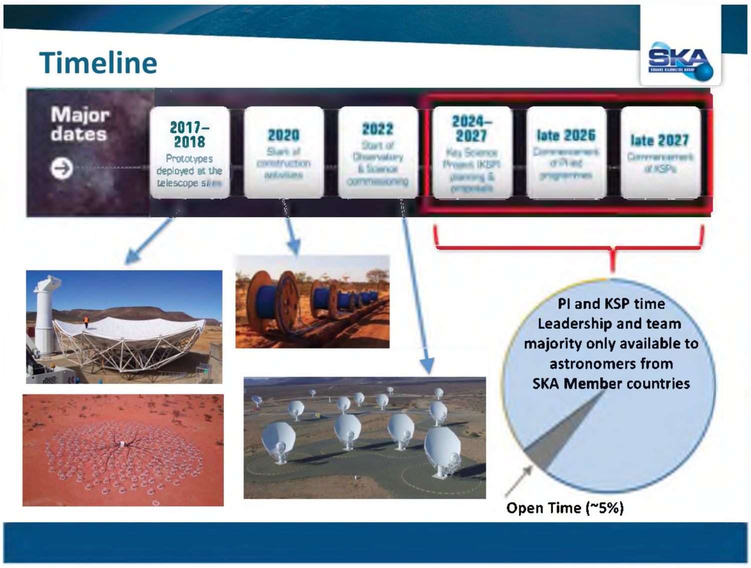

Timeline

Major dates

- **2017–2018** Prototypes deployed at the telescope sites
- **2020** Start of construction activities
- **2022** Start of Observatory & Science commissioning
- **2024–2027** Key Science Project (KSP) planning & proposals
- **late 2026** Commencement of PI-led programmes
- **late 2027** Commencement of KSPs

PI and KSP time
Leadership and team majority only available to astronomers from SKA Member countries

Open Time (~5%)

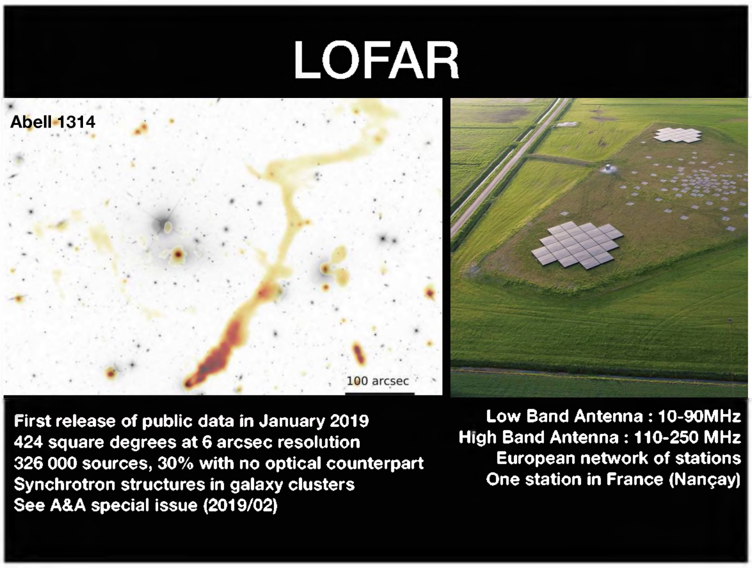

LOFAR

First release of public data in January 2019
424 square degrees at 6 arcsec resolution
326 000 sources, 30% with no optical counterpart
Synchrotron structures in galaxy clusters
See A&A special issue (2019/02)

Low Band Antenna : 10-90MHz
High Band Antenna : 110-250 MHz
European network of stations
One station in France (Nançay)

the Galactic centre

Meerkat, South Africa

2018/07

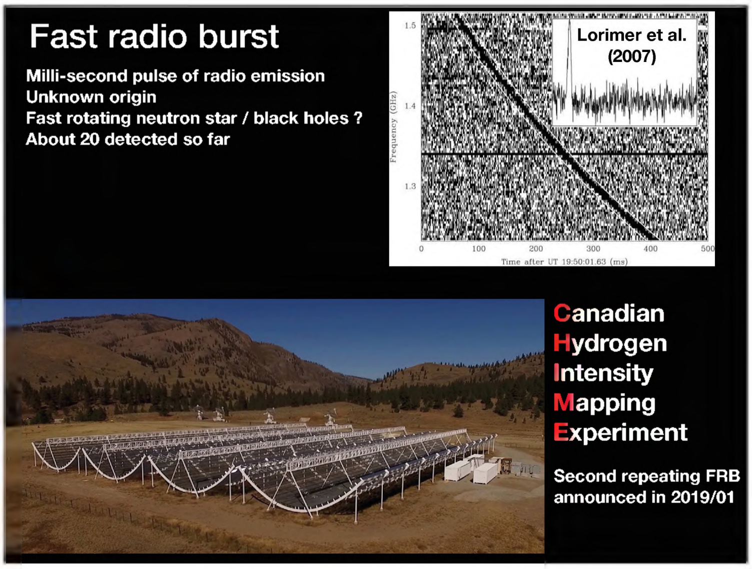

Fast radio burst

Milli-second pulse of radio emission
Unknown origin
Fast rotating neutron star / black holes ?
About 20 detected so far

Canadian
Hydrogen
Intensity
Mapping
Experiment

Second repeating FRB announced in 2019/01

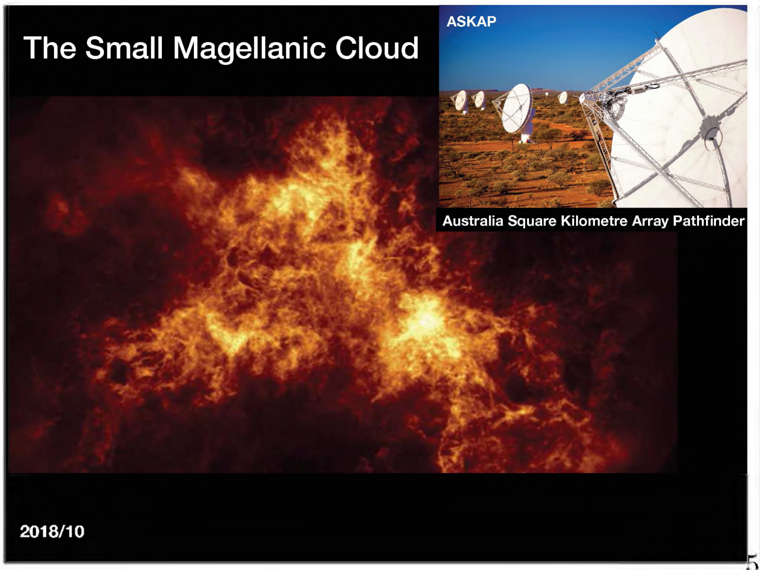

The Small Magellanic Cloud

ASKAP

Australia Square Kilometre Array Pathfinder

2018/10

The high potential for discoveries of the SKA

- Largest range of scales (LSS to planets)
- Largest range of time scales, from the firsts stars to now
- Large range of spectral diagnostics (21 cm, free-free synchrotron, RRL, molecular lines, Zeeman, Faraday rotation, dust emission)
- Increase of performance with time: with computing power and algorithms (hardware is cheap)
- New way to look at the sky (large field of view, high angular resolution (<arcsec), high mapping speed, evolution with time)
- Involved private sector: a new way of doing science

For more information

as-ska-lofar.fr [en francais]

Actualité

- **Ouverture de l'appel à propositions d'observations pour le Cycle 12 de LOFAR.** Date limite de réponse le 6 mars 2019 à 12h TU. [15-02-2019]
- **Invitation à participer à l'atelier « NenuFAR utilisateurs #1 »** à Nancay 18-20 mars 2019. Inscription avant le 10 février 2019. [17-01-2019]
- **Appel à propositions de Key Programmes sur NenuFAR**date limite 31 mars 2019. [17-01-2019]
- **Ouverture de l'appel d'offre de l'AS SKA-LOFAR** date limite de remise des dossier le 18 janvier 2019. [20-12-2018]
- **Lancement du premier data challenge SKA** [19-12-2018]

Les questions scientifiques abordées par la radio-astronomie

La radio-astronomie permet d'aborder un vaste domaine de questions de l'astrophysique et de la physique contemporaines, incluant de nouveaux tests de la théorie de la gravité, la détection d'ondes gravitationnelles, les grandes structures de l'Univers, la formation des premières étoiles, l'Univers transitoire, l'évolution des galaxies, la turbulence magnéto-hydrodynamique à toutes les échelles, la formation des étoiles, l'observations des exoplanètes, et la physique solaire et planétaire. La diversité de ces sujets scientifiques est illustrée par les trois liens suivants présentant divers travaux de reflexion et d'organisation du projet SKA.

Le livre officiel de la science de SKA

En septembre 2015, l'Organisation SKA a publié "Advancing Astrophysics with the Square Kilometer Array". Ce livre contient les actes de la conférence scientifique SKA qui s'est tenue à Giardini Naxos, Sicile en 2014. Les deux volumes de cet ouvrage sont constitués de 135 chapîtres écrits par 1213 auteurs de 31 nationalités, pour un total de plus de 2000 pages, couvrant tous les domaines de la science de SKA.

SKA pour scientifiques

Ce site de l'organisation SKA est à l'intention des astronomes et astrophysiciens. Il inclut des détails techniques, des définitions et des liens utiles. Il s'agit du portail d'accès principal aux SKA Scientific Working Groups. On y trouve également une page répondant aux questions fréquentes - FAQs

Le livre blanc SKA-France

En décembre 2017, la communauté française intéressée par le projet SKA a publié son livre blanc : The French Community towards the Square Kilometre Array. Ce document de 200 pages, rédigé par près de 200 auteurs provenant de 40 insituts de recherche et 6 compagnies issues du privé, détaille les intérêts français pour le projet SKA, autant des côtés scientifique, technique qu'industriel.

skatelescope.org

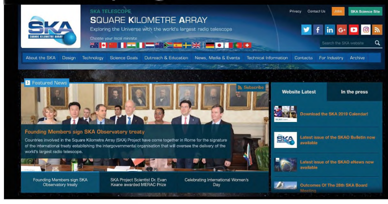

Founding Members sign SKA Observatory treaty

Countries involved in the Square Kilometre Array (SKA) Project have come together in Rome for the signature of the international treaty establishing the intergovernmental organisation that will oversee the delivery of the world's largest radio telescope.

- Download the SKA 2019 Calendar!
- Latest issue of the SKAO Bulletin now available
- Latest issue of the SKAO eNews now available
- Outcomes Of The 28th SKA Board Meeting

ska-france.oca.eu

The metrology of time

JS 19
APPROCHER LES DEUX INFINIS PAR
LES ONDES ELECTROMAGNETIQUES

Tests de physique fondamentale avec un ensemble d'horloges à atomes froids à l'Observatoire de Paris / *Fundamental physics tests with a cold-atom clock ensemble at Observatoire de Paris*

Guéna Jocelyne

Observatoire de Paris, PSL Université Paris, CNRS, Sorbonne Université, jocelyne.guena@obspm.fr

Mots clés : Fontaine atomique, horloges optiques, stabilité des constantes fondamentales, matière noire.
Key words: Atomic fountain, optical clocks, stability of fundamental constants, dark matter.

Résumé/Abstract

Une application scientifique stimulante des horloges atomiques aux incertitudes extrêmes est de contribuer aux tests de physique fondamentale et à la recherche de physique au-delà du modèle standard de la physique des particules. La fréquence d'une transition atomique dépend des paramètres des interactions fondamentales (électrofaible et forte), tels que la constante de structure fine α, et des propriétés fondamentales des particules comme par exemple la masse de l'électron. Des comparaisons répétées d'horloges atomiques de haute précision peuvent être exploitées pour rechercher une variation temporelle, ou encore une variation avec le potentiel de gravité, des rapports de fréquences atomiques, et, via des calculs de structure atomique et nucléaoire, variations des constantes fondamentales. Les horloges atomiques fournissent des tests de laboratoire indépendants de modèle cosmologique qui mettent des limites aux théories alternatives de gravitation et de mécanique quantique, contribuant ainsi à la recherche d'une théorie unifiée des interactions fondamentales. Nous présentons notre contribution à cette recherche en exploitant des comparaisons de haute précision de différents types d'horloges et oscillateurs menées à l'Observatoire de Paris sur les deux dernières décennies.

One exciting scientific application of atomic clocks with extreme uncertainties is to contribute to testing fundamental physical laws and searching for physics beyond the Standard Model of particle physics. The frequency of an atomic transition relates to parameters of fundamental interactions (strong interaction, electro-weak interaction), such as the fine-structure constant α, and to fundamental properties of particles like for instance the electron mass, me. Repeated highly accurate atomic clock comparisons can be used to look for a putative variation with time or with gravitational potential of atomic frequency ratios, and, via suitable atomic structure calculations, of natural constants. Clocks provide laboratory tests, independent of any cosmological model, that constrain alternative theories of gravity and quantum mechanics, thereby contributing to the quest for a unified theory of the three fundamental interactions. We present our contribution to this quest by exploiting repeated accurate comparisons of different types of atomic clocks and oscillators performed over the last two decades at Observatoire de Paris.

1 Introduction

Einstein equivalence principle (EEP) is one of the founding principle of General Relativity. Many experiments have been dedicated to test the validity of this principle [1]. Several of them search for variations of fundamental constants, either on cosmological timescales using astronomical and geochemical data, or in our present epoch by exploiting highly stable and accurate atomic clocks. Such variations would violate Local Position Invariance (LPI), one of the three components of EEP. The possibility that dimensionless fundamental constants might change in time or space is allowed or predicted by alternative theories aimed at unifying gravitation with the other fundamental interactions; hence the strong interest in this search which could reveal physics beyond general relativity and the standard model of particle physics. Besides, some of these alternative theories predict the existence of new scalar fields that would lead to a space-time dependence of fundamental constants via their coupling to standard matter. Such scalar fields, with non-zero mass, could be a candidate for dark matter or dark energy needed to explain some galactic and cosmological observations. Atomic clocks are best suited devices to search for variation of constants at the present epoch in laboratory-based experiments whose interpretation is fully independent of any cosmological model.

In this paper we present an overview of our contribution to these tests by exploiting the cold atom clock ensemble and high performance oscillators developed at Observatoire de Paris during the last decades. We will report more specifically on highly accurate Rb/Cs frequency comparisons performed with atomic fountains over more than 15 yr. We will also present repeated accurate measurements of the frequency ratios Sr/Cs which complement similar measurements performed in other laboratories.

2 The cold atom clock ensemble at Observatoire de Paris

Since the early nineties, SYRTE (Systèmes de Référence Temps Espace) at Observatoire de Paris is developing an ensemble of high performance atomic clocks comprising three laser-cooled atomic fountain clocks [2], three optical lattice clocks and ultra-stable microwave and optical oscillators including optical frequency combs. Figure 1 gives a schematic overview of this ensemble. Our last report on the developments of this clock ensemble is given in Ref. [3]. The main application of this ensemble is time and frequency metrology. Besides, such an ensemble provides many possibilities for testing fundamental physical laws, relying on the high accuracy and stability of these devices.

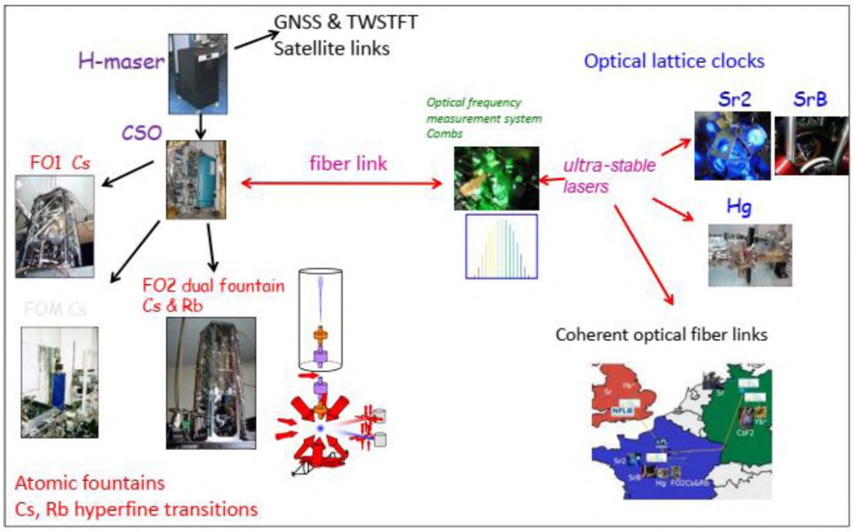

Figure 1: Overview of the LNE-SYRTE atomic clock ensemble at the Observatoire de Paris.

Atomic fountains are the first generation of the laser-cooled atomic frequency standards. They use the fountain geometry where spectroscopy of the clock transition is performed onto a free-falling sample of laser-cooled atoms which is beforehand launched upwards vertically (see, for instance, [2] and references therein). One of our three fountains called FO2 is a dual fountain operating simultaneously with rubidium and cesium atoms. The clock transitions are the ^{87}Rb and ^{133}Cs ground state hyperfine frequencies in the microwave domain. All three Cs fountains are primary frequency standards, the Rb part of FO2 is a secondary frequency standard and all four provide among the most accurate realizations of the SI second thus participating to the accuracy of the international atomic time, with uncertainties at the level of a few 10^{-16}.

To surpass atomic fountain performances, three optical lattice clocks (OLC), two using strontium atoms and one using mercury atoms, are currently under development at SYRTE (right side of fig. 1). The neutral atoms are dipole-trapped in an optical lattice and are interrogated by an ultra-stable "clock" laser in the optical part of the spectrum (1S0 - 3P0 in ^{87}Sr and ^{199}Hg). The uncertainties reached by the SYRTE strontium OLCs is a few 10^{-17}.

The link between the fountains and the optical clocks is performed via optical frequency combs spanning across the optical and microwave domains.

3 Tests of space-time variation of fundamental constants

The frequency of an atomic transition is a function of three constants, parameters of fundamental interactions (electro-weak and strong interactions): the fine-structure constant α, the ratio μ of the electron-to-proton mass m_e/m_p and the quark mass scaled properly. The ratio of two atomic transition frequencies is by definition independent on the unit of frequency and therefore its value depends only on these constants. We use repeated highly accurate atomic clock comparisons to look for a putative variation with time or with gravitational potential of atomic frequency ratios, and, via suitable atomic structure calculations, of natural constants [4]. Our comparisons between ^{87}Rb and ^{133}Cs hyperfine frequencies since the very first in 1998 are shown in Fig. 2. Since

2009, these comparisons are almost continuous using the dual Rb/Cs fountain FO2 alone. The measurements set a stringent limit to a putative variation with time of the Rb/Cs fractional frequency ratio at a level of a few 10^{-17} yr^{-1} (Fig.2, left). They also set the first limit to a fractional variation of the frequency ratio with gravitational potential (Fig. 2 right), providing a new stringent differential redshift test: difference in gravity redshift between Cs and Rb less than 4×10^{-7}. This test relies on exploiting the yearly modulation of the gravitational potential of the Sun due the eccentricity of the Earth orbit.

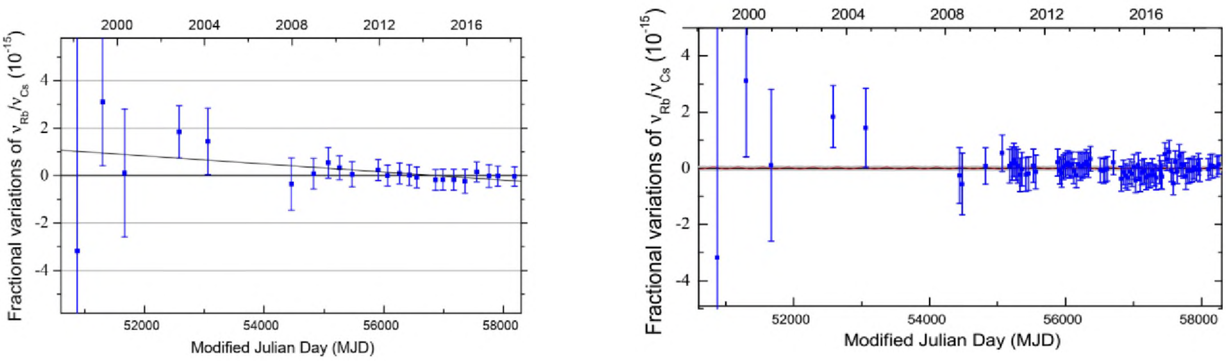

Figure 2: Temporal record of fractional variations of the Rb/Cs hyperfine frequency ratio. The error bars are the total 1σ uncertainties, dominated by the systematic uncertainties. Left: The solid red line is the weighted fit to a line. Right: Same data fitted by a modulation synchronized with the Earth's orbit around the Sun.

Frequency ratios between optical and microwave clocks offer a different sensitivity to natural constants than hyperfine frequency ratios. Repeated measurements of the frequency ratio between the strontium clock transition and the microwave Cs primary and Rb secondary frequency standards have been performed at SYRTE [5]. They are shown in Fig.3, together with other absolute frequency measurements of strontium optical lattice clocks against Cs fountain primary frequency standards over a decade. They give the linear drift with time of the Sr/Cs clock frequency ratio and a fit of its possible variation with the gravitational potential.

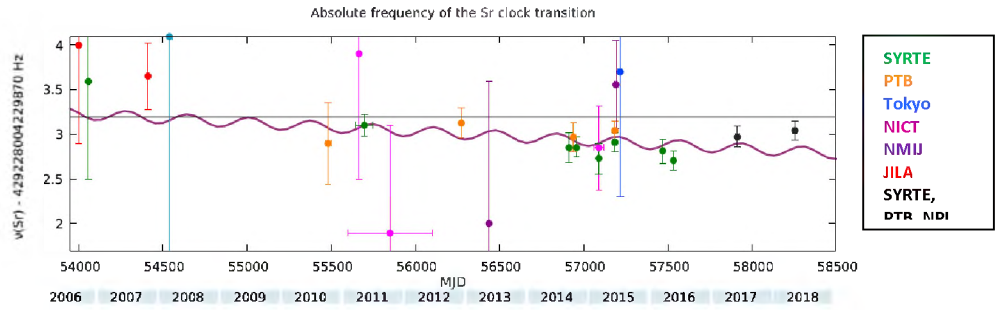

Figure 3: International comparisons of the Sr/Cs clock frequency ratio. A fit shows an upper bound on a drift of this ratio, and on a variation synchronized with the Earth's orbit around the Sun. Courtesy of J. Lodewyck.

Combining with other available highly accurate clock comparisons, we can extract independent constraints on the putative temporal variations of the three constants α, $\mu = m_e/m_p$ and scaled quark mass, at the present epoch, and on their putative couplings to gravity.

4 Search for scalar dark matter

We use 6 years of the hyperfine frequency comparison data of the dual rubidium and caesium fountain FO2 (data spanning November 2009 to February 2016) to search for a massive scalar dark matter candidate [6]. Such a scalar field can induce harmonic variations of the fine structure constant, of the mass of fermions, and of the quantum chromodynamic mass scale, which will directly impact the rubidium/caesium hyperfine transition frequency ratio. We find no signal consistent with a scalar dark matter candidate but provide improved constraints on the coupling of the putative scalar field to standard matter (Figure 4). Our limits are complementary to previous results that were sensitive to the fine structure constant only [7] and improve them by more than an order of magnitude when only a coupling to electromagnetism is assumed. They still provide the best present day constraints in a specific model of ultra-light (< 10^{-10} eV) dark matter.

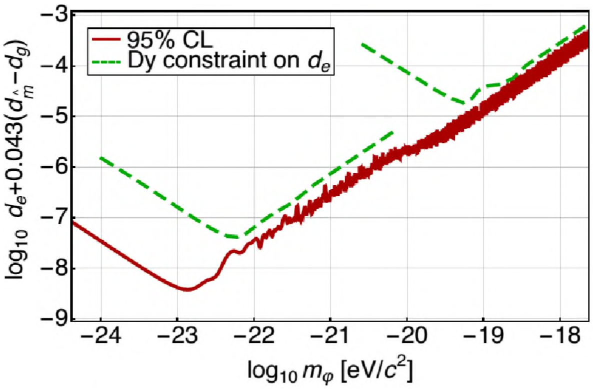

Figure 4: Upper limit on the linear combination of coupling constants d_i between a light scalar field and standard matter fields as a function of scalar field mass. Green dashed line: upper bound from Dy atoms [7].

5 Test of Lorentz Invariance in the matter sector

The SYRTE FO2 fountain has been used to perform a test of the Lorentz invariance postulate of general relativity entering the category of Hughes-Drever experiments [1]. In this experiment [8], the fountain sequence in tailored to probe opposing Zeeman transitions in ^{133}Cs in order to test for a putative variation of their frequencies when the orientation of the quantization axis changes (here, due the Earth rotation) with respect to a supposedly preferred frame, such as the frame of the Cosmic Microwave Background. The experiment was interpreted within the framework of the Lorentz violating Standard Model Extension (SME), where it is sensitive to proton parameters corresponding to a largely unexplored region of the SME parameter space. Several orders of magnitude were gained in constraining 4 parameters which were already constrained by other experiments and new parameters were constrained for the first time. A recent reinterpretation of the data is given in [9]. We recently repeated the measurements on opposing Zeeman transitions with FO2 fountain in the dual Rb/Cs configuration to improve and complement the early experiment.

6 Conclusion

We have presented valuable contributions of the atomic clock ensemble at Observatoire de Paris to various tests of fundamental physics, searches for variations of the fundamental constants at the present epoch and variations with respect to gravity, and search for dark matter fields. Clock tests in laboratories complement tests performed at higher redshift using astrophysical and geological data, providing inputs for developing unified theories. Future improved tests are foreseen by exploiting advanced remote comparison methods: coherent optical fiber links for long distance clock comparison [10] and ground-to-ground comparisons via the ACES/PHARAO space mission [11].

7 Acknowledgments

This work is presented on behalf of the two teams “Références Microondes et Echelles de Temps” and “Métrologie des Fréquences optiques” on the experimental side and the team “Théorie et métrologie” on theoretical aspects, at SYRTE, Observatoire de Paris. I am grateful to all the collegues and to the SYRTE general services deeply involved in this work over the last decades.

References

[1] C. M. Will, Living Rev. Relativity, 17 (1), 4, 2014; J.-P. Uzan, Living Rev. Relativity, 14, 2, 2011

[2] J. Guéna et al., IEEE Trans. Ultrason. Ferroelectr. Freq. Control, 56, 7, 1319–1326, 2009

[4] J. Guéna et al., Phys. Rev. Lett. 109, 080801, 2012

[3] M. Abgrall et al., C.R. Physique 16, 461-470, 2015

[5] J. Lodewyck et al., Metrologia 53, 1123, 2016

[6] A. Hees et al., Phys. Rev. Lett. 117, 061301, 2016

[7] K. Van Tilburg et al., Phys. Rev. Lett. 115, 011802, 2015

[8] P. Wolf et al., Phys. Rev. Lett. 96, 060801, 2006

[9] H. Pihan-Le Bars et al., Phys. Rev. D 95, 075026, 2017

[10] P. Delva et al., Phys. Rev. Lett. 118, 221102, 2017

[11] P. Laurent et al., C. R. Physique 16 (5), 540-552, 2015

Atmospheric phenomenas and waves

JS 19
APPROACHING BOTH INFINITIES
THROUGH ELECTROMAGNETIC WAVES

Radio detection of atmospheric air showers of particles
La radio-détection des gerbes de particules atmosphériques

A. Escudie[1]***, D. Charrier***[1,2]***, R. Dallier***[1,2]***, D. García-Fernández***[1]***, A. Lecacheux***[3]***, L. Martin***[1,2]***, and B. Revenu***[1,2]

[1] *SUBATECH, Institut Mines-Telecom Atlantique – CNRS/IN2P3 – Université de Nantes, Nantes, France*
[2] *Unité Scientifique de Nançay, Observatoire de Paris, CNRS, PSL, UO/OSUC, Nançay, France*
[3] *CNRS-Observatoire de Paris, Meudon, France*

Keywords: Cosmic rays, air showers, radio detection
Mots-clefs: Rayons cosmiques, gerbes atmosphériques, détection radio

Abstract:

Since 2002, the CODALEMA experiment located within the Nançay Radio Observatory studies the ultra-high energy cosmic rays (above 10^{17} eV) arriving in the Earth atmosphere. These cosmic rays interact with the component of the atmosphere, inducing an extensive air shower (EAS) composed mainly of charged particles (electrons and positrons). During the development of the shower in the atmosphere, these charged particles in movement generate a fast electric field transient (a few nanoseconds to a few tens of ns), detected at ground by CODALEMA with dedicated radio antennas over a wide frequency band (between 20 MHz and 200 MHz). The study of this electric field emitted during the shower development aims to determine the characteristics of the primary cosmic ray which has induced the particle shower: its nature, its arrival direction and its energy. After some theoretical considerations and a short description of the SELFAS simulation code, we will present the CODALEMA experiment, its performances and main results. At last, we will show how the EAS radio-detection technique could be used to observe very high energy gamma rays sources, with the NenuFAR radio telescope.

Résumé:

Depuis 2002, l'expérience CODALEMA, basée sur le site de l'Observatoire de radio-astronomie de Nançay, étudie les rayons cosmiques d'ultra haute énergie (RCUHE, au delà de 10^{17} eV) qui arrivent dans l'atmosphère terrestre. Ces rayons cosmiques interagissent avec les atomes de l'atmosphère, engendrant une cascade de particules secondaires chargées (électrons et positrons), communément appelée gerbe de particules. Lors du développement de la gerbe dans l'atmosphère, ces particules chargées en mouvement engendrent notamment l'émission d'une impulsion de champ électrique très brève (de quelques nanosecondes à quelques dizaines de ns), que CODALEMA détecte au sol avec des antennes radio dédiées, sur une large bande de fréquences (entre 20 MHz et 200 MHz). L'étude de ce champ électrique émis lors du développement de la gerbe a pour but de déterminer les caractéristiques du rayon cosmique primaire ayant engendré la gerbe de particules : sa nature, sa direction d'arrivée et son énergie. Après quelques considérations théoriques et une courte description du code de simulation SELFAS, nous présenterons l'expérience CODALEMA, ses performances et ses principaux résultats. Enfin, nous montrerons comment la technique de radio-détection des gerbes atmosphériques pourrait être utilisée pour l'observation de sources de rayons gamma d'ultra-haute énergie.

1 Introduction

Cosmic rays are commonly defined as relativistic atomic nuclei travelling through the Universe, and possibly arriving on Earth. The distribution of their flux according to their energy is one of the most remarkable and questioning in the modern physics, spreading over 32 orders of magnitude in flux and more than 13 orders of magnitude in energy (from a few hundred MeV up to more than 10^{20} eV for the most energetic ones observed so far, and that are not explained by any identified physical process). According to their energy, they constitute, just like electromagnetic radiation, a single source of information on phenomena of galactic (up to $\simeq 10^{15}$ eV) and extragalactic origin (above 10^{15} eV). However, the important interactions with the galactic and extragalactic magnetic fields complicate the interpretation of the collected data in order to determine their source and their nature.

Ultra-high energy cosmic ray (UHECR) physics refers to the experimental study of cosmic rays above 10^{14} eV. Above this limit, direct measurements of cosmic rays with balloons or satellites are limited by their small collecting area regarding the extremely low flux of particles (down to 1 per km^2 per century above 10^{20} eV). Instead, one has to detect the cascade of secondary particles, called extensive air shower (EAS), which follows the interaction of the cosmic rays with the Earth's atmosphere and spread at ground over very large areas. The interaction of a cosmic ray with a nucleus of the atmosphere can occur at energies much higher than that which one can reach in the laboratory (up to 800 times higher than the 14 TeV in the center of mass in proton-proton collisions in the LHC at CERN), making them also specially interesting to refine our view on the standard model of particle physics. The primary particle characteristics (energy, arrival direction, nature) are then indirectly inferred from the EAS measurements: detected ground particles, shower front arrival time at the detector locations and the longitudinal profile of the shower which is the distribution of the number of particle in the shower over time along the shower axis. The experimental challenge stands in the ability to determine these 3 quantities with a sufficient level of accuracy [1]. EAS are commonly observed by ground-based particle detectors and by telescopes that observe the fluorescent light emitted by the atmospheric di-nitrogen molecules excited by the passage of the cascade. The Pierre Auger observatory in Argentina [2], the largest cosmic ray observatory in the world today, combines these two detection techniques. However, a third detection method exists: the radio detection of EAS. First developed during the 1960's, then abandoned due to technological limitations but fully revisited at the digital era since 2002, this technique is based on the fact that, during the shower development in the atmosphere, the charged particles in movement generate a coherent, transient electric field. The latter has two main origins: transverse current variation induced by the geomagnetic field, and the charge excess mechanism [3, 4, 5, 6, 7]. Since 2002, the CODALEMA experiment located within the Nançay Radio Observatory is one of the pioneering and promotor experiment of this revival of the radio detection of EAS, which is today adopted by a flurry of experiments in the world. Coupled with an increasingly sophisticated understanding of the processes involved allowing the use of high-performance simulation codes, EAS radio-detection now reaches a level of maturity sufficient to match the more traditional methods for fundamental properties of UHECR.

In the most common way, the observations are carried out in the restricted range $[20 - 80]$ MHz (noted MF in the following, for Medium Frequencies) by experiments such as AERA [8], Tunka-Rex [9], TREND [10], Yakutsk experiment [11] or LOFAR [12]. The use of this band is mainly due to man-made broadcasting at low and medium frequencies (AM, FM bands) leading to the choice of relative low sampling rates (~ 200 MS $\cdot$ s^{-1}) of the digitizers used by experiments such as AERA and LOFAR. However, CODALEMA [13, 14] works with a sampling rate of 1 GS $\cdot$ s^{-1}, making it possible to extend observations up to the band $[110 - 200]$ MHz. The main limitation of the frequency band is then due to the bandwidth of the antenna used, which is $[20 - 200]$ MHz for CODALEMA, referred to as Extended Medium Frequencies (EMF) in the following.

CODALEMA is today the supporting experiment of the EXTASIS experiment [15], an array of 7 low-frequency antennas, which takes advantage of its existing infrastructure. EXTASIS aims to reinvestigate the [1-10] MHz band, and especially to study the so-called "Sudden Death" contribution, the expected electric field emitted by shower front when hitting the ground level. Currently, EXTASIS has confirmed some results obtained by the pioneering experiments, and tends to bring explanations to the other ones, for instance the role of the underlying atmospheric electric field [15].

In this paper, we will first briefly describe the processes involved in the generation of the EAS. Then, we will highlight the mechanisms at the origin of the transient electric field, and describe its complete expression as it is implemented in the SELFAS simulation code that we developed. In a third section, we will present the CODALEMA experiment and its principle of functioning, whose main results and performances will be exposed in the next section. At last, we will show how the EAS radio-detection technique could be used to observe very high energy gamma rays sources, with the NenuFAR radio telescope located nearby CODALEMA.

2 Extensive Air Showers

Extensive air showers are initiated by a series of interactions of high energetic primary cosmic ray hadron with the atmosphere constituent (N_2, O_2 and Ar). The secondary charged particles propagate in the atmosphere, forming a hadron cascade longitudinally along the primary cosmic ray trajectory, with a lateral dispersion due to their transverse momentum. During the interactions of the primary particle with the nuclei of the atmosphere, some pions π^0 and $\pi^{\pm}$ are created. The particles π^0 decay in two γ which produce e^- and e^+ by pair production. The e^+ are rapidly absorbed in the medium while the e^- could create γ by Bremsstrahlung. These γ decay in a e^+–e^- pair. This is the electromagnetic component of the shower, containing 90 % of the primary particle energy [16], that can reach very large dimensions depending on the primary cosmic ray energy. A simple illustration of extensive air shower is shown in figure 1.(a), with the point of first interaction X_1, the point of inflection X_{inf} where the production of secondary particles in the shower is maximum and the depth of maximum development X_{max} until which the number of particle increases. From this point, the available energy in the shower front is insufficient and the number of particles absorbed in the atmosphere is larger than the number of particles produced: the number of particles in the shower decreases till the shower extinction. The value X is calculated by integrating the density of air (taking its changes into account) along the trajectory of the shower, from the point of entry of the air shower at the top of the atmosphere to the point in question (units in g $\cdot$ cm^{-2}, increasing up to $\sim$ 1000 g $\cdot$ cm^{-2} at sea level). The longitudinal profile refers to the number of particles along the development of the shower.

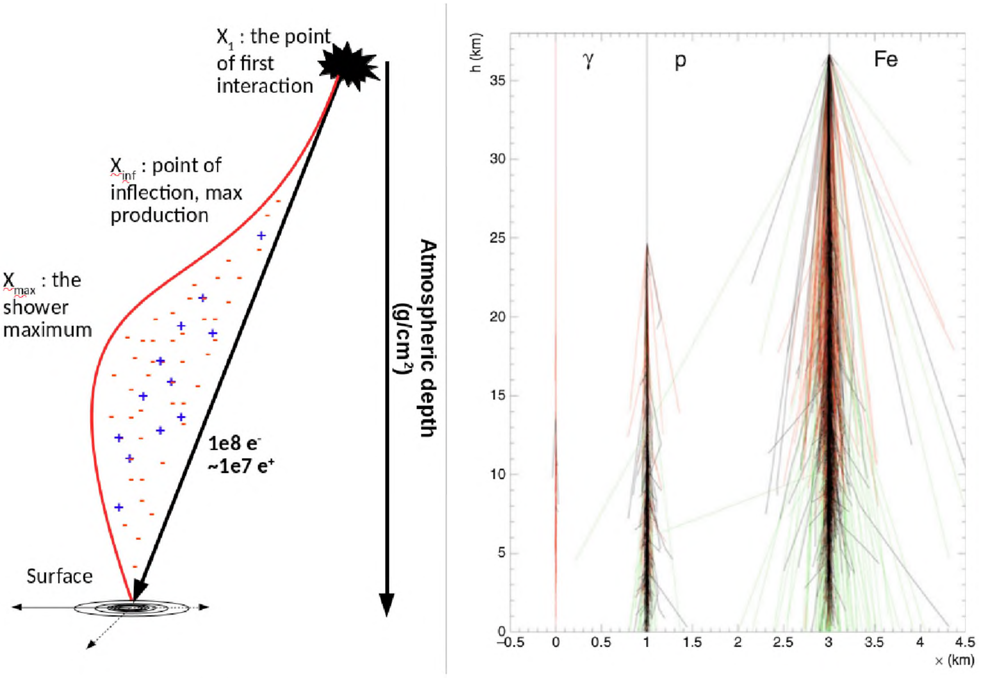

(a) (b)

Figure 1 – (a): Sketch of the geometry of an extensive air shower, with the parameters X_1*,* X_{inf} *and* X_{max}*. The approximate number of electrons and positrons is indicated for a primary proton with an energy of* 10^{17} eV*. (b): Extensive shower development for different primary cosmic ray. The three primaries are simulated with an energy of* 10^5 GeV*. Red component is for electromagnetic, green component for muons and black for hadrons. Adapted from [17].*

The shower development depends on the primary cosmic ray characteristics: its energy, its arrival direction and its nature. For very energetic primary, the shower front could reach the ground, and the maximum shower development occurs near the sea level. Inversely, a low energetic primary induces a small shower with a maximum of development reached at higher altitude in the atmosphere and only muons and neutrinos can reach the ground. Depending on the nature of the primary, the point of first interaction X_1 is different, because the cross-section depends on the mass number A and on the energy E (see Fig. 1). The lateral dispersion is also very different for the three primaries shown here (gamma photon, proton or iron nucleus), though they have the same energy of 10^5 GeV. On Fig. 1, only the secondary particles with an energy above 10 GeV are presented. If we considerer all the secondary particles, the γ-induced air shower has a dispersion radius – defined as the lateral dispersion measured from the shower axis at sea level – of $\simeq 100$ m, the proton-induced air shower has a dispersion radius of $\simeq 500$ m and the iron-induced air shower of ~ 1000 m. The shower maximum X_{max} is also different for the three primaries, being sensitive to both the primary mass and the primary energy. Knowing the latter, moreover rather easily measurable, measuring the X_{max} gives hints on the primary cosmic ray nature. X_{max} is directly observed in fluorescence telescopes (though with a quite low duty cycle of about 14 % [18]), while for particle detectors and radio it is most of the time reconstructed thanks to shower simulations by Monte-Carlo associated to particle interaction codes.

3 Radio emission from EAS

3.1 Physics of radio transient emission mechanisms

During the shower development in the atmosphere, the shower composed of charged particles in movement generates a coherent radio emission which has two origins: the charge excess mechanism, and the transverse current variation induced by the geomagnetic field [3, 4, 5, 6, 7]. The latter is the main mechanism of radio emission. Secondary electrons and positrons in the air shower are accelerated and multi-scattered by the geomagnetic field, and separated thanks to the Lorentz force $\overrightarrow{F} = q\overrightarrow{v} \times \overrightarrow{B}$ (with q the particle charge, $\overrightarrow{v}$ its velocity and $\overrightarrow{B}$ the geomagnetic field vector). The resulting currents will be, on average, perpendicular to the shower axis and are called "transverse currents". They vary with the air shower development and the number of secondary particles which first grows, reaches a maximum, and then decreases as the shower dies out. This time variation will lead to electromagnetic radiation [16]. The resulting electric field is linearly polarized and aligned along $\overrightarrow{F}$

(thus along $\overrightarrow{n} \times \overrightarrow{B}$), where the direction of propagation of the secondary particles can be assimilated with the shower axis $\overrightarrow{n}$. The intensity of the electric field depends on the arrival direction of the primary cosmic ray, in particular on the angle α between the arrival direction of the shower and the geomagnetic field.

At the second order, the charge excess mechanism comes in addition to the geomagnetic contribution. Actually, at high energy, the processes of pair production and bremsstrahlung dominate. As the shower develops, the average energy decreases and other processes appear, as Compton scattering, delta-ray production, knock-on electrons, and positron annihilation with pre-existing free atmospheric electrons, resulting in a net negative charge excess of $\approx$ 10 - 20 %. The ionization electrons are contained in the curved shower front, while the heavier positive ions stay behind. The same scheme as for the geomagnetic mechanism occurs: during the shower development, the net negative charge grows, reaches a maximum and finally decreases when the shower dies out. The time variation of the evolution of the charge excess also leads to radio transient emission [16]. Contrarily to the geomagnetic one, here the electric field vector is radially polarized with respect to the shower axis, and its orientation depends on the location of an observer. The overall resulting emission is a superposition of these two mechanisms, and appears as a fast electric field transient lasting few tens of nanoseconds, which can be detected by large bandwidth antennas and fast acquisition systems.

3.2 Formalism and prediction of the radio emission from EAS – The SELFAS simulation code

In addition to the shower development simulations codes like CORSIKA [19], CONEX [20] or AIRES [21], based on particle physics hadronic interaction models such as or Sybill [22] or EPOS [23] or QGSJET [24], several authors have implemented the calculation of the electric field emitted by the charged particles of the shower. Most of them have chosen a microscopic approach, using the simulated particle tracks as elementary sources of electric field ([25, 26]), and adding all the contributions at the observation point. Developed within the frame of CODALEMA, SELFAS (Simulation of Electric Field of Air Showers) uses the same approach, based on a complete and detailed formalism. But, instead of simulating each interaction in the shower along its development, SELFAS uses pre-defined particle distributions obtained from a large set of previous shower simulations ([27]), thus considerably reducing the computing time. The complete formalism used in SELFAS is obtained by rewriting Maxwell's equations in the form of two coupled equations by using the scalar and vector potentials and by using the Lorentz gauge which can be expressed as $\nabla \cdot \mathbf{A} + \mu\epsilon\frac{\partial\Phi}{\partial t} = 0$:

$$\begin{aligned}
\nabla \cdot \mathbf{D} = \nabla \cdot (\epsilon\mathbf{E}) = \epsilon\nabla \cdot \mathbf{E} &= \rho \\
&= \epsilon_0\nabla(-\frac{\partial \mathbf{A}}{\partial t} - \nabla\Phi) = \rho \\
&= -\nabla^2\Phi - \nabla(\frac{\partial \mathbf{A}}{\partial t}) = \frac{\rho}{\epsilon} \\
&\Rightarrow \boxed{\nabla^2\Phi - \frac{1}{c_n^2}\frac{\partial^2\Phi}{\partial t^2} = -\frac{\rho}{\epsilon}} \qquad (1)
\end{aligned}$$

where c_n is the speed of light in the dielectric medium. The same calculation can be made for the vector potential giving:

$$\boxed{\nabla^2\mathbf{A} - \frac{1}{c_n^2}\frac{\partial^2\mathbf{A}}{\partial t^2} = -\mu_0\mathbf{J}} \qquad (2)$$

To solve equations 1 and 2, we use retarded solutions known as Green functions, giving:

$$\Phi(\mathbf{x}, t) = \frac{1}{4\pi\epsilon}\int \mathrm{d}^3x'\frac{1}{R}\left[\rho(\mathbf{x}', t')\right]_{\mathrm{ret}} \qquad (3)$$

$$\mathbf{A}(\mathbf{x}, t) = \frac{\mu_0}{4\pi}\int \mathrm{d}^3x'\frac{1}{R}[\mathbf{J}(\mathbf{x}', t')]_{\mathrm{ret}} \qquad (4)$$

where $R = |\mathbf{x} - \mathbf{x}'|$ and t' is the retarded time defined as $t' = t - \frac{1}{c_n}|\mathbf{x} - \mathbf{x}'(t')|$. Using equations 3 and 4, we can derive the electric field and obtain:

$$\mathbf{E}(\mathbf{x}, t) = \frac{1}{4\pi\epsilon}\int \mathrm{d}^3x'\left[\frac{\hat{\mathbf{R}}}{R}[\rho(\mathbf{x}', t')]_{\mathrm{ret}} + \frac{\hat{\mathbf{R}}}{c_nR}\left[\frac{\partial\rho(\mathbf{x}', t')}{\partial t'}\right]_{\mathrm{ret}} - \frac{1}{c_n^2R}\left[\frac{\partial\mathbf{J}(\mathbf{x}', t')}{\partial t'}\right]_{\mathrm{ret}}\right] \qquad (5)$$

where $\hat{\mathbf{R}} = \frac{\mathbf{x}-\mathbf{x}'}{|\mathbf{x}-\mathbf{x}'|}$. The calculation of the electric field having been derived from the Maxwell equations, we need to define the source whose the electric field is to be calculated. Let us define the instant t_1 before which the charge density in all space is zero. Let us consider a neutral atom. At t_1 and position $\mathbf{x}_1$, a point-like source separates from the atom with the charge $-q$ and travels in a straight line at a constant speed until its sudden stop at instant t_2 and position $\mathbf{x}_2$. The associated charge density, which certifies that the charge is conserved, can be written as:

$$\begin{aligned} \rho(\mathbf{x}',t') &= -q\delta^3(\mathbf{x}'-\mathbf{x}_1)\Theta(t'-t_1) \\ &\quad +q\delta^3(\mathbf{x}'-\mathbf{x}_1)-\mathbf{v}(t'-t_1))[\Theta(t'-t_1)-\Theta(t'-t_2)] \\ &\quad +q\delta^3(\mathbf{x}'-\mathbf{x}_2)\Theta(t'-t_2) \end{aligned} \tag{6}$$

where δ is the Dirac delta function and Θ the Heaviside step function. The associated current density can be written as:

$$\mathbf{J}(\mathbf{x}',t') = q\mathbf{v}\delta^3(\mathbf{x}'-\mathbf{x}_1)-\mathbf{v}(t'-t_1))[\Theta(t'-t_1)-\Theta(t'-t_2)] \tag{7}$$

Finally, the electric field can be expressed as:

$$\begin{aligned} \mathbf{E}(\mathbf{x},t) &= \frac{q}{4\pi\epsilon}\Bigg\{ -\frac{\hat{\mathbf{R}}_1}{R_1^2}\Theta(t-t_1-R_1/c_n) - \frac{\hat{\mathbf{R}}_1}{c_nR_1}\delta(t-t_1-R_1/c_n) \\ &\quad + \left[\frac{\hat{\mathbf{R}}_1}{\kappa R^2}(\Pi(t',t_1,t_2))\right]_{\mathrm{ret}} + \frac{1}{c_n}\frac{\partial}{\partial t}\left[\frac{\hat{\mathbf{R}}_1}{\kappa R}(\Pi(t',t_1,t_2))\right]_{\mathrm{ret}} - \frac{\mathbf{v}}{c_n^2}\frac{\partial}{\partial t}\left[\frac{1}{\kappa R}(\Pi(t',t_1,t_2))\right]_{\mathrm{ret}} \\ &\quad + \frac{\hat{\mathbf{R}}_2}{R_2^2}\Theta(t-t_2-R_2/c_n) + \frac{\hat{\mathbf{R}}_2}{c_nR_2}\delta(t-t_2-R_2/c_n)\Bigg\} \end{aligned} \tag{8}$$

in which we have used $t' = t - R_i/c_n$ for $t' < t_1$ and $t' > t_2$. First (creation of the particle) and third (stop of the particle) lines of equation 8 contain a static Coulomb field which contributes at t_1 and t_2 respectively and an impulse radiation field with the form $\frac{\hat{\mathbf{R}}_i}{c_nR_i}\delta(t-t_i-R_i/c_n)$ which is due to the charge conservation and the use of a realistic charge density. The impulse radiation field is due to the changes in the charge density, which thus can be paired with the second line. The second line is equivalent to the Heaviside-Feynman expression used in [28] to calculate the electric field of a particle track, and is inseparable from the impulse radiation field. The equation 8 is able to describe the electric field created by a particle track [29], and has been implemented in the third version, SELFAS3, of the SELFAS Monte Carlo code.

4 Instrumental setup

CODALEMA [13, 14] is hosted since 2002 by the Nançay Radioastronomy Observatory. It is one of the pioneering experiments that have participated in the rebirth of radio detection of cosmic rays. Over the years, the experiment has seen the development of a large collection of detectors, intended to study the properties of the radio emission associated with cosmic ray induced air showers in the energy range from 10^{16} to 10^{18} eV. In its current version, CODALEMA consists essentially of:

- a square array (0.4×0.4 km^2) of 13 particle scintillator counters (surface detector),
- a set of 57 so-called “autonomous” crossed dipoles and synchronized by GPS dating, operating in the EMF band, distributed over 1 km^2,
- a so-called “Compact Array” of 10 cross-polarized antennas, arranged in a star shape of 150 m extension and whose signal acquisition (in the MF band) is triggered by the particle detector.

The autonomous station array is purely self-triggered, meaning that each station is independent. Transients coming from cosmic ray air showers or any other source (noise, planes...) are either stored on a distant disk for off-line analysis or directly sent to a central DAQ able to build on-line the event based on several station signals, respecting several selection criteria, which offers a large noise rejection factor (more than 99 %) and a very good efficiency on cosmic ray air shower transient detection. A crosscheck can be made off-line with the events detected by the particle detector or any of the triggered instruments (Compact Array or Low-Frequency stations). CODALEMA is installed in a very rich instrumental environment (Fig. 2), since the Nançay radio astronomy station houses a set of radio telescopes covering wavelengths from decametre to decimetre (frequency range [10 - 3500] MHz) [30]. As many international developments aim to finalise the SKA project, a special effort is being made at the moment on the decametric domain, with the installation of the FR606 station of the international radio telescope LOFAR [12] and the construction, already well advanced, of the NenuFAR array (“New Extension in Nançay Upgrading LOFAR”) [31], which is described in section 6.

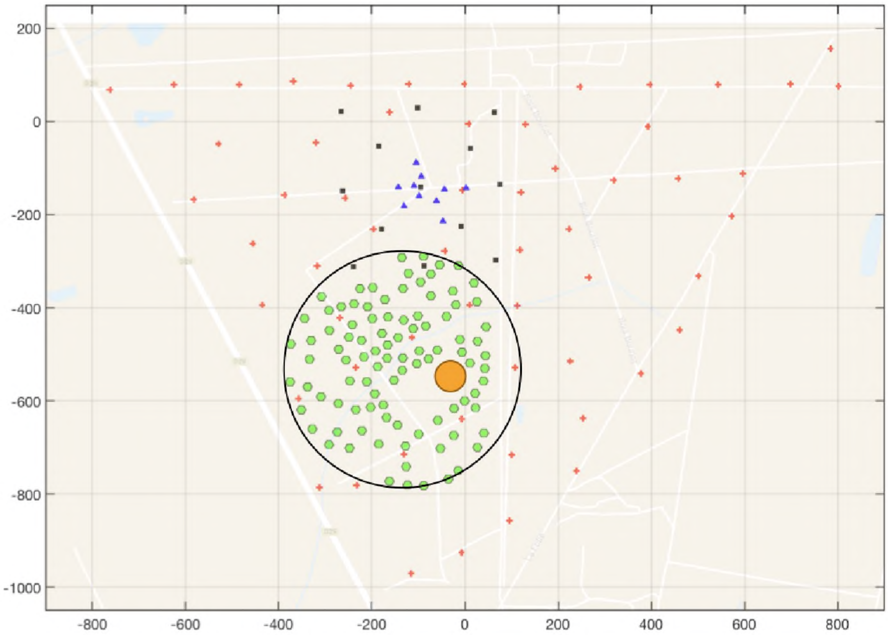

Figure 2 – Map of the Nançay observatory (North on top), featuring some of the setups currently involved in the radio detection of EAS. Red crosses feature the 57 CODALEMA autonomous radio detection stations, black squares the 13 scintillators, blue triangles the 10 antennas of the compact array. The location of the LOFAR FR606 LBA station is figured by the orange circle, while the NenuFAR radiotelescope mini-arrays are the green hexagons which fit into the black circle. The scale is indicated on the axis. The area covered by CODALEMA is ≃1.1 km^2.

5 Event reconstruction, results and performances

For the 57 standalone antennas, no particle trigger is sent as mentioned in section 4. Transients detected in coincidence on several of these standalone antennas build a "radio coincidence", characterized by an average radio event time that will be compared to the particle detector event. The criterion is that at least three standalone antennas are triggered within a time interval compatible with the propagation of a plane wave at the speed of light. The radio event is promoted as an actual shower if its timing is compatible with the timing of the scintillators and if the reconstructed arrival directions (the direction of arrival (DoA) is reconstructed using a plane fit) agree within 20° [13, 14]. Then, for each actual shower, a set of simulations is produced using SELFAS3: 40 protons showers and 10 iron showers at an arbitrary energy (10^{17} eV) with the corresponding DoA, on a virtual array. For different shower core positions, we compare the measured values of the electric field in the MF band to the simulated electric field times a scaling factor to correct from the arbitrary energy. The best agreement is obtained by minimising the chi-squared (see [32] for more details). A method of error propagation is used to calculate the errors on the estimation of the shower parameters. At each step of the comparison, an error on the measured values of the electric field is randomly calculated within the gaussian distribution of the electric field values. This error is added to the electric field values, and the comparison procedure is repeated. After the propagation of the errors, the estimated parameter distributions of the shower is obtained, see figure 3. To fully exploit the capabilities of the CODALEMA instruments, the reconstruction takes into account the high frequency data leading to a reconstruction in the EMF band (very useful for inclined showers), as well as the information from the Compact Array leading to an hybrid reconstruction. After these improvements, at the end of the analysis chain, the obtained accuracy is 15 m on the core position, 20 % on the primary energy and 20 $\mathrm{g \cdot cm^{-2}}$ on the atmospheric depth of the maximum of the shower development noted X_{max}. Figure 3 shows the reconstruction performances on an event detected by CODALEMA.

CODALEMA is a multi-wavelength experiment observing cosmic-ray induced air-showers in $[20 - 200]$ MHz. Its unique capabilities permit to better constrain the reconstruction of the cosmic ray properties, and to propose soon a composition of the cosmic rays with a sufficient level of accuracy. Contrarily to most of the worldwide radio experiments, the reconstruction of all of the cosmic ray parameters by CODALEMA is made only with the radio signal, which demonstrates the self-consistency and the maturity of the radio-detection method for EAS observations. However, even though the noise rejection rate reaches almost 100 % and even though we have a very good efficiency on cosmic ray air shower transient detection, there is still a lot of parasitic transients. As an example, for two weeks of data taking, 52.5 millions of events are built by the central DAQ and only 1 % are

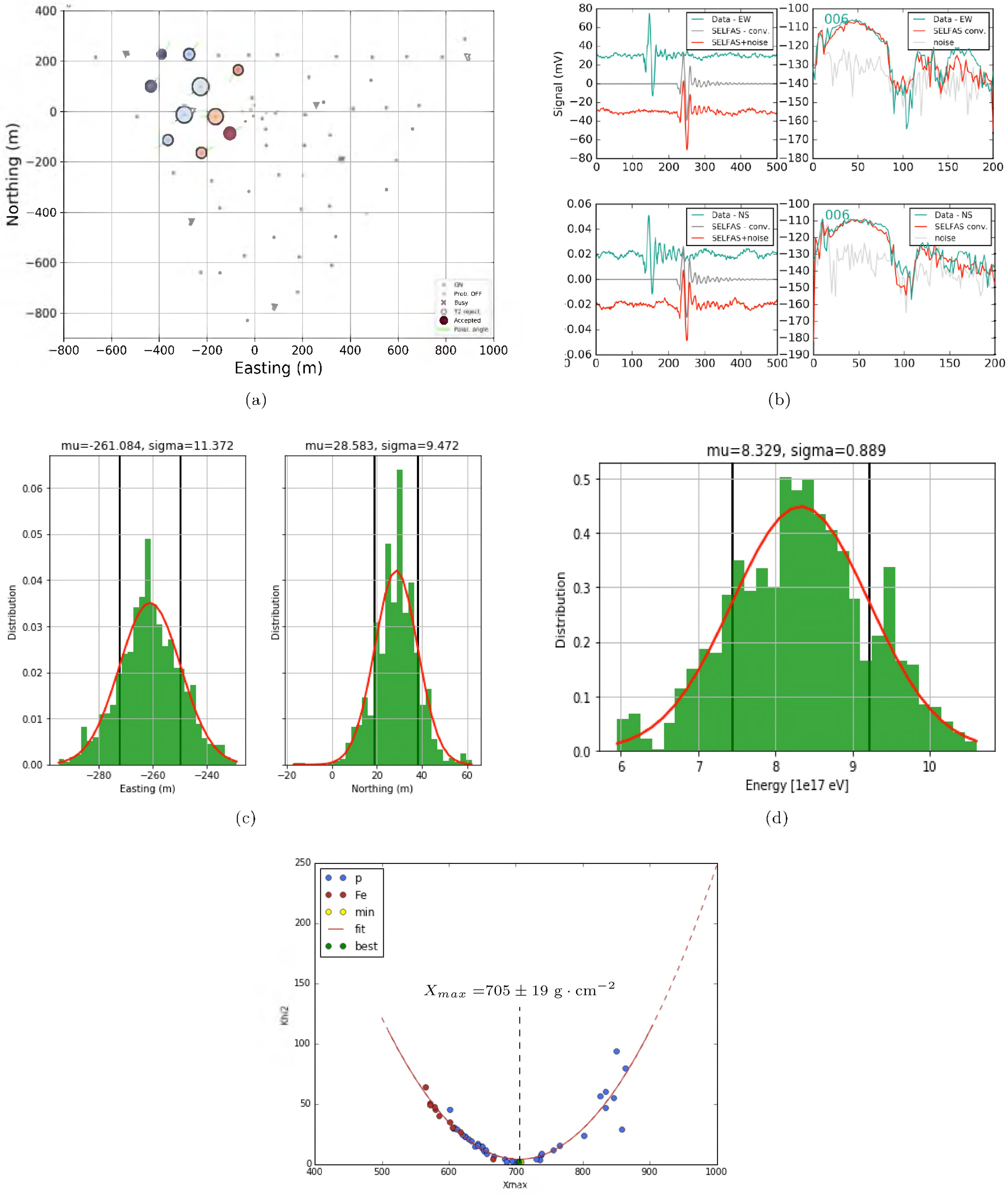

(a) (b) (c) (d) (e)

Figure 3 – Illustration of the reconstruction of one event. (a): map of the event. The grey dots represent the radio antennas of the experiment, the colored circles represent the triggered antennas. The size of the circles is proportional to the signal strength received by the antennas, the color gradient represent the timing order in which the signal is seen by each antenna (from blue to red). (b), left canvas: transient detected by one antenna (green) in the EW (above) and NS (below) polarization, associated to the transient simulated with SELFAS3 (red). (b), right canvas: power spectral density received by an antenna (green) in the EW (above) and NS (below) polarization, associated to the power spectrum density simulated with SELFAS3. The good agreement between data and the simulation shows that the radio detection technique and the response of our radio antennas are well mastered. The other plots (c), (d) and (e) indicate the accuracy on the shower parameters. The red curve is a Gaussian fit of the distributions, the black vertical lines represent the 1σ confidence level. The distributions are obtained by propagating the uncertainties on the measured values of the electric field. See text for more details.

selected after the different stages of rejection, corresponding roughly to 550,000 events. In these set of events, only 34 are tagged as cosmic ray events (0.006 % of the ~550,000 recorded events). Different methods are being studied to increase the rejection rate and to improve the efficiency of detection of cosmic rays.

6 Potential of the radio-detection technique for the detection of very high energy gamma rays

With the instrumental development of the H.E.S.S., MAGIC and VERITAS ground telescopes, the Fermi satellite and the flurry of results accompanying them, gamma astronomy is now reaching a mature stage, and this field routinely offers astronomers and physicists images and spectra from sources that are more and more numerous and distant. The big project for the future, CTA, will allow for the first time a deep study of the gamma sky observed at energies from a few tens of GeV to more than 100 TeV. However, one of the drawbacks of the technique is that the current telescopes observing the Cerenkov radiation of the showers created by the photons in the atmosphere have a rather low operating cycle, due to severe constraints on the necessary nighttime observation conditions (no Moon, no clouds ...). Moreover, if CTA should be able to reach or even exceed the energy limit currently held by HAWC ($\simeq$ 100 TeV), the standard average sensitivity of other telescopes is restricted to a few tens of TeV for the most energetic photons.

One of the specificities of UHECR detection is that it is impossible to know *a priori* in which direction to "look", and therefore the detection systems, whatever they are, must have maximum angular acceptance and availability in order to cover all possible directions of arrival. The UHECR radio detection arrays are no exception to this rule. Given the energy threshold of detection found for the UHECR on observations with individual antennas (of the order of few 10^{16} eV), this method is not suitable to detect air showers generated by hundreds of TeV gamma rays, though they are similar, in terms of charge contents, to that of UHECR. However, the signals of several antennas may be combined *a priori* or *a posteriori* in a given direction, in order to gain in sensitivity of detection, which also reduces the angular field of view: it is the principle of interferometers, widely used on past and current generations of so-called "digital" radio telescopes. Our idea is therefore to combine the principle of detection of atmospheric shower electric field transients, used in CODALEMA, with the ability of antennas to be phased towards a known source direction. Unlike the case of UHECR, we then know where the signal should come from. The immediate advantage is the gain in detection sensitivity, which varies in direct proportion to the square root of the number of antennas involved. Furthermore, combining several antenna beams into one single, directive beam makes the detector much less sensitive to noises sources generally located close to or at the horizon, and which generate the high noise transient rate observed at a single antenna level. Another advantage is the possibility of reaching a useful observation cycle close to 100 %, since the day/night alternation and the weather have no influence on the detection itself (except in case of large local atmospheric electric fields during thunderstorms). Based on our experience of ultrafast radio transient detection and on the context of the Nançay radio astronomy station which hosts the NenuFAR radio telescope, we propose to explore the possibilities offered by this idea and to try for the first time to detect the radio signal produced by ultra-high energy gamma of a few hundred TeV to a few tens PeV from an identified astrophysical source - provided they can produce gammas at such energies.

Also known as the LOFAR Super Station (LSS) in Nançay, NenuFAR [31] is a digital radio telescope consisting - in the long term - of 1824 crossed-dipoles antennas arranged in 96 mini-arrays (hereafter MA_{19}) of 19 antennas[1] (see Fig. 2). It has recently been recognized as a "pathfinder" of SKA. The NenuFAR antennas use the active amplifier developed for CODALEMA and are identical to the ones of its Compact Array (see section 4 and [13, 14]). The 96 MA_{19} are distributed over an approximate circle of 500 m radius (0.2 km^2), see Fig. 2. In classical operation, each of the MA_{19} is analogically phased in any direction of the sky and in the whole or any sub-band of the [10-85] MHz frequency window, leading to an instantaneous sensitivity $\sqrt{19}$ times higher than that of a single antenna. The whole NenuFAR thus has an instantaneous sensitivity much higher than that reached by a single LOFAR station of 96 single antennas [12], like the FR606 unit present at Nançay.

As already mentioned, the specificity of the gamma-ray sources is that we know their position in the sky, thus the arrival direction of the high-energy photon, contrarily to the UHECR case. It is therefore possible to use one or several mini-arrays phased together in the direction of the source and use them as a trigger on transient events. We can take benefit of the large memory depth of the remaining MA_{19}, which would be triggered by the trigger arrays, to roll-back in time and find the transient in their memories. Each MA_{19} would then be a sampling point of the shower footprint at ground, exactly as it is done in UHECR radio detection arrays with single antennas. This would allow knowing the electric field distribution and use it to recover the properties of the primary photon, notably its energy thanks to simulations.

As an illustration, Fig. 4 shows a simulation of the electric field that would be produced by a PeV and a 10 PeV gamma ray. Though sources able to produce such high energy photons (so-called "PeVatrons") are not yet known,

---

[1] In 2018, 54 MA_{19} of those 96 are installed and operational

but expected around the Galactic Center (unfortunately not visible from Nançay), it is rather encouraging: the electric field at 10 PeV is already almost the energy detection threshold for one single antenna, and the signal strength scales linearly with the energy. With a subsequent gain in sensitivity thanks to the phasing of several mini-arrays, we should be able to detect hundreds of TeV photons showers and maybe open the door to a new detection technique of very high energy gamma rays.

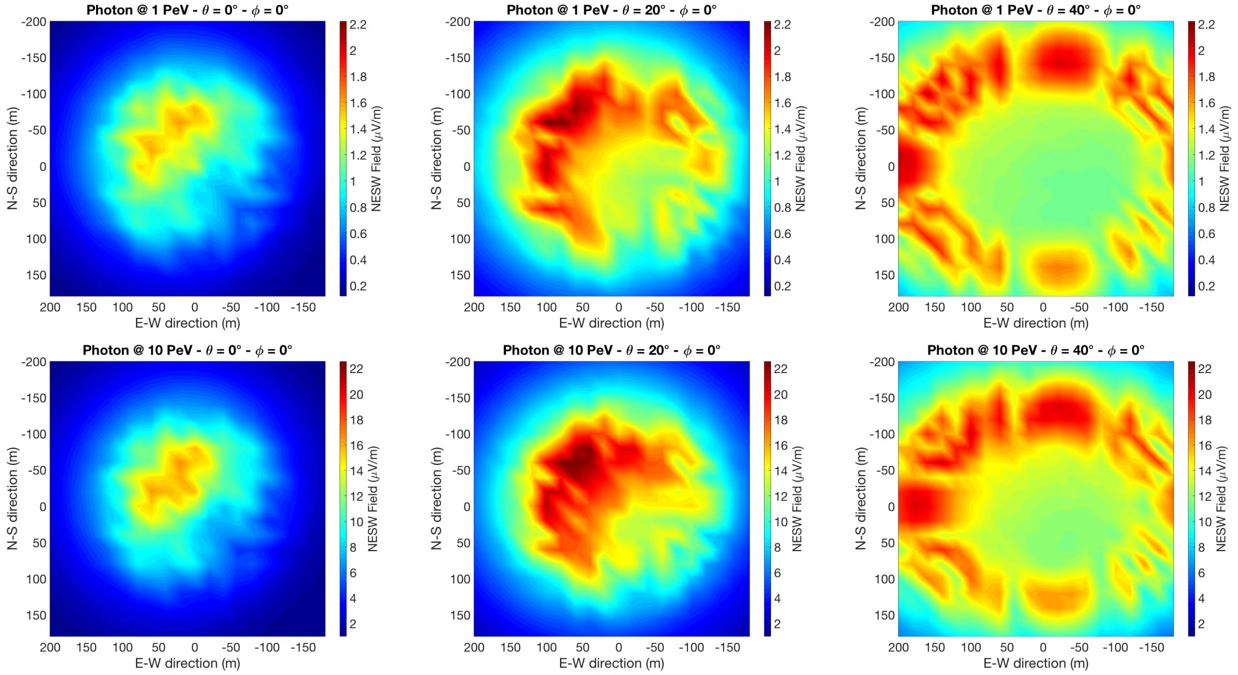

Figure 4 – Top figures: simulations of a 1 PeV photon shower coming from East at a zenith angle of 0, 20 and 40°, in NE-SW polarization, observed in the [24-82] MHz band. The footprint area fits well with the area of NenuFAR. The colour scale gives the electric field value in $\mu V.m^{-1}$. The Cerenkov ring is clearly visible with increasing zenith angle. Bottom figures: same, for 10 PeV photon showers. The colour scale is the same for all the plots.

7 Conclusion

Since 2002, the CODALEMA experiment located within the Nançay radio-astronomy observatory has been studying ultra-high energy cosmic rays arriving in the Earth's atmosphere through the study of the electric field emitted during the development of the shower of secondary charged particles. Among the precursors of this method, nowadays commonly used worldwide, CODALEMA is a laboratory of major technological innovations (autonomous triggering, hybrid reconstruction, very wide frequency band) and its high-performance antennas are exported to other sites or instruments (AERA on Auger, NenuFAR, prototypes in China, Greece...). CODALEMA has largely contributed to demonstrate that this detection method is able to determine the characteristics of the primary cosmic ray with the only radio signal, thanks to comparisons with shower's electric field simulations performed with the SELFAS code which has been specially developed. Today, SELFAS allows a faithful and realistic reconstruction of all the characteristics of the electric field at all frequencies. Its use is essential for the identification of the primary particle that initiated the shower.

Besides the long-standing study of charged UHECR, we also propose today to exploit the unique environment of CODALEMA to explore with NenuFAR the possibilities of radio-detection of atmospheric showers initiated this time by very high energy gammas. The central idea here is to combine a large set of NenuFAR antennas (several tens) in the direction of known sources emitting gammas (catalogs HESS, MAGIC, VERITAS ...) to significantly increase the sensitivity of detection and use the capabilities triggering on ultra fast transients controlled within the framework of CODALEMA. This would make it possible to observe the sources with a useful cycle close to 100 %, which is not possible with the current techniques of the aforementioned Cerenkov telescopes or their successors (i.e. CTA). Coming from the infinitely big, all these infinitely small, elementary particles inform us about the great structures of the Universe that emitted them.

Acknowledgements

We thank the Région Pays de la Loire for its financial support of the Astroparticle group of Subatech and in particular for its contribution to the EXTASIS experiment, and the PNHE (Programme National Hautes Energies) from the French institutes IN2P3 and INSU for having also always supported the CODALEMA experiment, both financially and scientifically. Lastly, we thank the technical support teams of the Nançay Radioastronomy Observatory for valuable assistance during and after the deployment of the EXTASIS antennas.

8 References

[1] A. Aab et. al. Evidence for a mixed mass composition at the 'ankle' in the cosmic-ray spectrum. *Physics Letters B*, 762:288 – 295, 2016.

[2] The pierre auger cosmic ray observatory. *Nuclear Instruments and Methods in Physics Research Section A: Accelerators, Spectrometers, Detectors and Associated Equipment*, 798:172 – 213, 2015.

[3] F. D. Kahn and I. Lerche. Radiation from cosmic ray air showers. *Proceedings of the Royal Society of London A: Mathematical, Physical and Engineering Sciences*, 289(1417):206–213, 1966.

[4] GA Askaryan. J. Exp. Theor. Phys. 21 (1962) 658.

[5] D. Ardouin, A. Belletoile, C. Berat *et al.* Geomagnetic origin of the radio emission from cosmic ray induced air showers observed by CODALEMA. *Astroparticle Physics*, 31:192–200, April 2009.

[6] A. Bellétoile, R. Dallier, A. Lecacheux *et al.* Evidence for the charge-excess contribution in air shower radio emission observed by the CODALEMA experiment. *Astroparticle Physics*, 69:50–60, September 2015.

[7] The Pierre Auger Collaboration. Probing the radio emission from cosmic-ray-induced air showers by polarization measurements. *Phys. Rev. D*, 89(052002), March 2014.

[8] Alexander Aab et al. The Pierre Auger Cosmic Ray Observatory. *Nucl. Instrum. Meth.*, A798:172–213, 2015.

[9] P.A. Bezyazeekov, N.M. Budnev, O.A. Gress *et al.* Measurement of cosmic-ray air showers with the Tunka Radio Extension (Tunka-Rex). *Nuclear Instruments and Methods in Physics Research Section A: Accelerators, Spectrometers, Detectors and Associated Equipment*, 802:89 – 96, 2015.

[10] Olivier Martineau-Huynh for the TREND collaboration. Status of the TREND project. *ArXiv e-prints*, April 2012.

[11] S. P. Knurenko and I. S. Petrov. Air Shower Radio Emission with Energy $E_0 \geq 10^{19}$ eV by Yakutsk Array Data. *Zh. Eksp. Teor. Fiz.*, 104:5, 2016.

[12] M. P. van Haarlem, M. W. Wise, A. W. Gunst *et al.* LOFAR: The LOw-Frequency ARray. *Astronomy & Astrophysics*, 556:A2, August 2013.

[13] R. Dallier, J.L. Béney, H. Carduner *et al.* Multi-scale and multi-frequency studies of cosmic ray air shower radio signals at the CODALEMA site. In *34th ICRC, The Hague, Netherlands*, The Hague, Netherlands, July 2015.

[14] B. Revenu, D. Charrier, R. Dallier *et al.* The CODALEMA/EXTASIS experiment: a multi-scale and multi-wavelength instrument for radio-detection of extensive air-showers. Bexco, Busan, South Korea, July 2017.

[15] Didier Charrier, Richard Dallier, Antony Escudie *et al.* Radio detection of cosmic rays below 10 MHz: the EXTASIS experiment, 2019. Submitted to Astroparticle Physics.

[16] T. Huege. Radio detection of cosmic ray air showers in the digital era. *Physics Reports*, 620:1–52, March 2016.

[17] Peter K.F Grieder. *Extensive Air Showers: High Energy Phenomena and Astrophysical Aspects - A Tutorial, Reference Manual and Data Book.* Springer, Berlin, Heidelberg, 2010.

[18] J. Abraham, P. Abreu, M. Aglietta *et al.* The fluorescence detector of the Pierre Auger Observatory. *Nuclear Instruments and Methods in Physics Research Section A: Accelerators, Spectrometers, Detectors and Associated Equipment*, 620(2):227 – 251, 2010.

[19] D Heck, Johannes Knapp, J-N Capdevielle *et al.* CORSIKA: A monte carlo code to simulate extensive air showers. 01 1998.

[20] Till Bergmann, R. Engel, D. Heck *et al.* One-dimensional Hybrid Approach to Extensive Air Shower Simulation. *Astropart. Phys.*, 26:420–432, 2007.

[21] Aires home page. `http://www2.fisica.unlp.edu.ar/auger/aires/`. Accessed: 2017-11-17.

[22] Eun-Joo Ahn, Ralph Engel, Thomas K. Gaisser *et al.* Cosmic ray interaction event generator SIBYLL 2.1. *Phys. Rev.*, D80:094003, 2009.

[23] T. Pierog and K. Werner. EPOS Model and Ultra High Energy Cosmic Rays. *Nucl. Phys. Proc. Suppl.*, 196:102–105, 2009.

[24] S. Ostapchenko. QGSJET-II: Towards reliable description of very high energy hadronic interactions. *Nucl. Phys. Proc. Suppl.*, 151:143–146, 2006.

[25] T. Huege, M. Ludwig, and C. W. James. Simulating radio emission from air showers with CoREAS. *AIP Conf. Proc.*, 1535:128, 2013.

[26] Jaime Alvarez-Muñiz, Washington R. Carvalho, Enrique Zas *et al.* Radio pulses from electromagnetic, hadronic and neutrino-induced showers up to eev energies. *Nuclear Instruments and Methods in Physics Research Section A: Accelerators, Spectrometers, Detectors and Associated Equipment*, 662(Supplement 1):S187 – S190, 2012. 4th International workshop on Acoustic and Radio EeV Neutrino detection Activities.

[27] S. Lafebre, R. Engel, H. Falcke *et al.* Universality of electron-positron distributions in extensive air showers. *Astroparticle Physics*, 31:243–254, April 2009.

[28] B. Revenu and V. Marin. Radio emission from the air shower sudden death. *ArXiv e-prints*, November 2012.

[29] Daniel García-Fernández, Benoît Revenu, Didier Charrier *et al.* Calculations of low-frequency radio emission by cosmic ray-induced particle showers. *Phys. Rev.*, D97(10):103010, 2018.

[30] Nançay radio observatory home page. `https://realtime.obs-nancay.fr/`.

[31] P. Zarka, J. N. Girard, M. Tagger *et al.* LSS/NenuFAR: The LOFAR Super Station project in Nançay. In S. Boissier, P. de Laverny, N. Nardetto *et al.*, editors, *SF2A-2012: Proceedings of the Annual meeting of the French Society of Astronomy and Astrophysics*, pages 687–694, December 2012.

[32] L. Martin, R. Dallier, A. Escudie *et al.* Main features of cosmic ray induced air showers measured by the CODALEMA experiment. Bexco, Busan, South Korea, July 2017.

Theoretical Investigation on HF-VHF Electromagnetic Emissions from Sprites

Etude Théorique des Émissions Électromagnétiques HF-VHF des Sprites

M.B. Garnung^{1,2}***, S. Celestin***^{1}***, and T. Farges***^{2}

^{1}*LPC2E, University of Orleans, CNRS, matthieu.garnung@cnrs-orleans.fr*
^{2}*CEA, DAM, DIF, 91297 Arpajon, France*

Keywords: Electromagnetic emission, streamer, sprite, simulation
Mots-clefs: Émission électromagnétique, streamer, sprite, simulation

Abstract:
Sprites are complex discharges that consist of many plasma filaments named streamers. They are produced high above thunderstorms (40 km to 90 km altitude), usually in association with positive cloud-to-ground lightning. It is known that sprites produce electromagnetic radiation observed typically in the extremely low (ELF) to ultra low (ULF) frequency bands [e.g., Cummer et al., GRL, 25, 1281, 1998]. More recently, sprites have been found to be associated with LF emissions in the range 50 to 350 kHz [Fullekrug et al., JGR, 115, A00E09, 2010], which emissions have later been proposed to be related to streamer expansion processes [Qin, et al., GRL, 39, L22803, 2012]. In a different context, Ihaddadene and Celestin [JGR, 122, 1000, 2017] have shown that collisions between streamers with opposite polarities would lead to strong electric field variation on the order of a few picoseconds in air at ground-level. The future space mission TARANIS funded by CNES will measure electromagnetic emissions associated with sprites. In this work, we present an effort on modeling relevant sprite streamer processes generating characteristic electromagnetic radiation with a focus on the possibility for streamer collisions to generate HF-VHF emissions (3 MHz to 300 MHz).

Résumé:
Les sprites sont des décharges complexes composées de filaments de plasma appelés streamers. Ils sont produits au dessus de cellules orageuses et s'étendent entre 40 km et 90 km d'altitude, et généralement associés à un éclair positif nuage-sol. Les sprites sont connus pour produire des émissions électromagnétiques habituellement observées dans la bande ELF-ULF [e.g., Cummer et al., GRL, 25, 1281, 1998]. Plus récemment, il a été découvert que les sprites ont également une émission dans la bande LF (50 Hz-350 kHz) [Fullekrug et al., JGR, 115, A00E09, 2010], laquelle a été proposée comme étant en lien avec le processus d'expansion des streamers [Qin, et al., GRL, 39, L22803, 2012]. Dans un contexte différent, Ihaddadene et Celestin [JGR, 122, 1000, 2017] ont montré que les collisions de streamers avec des polarités opposées devraient conduire à une forte variation du champ électrique de l'ordre de quelques picosecondes dans l'air à pression atmosphérique. La prochaine mission spatiale TARANIS financée par le CNES mesurera les émissions électromagnétiques associées aux sprites. Dans cette étude, nous présentons nos efforts sur la modélisation des processus producteurs de rayonnements électromagnétiques caractéristiques des streamers de sprites. Nous nous concentrons plus spécifiquement sur la possibilité que les collisions de streamers produisent un rayonnement dans la bande HF-VHF (3 MHz-300 MHz).

1 Introduction

Sprites are complex discharges that consist of many filaments named streamers. They are produced high above thunderstorms, typically between 40 km to 90 km and, usually associated with a positive cloud-to-ground lightning. Streamers are ionization waves that turn the medium in which there are propagating into filamentary plasma. They are known to have a strong electric field near their heads, which is able to ionize the air locally. This ionization process allows streamers to propagate step by step. We know that sprites produce electromagnetic radiation observed typically from the Extreme Low Frequency (ELF) to Ultra Low Frequency (ULF) [1]. More recently, sprites have been found to be associated with LF emissions in the range 50 to 350 kHz [2], which emissions have later been proposed to be related to streamer expansion processes [3]. Ihaddadene and Celestin [4] showed that collisions between streamers with opposite polarities would lead to strong electric field variation on the order of a few picoseconds in air at ground-level. In addition, these collisions between streamers are very common within sprites. The future space mission TARANIS [5] funded by CNES will measure electromagnetic emissions associated with sprite events in a band spreading from DC to 30 MHz. The quantification of this possible electromagnetic emission as well as related spectral signatures is therefore of prime importance for the preparation of TARANIS. In this work, we present an effort on sprite streamer electromagnetic radiation produced by a collision between two streamers at an altitude of 60 km and a spacecraft observing the event at $\sim$ 600 km of altitude.

2 Method

2.1 Model for streamers

The dynamics of a streamer can be described using drift diffusion equations for electrons, positive and negative ions, coupled with Poisson's equation in a cylindrical coordinate system [6]. In our model, the fluid equation is solved using an upwind scheme while Poisson's equation is iteratively solved via the Successive Over Relation (SOR) approach [7] [8]. The photoionization process is reduced to an uniform free electron background of $10^8\,\mathrm{m}^{-3}$ and we neglect the production of negative ions. The electric field is produced by two remote electrodes put at the opposite ends of the domain such that a uniform Laplacian field of $E_0 = 1130\,\mathrm{V\,m}^{-1}$ is established. The characteristic of the simulation domain is essentially based on [9] except that the size of the domain along the radial direction is twice larger to avoid streamer interaction with boundaries, and the system is set at 60 km altitude rather than at ground level. The initiation of streamers is done by placing two neutral Gaussian plasma clouds with a peak density of $5.5 \times 10^{12}\,\mathrm{m}^{-3}$ and a characteristic spatial decay scale of 0.8 m in the simulation domain at 6.8 m from the left and the right with respect to the center of the domain.

2.2 Model for electromagnetic emission

The analytical time domain solution for the azimuthal magnetic component of the electromagnetic field from a finite antenna of length $H = H_2 - H_1$ is given by [10] :

$$B_\theta(t) = \frac{\mu_0}{4\pi}\int_{H_1}^{H_2} \frac{\sin(\theta)}{R^2} i(z, t - \frac{R}{c})\, dz + \frac{\mu_0}{4\pi}\int_{H_1}^{H_2} \frac{\sin(\theta)}{cR}\frac{\partial i(z, t - \frac{R}{c})}{\partial t}\, dz \tag{1}$$

where $i(z,t)$ is the current flowing through the antenna, θ is the polar angle of the receiver with respect to the source location, R is the distance between the antenna and the receiver, c is the speed of light in vacuum and μ the permeability in vacuum. Figure 1 shows the situation studied. We consider a collision of two streamers occurring at 60 km of altitude, and a spacecraft flying at a distance $R = 600$ km. We also set the polar angle $\theta = 90°$. The first term of equation (1) is the induction part, second term is the radiative part. The length of the antenna is assimilated to the length of the streamer, so that $H = 50$ m. Since H is several order of magnitude lower than R, we neglect the induction part in (1) [3].

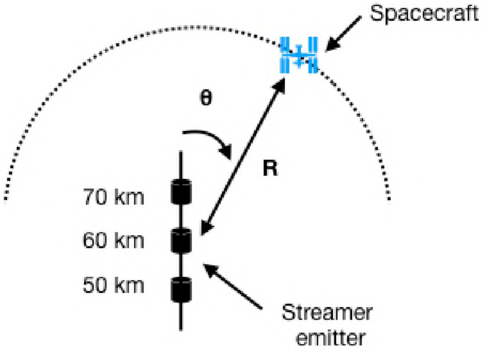

Figure 1 – Geometry of the electromagnetic radiation from a sprite at 60 km *altitude observed by spacecraft flying at* 600 km.

The current used in the simulation is the vertical current $I_z(z,t)$ flowing in the streamer body. It is calculated by integrating the current density along the radial direction.

3 Result

Figure 2 shows a cross-sectional view of the electric field at the time of the collision between two streamers. We observe in the bottom part of Figure 2, a peak in the electric field reaching about $7\,\mathrm{kV\,m}^{-1}$ in the colliding region. At the next moment, the electric field will suddenly collapse due to the large increase of the conductivity in this area [11]. After the propagation of an electrostatic wave, the streamer will have the same behavior as a double-headed streamer [12].

Figure 3 shows the azimuthal component of the magnetic field radiated by the streamer system. We notice that before the collision of streamers (before $t = 4.5\,\mu\mathrm{s}$), there is the lack of significant electromagnetic emission due to a weak variation of the current in time. On the other hand, around $4.5\,\mu\mathrm{s}$ we notice a strong peak of

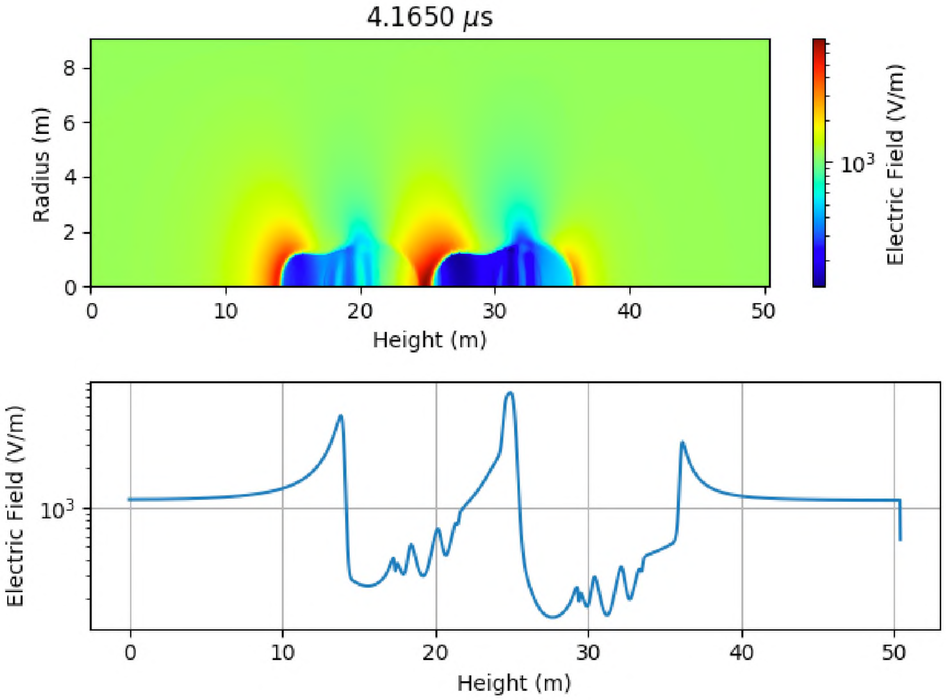

Figure 2 – Collision between two streamers of different polarity at an altitude of 60 km. *Top: Electric field in the simulation domain at the moment of the collision. The collision is occurring in the reddest region. We also observe that the highest electric field area is located in the vicinity of streamer heads. Bottom : Electric field along the height.*

the azimuthal magnetic component reaching almost 0.4 pT. This peak is the result of the collision of streamers which has led to a significant variation of the current in time.

4 Conclusion

The strong and rapid variation of the electric field in few nanoseconds is associated with a strong variation of the current. According to equation (1), this variation of the current in time will result in an electromagnetic radiation during the collision at streamers. On the other hand, during the propagation of streamers, no significant electromagnetic emission is observed, especially in the HF-VHF range. From these results, we will calculate specific signatures associated with streamer collisions taking place in sprites.

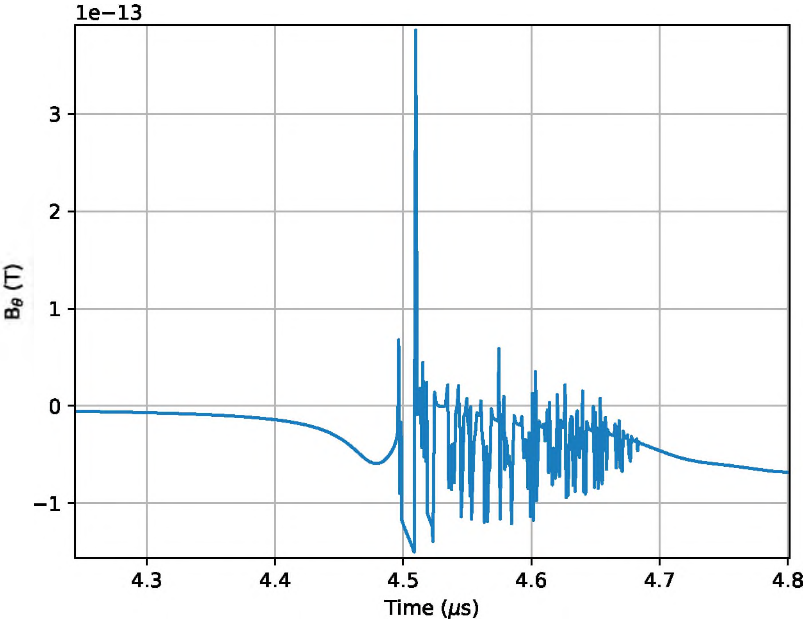

Figure 3 – Azimutal magnetic field component computed by using equation (1) *observed horizontally. We note the strong variation of the current around* 4.5 µs *as related to the collision of streamers.*

5 References

[1] S. A. Cummer, U. S. Inan, T. F. Bell, and C. P. Barrington-Leigh, "ELF radiation produced by electrical currents in sprites," *Geophysical Research Letters*, vol. 25, pp. 1281–1284, 4 1998.

[2] M. Füllekrug, R. Roussel-Dupré, E. M. D. Symbalisty, O. Chanrion, A. Odzimek, O. van der Velde, and T. Neubert, "Relativistic runaway breakdown in low-frequency radio," *Journal of Geophysical Research*, vol. 115, Jan. 2010.

[3] J. Qin, S. Celestin, and V. P. Pasko, "Low frequency electromagnetic radiation from sprite streamers," *Geophysical Research Letters*, vol. 39, Nov. 2012.

[4] M. A. Ihaddadene and S. Celestin, "Determination of sprite streamers altitude based on N_2 spectroscopic analysis," *Journal of Geophysical Research*, vol. 122, pp. 1000–1014, Jan. 2017.

[5] F. Lefeuvre, E. Blanc, J.-L. Pinçon, R. Roussel-Dupré, D. Lawrence, J.-A. Sauvaud, J.-L. Rauch, H. de Feraudy, and D. Lagoutte, *TARANIS—A Satellite Project Dedicated to the Physics of TLEs and TGFs*, pp. 301–315. Springer New York, 2008.

[6] N. Liu and V. P. Pasko, "Effects of photoionization on propagation and branching of positive and negative streamers in sprites," *Journal of Geophysical Research*, vol. 109, Apr. 2004.

[7] G. H. Golub and C. F. Van Loan, *Matrix Computations (4rd Ed.)*. Johns Hopkins University Press, 1996.

[8] W. H. Press, S. A. Teukolsky, W. T. Vetterling, and B. P. Flannery, *Numerical Recipes 3rd Edition: The Art of Scientific Computing*. New York, NY, USA: Cambridge University Press, 3 ed., 2007.

[9] A. Bourdon, V. P. Pasko, N. Y. Liu, S. Celestin, P. Ségur, and E. Marode, "Efficient models for photoionization produced by non-thermal gas discharges in air based on radiative transfer and the Helmholtz equations," *Plasma Sources Science and Technology*, vol. 16, 2007.

[10] M. A. Uman, K. Mclain, and E. Krider, "The electromagnetic radiation from a finite antenna," *American Journal of Physics*, vol. 43, pp. 33–38, 01 1975.

[11] M. A. Ihaddadene and S. Celestin, "Increase of the electric field in head-on collisions between negative and positive streamers," *Geophysical Research Letters*, vol. 42, pp. 5644–5651, July 2015.

[12] F. Shi, N. Liu, J. R. Dwyer, and K. M. A. Ihaddadene, "VHF and UHF electromagnetic radiation produced by streamers in lightning," *Geophysical Research Letters*, vol. 46, no. 1, pp. 443–451, 2019.

Electromagnetism and interaction with the cell;

Dosimétrie à l'échelle de la cellule de système d'exposition aux ondes électromagnétiques
Dosimetry at the microscopic level for EMF delivery system

Nefzi A[1], Carr L[2], Arnaud-Cormos D[3], Leveque P[4]

[1]Univ. Limoges, CNRS, XLIM, UMR 7252, F-87000 Limoges, nefzi.amani@unilim.fr
[2]Univ. Limoges, CNRS, XLIM, UMR 7252, F-87000 Limoges, lynn.carr@unilim.fr
[3]Univ. Limoges, CNRS, XLIM, UMR 7252, F-87000 Limoges, delia.arnaud-cormos@unilim.fr
[4]Univ. Limoges, CNRS, XLIM, UMR 7252, F-87000 Limoges, philippe.leveque@unilim.fr

Mots clés (en français et en anglais) : Dosimétrie, fluorescence, RF. Dosimetry, fluorescence, RF

Résumé/Abstract

Les interactions des ondes électromagnétiques avec le vivant ont fait l'objet de très nombreuses études au cours des dernières décennies.. Pour émettre des conclusions rigoureuses, ces études demandent une estimation précise des paramètres des champs électromagnétiques, des températures et des distributions du débit d'absorption spécifique (DAS) entre autres. On propose d'explorer une méthode de dosimétrie à l'échelle, basée sur l'intensité de fluorescence d'un marqueur, la Rhodamine B, dont la fluorescence est dépendante de la température. La taille des cibles, de l'ordre de la dizaine de µm, est extrêmement petite vis-à-vis des longueurs d'onde mise en jeu aux hyperfréquences. De plus, certaines expositions reposent sur l'utilisation de microdispositif. La détermination des possibilités et limites d'une méthode reposant sur la variation de la fluorescence d'un marqueur de type Rhodamine B est explorée.

The interaction of electromagnetic fields (EMF) with living entities has been the subject of a considerable amount of research in the past three decades. To reach rigorous conclusions, these studies require the accurate assessment of EMF parameters such as electric field, temperature and specific absorption rate (SAR). This paper aims to investigate dosimetry at a microscopic level, with a method based on the fluorescence intensity of the dye, Rhodamine B, which is temperature dependent. The size of the targets, of the order of ten microns, is extremely small compared to the wavelengths of the microwave. In addition, some exposures are based on microdevices. Determination of the potentiel and limitation of the fluorescence method with the Rhodamine B is explored.

1 Introduction/Introduction

Les interactions des ondes électromagnétiques (EM) avec le vivant ont fait l'objet de très nombreuses études au cours des dernières décennies. Ces études ont concerné un large panel de sujet, comme les effets sanitaires potentiels des signaux de télécommunications, les applications biomédicales telles que l'hyperthermie, l'électrochimiothérapie ou bien plus récemment l'utilisation des champs électriques pulsés de très forte amplitude et très courte durée. Pour émettre des conclusions rigoureuses, ces études demandent une estimation précise des paramètres des champs électromagnétiques, des températures et des distributions du débit d'absorption spécifique (DAS) entre autres. Cependant, de par les limites de l'instrumentation actuelle, l'estimation des paramètres d'exposition peut s'avérer délicate, en particulier à l'échelle microscopique.

On propose d'explorer une méthode de dosimétrie à l'échelle microscopique permettant de contribuer à la caractérisation de différents systèmes d'exposition. Cette microdosimétrie est basée sur l'intensité de fluorescence d'un marqueur, la Rhodamine B, dont la fluorescence est dépendante de la température. Cette approche a fait l'objet de premiers travaux dans un contexte d'exposition à 900 MHz [1]. Sur la base de premiers travaux réalisés [2], on cherchera dans ce travail à caractériser les limites de cette méthode et de l'appliquer sur un micro-dispositif. On s'appuiera sur une cellule TEM (transverse électromagnétique) pour quantifier et valider le potentiel et les limites de la méthode proposée.

2 Système d'exposition aux ondes EM et dosimétrie / EMF exposure system and dosimetry.

Un système d'exposition est proposé pour quantifier la dépendance en température du marqueur fluorescent lors d'une exposition microonde (voir Figure 1). Il est composé essentiellement d'une cellule TEM adaptée à des observations sous microscope. Une ouverture de 20 mm est effectuée dans la plaque inférieure de la cellule TEM permettant l'observation à partir de l'objectif de microscope. Cette ouverture et la positon de l'objectif joue un rôle important dans la distribution de champ électromagnétique dans l'échantillon exposé. Ce dernier est basé sur une boite de Petri spécifique dont le fond à une épaisseur de 170 µm parfaitement adapté à une observation sous microscope.

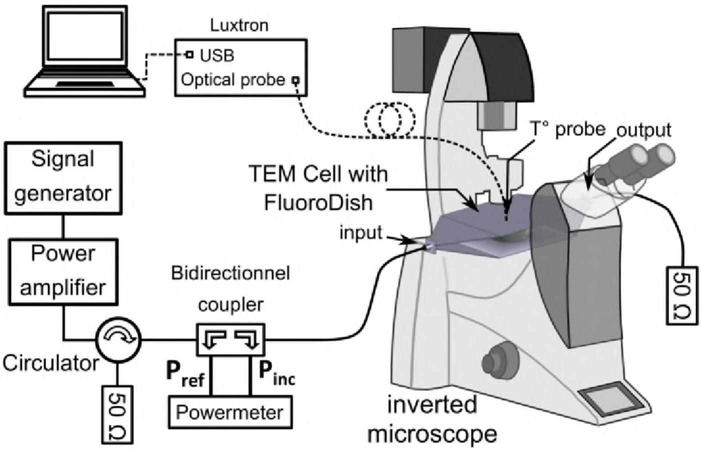

Figure 1 : Dispositif de mesure par microscopie de la fluorescence de la Rhodamine B.

L'influence de l'ouverture et de la position précise de l'objectif du microscope est analysée par simulation électromagnétique et par la mesure de la grandeur classiquement utilisée pour caractériser les niveaux d'exposition, à savoir le DAS qui s'exprime en W/kg. Dans ce cas, le DAS est estimé à partir de la mesure de l'élévation de la température obtenue à partir de la sonde fluorooptic.

La caractérisation de la fluorescence de la Rhodamine B fait l'objet d'une étude en fonction de plusieurs paramètres, à savoir : la concentration, la puissance de la source microonde, le volume de solution exposé, la technique d'acquisition de la fluorescence, en particulier en utilisant une mesure confocale.

Dans un premier temps, les mesures sont effectuées dans le volume en l'absence de cellules biologiques. Ces mesures servent à étalonner les variations de fluorescence en fonction de la température. Dans un second temps, le marqueur est inséré dans des cellules biologiques qui sont ensuite placées dans un milieu de culture. Ce dernier est traité pour éliminer au maximum la présence de la Rhodamine hors des cellules. Il est alors possible de suivre la variation de la fluorescence présente des cellules et de la relier à l'élévation de température. Une mise en évidence de l'influence de la concentration de le Rhodamine présente dans le cytoplasme de la cellule est effectuée. Il s'agit ici d'un élément clé pour faire le lien entre variation de fluorescence et de température. L'apport de l'utilisation d'une mesure en confocal est exploré.

3 Conclusion/Conclusion

La maitrise des expositions aux ondes électromagnétiques de milieux biologiques est un point essentiel dans le domaine du bioélectromagnétisme. La taille des cibles, de l'ordre de la dizaine de µm, est extrêmement petite vis-à-vis des longueurs d'onde mise en jeu aux hyperfréquences. De plus, certaines expositions reposent sur l'utilisation de microdispositif. La détermination des possibilités et limites d'une méthode reposant sur la variation de la fluorescence d'un marqueur de type Rhodamine B est explorée. Une première phase de calibration est effectuée en comparant les variations avec une mesure de température à l'échelle macroscopique. Elle montre que dans certaines conditions, il est possible de suivre la variation de température à partir de la mesure de fluorescence. Des travaux sont en cours pour définir les limites de la méthode sur les mesures au sein même de la cellule.

Références bibliographiques/ References

[1] J. F. Bermingham, Y. Y. Chen, R. L. McIntosh, and A. W. Wood, "AMeasurement andModeling Studyof Temperaturein Livingand Fixed TissueDuring andAfterRadiofrequency Exposure," Bioelectromagnetics, vol. 35, pp. 181-191, 2014.

[2] S. Kohler, R. P. O'Connor, V. Thi Dan Thao, P. Leveque, and D. Arnaud-Cormos, "Experimental Microdosimetry Techniques for Biological Cells Exposed to Nanosecond Pulsed Electric Fields Using Microfluorimetry," Microwave Theory and Techniques, IEEE Transactions on, vol. 61, pp. 2015-2022, 2013.

Cells Electroporation using sine waves: a frequency-dependent phenomenon

Electroporation des cellules avec des ondes sinusoïdales : un phenomène dépendant de la fréquence

***Tomás García-Sánchez*[1] *and Lluis M. Mir*[2]**

[1] Department of Information and Communication Technologies, Universitat Pompeu Fabra, Barcelona, Spain.
tomas.garcia-sanchez@outlook.com
[2] Vectorology and Anticancer Therapies, UMR 8203, CNRS, Univ. Paris-Sud, Gustave Roussy, Université Paris-Saclay, 94805 Villejuif, France,

Mots clés (en français et en anglais) : Electroporation, radiofréquence, champ électrique. Electroporation, radiofrequency, electric field

---

Résumé/Abstract

L'électroporation de la membrane cellulaire causée par des ondes sinusoïdales a été étudiée. Des rafales uniques de différentes durées et intensités ont été appliquées aux cellules. Des impulsions à onde carrée présentant des caractéristiques équivalentes ont également été appliquées à des fins de comparaison. L'efficacité de l'électroperméabilisation de la membrane cellulaire a été étudiée à la fois in vitro et in vivo. En accord avec la théorie, les résultats montrent une nette dépendance du degré de perméabilisation de la membrane cellulaire en fonction de la fréquence des ondes. Les résultats obtenus montrent la capacité des signaux sinusoïdaux à provoquer l'électroporation des cellules et comment, en modifiant la fréquence du champ électrique oscillant appliqué, il est possible de moduler avec précision l'ampleur de la perméabilisation causée à la membrane cellulaire.

In this study cell electroporation using AC sine waves was studied. Single bursts of different durations and intensities were used. Also square wave electric pulses with the same characteristics were applied for the comparison. The efficacy of the electropermeabilization of the cell membrane was studied both *in vitro* and *in vivo*. In agreement with theory, results show a clear frequency dependence in the extent of the permeabilization of cell membrane. The results obtained show the ability of sine signals to perform electroporation and how by modifying the frequency of the oscillating electric field applied it is possible to accurately modulate the extent of permeabilization performed to the cell membrane.

1 Introduction

The interaction of the cell membrane with high intensity pulsed electric fields is routinely used to provoke the transient permeabilization of the cell membrane in a phenomenon termed electroporation. This technique has traditionally used short square direct current (DC) pulses. On the contrary, although theoretically described, few experimental reports have deeply studied the ability of alternating current (AC) signals to cause cell permeabilization [1]. According to Schwann equation, the induced transmembrane potential (ITP) by an oscillating electric field varies with frequency and it is negligible for frequencies above 1 MHz [2]. If the ITP reaches a given threshold, the cell membrane is electropermeabilized.

Nowadays, one of the main applications of electroporation is Electrochemotherapy (ECT)[3] . In this technique, reversible electroporation is applied to tumour tissue in order to facilitate the penetration of chemotherapeutic agents into cancerous cells. ECT represents a clinical option for the treatment of patients with superficial tumours with very successful results [4].

2 Methods

In order to correctly assess the frequency dependence of membrane permeabilization, it is necessary to concentrate the energy delivered to cells in a narrow spectral band. For that purpose, in the present study we used single sinusoidal bursts of different frequencies to study the frequency-dependent response of the cells in vitro. Afterwards, we applied the same concept to study the efficiency of ECT treatment in a model of subcutaneous tumour in mice.

3 Results

Results show how sinusoidal waves are suitable for performing electroporation of both cells and living tissues. The results demonstrate the expected frequency dependence and how by only modifying the frequency of the applied signal it is possible to control the extent of permeabilization. The electroporation efficiency shows a low pass filter frequency dependence with a loss of efficacy for increasing frequencies.

Additionally, the comparison with square waves allowed us to assess the equivalence between both types of wave forms. These results show that there exists a relation in terms of Root Mean Square (RMS) values.

4 Conclusion

Sine waves exposure represents an interesting and effective alternative for the electropermeabilization of biological tissues. The application of the energy to cell membrane in a narrow spectral band can help to better understand the still poorly known mechanism of membrane electroporation. Further research is necessary to explore the possible limitations or improvements of this type of electric field exposure

Our data suggests that depending on the electric field AC frequency it is possible to modulate the amount of permeabilization performed to cells. By only varying the frequency of the signal applied, instead of amplitude, duration or number of pulses we could control the extent of permeabilization performed in the biological sample exposed.

Références bibliographiques

[1] S. Katsuki, et al. “Biological Effects of Narrow Band Pulsed Electric Fields,” IEEE Trans. Dielectr. Electr. Insul., vol. 14, no. 3, pp. 663–668, 2007.

[2] C. Grosse and H. P. Schwan, “Cellular membrane potentials induced by alternating fields,” Biophys. J., vol. 63, no. 6, pp. 1632–1642, 1992.

[3] L.M. Mir, S. Orlowski, J. Belehradek Jr., C. Paoletti, Electrochemotherapy potentiation of antitumour effect of bleomycin by local electric pulses, Eur. J. Cancer 27 (1991) 68–72.

[4] Bertino, G., Sersa, G., De Terlizzi, F., Occhini, A., Plaschke, C. C., Groselj, A., … Benazzo, M. (2016). European Research on Electrochemotherapy in Head and Neck Cancer (EURECA) project: Results of the treatment of skin cancer. European Journal of Cancer, 63, 41–52. https://doi.org/10.1016/j.ejca.2016.05.001

Imagerie Cérébrale Haute Résolution Basée sur des Solveurs Électromagnétiques Hétérogènes pour des Systèmes de Navigation Intracrânienne en Temps Réel

Hybrid EEG Solvers Enabled High Resolution Brain Imaging for Intracranial Navigation Environments in Real Time

Adrien Merlini, Lyes Rahmouni, Maxime Monin et Francesco P. Andriulli
Politecnico di Torino, Turin, Italie, francesco.andriulli@polito.it

Mots clés: EEG Haute Résolution, Solveurs Électromagnétiques, Navigation Intracrânienne

L'imagerie cérébrale, cruciale dans de nombreux domaines allant du diagnostic pré-chirurgical pour l'épilepsie aux interfaces cerveau-machine, est très sensible à la précision des modèles électromagnétiques du cerveau et de leurs paramètres physiques. La résolution du processus de reconstruction de l'activité cérébrale peut donc être drastiquement améliorée par une augmentation de la fidélité de ces modèles. Nous proposons une approche basée sur l'agrégation des solutions de plusieurs solveurs innovants à haute-fidélité pour capturer les différents aspects de la réaction des tissus cérébraux aux champs électromagnétiques. Cette approche permet de compenser la variabilité des multiples paramètres des modèles et permet ainsi une reconstruction plus fiable. Les modèles incluent des formulations aux éléments de frontière volumique, surfacique et filaire qui permettent de modéliser, entre autres, l'anisotropie du milieu cérébral. Ces formulations font l'objet d'une étude spectrale en vue de leur préconditionnement avec pour objectif la réduction de la complexité et du coût de leurs processus de résolution lorsqu'elles sont combinées avec des solveurs rapides. Les différents solveurs haute résolution ont été intégrés dans un système de navigation intracrânienne en réalité virtuelle pour permettre d'exploiter, en temps réel, les données obtenues par les différents solveurs avec une lisibilité accrue.

This work was supported by the European Research Council (ERC) under the European Union's Horizon 2020 research and innovation programme (grant agreement No 724846, project 321).

Imagerie Cérébrale Haute Résolution Basée sur des Solveurs Électromagnétiques Hétérogènes pour des Systèmes de Navigation Intracrânienne en Temps Réel

A. Merlini, L. Rahmouni, M. Monin,
Francesco P. Andriulli
Politecnico di Torino

European Research Council
Established by the European Commission

Outline

- Something about us
- Brain and brain imaging
- Computational challenges in brain imaging
- On some recent contributions and applications
- Perspectives for future investigations

Something about us

Politecnico di Torino (Turin, Italy)

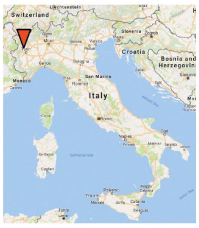

Brain imaging

Structural imaging: provides imaging of brain regions, boundary and material properties (as the electric conductivity)

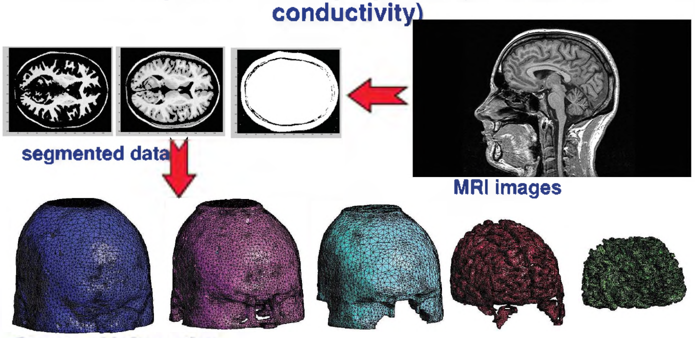

Structural information

Brain imaging

Functional imaging: provides imaging of brain *activity*, either electric/magnetic (direct measures, like in EEG or in MEG) or indirect (like in functional MRI, NIRS, or PET)

EEG

MEG

Functional MRI

NIRS

Electroencephalography (EEG)

In non-invasive EEG, electrodes are placed on the scalp which measure scalp electric potential generated by neuronal activity

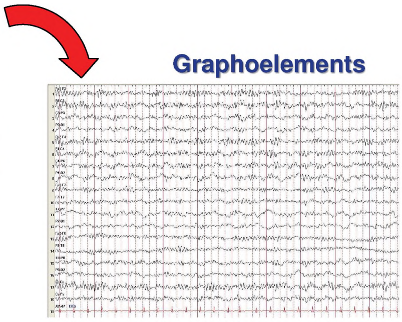

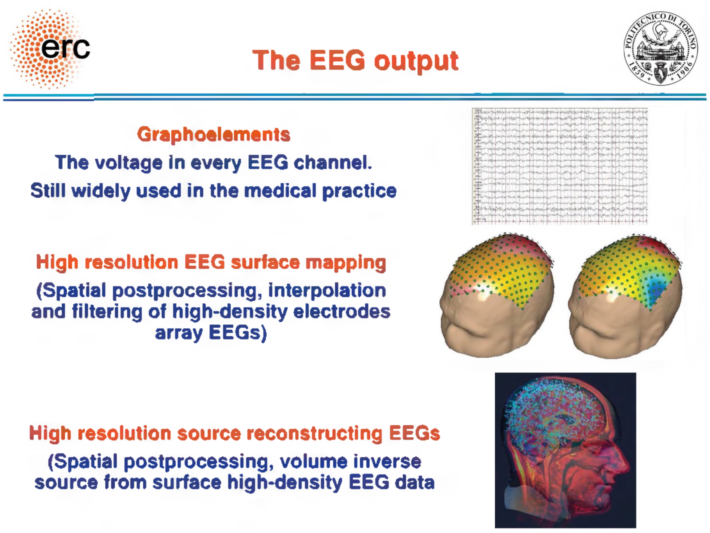

The EEG output

Graphoelements

The voltage in every EEG channel.

Still widely used in the medical practice

High resolution EEG surface mapping

(Spatial postprocessing, interpolation and filtering of high-density electrodes array EEGs)

High resolution source reconstructing EEGs

(Spatial postprocessing, volume inverse source from surface high-density EEG data

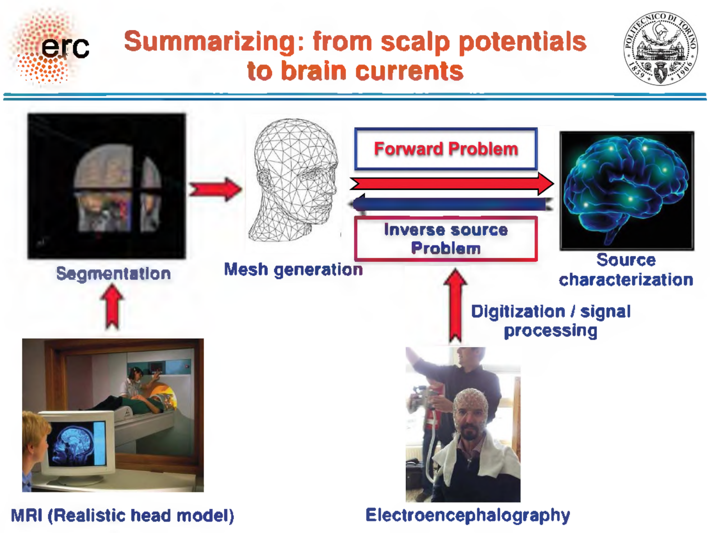

Summarizing: from scalp potentials to brain currents

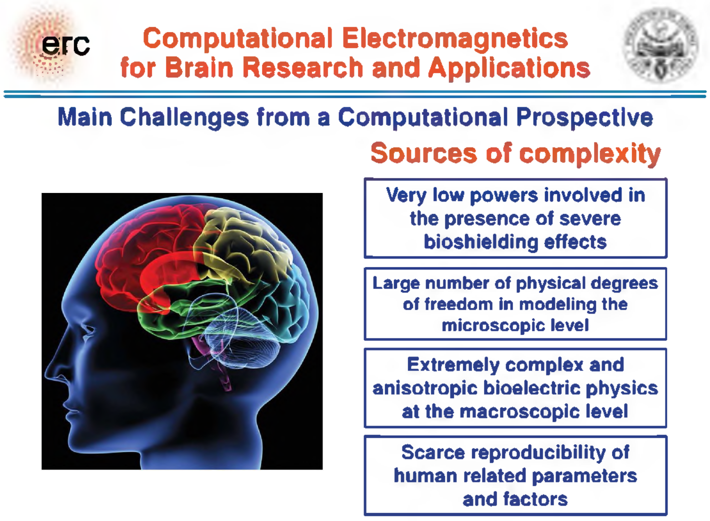

Computational Electromagnetics for Brain Research and Applications

Main Challenges from a Computational Prospective

Sources of complexity

- Very low powers involved in the presence of severe bioshielding effects
- Large number of physical degrees of freedom in modeling the microscopic level
- Extremely complex and anisotropic bioelectric physics at the macroscopic level
- Scarce reproducibility of human related parameters and factors

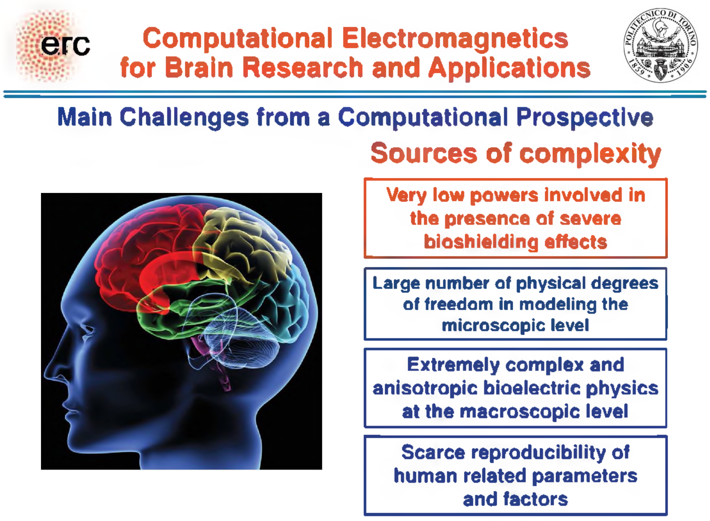

Computational Electromagnetics for Brain Research and Applications

Main Challenges from a Computational Prospective

Sources of complexity

- Very low powers involved in the presence of severe bioshielding effects
- Large number of physical degrees of freedom in modeling the microscopic level
- Extremely complex and anisotropic bioelectric physics at the macroscopic level
- Scarce reproducibility of human related parameters and factors

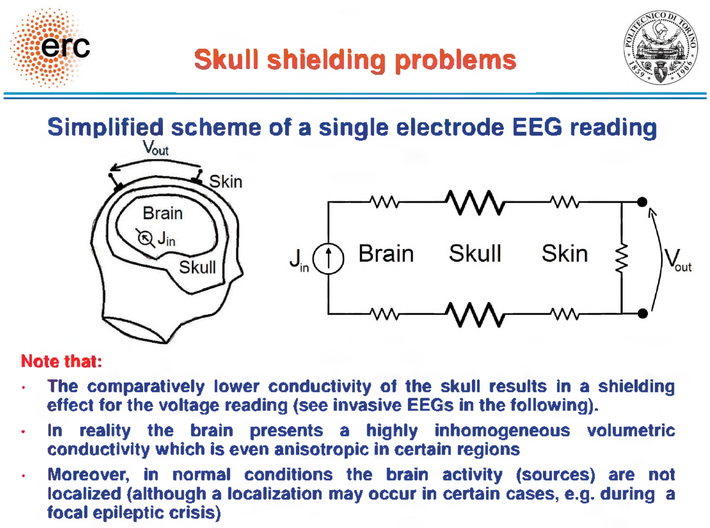

Skull shielding problems

Simplified scheme of a single electrode EEG reading

Note that:

- The comparatively lower conductivity of the skull results in a shielding effect for the voltage reading (see invasive EEGs in the following).
- In reality the brain presents a highly inhomogeneous volumetric conductivity which is even anisotropic in certain regions
- Moreover, in normal conditions the brain activity (sources) are not localized (although a localization may occur in certain cases, e.g. during a focal epileptic crisis)

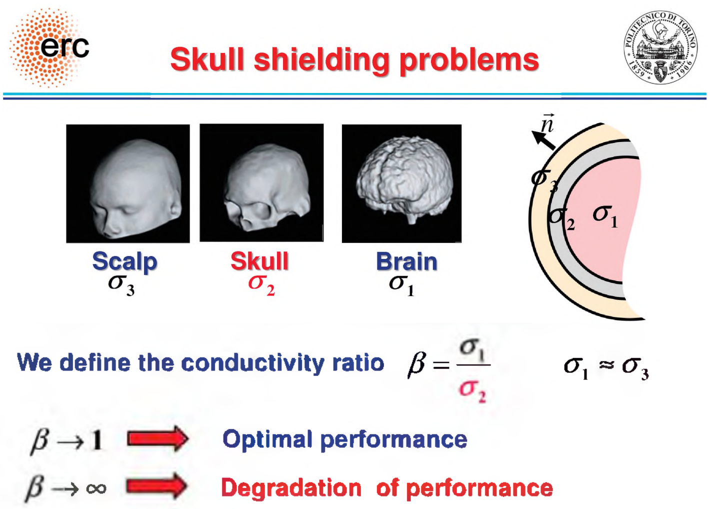

Skull shielding problems

We define the conductivity ratio $\beta = \frac{\sigma_1}{\sigma_2}$ $\quad \sigma_1 \approx \sigma_3$

$\beta \to 1$ ➡ Optimal performance

$\beta \to \infty$ ➡ Degradation of performance

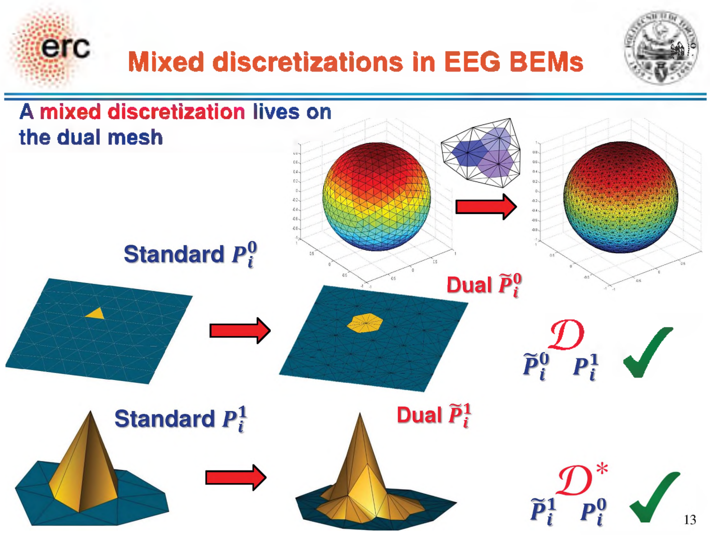

Mixed discretizations in EEG BEMs

A **mixed discretization** lives on the dual mesh

Standard P_i^0

Dual $\widetilde{P}_i^0$

$\mathcal{D}$

$\widetilde{P}_i^0 \quad P_i^1$ ✓

Standard P_i^1

Dual $\widetilde{P}_i^1$

$\mathcal{D}^*$

$\widetilde{P}_i^1 \quad P_i^0$ ✓

13

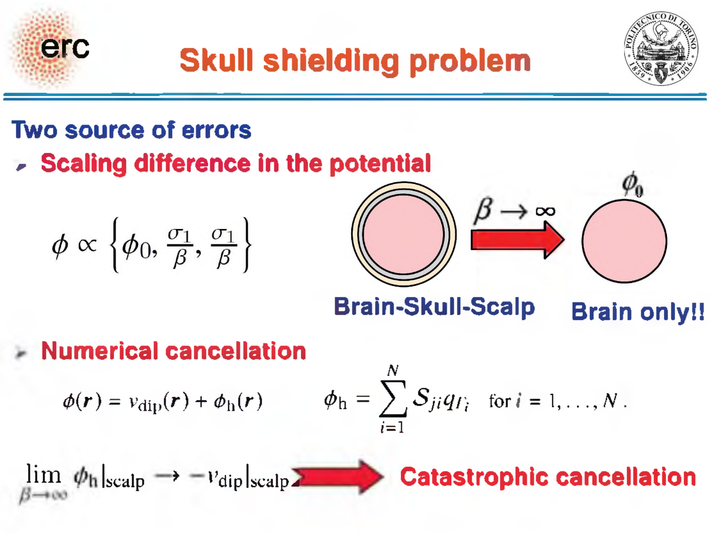

Skull shielding problem

Two source of errors

- **Scaling difference in the potential**

$$\phi \propto \left\{\phi_0, \frac{\sigma_1}{\beta}, \frac{\sigma_1}{\beta}\right\}$$

- **Numerical cancellation**

$$\phi(\boldsymbol{r}) = v_{\mathrm{dip}}(\boldsymbol{r}) + \phi_{\mathrm{h}}(\boldsymbol{r}) \qquad \phi_{\mathrm{h}} = \sum_{i=1}^{N} \mathcal{S}_{ji} q_{\Gamma_i} \quad \text{for } i = 1, \ldots, N\,.$$

$$\lim_{\beta\to\infty} \phi_{\mathrm{h}}|_{\mathrm{scalp}} \to -v_{\mathrm{dip}}|_{\mathrm{scalp}}$$ ⇒ **Catastrophic cancellation**

Indirect Adjoint Double Layer formulation

IADL: New Integral formulation ⇒ **high accuracy independently of β**

- The electric potential is harmonic in the outermost layer

$$\Delta\phi = 0$$

- Write the potential as a contribution of monopole sources $J\,|_{\Gamma 2}$ and $J\,|_{\Gamma 3}$.

$$\phi(\boldsymbol{r}) = \mathcal{S}J|_{\Gamma_2}(\boldsymbol{r}) + \mathcal{S}J|_{\Gamma_3}(\boldsymbol{r})$$

- Applying the gradient operator in the normal direction

$$\partial_{\boldsymbol{n}}\phi|_{\Gamma_i} = \pm\frac{J_{\Gamma_i}}{2} + \mathcal{D}^*_{j2}J_{\Gamma_2} + \mathcal{D}^*_{j3}J_{\Gamma_3}$$

Indirect Adjoint Double Layer formulation

- The operator $\mathcal{S}u|_{\Gamma_i}$ is continuous across and interface

$$\Rightarrow \quad [\phi] = 0 \quad ✓$$

- The operator $\mathcal{D}^*u|_{\Gamma_i}$ is discontinuous across and interface

$$\boldsymbol{n}\cdot\sigma_j\nabla\phi|^-_{\Gamma_j} = \boldsymbol{n}\cdot\sigma_{j+1}\nabla\phi|^+_{\Gamma_j} \quad ✗$$

This leads to the following

$$\boldsymbol{n}\cdot\nabla\phi|_{\Gamma 3} = 0 \quad \Rightarrow \quad \partial_{\hat{\boldsymbol{n}}}\phi|_{\Gamma_3} = 0$$

$$[n\cdot\sigma\nabla\phi] = 0 \quad \Rightarrow \quad \partial_{\hat{\boldsymbol{n}}}\phi|_{\Gamma_2} = -\frac{1}{2}q_{\Gamma_2} + \sum_{i=1}^{N}\mathcal{D}^*_{2i}q_{\Gamma_i} + \partial_{\hat{\boldsymbol{n}}}v_{s1}|_{\Gamma_2} = \frac{\sigma_2}{\sigma_3-\sigma_2}q_{\Gamma_2}$$

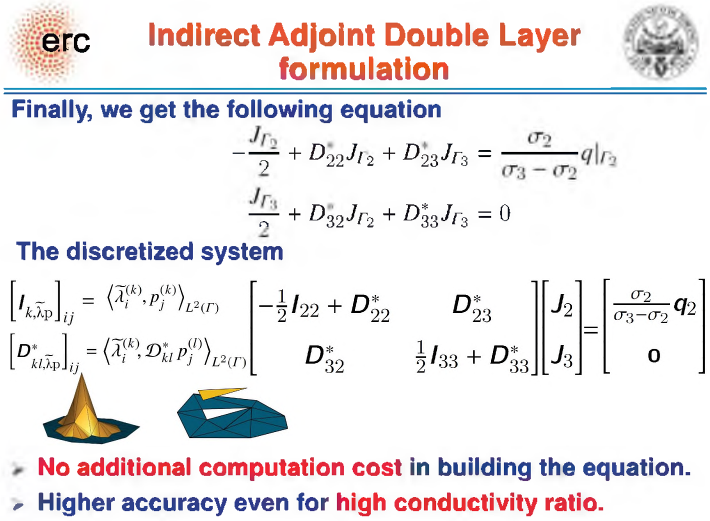

Indirect Adjoint Double Layer formulation

Finally, we get the following equation

$$-\frac{J_{\Gamma_2}}{2} + D^*_{22}J_{\Gamma_2} + D^*_{23}J_{\Gamma_3} = \frac{\sigma_2}{\sigma_3-\sigma_2}q|_{\Gamma_2}$$

$$\frac{J_{\Gamma_3}}{2} + D^*_{32}J_{\Gamma_2} + D^*_{33}J_{\Gamma_3} = 0$$

The discretized system

$$\left[\boldsymbol{I}_{k,\widetilde{\lambda}\mathrm{p}}\right]_{ij} = \left\langle\widetilde{\lambda}_i^{(k)}, p_j^{(k)}\right\rangle_{L^2(\Gamma)} \qquad \left[\boldsymbol{D}^*_{kl,\widetilde{\lambda}\mathrm{p}}\right]_{ij} = \left\langle\widetilde{\lambda}_i^{(k)}, \mathcal{D}^*_{kl}\,p_j^{(l)}\right\rangle_{L^2(\Gamma)}$$

$$\begin{bmatrix} -\frac{1}{2}\boldsymbol{I}_{22} + \boldsymbol{D}^*_{22} & \boldsymbol{D}^*_{23} \\ \boldsymbol{D}^*_{32} & \frac{1}{2}\boldsymbol{I}_{33} + \boldsymbol{D}^*_{33} \end{bmatrix}\begin{bmatrix} \boldsymbol{J}_2 \\ \boldsymbol{J}_3 \end{bmatrix} = \begin{bmatrix} \frac{\sigma_2}{\sigma_3-\sigma_2}\boldsymbol{q}_2 \\ \mathbf{0} \end{bmatrix}$$

- **No additional computation cost** in building the equation.
- Higher accuracy even for **high conductivity ratio.**

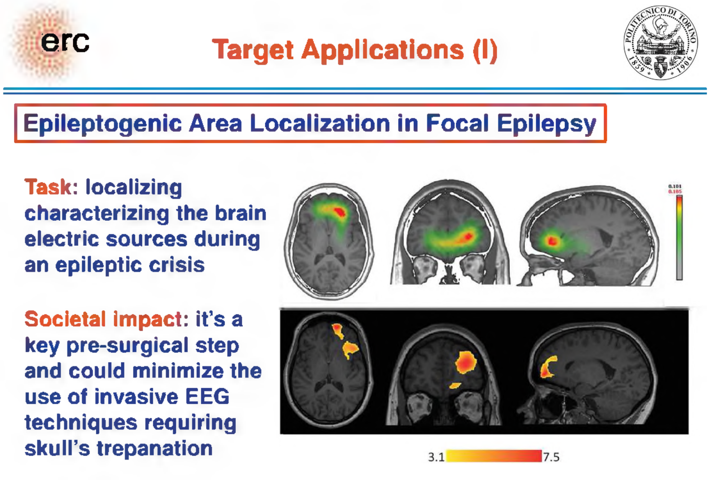

Target Applications (I)

Epileptogenic Area Localization in Focal Epilepsy

Task: localizing characterizing the brain electric sources during an epileptic crisis

Societal impact: it's a key pre-surgical step and could minimize the use of invasive EEG techniques requiring skull's trepanation

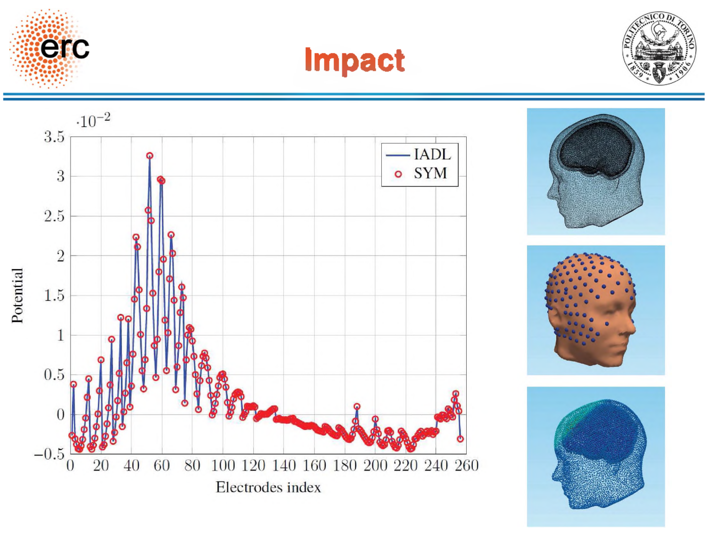

Impact

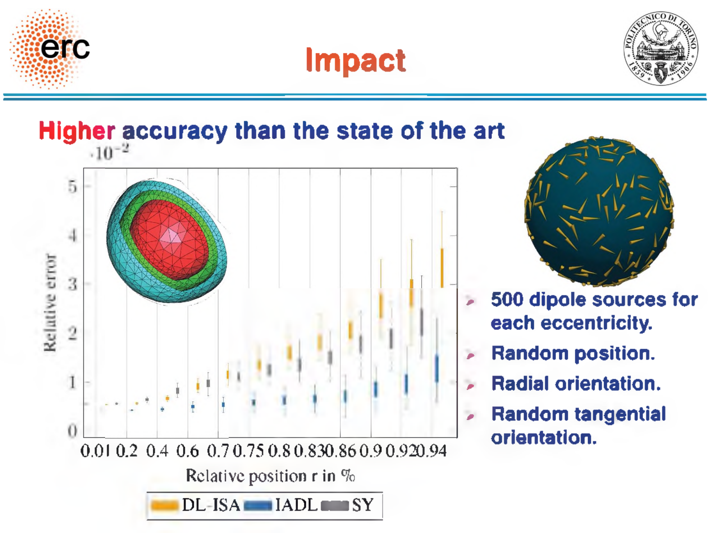

Impact

Higher accuracy than the state of the art

- 500 dipole sources for each eccentricity.
- Random position.
- Radial orientation.
- Random tangential orientation.

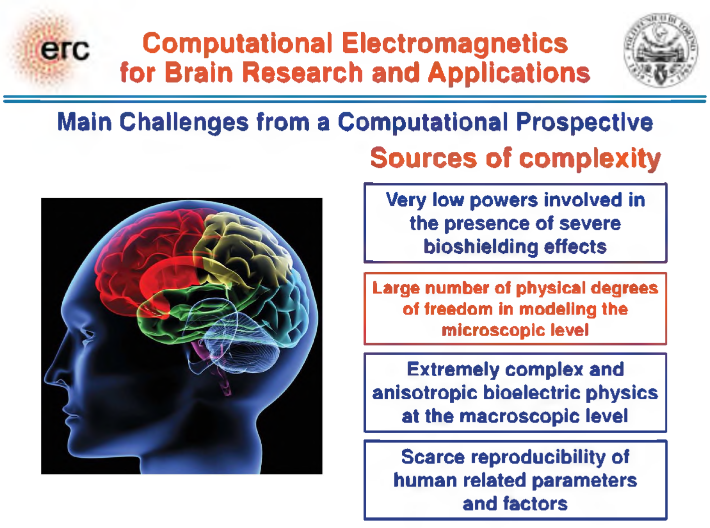

Computational Electromagnetics for Brain Research and Applications

Main Challenges from a Computational Prospective

Sources of complexity

- Very low powers involved in the presence of severe bioshielding effects
- Large number of physical degrees of freedom in modeling the microscopic level
- Extremely complex and anisotropic bioelectric physics at the macroscopic level
- Scarce reproducibility of human related parameters and factors

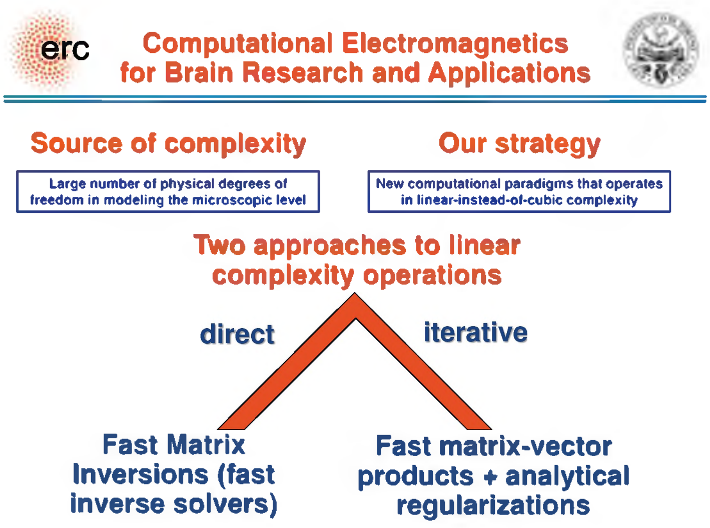

Computational Electromagnetics for Brain Research and Applications

Source of complexity	Our strategy
Large number of physical degrees of freedom in modeling the microscopic level	New computational paradigms that operates in linear-instead-of-cubic complexity

Two approaches to linear complexity operations

direct

Fast Matrix Inversions (fast inverse solvers)

iterative

Fast matrix-vector products + analytical regularizations

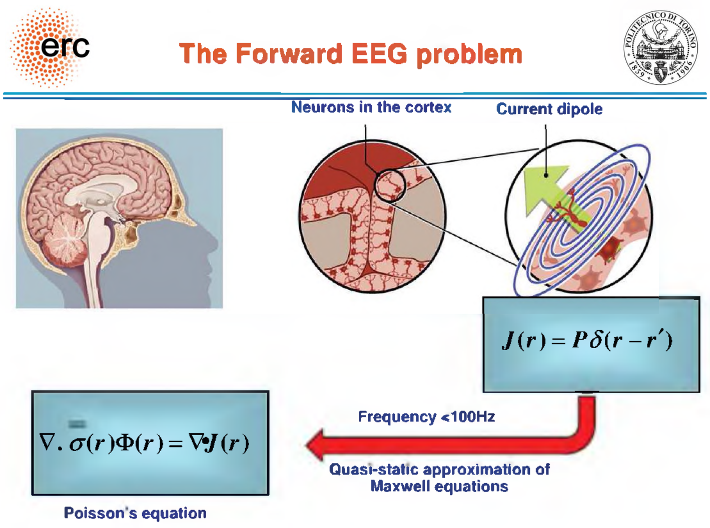

The Forward EEG problem

$$J(r) = P\delta(r - r')$$

Frequency <100Hz

Quasi-static approximation of Maxwell equations

$$\nabla.\bar{\bar{\sigma}}(r)\Phi(r) = \nabla\bullet J(r)$$

Poisson's equation

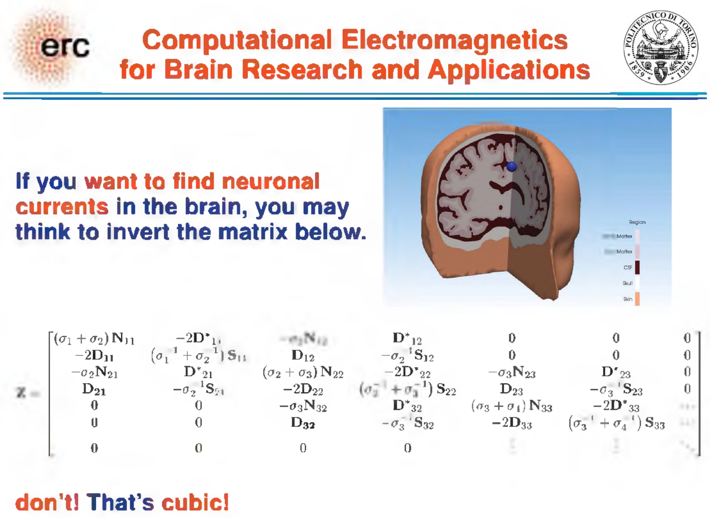

Computational Electromagnetics for Brain Research and Applications

If you want to find neuronal currents in the brain, you may think to invert the matrix below.

$$\mathbf{Z} = \begin{bmatrix} (\sigma_1+\sigma_2)\mathbf{N}_{11} & -2\mathbf{D}^*_{11} & -\sigma_2\mathbf{N}_{12} & \mathbf{D}^*_{12} & 0 & 0 & 0 \\ -2\mathbf{D}_{11} & (\sigma_1^{-1}+\sigma_2^{-1})\mathbf{S}_{11} & \mathbf{D}_{12} & -\sigma_2^{-1}\mathbf{S}_{12} & 0 & 0 & 0 \\ -\sigma_2\mathbf{N}_{21} & \mathbf{D}^*_{21} & (\sigma_2+\sigma_3)\mathbf{N}_{22} & -2\mathbf{D}^*_{22} & -\sigma_3\mathbf{N}_{23} & \mathbf{D}^*_{23} & 0 \\ \mathbf{D}_{21} & -\sigma_2^{-1}\mathbf{S}_{21} & -2\mathbf{D}_{22} & (\sigma_2^{-1}+\sigma_3^{-1})\mathbf{S}_{22} & \mathbf{D}_{23} & -\sigma_3^{-1}\mathbf{S}_{23} & 0 \\ 0 & 0 & -\sigma_3\mathbf{N}_{32} & \mathbf{D}^*_{32} & (\sigma_3+\sigma_4)\mathbf{N}_{33} & -2\mathbf{D}^*_{33} & \cdots \\ 0 & 0 & \mathbf{D}_{32} & -\sigma_3^{-1}\mathbf{S}_{32} & -2\mathbf{D}_{33} & (\sigma_3^{-1}+\sigma_4^{-1})\mathbf{S}_{33} & \cdots \\ 0 & 0 & 0 & 0 & \vdots & \vdots & \ddots \end{bmatrix}$$

don't! That's cubic!

Computational Electromagnetics for Brain Research and Applications

$$\mathbf{Z} = \begin{bmatrix} (\sigma_1+\sigma_2)\mathbf{N}_{11} & -2\mathbf{D}^*_{11} & -\sigma_2\mathbf{N}_{12} & \mathbf{D}^*_{12} & 0 & 0 & 0 \\ -2\mathbf{D}_{11} & (\sigma_1^{-1}+\sigma_2^{-1})\mathbf{S}_{11} & \mathbf{D}_{12} & -\sigma_2^{-1}\mathbf{S}_{12} & 0 & 0 & 0 \\ -\sigma_2\mathbf{N}_{21} & \mathbf{D}^*_{21} & (\sigma_2+\sigma_3)\mathbf{N}_{22} & -2\mathbf{D}^*_{22} & -\sigma_3\mathbf{N}_{23} & \mathbf{D}^*_{23} & 0 \\ \mathbf{D}_{21} & -\sigma_2^{-1}\mathbf{S}_{21} & -2\mathbf{D}_{22} & (\sigma_2^{-1}+\sigma_3^{-1})\mathbf{S}_{22} & \mathbf{D}_{23} & -\sigma_3^{-1}\mathbf{S}_{23} & 0 \\ 0 & 0 & -\sigma_3\mathbf{N}_{32} & \mathbf{D}^*_{32} & (\sigma_3+\sigma_4)\mathbf{N}_{33} & -2\mathbf{D}^*_{33} & \cdots \\ 0 & 0 & \mathbf{D}_{32} & -\sigma_3^{-1}\mathbf{S}_{32} & -2\mathbf{D}_{33} & (\sigma_3^{-1}+\sigma_4^{-1})\mathbf{S}_{33} & \cdots \\ 0 & 0 & 0 & 0 & \vdots & \vdots & \ddots \end{bmatrix}$$

To get it done linearly, pre-multiply it instead with its dual magneto-to-electric and electro-to-magnetic counterpart

$$\tilde{\mathbf{C}} = \begin{bmatrix} c_{11}\tilde{\mathbf{S}}_{11} & c_{12}\tilde{\mathbf{D}}_{11} & c_{13}\tilde{\mathbf{S}}_{12} & c_{14}\tilde{\mathbf{D}}_{12} & 0 & 0 & 0 \\ c_{21}\tilde{\mathbf{D}}^*_{11} & c_{22}\tilde{\mathbf{N}}_{11} & c_{23}\tilde{\mathbf{D}}^*_{12} & c_{24}\tilde{\mathbf{N}}_{12} & 0 & 0 & 0 \\ c_{31}\tilde{\mathbf{S}}_{21} & c_{32}\tilde{\mathbf{D}}_{21} & c_{33}\tilde{\mathbf{S}}_{22} & c_{34}\tilde{\mathbf{D}}_{22} & c_{35}\tilde{\mathbf{S}}_{23} & c_{36}\tilde{\mathbf{D}}_{23} & 0 \\ c_{41}\tilde{\mathbf{D}}^*_{21} & c_{42}\tilde{\mathbf{N}}_{21} & c_{43}\tilde{\mathbf{D}}^*_{22} & c_{44}\tilde{\mathbf{N}}_{22} & c_{45}\tilde{\mathbf{D}}^*_{23} & c_{46}\tilde{\mathbf{N}}_{23} & 0 \\ 0 & 0 & c_{53}\tilde{\mathbf{S}}_{32} & c_{54}\tilde{\mathbf{D}}_{32} & c_{55}\tilde{\mathbf{S}}_{33} & c_{56}\tilde{\mathbf{D}}_{33} & \cdots \\ 0 & 0 & c_{63}\tilde{\mathbf{D}}^*_{32} & c_{64}\tilde{\mathbf{N}}_{32} & c_{65}\tilde{\mathbf{D}}^*_{33} & c_{66}\tilde{\mathbf{N}}_{33} & \cdots \\ 0 & 0 & 0 & 0 & \vdots & \vdots & \ddots \end{bmatrix}$$

Computational Electromagnetics for Brain Research and Applications

To get it done linearly, pre-multiply it instead with its dual magneto-to-electric and electro-to-magnetic counterpart

In fact the following identities can be proved

$$S_{ii}N_{ii} = \frac{1}{4}I - D_{ii}^2$$

$$N_{ii}S_{ii} = \frac{1}{4}I - D_{ii}^{*2}$$

and the product reads

$$CZ = \begin{bmatrix} (\sigma_1+\sigma_2)^2\boxed{S_{11}N_{11}} + K_{11} & K_{12} & K_{13} & \cdots \\ K_{21} & (\sigma_1^{-1}+\sigma_2^{-1})^2\boxed{N_{11}S_{11}} + K_{22} & K_{23} & \cdots \\ K_{31} & K_{32} & (\sigma_2+\sigma_3)^2\boxed{S_{22}N_{22}} + K_{33} & \cdots \\ \vdots & \vdots & \vdots & \ddots \end{bmatrix}$$

This basically gives you points 1) and 2) of the general recipe

Point 3) is obtained by discretizing things properly…

Computational Electromagnetics for Brain Research and Applications

Point 3) is obtained by permeating the discretization choice by the "electromagnetic duality": electric unknowns on one graph, magnetic ones on a dual graph…

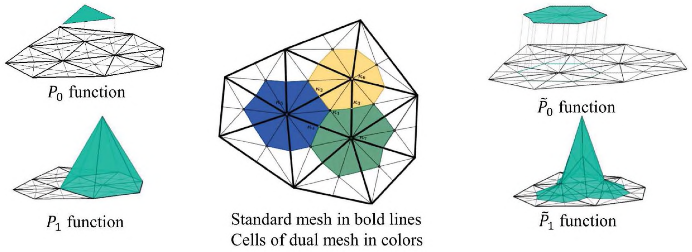

P_0 function

P_1 function

Standard mesh in bold lines
Cells of dual mesh in colors

$\tilde{P}_0$ function

$\tilde{P}_1$ function

Computational Electromagnetics for Brain Research and Applications

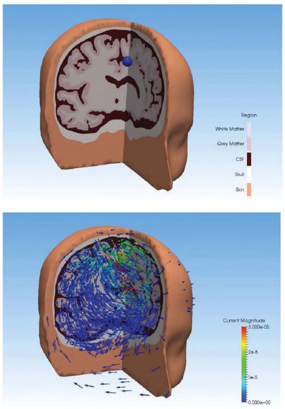

The result of the overall process ensures orders of magnitude accelerations and a change from a cubic to linear computational complexity!

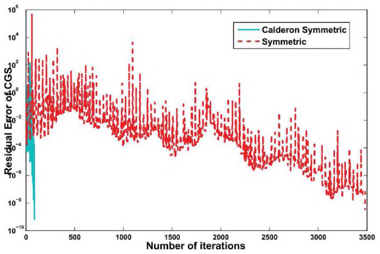

Computational Electromagnetics for Brain Research and Applications

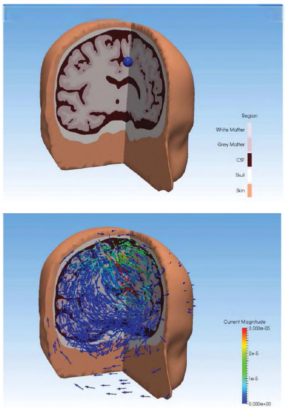

The result of the overall process ensures orders of magnitude accelerations and a change from a cubic to linear computational complexity!

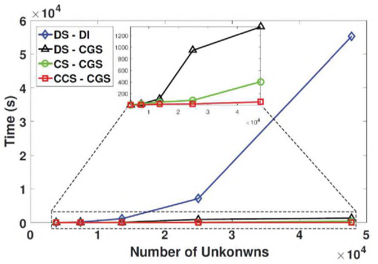

Target Applications (II)

Brain Computer Interfaces

Task: create an extra-muscular channel to connect the Brain with the external world

Societal impact: BCIs are a key resource for locked-in patients and are also of increasing interest for general public applications

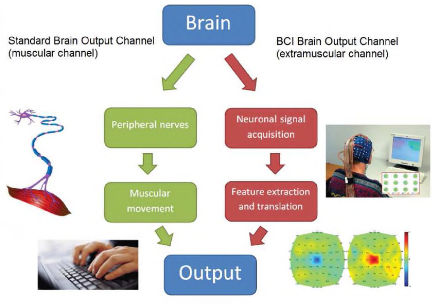

Brain Computer Interfaces

Standard pipeline

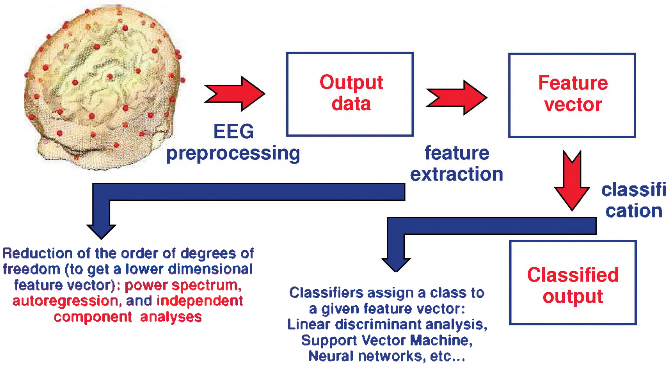

Output data

Feature vector

EEG preprocessing

feature extraction

classifi cation

Classified output

Reduction of the order of degrees of freedom (to get a lower dimensional feature vector): power spectrum, autoregression, and independent component analyses

Classifiers assign a class to a given feature vector: Linear discriminant analysis, Support Vector Machine, Neural networks, etc…

Brain Computer Interfaces

Standard pipeline – generating output data

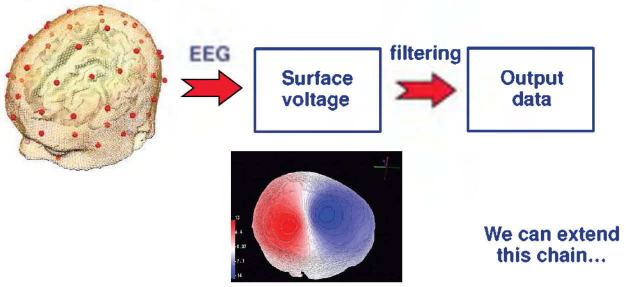

EEG

Surface voltage

filtering

Output data

We can extend this chain…

Brain Computer Interfaces

Our work: extended pipeline – generating output data

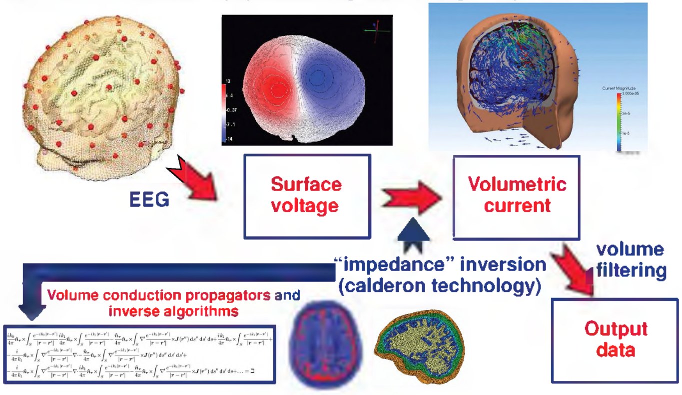

EEG

Surface voltage

Volumetric current

“impedance” inversion (calderon technology)

volume filtering

Output data

Volume conduction propagators and inverse algorithms

Computational Electromagnetics for Brain Research and Applications

Main Challenges from a Computational Prospective

Sources of complexity

- Very low powers involved in the presence of severe bioshielding effects
- Large number of physical degrees of freedom in modeling the microscopic level
- Extremely complex and anisotropic bioelectric physics at the macroscopic level
- Scarce reproducibility of human related parameters and factors

---

The head is not homogeneous

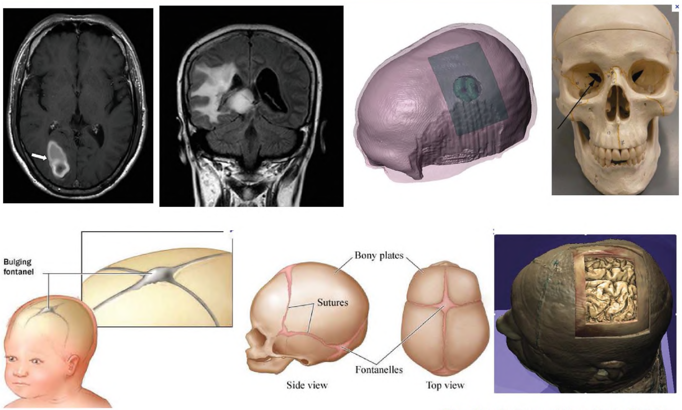

The City College of New York, CUNY

The head is not isotropic

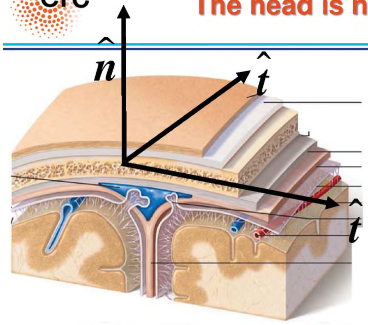

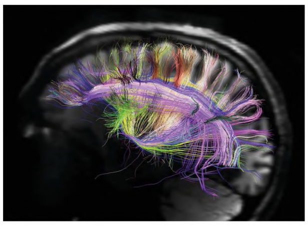

$$\overline{\overline{\sigma}} = \begin{bmatrix} \sigma_{xx} & \sigma_{xy} & \sigma_{xz} \\ \sigma_{yx} & \sigma_{yy} & \sigma_{yz} \\ \sigma_{zx} & \sigma_{zy} & \sigma_{zz} \end{bmatrix}$$

The electric conductivity is, in general, a varying-in-space tensor

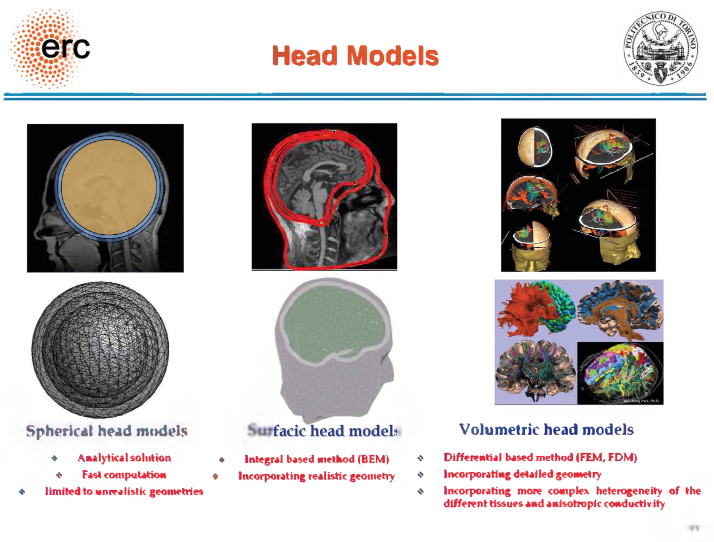

Head Models

Spherical head models
- Analytical solution
- Fast computation
- limited to unrealistic geometries

Surfacic head models
- Integral based method (BEM)
- Incorporating realistic geometry

Volumetric head models
- Differential based method (FEM, FDM)
- Incorporating detailed geometry
- Incorporating more complex heterogeneity of the different tissues and anisotropic conductivity

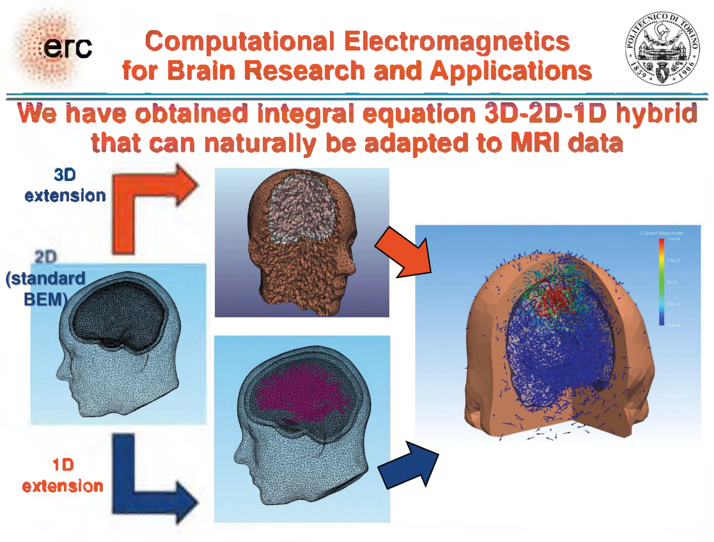

Computational Electromagnetics for Brain Research and Applications

We have obtained integral equation 3D-2D-1D hybrid that can naturally be adapted to MRI data

3D extension

2D (standard BEM)

1D extension

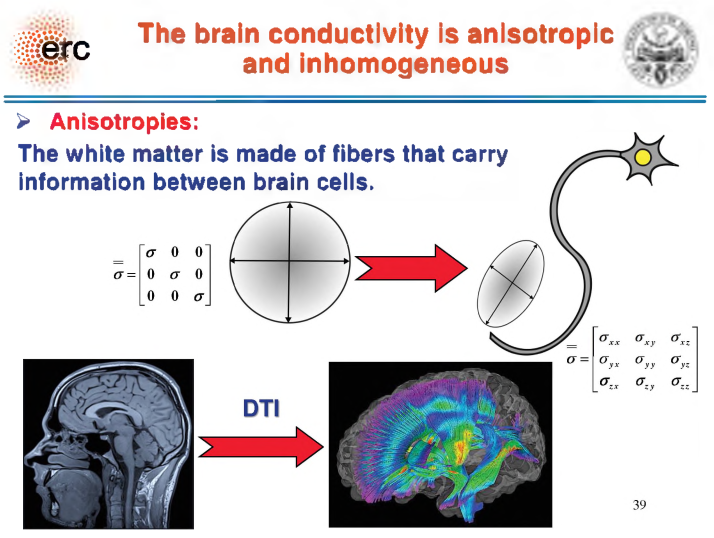

The brain conductivity is anisotropic and inhomogeneous

- **Anisotropies:**

The white matter is made of fibers that carry information between brain cells.

$$\bar{\bar{\sigma}}=\begin{bmatrix}\sigma & 0 & 0\\ 0 & \sigma & 0\\ 0 & 0 & \sigma\end{bmatrix}$$

$$\bar{\bar{\sigma}}=\begin{bmatrix}\sigma_{xx} & \sigma_{xy} & \sigma_{xz}\\ \sigma_{yx} & \sigma_{yy} & \sigma_{yz}\\ \sigma_{zx} & \sigma_{zy} & \sigma_{zz}\end{bmatrix}$$

DTI

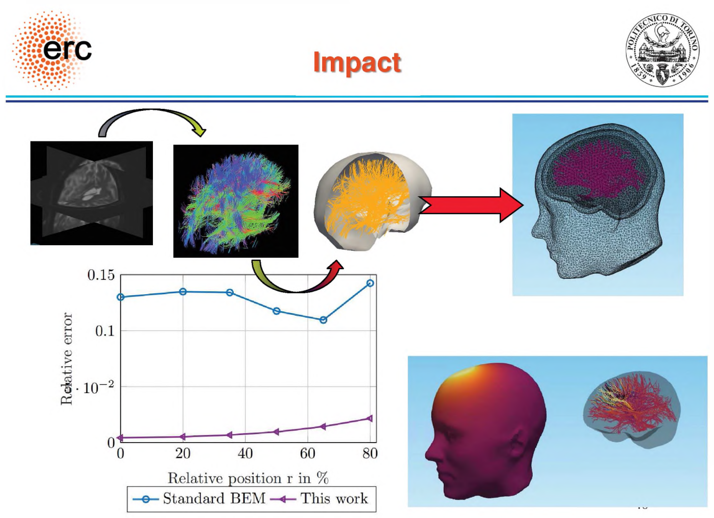

Impact

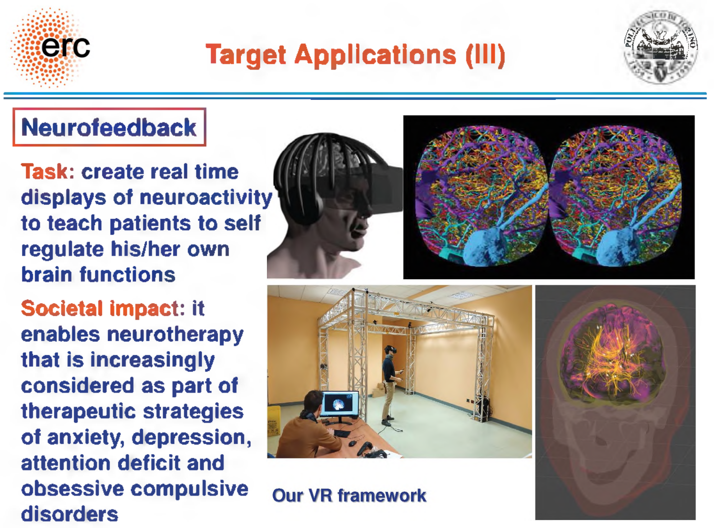

Target Applications (III)

Neurofeedback

Task: create real time displays of neuroactivity to teach patients to self regulate his/her own brain functions

Societal impact: it enables neurotherapy that is increasingly considered as part of therapeutic strategies of anxiety, depression, attention deficit and obsessive compulsive disorders

Our VR framework

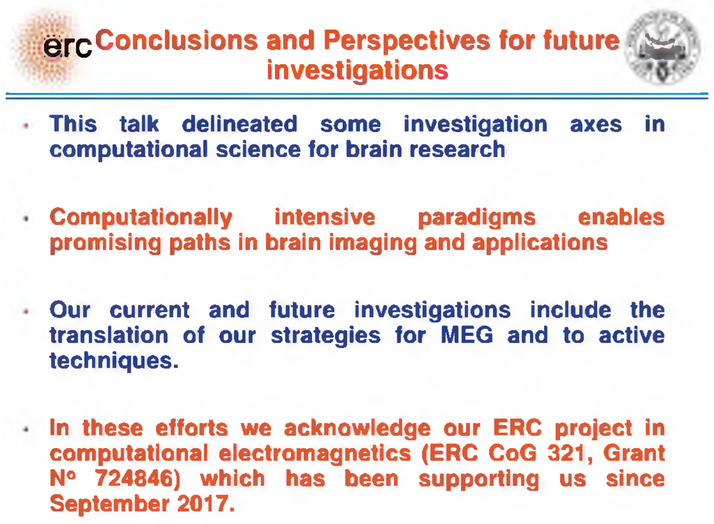

Conclusions and Perspectives for future investigations

- This talk delineated some investigation axes in computational science for brain research
- Computationally intensive paradigms enables promising paths in brain imaging and applications
- Our current and future investigations include the translation of our strategies for MEG and to active techniques.
- In these efforts we acknowledge our ERC project in computational electromagnetics (ERC CoG 321, Grant Nº 724846) which has been supporting us since September 2017.

Microspectroscopie DRASC en temps réel pour suivre les changements de l'eau associée aux membranes cellulaires induits par l'électropulsation de liposomes

Real-time CARS microspectroscopy to follow changes of membrane associated water molecules induced by the electropulsation of liposomes

C. Merla,[1], B. Attal-Tretout[2], M. Nardoni[3], S. Petralito[3] , M. Scherman[2], F. Apollonio[4], M. Liberti[4], and L. M. Mir[5].

[1]ENEA Divsion of Health Protection Technologies, Rome, Italy, {caterina.merla}@enea.it
[2]ONERA, Paileseaux, cedex, France , {brigitte.attal-tretout}@onera.fr
[3]Department of Pharmaceutical Technologies, Sapienza University of Rome, Italy, {stefania.petralito}@uniroma1.it
[4]Department of Information Engineering Electronic and Telecommunication, Sapienza University of Rome, Italy, {apollonio}@diet.uniroma1.it
[5]Vectorology and Anticancer Therapies, UMR 8203, CNRS, Univ. Paris-Sud, Gustave Roussy, Université Paris-Saclay, 94805 Villejuif, France, {luis.mir}@cnrs.fr

Mots clé: DRASC, champs électriques pulsés, suspensions de liposomes, modes vibrationnels de l'eau.
Key words: CARS, pulsed electric fields, liposome suspensions, water vibrational modes.

Abstract

To deep more insight into basic phenomena occurring during and after electropulsation of biological membranes, a new experimental modality has been used. It combines a wide field Coherent Anti Stokes Raman Spectroscopy system with a coplanar wave guide able to deliver nanosecond pulsed electric fields to different in vitro samples. The experiments have been conducted on liposome suspensions. These systems well mimic phospholipid double layers. Spectra of liposome suspensions have been acquired immediately after electropulsation. Liposome suspension evidenced an increase of the vibrational modes around 3345 cm^{-1} for pulsed samples with respect to the non-pulsed ones. These vibrational signatures seem associated to the so called lipid associated water molecules. These molecules represent a water structure in which the intermolecular OH bonds become weak leading to the possibility that single water molecules can interact with the liposome lipidis making the pulsed membranes more permeable. Membranes assumed a less organized structure due to the persistence of these water defects.

Résumé

Pour mieux comprendre les phénomènes basiques qui se produisent pendant et après l'électroperméabilisation des membranes biologiques, une nouvelle configuration expérimentale a été mise en place. Le système combine un microscope DRASC (Diffraction Raman Anti Stokes Cohérente) et un guide coplanaire pour l'application des impulsions électriques et électromagnétiques. Les expériences ont été conduites avec des suspensions de liposomes qui sont des vésicules de phospholipides. Ces liposomes sont très similaires aux parties lipidiques des membranes des cellules biologiques. Des spectres DRASC des suspensions de liposomes ont été acquis immédiatement après l'application d'impulsions électriques de 10 nanosecondes de durée. Ces spectres montrent une augmentation des modes vibrationnels de l'eau associée aux lipides à 3345 cm^{-1} en comparaison avec les suspensions liposomales non exposées aux impulsions électriques. Les signatures observées peuvent être associées à des molécules d'eau avec des liaison OH intermoléculaires très faibles comme celles engagées dans l'interaction des molécules d'eau isolées avec les lipides. Cette restructuration rend la membrane des vésicules plus perméable grâce à l'installation de cette eau désorganisée qui permet hydratation des lipides.

1 Introduction

To deep more insight into basic phenomena occurring during and after electropulsation of biological membranes, a new experimental modality has been used combining a wide field Coherent Anti Stokes Raman Spectroscopy system [1] with a coplanar wave guide able to deliver nanosecond pulsed electric fields to different *in vitro* samples [2]. This setup allows to acquire CARS hyper-spectra at specific Raman bands from 2900 to 3500 cm^{-1} (into the so called water vibration region) as well as to acquire in real time the CARS signature at specific wavelengths with a spectral resolution of few ns. This time scale is comparable to the duration of the electrical stimulation synchronised to the laser emission. As the biophysical and chemical bases of cells electropermeabilization are still debated, our setup will allow the experimental assessment of the role of water molecules and phospholipid bilayers during the occurrence of this phenomenon which is used in various biotechnological, biological and medical applications.

2 Experimental Setup

The experiments have been conducted on liposome suspensions placed between the central and lateral (ground) electrodes a grounded closed coplanar waveguide (GCCPW) [2], assuring the transmission of short pulses (10 ns, and even shorter) to the biological samples without distortions. Liposomes, that is lipid spherical unilamelar vesicles, where chosen as a suitable synthetic system to mimic phospholipid double layers as they are similar to the structure of real cell membranes. The GCCPW inter electrodes gap was fixed to 0.5 µm in order to allow the pump and Stokes laser beams (diameters of about 100 µm) alignment and focusing into the liposomes suspension in a controlled way. The liposome suspension was contained in a PDMS holder with a total volume of 30 µL. The illumination scheme of the CARS microscope followed a non-phase-matched geometry as suggested in [1]. The pump/probe laser axis was kept parallel to the microscope objective one, while the Stokes beam was tilted by 7° to efficiently attenuate the non-resonant signal. An inverted microscope (Zeiss Axiovert 200) was used and the sample was imaged by means of a 50×, NA=0.55 objective. Image of the observation plane was formed on an intensified CCD camera (PIMAX 3 Camera, Roper Technologies, Sarasota, Florida). The bandpass filters (F1=CVI-CP-AG-540 and Semrock, F2=FF01-534/42 respectively, Fig. 1) were placed in order to reflect the pump/probe and Stokes beams right after interacting with the sample of interest. Additionally, a further bandpass filter (Semrock, F3=FF01-534/42, Fig. 1) was placed at the exit of the objective in front of the CCD camera to block residual light. The camera was triggered by the laser pulse using a delay generator (DG 545, Princeton instruments) with a temporal gate of 40 ns. A scheme of the experimental setup is reported in Fig. 1, together with the laser beams focusing into the GCCPW electrodes is also shown.

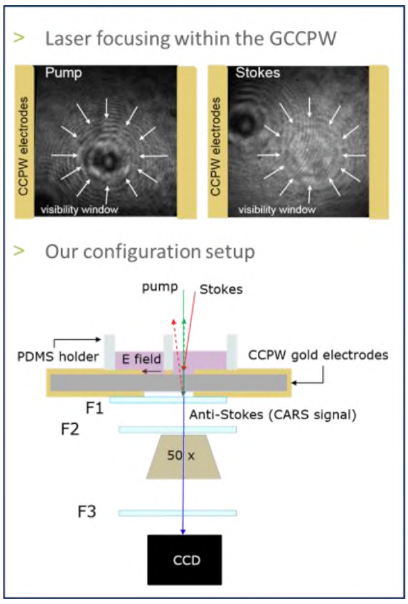

Fig. 1: Scheme of the experimental setup: combination of a ground closed coplanar waveguide (GCCPW) and a coherent anti-Stokes Raman microscope. The laser beams focused into the GCCPW electrodes are also sketched.

3 Results

Spectra of liposomes suspensions were acquired immediately after electropulsation evidencing an increase of the vibrational modes around 3345 cm-1 in the pulsed samples with respect to the non-pulsed one as shown in Fig. 2. Pulsed samples received 2000 pulses consecutively at 1 Hz and at an amplitude of 9 MV/m. This vibrational signature (3345 cm-1) seems to be related to the so called lipid associated water molecules, representing a water structure in which the intermolecular OH bonds become weak (asymmetric OH stretch modes) leading to the interaction of single water molecules with lipids. This association makes the pulsed membrane more permeable due to this less organized and persistent structure of the water molecules. The appearance of this vibrational mode has been also verified during the exposure, in real-time specific experiments.

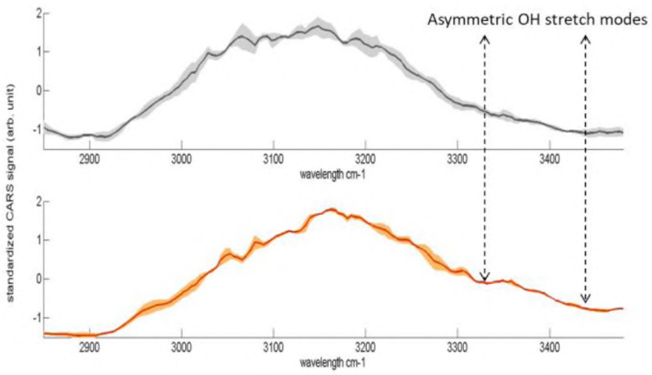

Fig. 2: Spectra of the liposomes suspension in exposed and unexposed conditions. Asymmetric vibrational bands modification is highlighted.

Finally, the effective permeabilization of liposome suspensions after the electric pulses delivery was verified looking at the release of a fluorescent dye (5-6-carboxfluorescein) included into the liposomes' core as presented in Fig. 3 (panel A). Dynamic light scattering measurements (performed before and after the exposure) demonstrated the maintenance of the vesicles integrity (Fig. 3 panel B) supporting the permanent hydration of the liposome membranes after electropulsation.

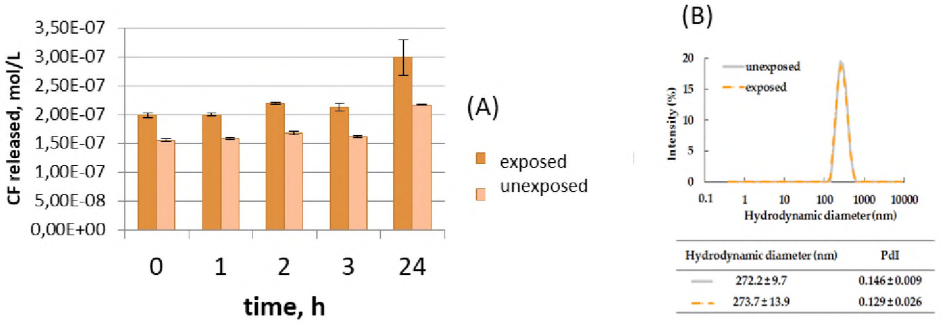

	Hydrodynamic diameter (nm)	PdI
—	272.2±9.7	0.146±0.009
- -	273.7±13.9	0.129±0.026

Fig. 3: 5-6CF release demonstrating the permeabilization of the liposomes under the action of the electric pulses. Dynamic light scattering performed before and after the liposomes exposure does not shown modification of the liposomal structure.

4 Conclusions

In summary, CARS, employing nanosecond lasers pulses and the properties of our wide field microscope and its intrinsic ability to sense complex interferences, has provided us with an appropriate diagnostic tool. Thanks to this setup, we were able to observe the spectra arising from interfacial and interstitial water molecules in liposome suspensions. The liposomes permeabilization was also confirmed by 5-(6) CF release after the exposure evidencing the interest of our results not only for the basic understanding of electropulsation mechanisms but also for their possible exploitation to smart drug delivery applications mediated by electric pulses. In a future, the underlined mechanism will be investigated on cells, hence taking into account recovery processes as well as the different interactions elicited by the application of longer µs electric pulses.

Acknowledges: Funding from European Union's Horizon 2020 Research and Innovation Program under Marie Sklodowska-Curie IF grant agreement No. 661041 OPTIC BIOEM are greatly acknowledged. This work was also supported by CNRS, Univ. Paris-Sud, Gustave Roussy, ITMO Plan Cancer ("Project Dynamo") and ONERA; it was also performed in the framework of the European Associated Laboratory (LEA) entitled "Pulsed Electric Fields Applications in Biology and Medicine" (EBAM), and the COST Action BM1609 EMF-Med (European network for innovative uses of electromagnetic fields in biomedical applications).

References

[1] A. Silve, N. Dorval, T. Schmid, L. M. Mir, and B. Attal-Trétout, A wide-field arrangement for single shot CARS imaging of living cells. J. Raman Spectrosc, 43, 644-650, 2012.

[2] C. Merla, M. Liberti, P. Marracino, A. Muscat, A. Azan, F. Apollonio, L. M. Mir, A wide-band bio-chip for real-time optical detection of bioelectromagnetic interactions with cells. Scientific Reports, 8, 5044, 2018.

Body-centric communications in the 60-GHz band: from antennas and on-body propagation to exposure reduction

Maxim ZHADOBOV

Institut d'Électronique et de Télécommunications de Rennes (IETR), UMR CNRS 6164
maxim.zhadobov@univ-rennes1.fr

Abstract

Body-centric wireless networks constitute an attractive next-generation wireless technology representing a cognitive interface to higher-level networks. Recently, the 60 GHz band has been identified as highly promising for body-centric wireless communications including body-area network technologies. A massive deployment of wireless devices equipped with 60 GHz Tx / Rx modules is foreseen in coming years. The corresponding new usages and services will involve near-field interaction of radiating devices with the human body, both in terms of the body impact on wireless device performances as well as in terms of user exposure. This presentation will provide an overview of main features and recent advances in the field of antenna / human body interactions in the 60 GHz band.

Body-centric wireless networks constitute an extremely attractive next-generation wireless technology representing a cognitive interface to higher-level networks (WPAN, WLAN, WMAN, etc.). These emerging systems open new possibilities in the fields of wireless communications, remote monitoring and sensing of the human body activity, detection and localization for a great number of applications (medical, entertainment, defence, smart homes and cities, sport, etc.). They could also play a key role in wireless sensor networks (WSN) and internet of things (IoT) whose economic impact is growing exponentially. Body-centric wireless networks have emerged as an alternative or add-on to traditional wired network systems (e.g. in medical environments), and new exciting applications are now under development (e.g. high-data-rate body-to-body streaming, remote monitoring of patients at home).

The upper limit of the spectrum used for wireless networking has been recently progressively shifting towards the millimeter-wave (MMW) band due to the increasing need in network capacity and high data rates [1]. Wireless data traffic is rising exponentially (nearly a threefold increase in traffic is expected from 2018 to 2021 according to the Cisco global mobile data traffic forecast [2]). Recently, the 60 GHz band has been identified as highly promising for body-centric wireless communications including body-area network (BAN) technologies. One of the main features differentiating the 60 GHz BAN from a lower frequency BAN is confidentiality and low interference with neighboring networks, which has been demonstrated to be crucial for body-centric and inter-BAN communications [3], for instance in military scenarios where communication security is vital [4]. Limited operating range in this band (e.g. shifting the frequency from 70 / 80 GHz to 60 GHz decreases the operating range from 3 km to 400 m [5]) is mainly related to the strong oxygen-induced atmospheric attenuation (typically 16 dB/km). Besides, high data rates can be achieved [beyond several Gb/s], which is extremely attractive to support the increasing demand in data traffic and high data rate transmissions. In addition, the 60 GHz band provides other advantages, such as miniature size of antennas and sensors compared to their counterparts in the lower part of the microwave spectrum. Today, MMW circuits and antennas can be implemented with a high level integration and reasonable cost. Finally, this band provides high accuracy that can be beneficially used for high-resolution localization (this can be exploited for new applications, such as immersive video games).

The implementation of 60 GHz technologies, including body-centric applications, is an unavoidable evolution of wireless networks, and first commercial solutions have already emerged for WPAN (e.g. Dell Latitude 6430u, first ultrabook using Qualcomm / Wilocity 60 GHz chipset). The 60 GHz band is unlicensed. Different spectra are allocated depending on countries (e.g. 57–66 GHz in Europe, 57–64 GHz in North America and South Korea, 59.4–62.9 GHz in Australia, 59–66 GHz in Japan [6]). Note that the available bandwidth is hundreds times higher compared to existing wireless technologies at lower microwave frequencies.

A massive deployment of wireless devices equipped with 60 GHz Tx / Rx modules is foreseen in coming years. The corresponding new usages and services will unavoidably involve coupling of radiating devices with the human body, both in terms of the body impact on wireless device performances as well as in terms of user exposure [7]. This includes the near-field interactions of wearable and mobile devices operating in the vicinity of the human body.

This presentation will provide an overview of main features and recent advances in the field of antenna / human body interactions in the 60 GHz band.

REFERENCES

[1] R.C. Daniels, J.N. Murdock, T.S. Rappaport, R.W. Heath, "60 GHz wireless: up close and personal," *IEEE Microwave Magazine*, vol. 11, pp. 44–50, 2010.

[2] 'Cisco Visual Networking Index: Global Mobile Data Traffic Forecast Update 2014–2019 White Paper. Available online at www.cisco.com/c/en/us/solutions/collateral/service-provider/visual-networking-index-vni/mobile-white-paper-c11-520862.html

[3] S.L. Cotton, W.G. Scanlon, P.S. Hall, "A simulated study of co-channel inter-BAN interference at 2.45 GHz and 60 GHz," *European Wireless Technology Conference* (EuWIT), pp. 61–64, Paris, France, Sep. 2010.

[4] S.L. Cotton, W.G. Scanlon, B.K. Madahar, "Millimeter-wave soldier-to-soldier communications for covert battlefield operations," *IEEE Communications Magazine*, vol. 47, 72–81, 2009.

[5] J. Wells, "Faster than fiber: the future of multi Gb/s wireless," *IEEE Microwave Magazine*, vol. 10, pp. 104–112, 2009.

[6] A. Pellegrini, A. Brizzi, L. Zhang, K. Ali, Y. Hao, X. Wu, C. C. Constantinou, Y. Nechayev, P. S. Hall, N. Chahat, M. Zhadobov, R. Sauleau, "Antennas and propagation for body-centric wireless communications at millimeter-wave frequencies: A review," *IEEE Antennas and Propagation Magazine*, 55, pp. 262–287, 2013.

[7] M. Zhadobov, C. Leduc, A. Guraliuc, N. Chahat, R. Sauleau, "Antenna / human body interactions in the 60 GHz band: state of knowledge and recent advances," *State-of-the-Art in Body-Centric Wireless Communications and Associated Applications*, IET, pp. 97–142, 2016.

Electromagnetism and interaction with the cell (Posters)

Microscope Holographique Numérique : amélioration de l'imagerie par traitement numérique permettant une analyse quantitative de cellules vivantes

***Amira MESSAOUDI*[1]*, Youssef KEBBATI*[2]*, Yacine BENNANI*[3]**
[1] *Université des sciences et de la technologie Med Boudiaf d'Oran, Algérie*
[2] *Université d'Orléans, LPC2E, France*
[3] *Université Saad Dahlab de Blida, Algérie*

Abstract

Dans cet article, nous présentons une méthode d'amélioration de l'imagerie issue d'un microscope holographique numérique DHM. L'objectif est d'aboutir à une visualisation et une analyse quantitative de cellules vivantes. Cette méthode est basée sur : le développement algorithmique d'un polynôme de masque de phase directement de l'image du microscope puis, le traitement numérisé et automatisé permettant une extraction de paramètres quantitatifs. Des exemples sont présentés montrant la pertinence de la technique pour la biologie. Il est à noter qu'il ne s'agit pas ici d'un modèle de simulation mais d'une modélisation numérique permettant un suivie en temps « réel » de cellules vivantes.

Le microscope holographique numérique en biologie

En imagerie biologique, la plupart des objets visualisés et en particulier les cellules vivantes sont transparentes et ne diffères que légèrement par rapport à leurs environnements. Cette légère différence induit néanmoins un modeste changement dans le parcours de l'onde lumineuse et aussi de sa phase [1]. De ce fait, le DHM est un instrument puissant pour l'étude d'échantillons biologiques, et dans notre cas des cellules vivantes, en récupérant l'amplitude et la phase de l'onde réfléchie ou transmise. La reconstruction de phase est particulièrement intéressante car elle permet de mesurer la topographie de surface avec une résolution verticale de l'ordre du nanomètre. Le DHM est utilisé avec deux configurations fonctionnelles : réflexion et transmission. La figure 1 présente l'instrumentation utilisée pour les deux modes de fonctionnement [2].

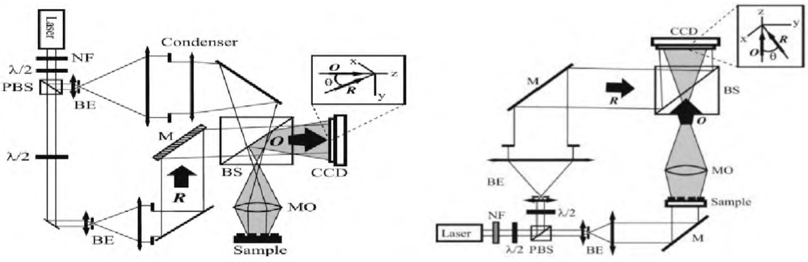

a) b)

Figure 1 : microscope holographique en a) réflexion, b) transmission

Développement algorithmique

Le microscope étant un interféromètre, l'interférence entre l'onde objet O et l'onde de référence R crée l'intensité de sortie de l'hologramme. La transmission de la sortie à l'ordinateur se fait après digitalisation de l'image à travers une caméra CDD noir et blanc. L'équation 1 de reconstruction décrit la propagation de Fresnel du front d'onde reconstruit, sur une distance *d*, des plans $0xy$ et $0\xi\eta$. R_D et le masque de phase [3] et définit comme l'onde image calculée de l'onde de référence expérimentale *R*.

$$\psi(\xi,\eta) = \Phi(\xi,\eta) \times \frac{exp(\frac{2i\pi}{d})}{id\lambda} \times exp\left[\frac{i\pi}{d\lambda}(\xi^2+\eta^2)\right] \times \iint R_D(x,y) I_H(x,y) \times exp\left[\frac{i\pi}{d\lambda}[(x-\xi)^2+(y-\eta)^2]\right] dxdy$$

$$avec\ \Phi(\xi,\eta) = exp\left[\frac{-i\pi}{d\lambda}[\xi^2+\eta^2]\right] \qquad (1)$$

Le paramètre Φ étant l'expression du masque numérique de phase. Une amélioration de cet algorithme a été introduite par Colomb [2] pour palier, par exemple, aux erreurs d'ordre supérieur à 2 dû aux déformations des optiques. L'équation 1 se trouve ainsi formulée

$$\Psi(\xi,\ \eta) = -i\ \exp(i2\pi d/\lambda)\Gamma(\xi,\ \eta)\mathfrak{F}_\tau\,[I_H](\xi,\ \eta) \quad \text{avec} \quad \Gamma(\xi,\ \eta) = \exp\left[\frac{i\pi}{\lambda}\left(2k_x\xi + 2k_y\eta - \frac{\xi^2+\eta^2}{D}\right) + i\phi'(k_x,\ k_y,\ t)\right]. \qquad (2)$$

Avec Γ le masque numérique de phase sous forme polynomiale.

Traitement numérisé et résultats

A partir de l'équation 2, nous avons effectué, équation 3, la numérisation de l'image en discrétisant l'équation de Fresnel [2][4]. La DFT étant la Transformée de Fourrier Discrète.

$$\Psi'(m,\, n) = A\Gamma(m,\, n)\exp\left[\frac{i\pi}{\lambda d}\left(m^2\Delta\xi^2 + n^2\Delta\eta^2\right)\right] \times \mathrm{DFT}\left\{I_H(k,\, l)\exp\left[\frac{i\pi}{\lambda d}\left(k^2\Delta x^2 + l^2\Delta y^2\right)\right]\right\}_{m,n} \quad (3)$$

La modélisation sous Matlab a permis ainsi de transformer l'image issu du microscope en son équivalent numérique. Pour illustrer cette technique, nous avons choisi de l'appliquer aux cellules vivantes. Il est à noter qu'il ne s'agit pas ici d'un modèle de simulation mais d'une modélisation numérique permettant un suivie en temps « pseudo réel » (décalage dû au temps de traitement de l'image). En effet, la cadence de prise des images est de 1 seconde.

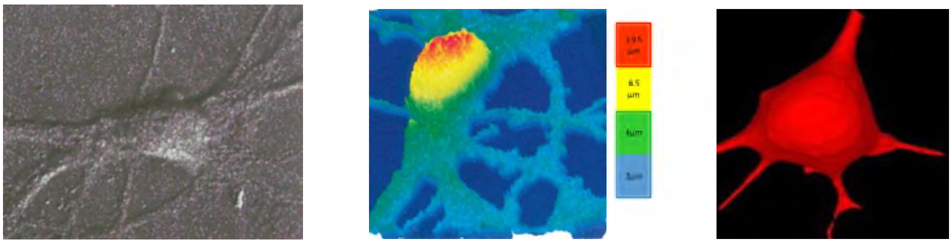

Figure 2 : a) image du DHM, b) image avec Matlab, c) modification de la forme de la cellule

La figure 2 montre l'image issue du DHM sans traitement puis son traitement avec Matlab ainsi que la modification de la forme de la cellule. Dans cet exemple, nous pouvons voir l'évolution de la forme des cellules de manière automatisée. Ceci permet en autre de détecter des cellules cancéreuses par exemple. La figure 3 présente, le suivie d'un virus par un globule blanc jusqu'à son absorption ainsi que le suivie de trajectoire avec Matlab. A travers ces deux exemples, nous pouvons voir que notre technique est aussi adaptée pour suivre le mouvement des globules rouges, la détection d'agglomération de ces globules (embolie) ou bien la détection de modification de la forme géométrique qui peut être synonyme de pathologies diverses.

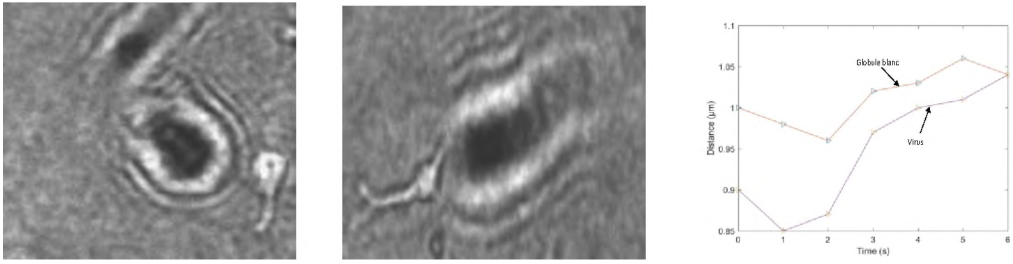

Figure 3 : a) le suivie d'un virus par un globule blanc, b) l'absorption du virus, c) le suivie de trajectoire

Conclusion

Dans cet article, nous avons présenté une méthode de traitement d'images biologiques en temps réel issue du microscope holographique numérique. Cette technique permet, à moindre coût de temps de calcul, d'obtenir une image numérisée de cellules vivantes. L'objectif est d'aboutir à une visualisation et une analyse quantitative de cellules vivantes. Les résultats montrent une adéquation de notre démarche pour le domaine biologique. Ainsi, cette technique est un support d'aide automatisée dédiées aux biologistes permettant une détection rapide de pathologies par le suivie quantitative de déformation structurelle, de taille, de trajectoire, d'agglomération etc. des cellules.

Références

[1] P. Ferraro and all, « Compensation of the inherent front curvature in digital holographic coherent microscopy for quantitative phase-contrast imaging », Appl. Opt. 42, 2003.

[2] T. Colomb and all, « Automatic procedure for aberration compensation in digital holographic microscopy and applications to specimen shape compensation », Appl. Opt. 45, 2006.

[3] E. Cuche, P.Marquet, « Ssimultaneous amplitude and quantitative phase-contrast microscopy by numerical reconstruction of Fresnel off-axis holograms », Appl. Opt, 38, 1999

[4] M. Liebling, « On Fresnel, interferance fringes, and digital holography », PhD thesis, EPFL, 2004.

Ultra hot plasmas

Échelles et dynamique de la turbulence, observations par diffusion micro-onde dans les plasmas de tokamak

---

Pascale Hennequin

Laboratoire de Physique des Plasmas (LPP)
CNRS-UPMC-Ecole Polytechnique

Antennes radiofréquences de fortes puissances pour les expériences sur la fusion nucléaire

High Power Radio-frequency Antennas for Nuclear Fusion Experiments

Julien Hillairet[1]

[1] *CEA, IRFM, F-13108 St-Paul-Lez-Durance, France. julien.hillairet@cea.fr*

Mots clés : antennes radiofréquences, fusion nucléaire. Radio-frequency antennas, nuclear fusion.

Résumé

La maîtrise des réactions de fusion nucléaire pour la génération d`électricité permettrait d'apporter une réponse supplémentaire aux besoins énergétiques à venir. Toutefois, amorcer les réactions de fusion de noyaux atomiques nécessite d`obtenir et de maintenir des plasmas dont les températures sont de l`ordre de la centaine de millions de degrés. Pour obtenir ces températures, des systèmes radiofréquences sont utilisés couramment sur différentes installations expérimentales dans le monde. Selon la fréquence utilisée, les ondes électromagnétiques vont, une fois couplées au plasma, transférer leur énergie de préférence aux ions ou aux électrons. À quelques dizaines de mégahertz, des antennes électriquement courtes sont utilisées pour chauffer préférentiellement les ions du plasma. À quelques gigahertz, des antennes constituées de réseaux phasés de guides d`ondes rectangulaires permettent d`accélérer les électrons afin de maintenir la configuration magnétique sur des durées plus longues. Au-delà d`une centaine de gigahertz, la puissance des ondes électromagnétiques permet d`accélérer et de chauffer les électrons de manière locale dans le plasma grâce à des miroirs réglables. Cet article présente les principaux aspects technologiques de ces antennes radiofréquences sur les expériences actuelles et futures.

Abstract

The goal of nuclear fusion research is to demonstrate the fusion power feasibility for electricity-generation. To achieve the necessary conditions of temperature for fusion reactions to happen, hundreds of millions of degrees plasmas must be generated and sustained, ideally for long durations. For this purpose, antennas delivering few megawatts of radio-frequency (RF) power are commonly used in experimental fusion devices around the world. Depending of the frequency involved, the electromagnetic waves will resonate and transfer their energy mainly with either the ion or electron population of the plasma. In the megahertz range of frequencies, high power electrically short antennas are used to preferentially heat an ion species of the plasma. In the gigahertz range of frequencies, high power rectangular waveguide phased arrays are used to extend the plasma duration. At the hundreds of gigahertz, high power electromagnetic waves which behavior is quasi-optical are launched into the plasma by steerable mirrors for local electron heating. This paper reviews some of the technological aspects of these RF antennas for present and experimental future devices.

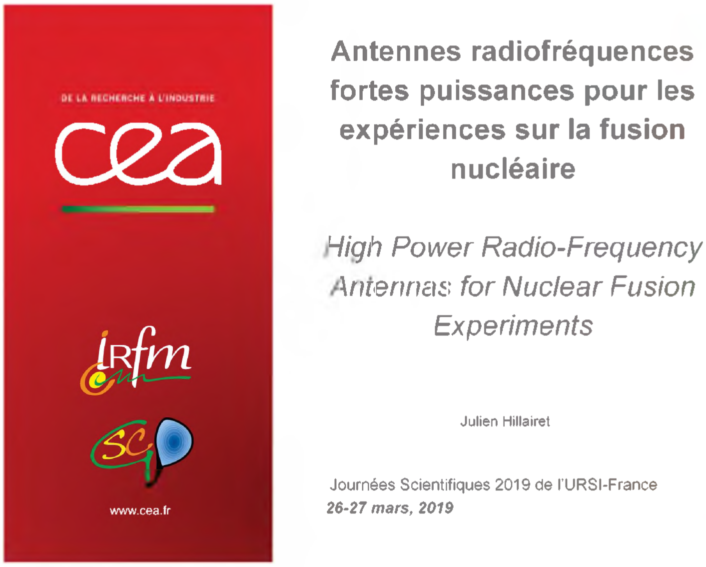

Antennes radiofréquences fortes puissances pour les expériences sur la fusion nucléaire

High Power Radio-Frequency Antennas for Nuclear Fusion Experiments

Julien Hillairet

Journées Scientifiques 2019 de l'URSI-France
26-27 mars, 2019

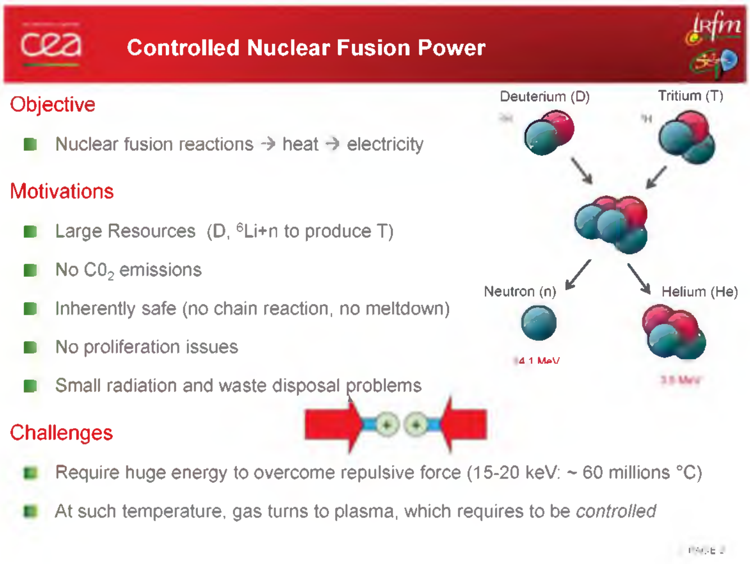

Controlled Nuclear Fusion Power

Objective

- Nuclear fusion reactions → heat → electricity

Motivations

- Large Resources (D, ^{6}Li+n to produce T)
- No $C0_2$ emissions
- Inherently safe (no chain reaction, no meltdown)
- No proliferation issues
- Small radiation and waste disposal problems

Challenges

- Require huge energy to overcome repulsive force (15-20 keV: ~ 60 millions °C)
- At such temperature, gas turns to plasma, which requires to be *controlled*

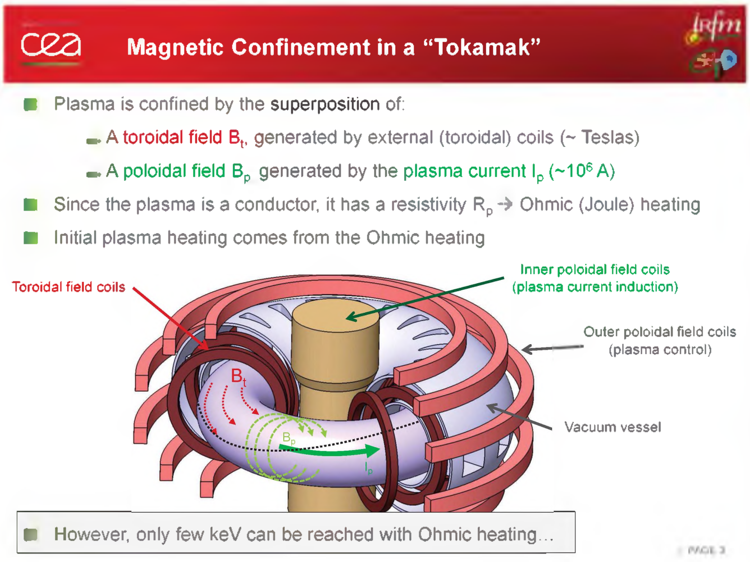

Magnetic Confinement in a "Tokamak"

- Plasma is confined by the **superposition** of:
  - A toroidal field B_t, generated by external (toroidal) coils (~ Teslas)
  - A poloidal field B_p generated by the plasma current I_p (~10^6 A)
- Since the plasma is a conductor, it has a resistivity R_p → Ohmic (Joule) heating
- Initial plasma heating comes from the Ohmic heating

- However, only few keV can be reached with Ohmic heating…

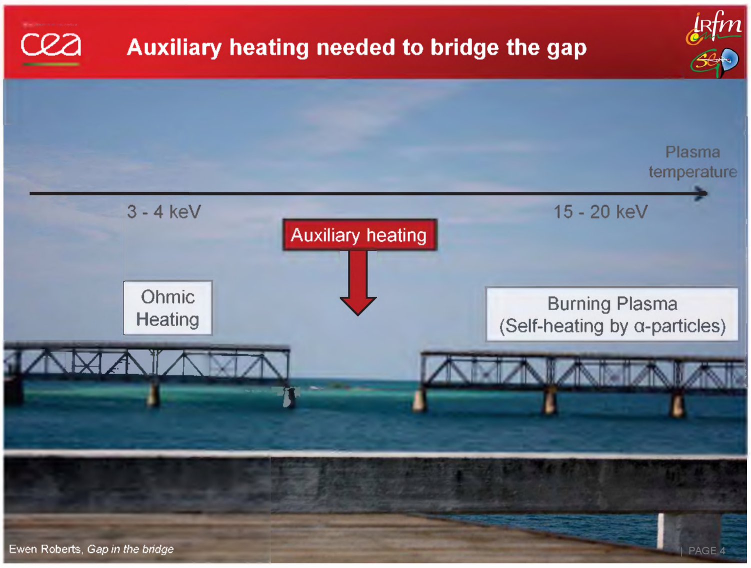

Auxiliary heating needed to bridge the gap

Ewen Roberts, *Gap in the bridge*

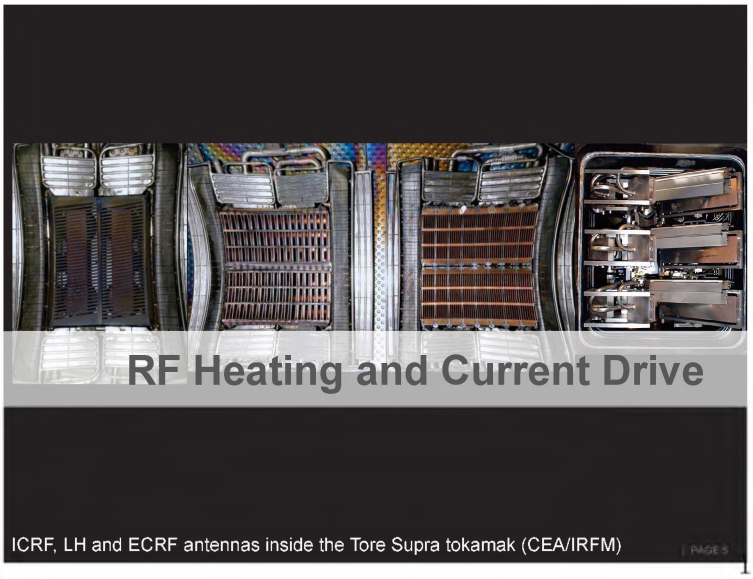

RF Heating and Current Drive

ICRF, LH and ECRF antennas inside the Tore Supra tokamak (CEA/IRFM)

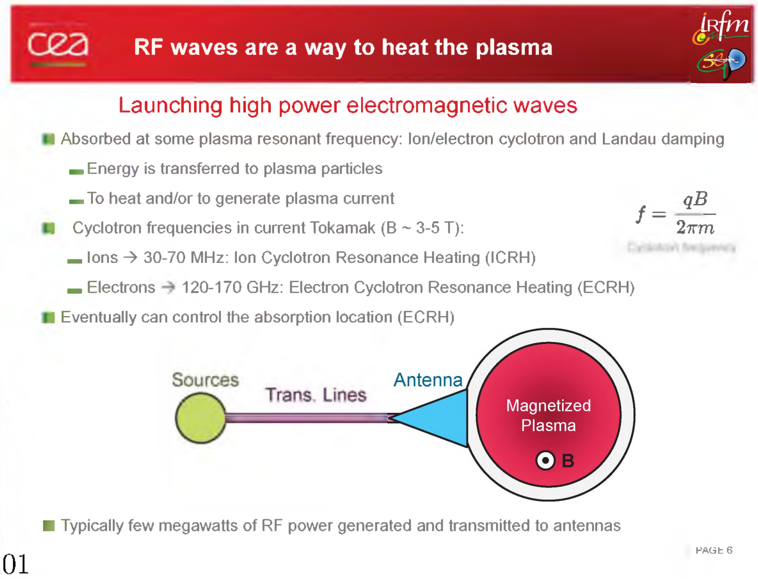

RF waves are a way to heat the plasma

Launching high power electromagnetic waves

- Absorbed at some plasma resonant frequency: Ion/electron cyclotron and Landau damping
  - Energy is transferred to plasma particles
  - To heat and/or to generate plasma current
- Cyclotron frequencies in current Tokamak (B ~ 3-5 T):
  - Ions → 30-70 MHz: Ion Cyclotron Resonance Heating (ICRH)
  - Electrons → 120-170 GHz: Electron Cyclotron Resonance Heating (ECRH)
- Eventually can control the absorption location (ECRH)

$$f = \frac{qB}{2\pi m}$$

Cyclotron frequency

- Typically few megawatts of RF power generated and transmitted to antennas

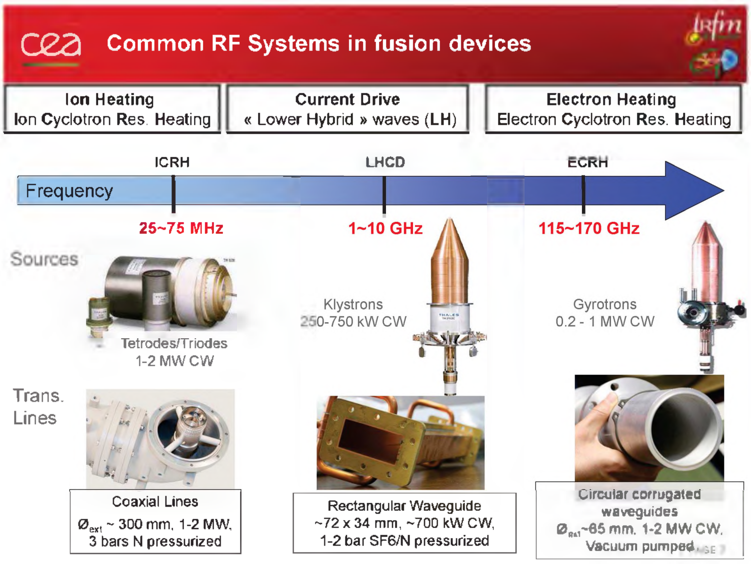

Common RF Systems in fusion devices

Ion Heating Ion Cyclotron Res. Heating	Current Drive « Lower Hybrid » waves (LH)	Electron Heating Electron Cyclotron Res. Heating
ICRH	LHCD	ECRH
25~75 MHz	1~10 GHz	115~170 GHz

Frequency

Sources

Tetrodes/Triodes
1-2 MW CW

Klystrons
250-750 kW CW

Gyrotrons
0.2 - 1 MW CW

Trans. Lines

Coaxial Lines
$Ø_{ext}$ ~ 300 mm, 1-2 MW,
3 bars N pressurized

Rectangular Waveguide
~72 x 34 mm, ~700 kW CW,
1-2 bar SF6/N pressurized

Circular corrugated waveguides
$Ø_{ext}$~65 mm, 1-2 MW CW,
Vacuum pumped

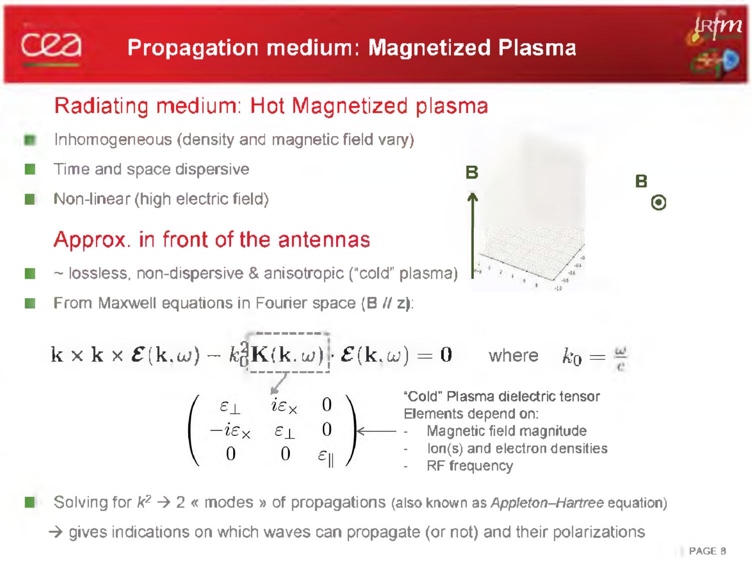

Propagation medium: Magnetized Plasma

Radiating medium: Hot Magnetized plasma

- Inhomogeneous (density and magnetic field vary)
- Time and space dispersive
- Non-linear (high electric field)

Approx. in front of the antennas

- ~ lossless, non-dispersive & anisotropic ("cold" plasma)
- From Maxwell equations in Fourier space (B // z):

$$\mathbf{k} \times \mathbf{k} \times \boldsymbol{\mathcal{E}}(\mathbf{k},\omega) - k_0^2 \mathbf{K}(\mathbf{k},\omega) \cdot \boldsymbol{\mathcal{E}}(\mathbf{k},\omega) = \mathbf{0} \quad \text{where} \quad k_0 = \frac{\omega}{c}$$

$$\begin{pmatrix} \varepsilon_\perp & i\varepsilon_\times & 0 \\ -i\varepsilon_\times & \varepsilon_\perp & 0 \\ 0 & 0 & \varepsilon_\parallel \end{pmatrix}$$

"Cold" Plasma dielectric tensor
Elements depend on:
- Magnetic field magnitude
- Ion(s) and electron densities
- RF frequency

- Solving for k^2 → 2 « modes » of propagations (also known as *Appleton–Hartree* equation)

→ gives indications on which waves can propagate (or not) and their polarizations

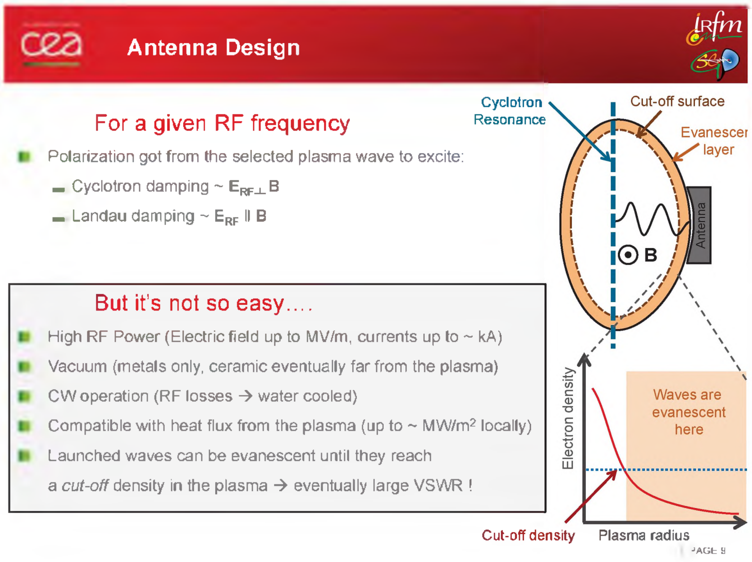

Antenna Design

For a given RF frequency

- Polarization got from the selected plasma wave to excite:
  - Cyclotron damping ~ $E_{RF\perp}$ B
  - Landau damping ~ E_{RF} ∥ B

But it's not so easy….

- High RF Power (Electric field up to MV/m, currents up to ~ kA)
- Vacuum (metals only, ceramic eventually far from the plasma)
- CW operation (RF losses → water cooled)
- Compatible with heat flux from the plasma (up to ~ MW/m² locally)
- Launched waves can be evanescent until they reach a *cut-off* density in the plasma → eventually large VSWR !

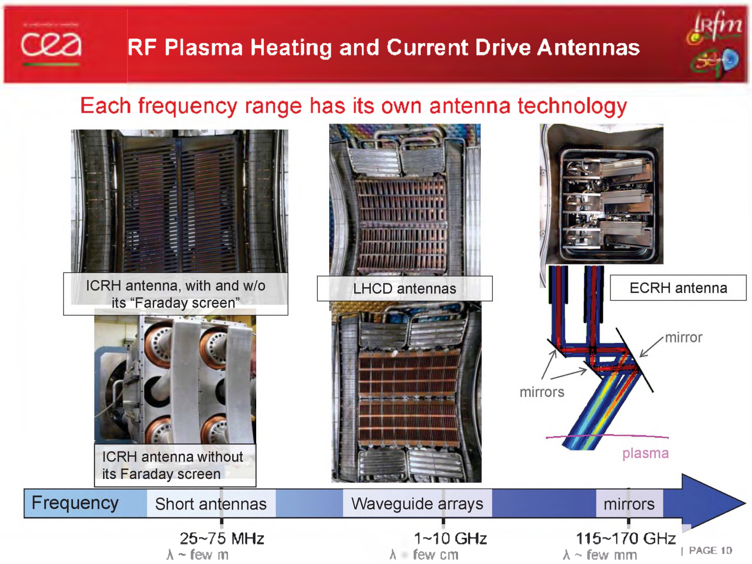

RF Plasma Heating and Current Drive Antennas

Each frequency range has its own antenna technology

ICRH antenna, with and w/o its "Faraday screen"

LHCD antennas

ECRH antenna

ICRH antenna without its Faraday screen

Frequency	Short antennas	Waveguide arrays	mirrors
	25~75 MHz λ ~ few m	1~10 GHz λ ~ few cm	115~170 GHz λ ~ few mm

Ion Cylotron Resonance Heating (ICRH)

Picture of the front face of the WEST ICRH Antenna during RF tests in vacuum

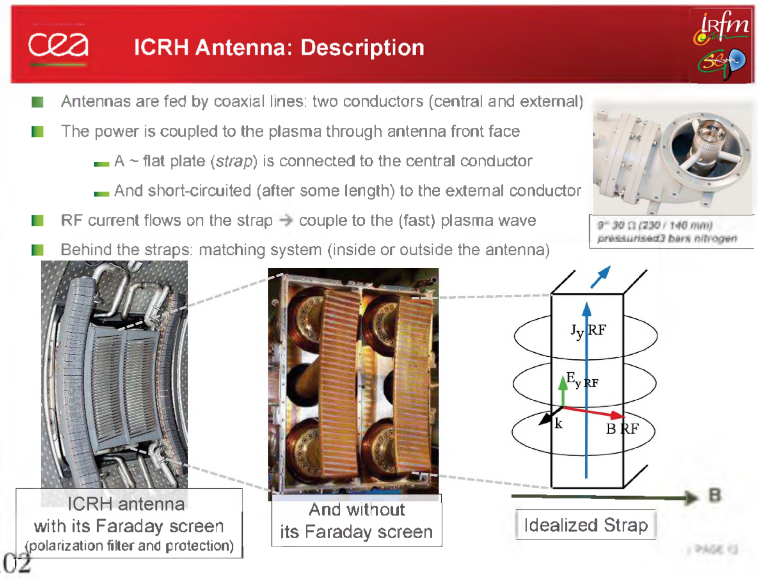

ICRH Antenna: Description

- Antennas are fed by coaxial lines: two conductors (central and external)
- The power is coupled to the plasma through antenna front face
  - A ~ flat plate (*strap*) is connected to the central conductor
  - And short-circuited (after some length) to the external conductor
- RF current flows on the strap → couple to the (fast) plasma wave
- Behind the straps: matching system (inside or outside the antenna)

9" 30 Ω (230 / 140 mm) pressurised3 bars nitrogen

ICRH antenna
with its Faraday screen
(polarization filter and protection)

And without
its Faraday screen

Idealized Strap

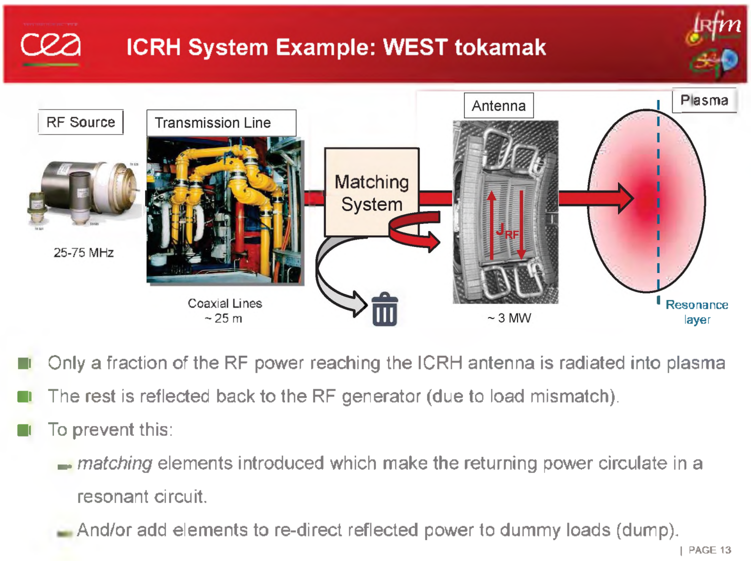

ICRH System Example: WEST tokamak

- Only a fraction of the RF power reaching the ICRH antenna is radiated into plasma
- The rest is reflected back to the RF generator (due to load mismatch).
- To prevent this:
  - *matching* elements introduced which make the returning power circulate in a resonant circuit.
  - And/or add elements to re-direct reflected power to dummy loads (dump).

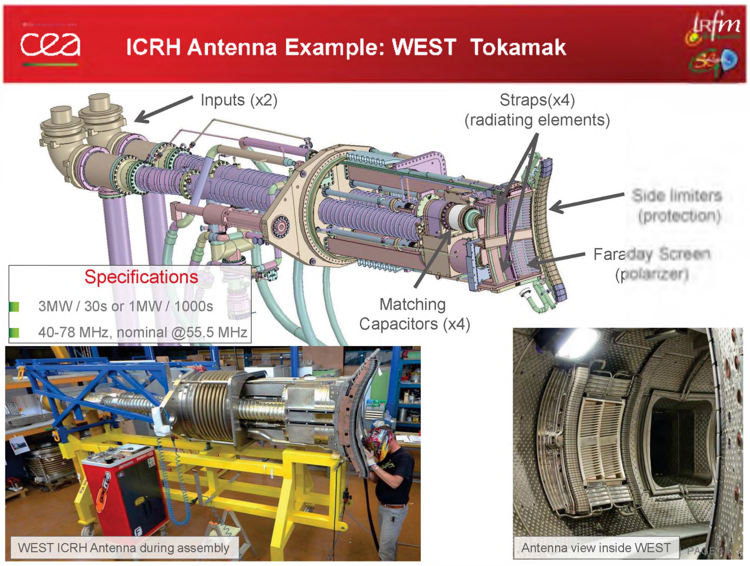

ICRH Antenna Example: WEST Tokamak

Specifications

- 3MW / 30s or 1MW / 1000s
- 40-78 MHz, nominal @55.5 MHz

WEST ICRH Antenna during assembly

Antenna view inside WEST

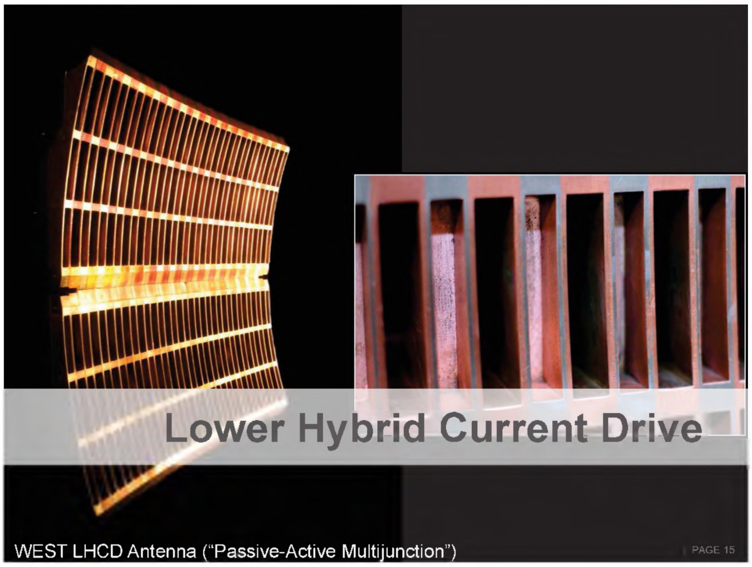

Lower Hybrid Current Drive

WEST LHCD Antenna ("Passive-Active Multijunction")

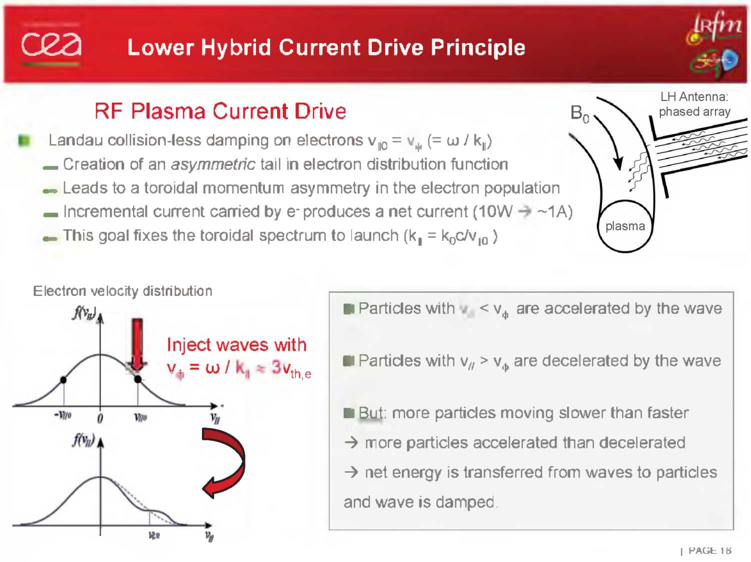

Lower Hybrid Current Drive Principle

RF Plasma Current Drive

- Landau collision-less damping on electrons $v_{\parallel 0} = v_\phi$ (= $\omega / k_\parallel$)
  - Creation of an *asymmetric* tail in electron distribution function
  - Leads to a toroidal momentum asymmetry in the electron population
  - Incremental current carried by e^- produces a net current (10W → ~1A)
  - This goal fixes the toroidal spectrum to launch ($k_\parallel = k_0 c/v_{\parallel 0}$)

Electron velocity distribution

Inject waves with
$v_\phi = \omega / k_\parallel \approx 3v_{th,e}$

- Particles with $v_{//} < v_\phi$ are accelerated by the wave
- Particles with $v_{//} > v_\phi$ are decelerated by the wave
- But: more particles moving slower than faster

→ more particles accelerated than decelerated

→ net energy is transferred from waves to particles and wave is damped.

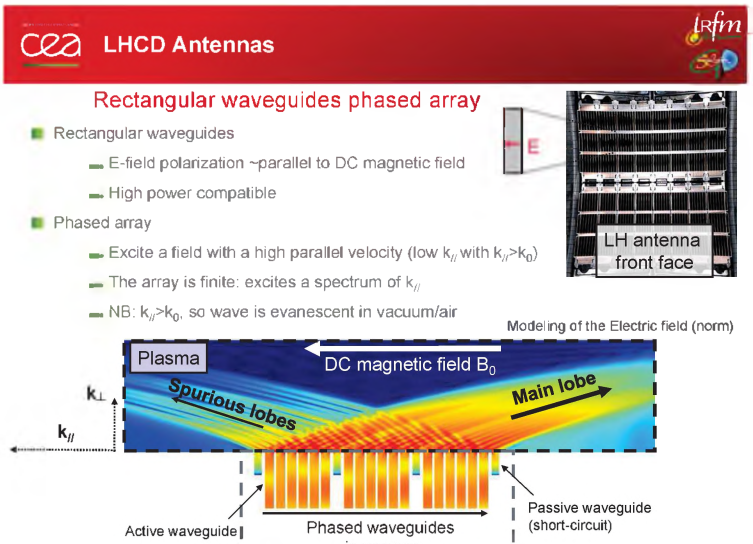

LHCD Antennas

Rectangular waveguides phased array

- Rectangular waveguides
  - E-field polarization ~parallel to DC magnetic field
  - High power compatible
- Phased array
  - Excite a field with a high parallel velocity (low $k_{//}$ with $k_{//}>k_0$)
  - The array is finite: excites a spectrum of $k_{//}$
  - NB: $k_{//}>k_0$, so wave is evanescent in vacuum/air

Modeling of the Electric field (norm)

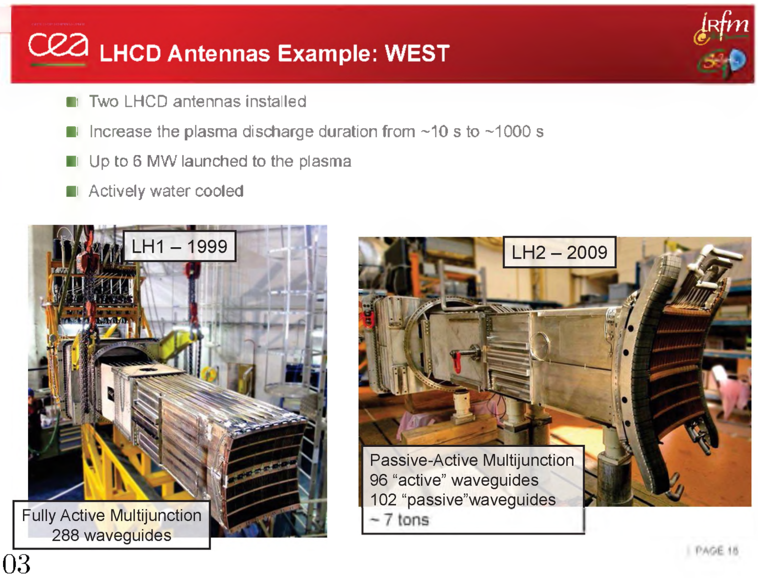

LHCD Antennas Example: WEST

- Two LHCD antennas installed
- Increase the plasma discharge duration from ~10 s to ~1000 s
- Up to 6 MW launched to the plasma
- Actively water cooled

LH1 – 1999

Fully Active Multijunction
288 waveguides

LH2 – 2009

Passive-Active Multijunction
96 "active" waveguides
102 "passive"waveguides
~ 7 tons

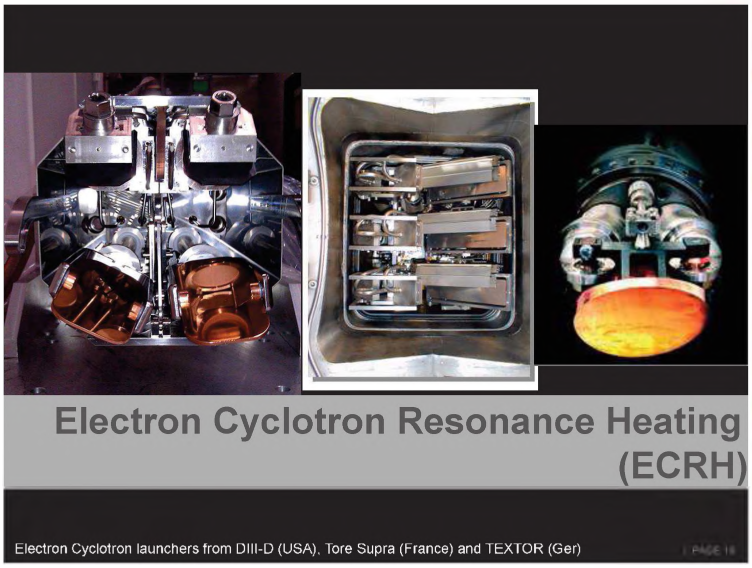

Electron Cyclotron Resonance Heating (ECRH)

Electron Cyclotron launchers from DIII-D (USA), Tore Supra (France) and TEXTOR (Ger)

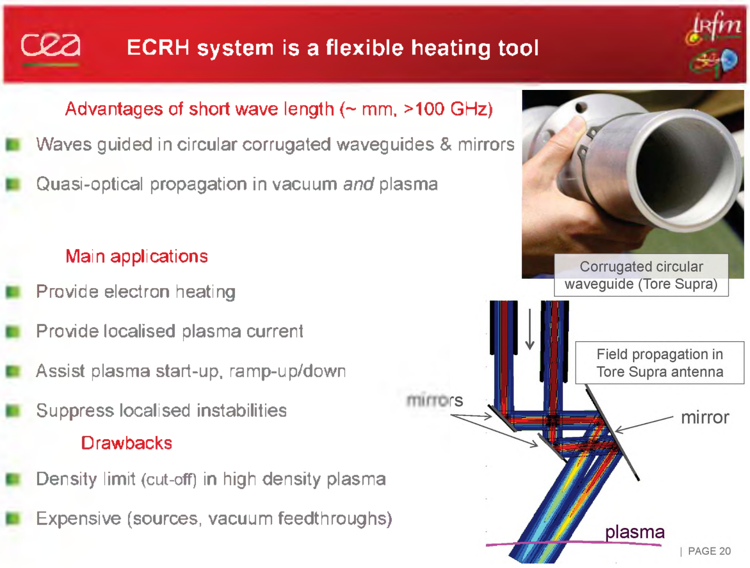

ECRH system is a flexible heating tool

Advantages of short wave length (~ mm, >100 GHz)

- Waves guided in circular corrugated waveguides & mirrors
- Quasi-optical propagation in vacuum *and* plasma

Main applications

- Provide electron heating
- Provide localised plasma current
- Assist plasma start-up, ramp-up/down
- Suppress localised instabilities

Drawbacks

- Density limit (cut-off) in high density plasma
- Expensive (sources, vacuum feedthroughs)

Corrugated circular waveguide (Tore Supra)

Field propagation in Tore Supra antenna

Summary

Picture of the front face of the WEST ICRH Antenna during RF tests in vacuum

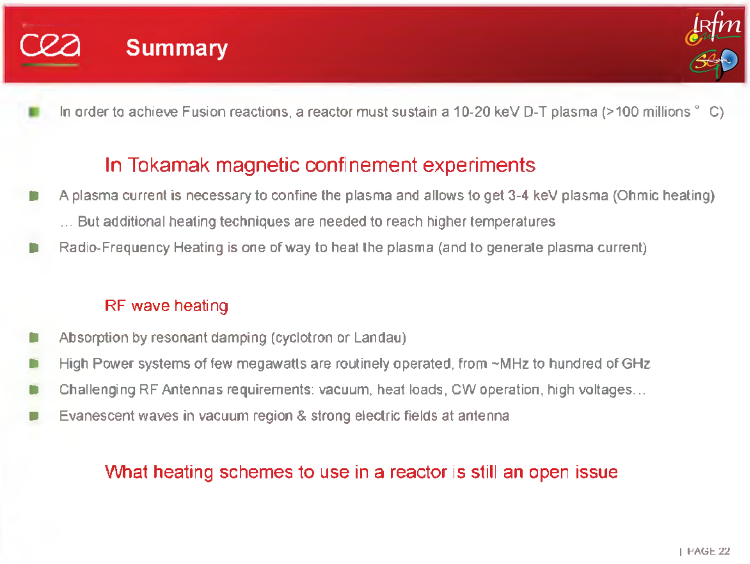

Summary

- In order to achieve Fusion reactions, a reactor must sustain a 10-20 keV D-T plasma (>100 millions ° C)

In Tokamak magnetic confinement experiments

- A plasma current is necessary to confine the plasma and allows to get 3-4 keV plasma (Ohmic heating)
  … But additional heating techniques are needed to reach higher temperatures
- Radio-Frequency Heating is one of way to heat the plasma (and to generate plasma current)

RF wave heating

- Absorption by resonant damping (cyclotron or Landau)
- High Power systems of few megawatts are routinely operated, from ~MHz to hundred of GHz
- Challenging RF Antennas requirements: vacuum, heat loads, CW operation, high voltages…
- Evanescent waves in vacuum region & strong electric fields at antenna

What heating schemes to use in a reactor is still an open issue

Summary

Thank you for your attention

Inside the WEST vacuum vessel (CEA/IRFM)

Preparations for measurements of impulsive electromagnetic signals on Mars, on the low Earth orbit, and at Jupiter in a broad (but still finite) interval of frequencies

Préparations pour les mesures des signaux électromagnétiques impulsifs sur Mars, sur l'orbite orbite terrestre basse et près de Jupiter dans un large (mais toujours fini) intervalle de fréquences

---

Ondrej Santolik [1,2] ***and Ivana Kolmasova*** [1,2]

[1] Department of Space Physics, Institute of Atmospheric Physics, The Czech Academy od Sciences, Prague, Czechia
[2]Faculty of Mathematics and Physics, Charles University, Prague, Czechia

---

Keywords : Spacecraft measurements, lightning, sprites, Mars
Mesures d'instruments spatiaux, éclairs, sprites, Mars

Résumé/Abstract

Dans un proche avenir, de nouvelles mesures de signaux électromagnétiques impulsifs seront effectuées par le satellite français TARANIS, par la mission JUICE (Jupiter icy moons explorer) de l'Agence spatiale européenne et par la plate-forme de surface ExoMars 2020.

In the near future, new measurements of impulsive electromagnetic signals will be done by the French satellite TARANIS, by the JUICE (Jupiter icy moons explorer) mission of the European Space Agency, and by the ExoMars 2020 Surface Platform.

1 Low Earth orbit

The French satellite TARANIS (Tool for the analysis of radiation from lightning and sprites) will be launched in 2020 on a polar low Earth orbit with an altitude of 700 km. Department of Space Physics of the Institute of Atmospheric Physics in Prague in cooperation with French colleagues developed a receiver for the IME-HF instrument (Instrument de Mesure du champ Electrique Haute Fréquence), designed to study electromagnetic radiation from lightning discharges and associated transient luminous events occurring above thunderstorms. The analyzed frequency band is from 5 kHz to 35 MHz and interesting parts of the electric field waveform sampled at 80 MHz will be selected by a flexible detection algorithm.

Observations of electromagnetic radiation from space will provide us with important information about lightning properties, mainly in the case of intra-cloud discharges which are difficult to detect optically. We prepare a ground-based observational campaign with an identical high frequency analyzer. After the launch of the TARANIS satellite this campaign will complement the observations from space.

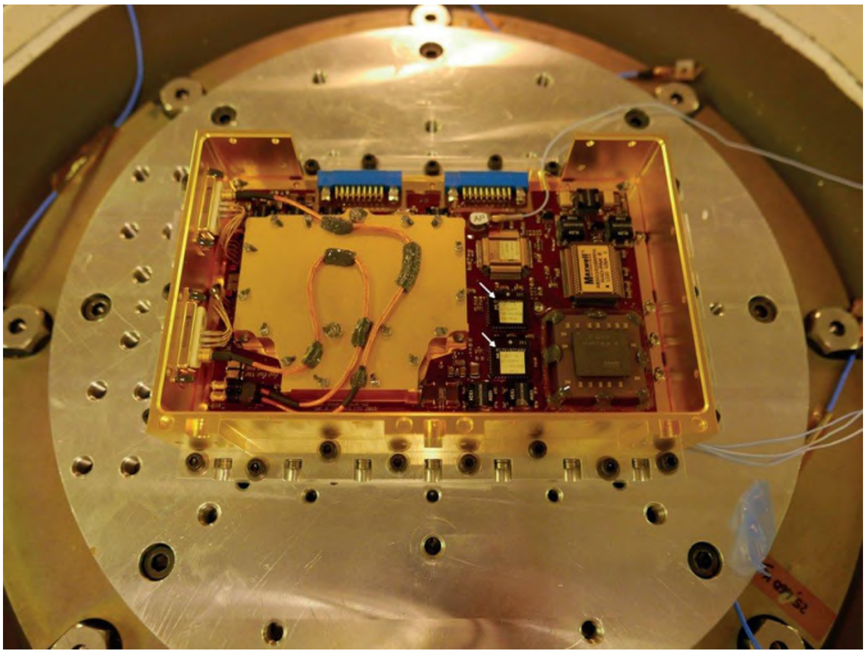

Figure 1: The IME-HF analyzer during the vibration tests

2 Jovian icy moons

The JUICE (Jupiter icy moons explorer) mission of the European Space Agency is scheduled for launch in 2022 and in 2030 it will arrive to Jupiter and its icy moons. The Radio and Plasma Waves Investigation instrument is being developed in a broad international cooperation of 25 institutions from 9 countries. Our receiver within this instrument will provide multi-component measurements of electromagnetic fields at frequencies up to 20 kHz.

These measurements will concentrate on research of electromagnetic waves in the Jovian magnetosphere and in the vicinity of Jovian moons, especially Ganymede where the Galileo probe discovered impulsive electromagnetic signals similar to those which accelerate electrons in the Earth's radiation belts.

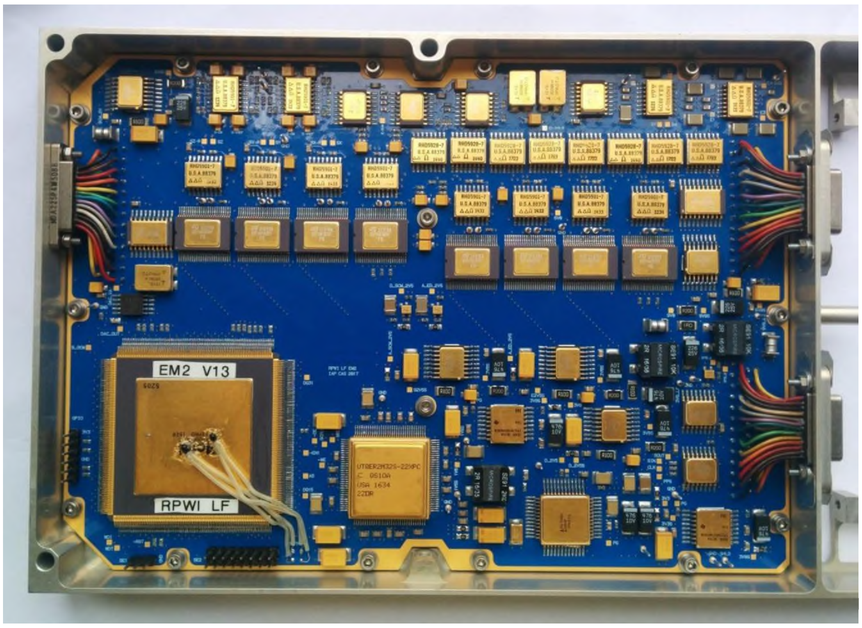

Figure2: The second engineering model of the LF analyzer for the JUICE/RPWI instrument

3 Surface of Mars

The ExoMars 2020 Surface Platform (to be launched in 2020, and landed on Mars in 2021) will conduct environmental and geophysical measurements with the aim to study the Martian surface and subsurface environment at the landing site. As a part of the scientific goals of the project, we will investigate electromagnetic waves in a broad range of frequencies up to 8 MHz by a wave analyzer module, consisting of an assembly of magnetic and electric antennae and dedicated analyzer electronics. The scientific questions which we plan to address have never been answered by direct measurements on the surface of the planet.

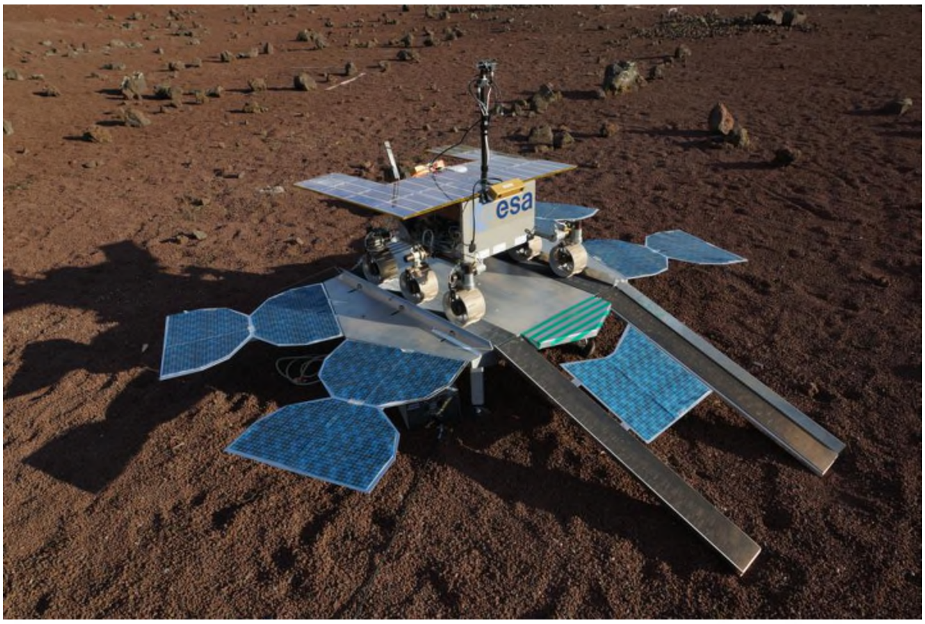

Figure 3: Model of the ExoMars 2020 surface platform and rover during tests in Toulouse

(Credits: ESA)

We plan to analyze emissions of atmospheric origin and possible wave activity originated in electrical discharges in dust storms. The wave activity linked to the interactions of interplanetary plasma medium with Martian ionosphere and Martian magnetic anomalies and interactions related to space weather effects will be also investigated.

The immediate questions to be answered are:

i) Can we observe electromagnetic radiation propagating from the interplanetary space down to the surface of the planet?

ii) Can we observe electromagnetic radiation from hypothetical electric discharges in the Martian dust storms or dust devils?

COMITÉ NATIONAL FRANÇAIS DE RADIOÉLECTRICITÉ SCIENTIFIQUE
UNION RADIO SCIENTIFIQUE INTERNATIONALE
SIÈGE SOCIAL : ACADÉMIE DES SCIENCES, 23 QUAI DE CONTI, PARIS 6EME

JS 19

JOURNÉES SCIENTIFIQUES, *WORKSHOP*

APPROCHER LES DEUX INFINIS PAR LES ONDES ELECTROMAGNÉTIQUES
APPROCHING BOTH INFINITIES THROUGH ELECTROMAGNETIC WAVES WAVES

26 / 27 MARS, 2019
OBSERVATOIRE DE VERSAILLES SAINT-QUENTIN-EN-YVELINES

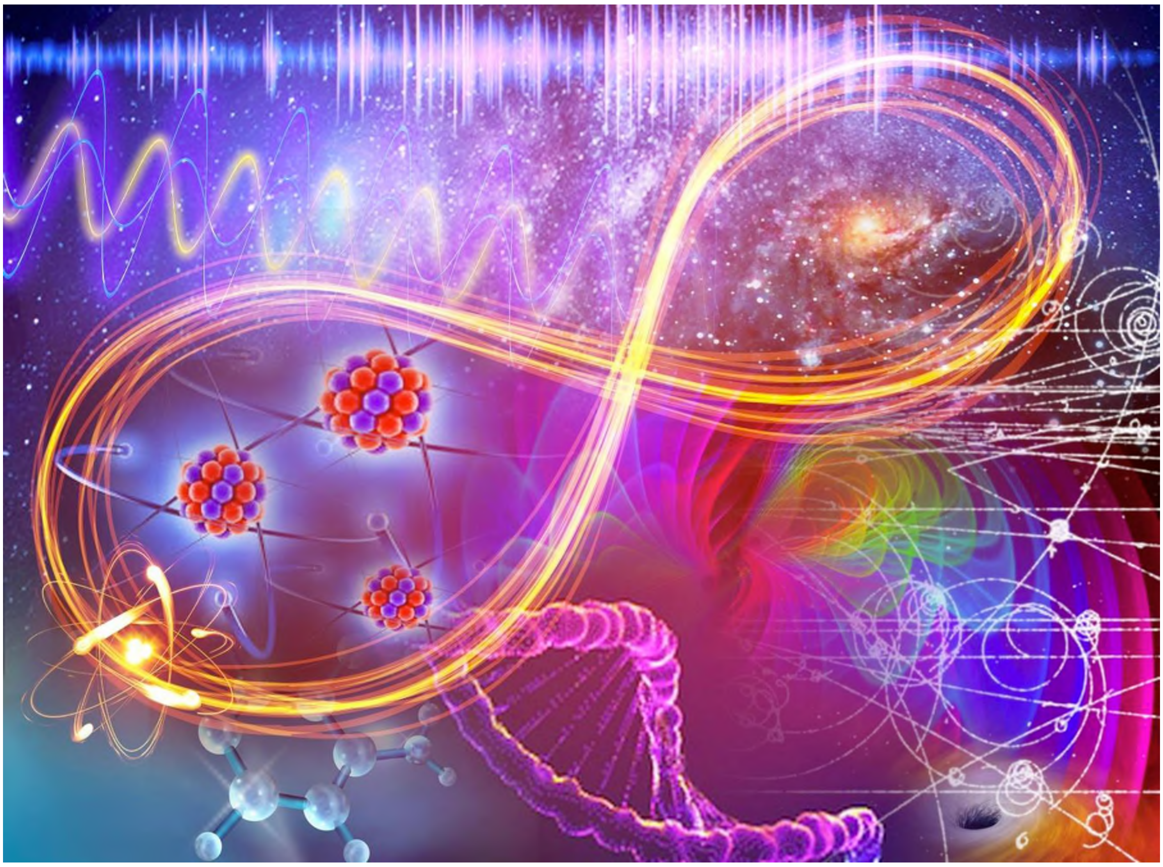

ACTES *PROCEEDINGS*

Étude de turbulence dans les plasmas de fusion à l'aide du radar FMCW ultra-rapide

Study of turbulence in fusion plasmas with the ultra-fast FMCW radar

Anna Medvedeva[1], Frederic Clairet[1], Christine Bottereau[1], Robin Marcille[2], Sebastien Hacquin[1,3], Guilhem Dif-Pradalier[1], ASDEX Upgrade Team[4], EUROfusion MST1 and JET1 team[5]

[1]CEA, IRFM, F-13108 Saint-Paul-lez-Durance, anna.medvedeva@cea.fr
[2]Ecole Polytechnique, F- 91128 Palaiseau, robin.marcille@polytechnique.edu
[3] EUROfusion Programme Management Unit, Culham Science Centre, OX14 3DB, UK
[4]Max-Planck-Institut für Plasmaphysik, D-85748 Garching
[5] For a list of members, see H.Meyer et al, Nucl. Fusion 57 102014 (2017)

Fusion, turbulence, micro-ondes, réflectométrie
Fusion, turbulence, microwaves, reflectometry

Abstract

The description of the relationship between plasma turbulence, flows and confinement is one of the milestones in the global understanding of fusion plasma physics. In order to study the turbulence dynamics with the best possible spatial and temporal resolution, we developed a FMCW (frequency-modulated continuous-wave) microwave radar diagnostic. The density fluctuation is recorded by the reflected signal. The time resolution of 1 µs and the spatial resolution of a few millimetres allow to study the turbulence spectra and the fast density dynamics due to confinement transitions. The ongoing work is dedicated to the development of a synthetic diagnostic which couples the turbulence maps resulted from gyrokinetic simulations with the 2D wave propagation code to be compared with the experimental reflectometry data.

Résumé

La description de la relation entre la turbulence, les écoulements et le confinement dans le plasma est l'une des étapes importantes de la compréhension globale de la physique des plasmas de fusion. Afin d'étudier la dynamique de la turbulence avec la meilleure résolution spatiale et temporelle possible, nous avons développé un diagnostic radar micro-ondes FMCW (à onde continue à modulation de fréquence). La fluctuation de densité est enregistrée par le signal réfléchi. La résolution temporelle de 1 µs et la résolution spatiale de quelques millimètres permettent d'étudier les spectres de turbulence et la dynamique rapide de densité due aux transitions de confinement. Les travaux en cours sont consacrés à la mise au point d'un diagnostic synthétique couplant les cartes de turbulence issues des simulations gyrocinétiques au code de propagation d'ondes 2D pour être comparés aux données expérimentales de réflectométrie.

1 Introduction

The new generation of fusion installations has been built to implement the industrial reactor project. The future tokamak reactor will achieve the necessary parameters to allow the production of energy through the fusion of the hydrogen nuclei present in the plasma. However, the confinement time of the tokamak plasma is currently limited by the particles and energy transport. Turbulence plays the most important role in this transport, but the complete understanding of its properties and mechanisms has not been reached. One of the major objectives is to explain the rapid transition between a mode of operation with a short plasma confinement time (L-mode from "low confinement") and a plasma mode with fewer losses of energy (H-mode) where the turbulence is reduced. In order to study the radial and temporal dynamics of this transition with the best possible resolution microwave radar diagnostics are used on most tokamaks.

Plasma microwave reflectometry is based on the dependence of the plasma refractive index on the electron density. Reflectometry was first used for the radiowaves reflected from the ionosphere [1] and now is widely applied for laboratory plasmas as a non-perturbative density diagnostic [2]. A microwave propagates in an inhomogeneous plasma until it reaches the so-called cutoff layer where it gets reflected. As the position of the cutoff depends on the wave frequency, the plasma density can be measured at different magnetic surfaces. By using several frequencies of the probing wave, the electron density profile can be reconstructed. The first frequency modulated continuous-wave (FMCW) reflectometry measurements were performed at CEA on the tokamaks TFR [3] and Petula-B [4]. This type of diagnostic was installed shortly after at many other fusion devices (ASDEX [5], TFTR [6], JET [7], JT60 [8], URAGAN-3M [9]).

In this contribution we discuss a FMCW radar system used to measure density and its fluctuation with the unprecedented time resolution of 1 μs. The capabilities of this ultra-fast reflectometer are presented through an overview of the recent results on the turbulence dynamics. The ongoing work on a synthetic diagnostic which couples the turbulence maps resulted from gyrokinetic simulations with the 2D wave propagation code is covered to complete the paper.

2 Ultra-fast swept reflectometer

The technique of a swept reflectometer is based on the modulation of the probing wave frequency. The wave propagation introduces a time dependent phase shift $\Delta\Phi$ containing the beat frequency F_{beat}:

$$\Delta\Phi = 2\pi F_{\mathrm{beat}} t. \qquad (1)$$

The beat frequency is proportional to the time of flight τ_{flight} of the probing wave of frequency F:

$$F_{\mathrm{beat}} = \tau_{\mathrm{flight}} \frac{dF}{dt} \qquad (2)$$

and therefore defines the position of the cutoff layer. The principle of the heterodyne detection compared to the homodyne scheme is to mix the signal carrying the beat frequency with a low frequency modulation. The Fig. 1 depicts a typical design of a heterodyne reflectometer used for the swept reflectometers developed at CEA. The probing wave with swept frequency (12–20 GHz) is generated by a voltage controlled oscillator (VCO). The signal is separated in two parts: one launched into the plasma (RF) and the other serving as a reference signal (LO). The single side band modulator adds a modulation frequency f_m to the main frequency F. Before launching the probing wave to the plasma through the emitting antenna at the midplane of the tokamak, its frequency is multiplied by n, in the case of V- and W-band equal to 4 and 6 respectively. After the reflection from the cutoff layer, in the case of bistatic system the wave is received by the second antenna. The reference signal (also multiplied by n) compensates the propagation of the probing wave into the wave guides and mixes to the reflected probing signal. At the mixer output the signal (IF) contains only $F_{\mathrm{beat}} + nf_m$ frequency.

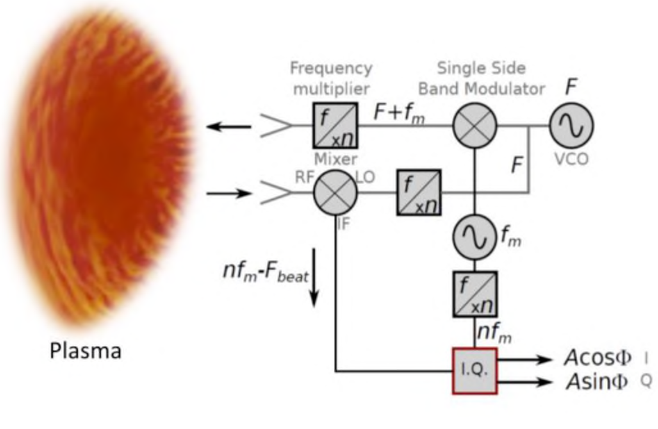

Figure 1 : Ultra-fast swept reflectometer design

The shift of the signal by the carrying frequency ensures the good signal quality [10]. At the end the modulation frequency is removed and an I/Q detector is used to separate the two parts of the signal shifted by π/2. This separation allows to measure independently $A\cos\Phi$ and $A\sin\Phi$, where A is the signal amplitude. The turbulence measurements extracted from the phase fluctuation became possible after improving the signal-to-noise ratio to about 30 dB.

The V- (50–75 GHz) and W-band (75–110 GHz) ultra-fast swept reflectometers (UFSR) are a result of the upgrade of the acquisition system and of the increased modulation frequency [11]. The sweep time decreased to 1 μs ensures to have a frozen density profile including the density fluctuations over the probing time. The X-mode polarisation provides a large radial access from the very edge to the centre of plasma for central densities up to $5 \cdot 10^{19}$ m^{-3} with a spatial resolution of a few millimeters. As for the X-mode the position of the cutoff depend both on the magnetic field and density, the Bottollier-Curtet algorithm [4] is used to determine the positions of cutoff layers step by step, starting from the edge of the plasma.

The phase fluctuation, being induced by density fluctuations, give information about the turbulence level, frequency and wavenumber turbulence spectra. The UFSR time resolution allows to reconstruct the frequency spectra up to 400 kHz and to study fast plasma turbulent events of the order of few microseconds. In the case of low-amplitude turbulence and O-mode polarization, the phase fluctuation wavenumber spectrum is directly proportional to the density fluctuation spectrum [12]. We have extended the concept to the X-mode and introduced a k_r-dependent transfer function which links the phase fluctuation and the density fluctuation. The transfer function needs to be found for each radial position and time using a 1D full-wave propagation simulation [13]. However, it was shown that 2D effects should be introduced [14]. The ongoing work aims to investigate these findings and integrate turbulence maps provided by gyrokinetic calculations to be coupled to 2D full wave code for the analysis of the reflectometer data. This coupling with simulations would provide a better interpretation of the reflectometer data and a tool of validation of the gyrokinetic codes.

3 Turbulence study with reflectometry

Above a threshold of additional heating power, tokamak plasmas have been shown to spontaneously organise into regimes of high confinement (H-mode), with respect to “usual” low confinement modes (L-mode). This transition occurs when turbulence is suppressed due to sheared E × B flows as the radial electric field forms a deep well in the plasma edge region. Dynamic interplay between local gradients, radial shear of the electric field, flow velocity and turbulence has been evidenced during the intermediate phase between L and H-mode, called I-phase [15]. The ultra-fast swept reflectometers have been installed on Tore Supra, ASDEX Upgrade and WEST tokamaks. On ASDEX Upgrade the UFSR has provided the measurements of the fast density and density fluctuation evolution across major parts of tokamak plasma radius. In addition, several channels of Doppler reflectometer have been used for the measurements of the poloidal flow velocity and electric field. Thus, the L-H transitions in a series of plasma discharges in ASDEX Upgrade have been studied with a high temporal resolution. In H-mode the turbulence and the turbulent transport are reduced in the edge region due to the increased radial electric field shear. A phase shift between the turbulence and the radial electric field has been observed in the beginning of the I-phase, indicating that the turbulence grows first and the radial electric field increase follows. After a few limit-cycle oscillations the electric field and the turbulence continue oscillating in phase, while an edge transport barrier develops due to the turbulence reduction. The absence of the phase shift supports the description of the I-phase as type III ELM-like phenomenon [16].

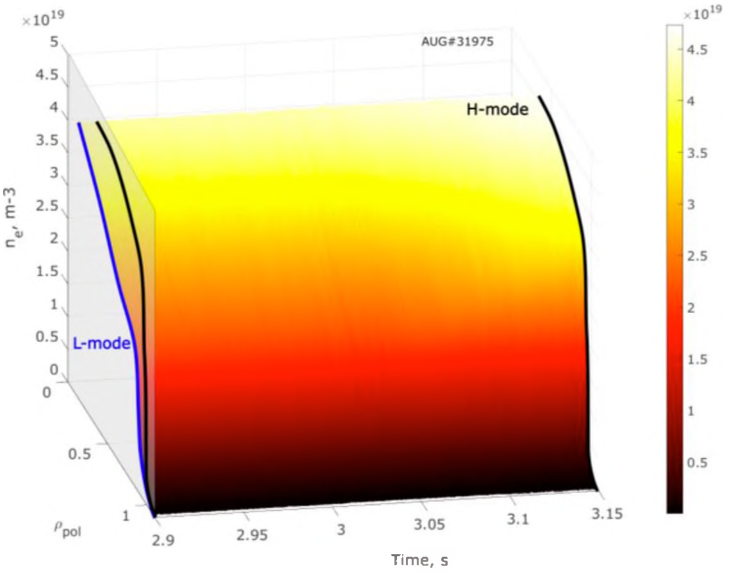

Figure 2 : Electron density evolution during L-H transition

An example of electron density profiles reconstructed from the ultra-fast swept reflectometer data is shown in Fig. 2. The profile builds up inside $\rho_{\mathrm{pol}} = 0.99$ of normalized plasma radius from shallow in the L-mode (2.9 s, blue line in Fig. 2) to steep in the H-mode (after 3.1 s, black line in Fig. 2) due to the better confinement. The precise density profile reconstruction, confirmed through the cross-comparison with other diagnostics, was used for the study of the density gradient during I-phase [16], of the boundary displacements due to ideal kink modes [17] and of the density curvature effect on the plasma intrinsic rotation [18].

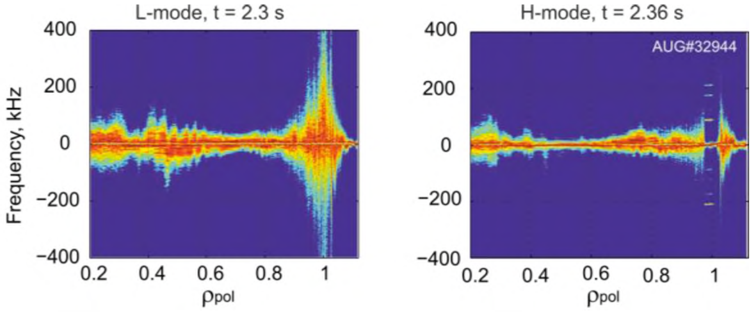

Figure 3 : Turbulence frequency spectra in L- and H-mode

If the density profile is reconstructed, the probing frequency can be expressed as a monotonic function of the radial position $F(R)$. Hence the frequency spectra of turbulence can be interpolated to the radial points of the averaged density profile. Figure 3 depicts the frequency power spectra of the density fluctuation. Two time windows of 12.5 ms each have been chosen to describe the spectra modification in L-mode (left) and H-mode (right). In the pedestal region, $0.95 < \rho_{\mathrm{pol}} < 1$, during the I-phase the fluctuation amplitude decreases and the spectra become narrower compared to the L-mode broadband turbulence due to the radial electric field shear [16]. The frequency spectra reconstruction for different radial positions equally allowed to investigate the LOC-SOC confinement transition in Ohmic plasma [19] and turbulent trapped electron modes [20].

4 Synthetic diagnostic

The ongoing research with the ultra-fast swept reflectometer is focused on the experimental study of the flows and their influence on the turbulent transport in L- and H-mode. The main objective is to interpret reflectometry data using a synthetic diagnostic. The synthetic diagnostic couples the turbulence maps resulted from the gyrokinetic simulations with the 2D full-wave code used for the simulation of the reflectometer signal. The wave propagation 2D code has been developed and commissioned. Optimisation of the numerical calculation led to a factor of hundred improvement of the simulation speed.

The code exploits the Yee discrete scheme of the Finite Domain Time Difference method (FDTD) [21]. The computational grid simulates the propagation of an electromagnetic wave in 2D in X-mode polarisation. Absorbing boundaries were implemented to avoid parasitic reflections. The probing wave emission simulates the realistic antenna radiation pattern of a Gaussian beam. At each time step, the source beam is added to the calculated field forming a so-called soft source. The phase and the amplitude of the reflectometer signal are extracted from the field value in the centre of the source. The comparison between a simulated Gaussian beam and an analytical solution in the vacuum gives a precision of 1%. The code efficiency has therefore been proved in terms of propagation, boundary absorption and cutoff reflection. Work has progressed on the coupling with gyrokinetic simulations. The turbulence maps were constructed from the results of the GYSELA simulations [22]. The interpolation of GYSELA data was implemented into the 2D full-wave code as an input through HDF5 files.

5 Conclusion

Plasma turbulence is one of the most important factors which limit the plasma confinement in a tokamak. In H-mode the improved confinement is reached after an intermediate phase, when an edge transport barrier develops due to the turbulence reduction. The temporal evolution of the density profile, its gradient and the density fluctuation level were studied using the ultra-fast swept reflectometer. The potential of the UFSR as turbulence diagnostic exceeds the results presented in this contribution. Its fast temporal resolution allows to measure density dynamics and density fluctuation characteristics, such as frequency and wavenumber spectra, correlation lengths and time during fast transitions in a plasma discharge.

Acknowledgments

This work has been carried out within the framework of the EUROfusion Consortium and has received funding from the Euratom research and training programme 2014-2018 and 2019-2020 under grant agreement No 633053. The views and opinions expressed herein do not necessarily reflect those of the European Commission. This work also received some support from the French Embassy in London, who funded R. Marcille's 4-months internship at the Culham Science Center in 2017.

Bibliography

[1] K. G. Budden. The propagation of radio waves: the theory of radio waves of low power in the ionosphere and magnetosphere. Cambridge University Press (1988).

[2] E. Mazzucato. Microwave reflectometry for magnetically confined plasmas. Rev. Sci. Instrum. 69.6 (1998), pp. 2201–2217.

[3] F. Simonet. Measurement of electron density profile by microwave reflectometry on tokamaks. Rev. Sci. Instrum. 56.5 (1985), pp. 664–669.

[4] H. Bottollier-Curtet et al. Microwave reflectometry with the extraordinary mode on tokamaks: Determination of the electron density profile of Petula-B. Rev. Sci. Instrum. 58.4 (1987), pp. 539–546.

[5] A. Silva et al. Ultrafast broadband frequency modulation of a continuous wave reflectometry system to measure density profiles on ASDEX Upgrade. Rev. Sci. Instrum. 67.12 (1996), pp. 4138–4145.

[6] G. R. Hanson et al. A swept two-frequency microwave reflectometer for edge density profile measurements on TFTR. Rev. Sci. Instrum. 63.10 (1992), pp. 4658–4660.

[7] A. E. Costley et al. Recent developments in microwave reflectometry at JET. Rev. Sci. Instrum. 61.10 (1990), pp. 2823–2828.

[8] T. Fukuda et al. Broadband reflectometry for the density profile and fluctuation measurements in the JT-60 tokamak. Rev. Sci. Instrum. 61.11 (1990), pp. 3524–3527.

[9] A. Skibenko et al. Measurement of plasma density profile and fluctuations in the URAGAN-3M torsatron using bipolarization reflectometry. Plasma Physics Reports 20.1 (1994).

[10] R. Sabot et al. Single sideband modulator, a key component of Tore-Supra heterodyne reflectometers. Rev. Sci. Instrum. 75.8 (2004), pp. 2656–2659.

[11] F. Clairet et al. Fast sweeping reflectometry upgrade on Tore Supra. Rev. Sci. Instrum. 81.10 (2010), p. 10D903.

[12] C. Fanack et al. Ordinary-mode reflectometry: modification of the scattering and cut-off responses due to the shape of localized density fluctuations. Plas. Phys. and Cont. Fusion 38.11 (1996), p. 1915.

[13] S Heuraux et al. Radial wave number spectrum of density fluctuations deduced from reflectometry phase signals. Rev. Sci. Instrum. 74.3 (2003), pp. 1501–1505.

[14] E. Z. Gusakov et al. 2D modeling of turbulence wave number spectra reconstruction from radial correlation reflectometry data. Plas. Phys. and Cont. Fusion 57.7 (2015), p. 075009.

[15] G. D. Conway et al. Mean and Oscillating Plasma Flows and Turbulence Interactions across the L-H Confinement Transition. Phys. Rev. Lett. 106.6 (2011), p. 065001.

[16] A. Medvedeva et al. Density profile and turbulence evolution during L-H transition studied with the ultra-fast swept reflectometer on ASDEX Upgrade, Plas. Phys. and Cont. Fusion, 59, 12 (2017).

[17] M. Willensdorfer et al. Three dimensional boundary displacement due to stable ideal kink modes excited by external n = 2 magnetic perturbations. Nuclear Fusion, 57, 11 (2017)

[18] W.A. Hornsby et al. Global gyrokinetic simulations of intrinsic rotation in ASDEX Upgrade Ohmic L-mode plasmas, Nuclear Fusion, 58, 5 (2018)

[19] H. Arnichand et al. Identification of trapped electron modes in frequency fluctuation spectra. Plas. Phys. and Cont. Fusion 58.1 (2015), p. 014037.

[20] A. Lebschy et al. Indirect measurement of the poloidal rotation velocity in the core of ASDEX Upgrade plasmas with charge exchange recombination spectroscopy. 42nd EPS proceedings (2015)

[21] F. da Silva et al. Numerical advances in kernels for FDTD Maxwell codes using the Yee algorithm, 11th Int. Reflectometry Workshop 2013, Palaiseau, France

[22] V. Grandgirard et al. A 5D gyrokinetic full-f global semi-Lagrangian code for flux-driven ion turbulence simulations, Computer Physics Communications 207 (2016), p. 35-68.

Antennas, propagation and information

LES STRUCTURES GÉOMÉTRIQUES ÉLÉMENTAIRES DE L'INFORMATION DIGITALE ÉLECTROMAGNÉTIQUE

Caractérisation statistique de la mesure digitale des fluctuations spatio-Doppler et polarimétrique de l'onde électromagnétique radar

***Frédéric Barbaresco**[1]**, Yann Cabanes**[1,2]*
[1]Thales Land & Air Systems, Advanced Radar Concepts, frederic.barbaresco@thalesgroup.com
[2]Institut de Mathématiques de Bordeaux, yann.cabanes@gmail.com

Mots clés : Onde électromagnétique, Radar, Fluctuation Statistique, Géométrie de l'Information, classification non-supervisée, fouillis radar, Electromagnetic wave, Statistical Fluctuations, Information Geometry, unsupervised classification, radar clutter

Résumé/Abstract

Il s'agit de décrire de nouvelles approches géométriques pour définir les statistiques de mesures spatio-temporelles et polarimétrique des états d'une onde électromagnétique, en utilisant les travaux de Maurice Fréchet, Jean-Louis Koszul et Jean-Marie Souriau, avec en particulier la notion d'état « moyen » de cette mesure digitale comme barycentre de Fréchet dans un espace métrique et un modèle issu de la mécanique statistique pour définir et calculer une densité à maximum d'entropie (extension de la notion de gaussienne) pour décrire les fluctuations de l'onde électromagnétique. L'article illustrera ces outils nouveaux avec des exemples d'application en radar pour la mesure Doppler, spatio-temporelle et polarimétrique de l'onde électromagnétique en introduisant une distance sur les matrices de covariance du signal digital électromagnétique, basé sur la métrique de Fisher issue de la Géométrie de l'Information.

1 La mesure digitale de l'onde électromagnétique radar

Au XXième siècle, l'Homme a domestiqué les ondes électromagnétiques qui ont profondément bouleversé ses modes de vies pour communiquer, localiser et observer la Nature et l'Univers. Dans ce contexte, le RADAR a une longue histoire plus que centenaire mais la ***digitalisation récente spatiale et temporelle complète***, de la mesure des ondes électromagnétiques par ***des antennes tout numériques*** ouvre la voie à la manipulation plus efficace de l'Information inscrite dans ce signal aléatoire. Cette digitalisation spatio-temporelle de l'onde électromagnétique a révélé les structures géométriques intimes qui décrivent cette Information. Ces structures révèlent des affinités naturelles avec les outils mathématiques les plus récents comme la géométrie des espaces métriques et la géométrie Symplectique. Nous parcourrons ces avancées récentes du traitement du signal électromagnétique RADAR. Nous soulignerons au fil de l'exposé comment interviennent les intuitions lumineuses et le plus souvent oubliées présentes dans cette filiation des idées de Clairaut, Legendre, Massieu, Poincaré, Cartan, Fréchet, Koszul, Balian et Souriau, pour décrire les outils géométriques développés pour caractériser les fluctuations statistiques de l'onde électromagnétique, et permettant de décrire des densités de probabilités pour ces états aléatoires localement stationnaires de l'onde.

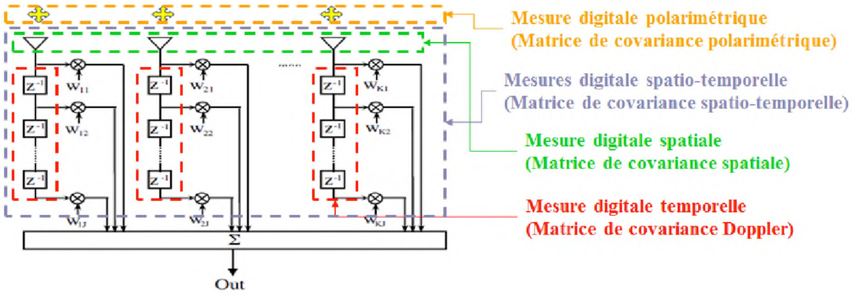

Figure 1 : illustration d'antenne tout numérique :
digitalisation spatiale, temporelle et polarimétrique de la mesure de l'onde électromagnétique

2 Caractérisation statistique de la mesure digitale des fluctuations de l'onde électromagnétique radar

L'idée, qui sera exposé dans l'article, est de « coder » l'état stationnaire d'une mesure digitale de l'onde électromagnétique (Direction, Doppler et Polarimétrie) par un point dans un espace métrique. Comme il s'agit d'une mesure statistique, nous montrerons que la métrique la plus « naturelle » est donnée en Géométrie de l'Information par la métrique de Fisher du processus stationnaire.

L'extension des statistiques dans les espaces métriques a été introduite par Maurice Fréchet à travers la notion « d'espace distancié ». L'approche par les espaces métriques permet de définir la moyenne ou la médiane d'éléments dans un espace distancié par le barycentre géodésique de Fréchet calculé par le flot de gradient introduit dans les années 70 par Hermann Karcher. Pour définir ces espaces distanciés pour une onde électromagnétique, il nous faut au préalable introduire une distance entre des mesures digitales des états de l'onde. La métrique de Fisher de la « Géométrie de l'Information » fournit une distance naturelle, disposant des qualités d'invariances souhaitées (invariance par reparamétrisation, invariance liée aux symétries du signal électromagnétique). La métrique de Fisher peut être généralisée dans les espaces décrivant les états de l'onde électromagnétique à partir des structures géométriques introduites par Jean-Louis Koszul (fonction caractéristique de Koszul-Vinberg, 2-forme de Koszul). L'étape suivante consiste à généraliser la notion de densité gaussienne pour les états de l'onde électromagnétiques, en généralisant la notion de densités à maximum d'entropie (densité de Gibbs), ce qui nous oblige à généraliser la définition de l'entropie. Partant des fonctions caractéristiques de François Massieu (introduite en thermodynamiques par François Massieu), cette généralisation a été établie par Jean-Marie Souriau en Mécanique Statistique dans le cadre de la Mécanique Géométrique, avec un modèle qui a été appelé « thermodynamique des groupes de Lie », dont on déduit une densité (de Gibbs) de probabilités et une métrique de Fisher-Souriau pour décrire l'état moyen (barycentre de Fréchet) des fluctuations spatio-Doppler et polarimétrique des mesures digitales de l'onde électromagnétique.

Dans le cas d'un signal stationnaire, en utilisant, les structures Toeplitz (respectivement Blocs-Toeplitz) des matrices de covariance du signal temporel [Doppler] ou spatial [direction] (respectivement spatio-temporelle), on démontre que la métrique naturelle est Kählérienne dans l'espace produit du polydisque de Poincaré (codage de information Doppler) et du polydisque de Siegel (codage de l'information spatio-temporelle).

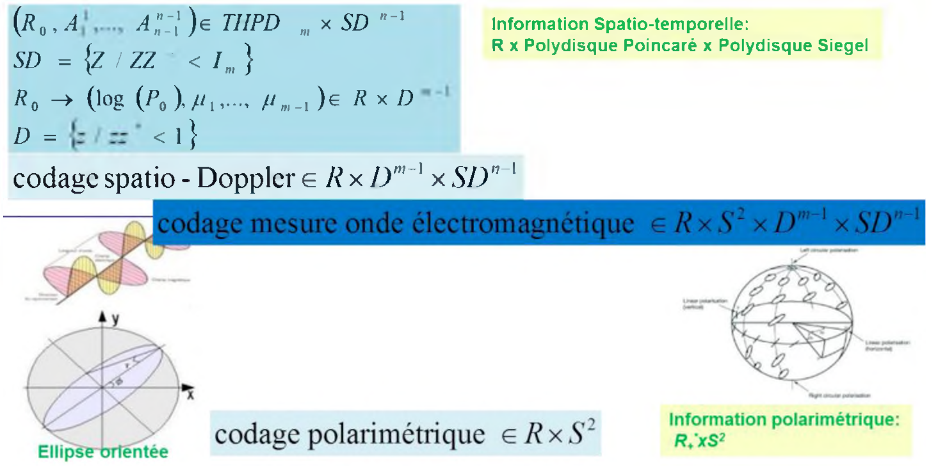

Figure 2 : Codage de la mesure spatio-Doppler et polarimétrique dans l'espace métrique $\Re \times S^2 \times D^{m-1} \times SD^{n-1}$

Dans le cas d'un signal localement stationnaire, on caractérise le signal spatio-temporel électromagnétique par un modèle autorégressif matriciel (extension matricielle du théorème de Trench-Verblunsky), basé sur la théorie MOPUC (Matrix Orthogonal Polynomial on the Unit Circle). A partir de la mesure digitale spatio-temporelle de l'onde électromagnétique, on estime une série de N matrices de covariance THDP (Toeplitz Hermitienne Définie Positive) $\{R_0, \ldots R_{N-1}\}$. Cette série temporelle est ensuite paramétrée par un modèle autorégressif matriciel $\left(R_0, \{A_k^k\}_{k=1}^{N-1}\right) \in THPD \times SD^{N-1}$ avec $R_0 \in THPD_n$ une matrice THDP, et $A_k^k \in SD$, $k = 1, \ldots, N-1$ les coefficients de réflexion/Verblunsky matriciels dans le disque de Siegel unité SD, tel que $A_k^k \left(A_k^k\right)^+ < I$ (où + signifie trans-conjugué et I la matrice identité). La matrice R_0 peut elle-même être décrite par un modèle autorégressif classique complexe, de paramètres $\left(P_0, \{\mu_k\}_{k=1}^{m-1}\right) \in \Re^{+*} \times D^{m-1}$ avec P_0 le terme de puissance, dont on prend classiquement le logarithme $\log(P_0) \in \Re$ et $\mu_k \in D, k = 1, \ldots, m-1$ les coefficients de réflexion/Verblunsky dans le disque unité de Poincaré D, tel que $\mu_k \mu_k^* = |\mu_k|^2 < 1$. On a ainsi pour une onde électromagnétique localement stationnaire, un codage de l'information dans un espace métrique $\left(\log(P_0), \{\mu_k\}_{k=1}^{m-1}, \{A_k^k\}_{k=1}^{N-1}\right) \in \Re \times D^{m-1} \times SD^{n-1}$, à laquelle on peut rajouter $\mathbb{S}^2$: la sphère de Poincaré pour l'information polarimétrique. Le signal étant finalement codé sur l'espace produit $\mathbb{R} \times \mathbb{S}^2 \times D^{m-1} \times SD^{n-1}$.

La théorie de la « Géométrie de l'Information » introduite par Rao et Fréchet permet de définir une métrique naturelle entre densité de probabilité dans l'espace des paramètres et qui est invariante par à rapport à un changement de paramétrisation. En particulier, on peut définir la métrique par le hessien de l'Entropie. En considérant le processus stationnaire décrivant l'état spatio-temporel de l'onde électromagnétique par la matrice de covariance du vecteur spatio-temporel et sa matrice de covariance associée Toeplitz-Blocs-Toeplitz :

$R_{N,p} = \begin{bmatrix} R_0 & R_1 & \cdots & R_{N-1} \\ R_1^+ & R_0 & \ddots & \vdots \\ \vdots & \ddots & \ddots & R_1 \\ R_{N-1}^+ & \cdots & R_1^+ & R_0 \end{bmatrix}$, l'entropie est donnée par $S(R_{p,N}) = \tilde{\Phi}(R_{p,N}) = -\log(\det R_{p,N}) + cste$, qui avec les paramètres autorégressifs matriciels s'écrit: $S(\overline{R}_{p,N}) = -\sum_{k=1}^{N-1} (N-k).\log\det\left[1 - \overline{A}_k^k \overline{A}_k^{k+}\right] - N.\log\left[\pi.e.\det \overline{R}_0\right]$

où $\overline{X}$ représente l'estimation de X. En considérant, la paramétrisation $\theta^{(N-1)} = \begin{bmatrix} \overline{R}_0 & \overline{A}_1^1 & \cdots & \overline{A}_{N-1}^{N-1} \end{bmatrix}^T$, la métrique est alors donnée par le hessien de l'Entropie ce qui donne :

$$ds^2 = d\theta^{(N-1)+} \left[\frac{\partial^2 S}{\partial \theta_i^{(N-1)} \partial \theta_j^{(N-1)}} \right]_{i,j} d\theta^{(N-1)} = N.Tr\left[\left(\overline{R}_0^{-1} d\overline{R}_0 \right)^2 \right] + \sum_{k=1}^{N-1} (N-k) Tr\left[\left(I_n - \overline{A}_k^k \overline{A}_k^{k+} \right)^{-1} d\overline{A}_k^k \left(I_n - \overline{A}_k^{k+} \overline{A}_k^k \right)^{-1} d\overline{A}_k^{k+} \right]$$

On peut intégrer cette métrique pour définir une distance en paramétrisation $\left\{ \overline{R}_0, \overline{A}_1^1, \ldots, \overline{A}_{N-1}^{N-1} \right\}$ permettant de déterminer une distance entre 2 matrices de covariance spatio-temporelle de l'onde électromagnétique $R_{(1)}$ et $R_{(2)}$:

$$\begin{cases} d^2\left(R_{(1)}, R_{(2)}\right) = N.\left\| \log\left(\overline{R}_{(1),0}^{-1/2} \overline{R}_{(2),0} \overline{R}_{(1),0}^{-1/2} \right) \right\|_F^2 + \sum_{k=1}^{N-1} (N-k) \log^2 \left(\dfrac{1 + \left\| \Phi_{A_{(1),k}^k} \left(\overline{A}_{(2),k}^k \right) \right\|}{1 - \left\| \Phi_{A_{(1),k}^k} \left(\overline{A}_{(2),k}^k \right) \right\|} \right) \\ \Phi_Z(W) = \left(I - ZZ^+ \right)^{-1/2} (W - Z) \left(I - Z^+ W \right)^{-1} \left(I - Z^+ Z \right)^{1/2} \end{cases}$$

Dans l'article final, on décrira le modèle de Souriau pour définir une densité à Maximum d'Entropie pour les mesures d'états spatio-temporel de l'onde éléctromagnétique radar, qui est covariante sous l'action du groupe de Lie qui agit de façon homogène dans l'espace de représentation de l'onde électromagnétique.

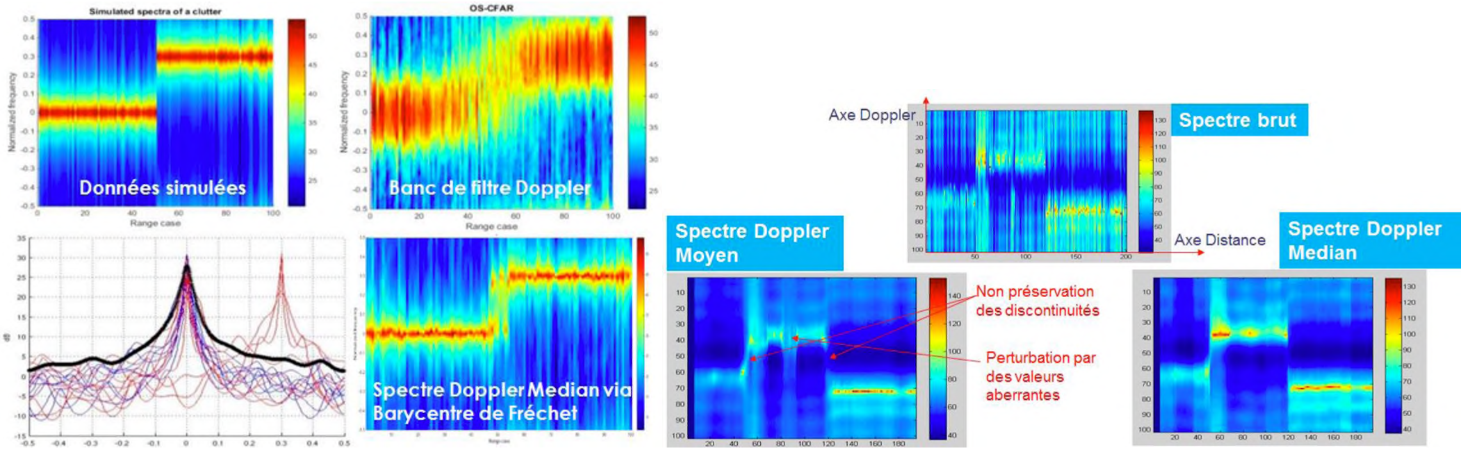

Figure 3 : Exemple de calcul de spectre Doppler ***médian*** *(défini comme barycentre géodésique de Fréchet via la métrique de Fisher) pour les matrices de covariance temporelle du signal Doppler de l'onde électromagnétique (on remarque la propriété de robustesse du « médian » à des valeurs parasites suivants l'axe distance)*

3 Application de l'analyse Doppler dans les espaces métriques à la classification non-supervisée du fouillis radar

3.1 Des données radar aux matrices complexes

Pour simplifier notre étude, les données d'entrée seront prises sur une seule rafale pour le faisceau d'élévation nulle. Le radar nous fournit donc une matrice complexe U de taille : (#impulsions) × (#cases distance).

Le nombre d'impulsion d'une rafale varie pour nos données entre 8 et 20 ; le nombre de cases distance varie également, il est de l'ordre de 1000. Une case distance mesure environ 60 mètres de longueur.

Le coefficient complexe $U_{i,j}$ représente l'amplitude et la phase après compression d'impulsion de l'écho revenant de la case distance i après l'impulsion j.

Les données que nous allons classifier sont les cases distance, chaque case distance étant représentée par une colonne de la matrice U.

3.2 Hypothèses de modélisation

Nous nous concentrons à présent sur une case distance, dont nous analysons le signal comme étant une série temporelle indexée par le numéro de l'impulsion.

Nous supposons que le signal est stationnaire dans la rafale et de moyenne nulle.

Nous supposons également que le signal peut être modélisé par un processus autorégressif Gaussien.

3.3 Espace métrique de représentation des données

Nous cherchons à classifier les cases distance en associant à chacune d'entre elle la matrice d'autocorrélation de la série temporelle associée, puis en classifiant les matrices d'autocorrélation.

Cela nous amène à construire un nouvel espace métrique dans lequel les matrices d'autocorrélation « proches » seront regroupées dans un même cluster.

Chaque matrice d'autocorrélation peut être représentée façon équivalente par des coefficients dans l'espace $\mathbb{R}_+^* \times D^{n-1}$, où D est le disque unité complexe et n est le nombre d'impulsions.

Ces coefficients sont les coefficients d'un modèle autorégressif temporel ; ils sont calculés en utilisant l'algorithme de Burg régularisé.

Nous munissons cet espace d'une métrique naturelle issue de la géométrie de l'information.

3.4 Classification

3.4.1 *Simulation de données*

Pour pouvoir tester la performance des algorithmes de classification mis au point, il faut disposer de plusieurs jeux de données, chaque jeu étant homogène (réalisation de variables aléatoires iid). L'homogénéité est quelque chose de difficilement contrôlable concernant les données de terrain. Pour pallier à cette difficulté, nous avons mis au point un algorithme de simulation de données radar, en utilisant un modèle SIRV (Spherically Invariant Random Vectors). Ce modèle est paramétrique. Les paramètres utilisés pour simuler des données dépendent du type de fouillis que l'on souhaite simuler.

Pour tester les algorithmes de classification, nous simulons donc deux groupes de données, un premier groupe avec un paramètre P1, puis un second avec un paramètre P2. Un bon algorithme de classification regroupera dans un même cluster les données issues de P1, et dans un autre cluster les données issues de P2.

3.4.2 *Classification par l'agorithme des k-means*

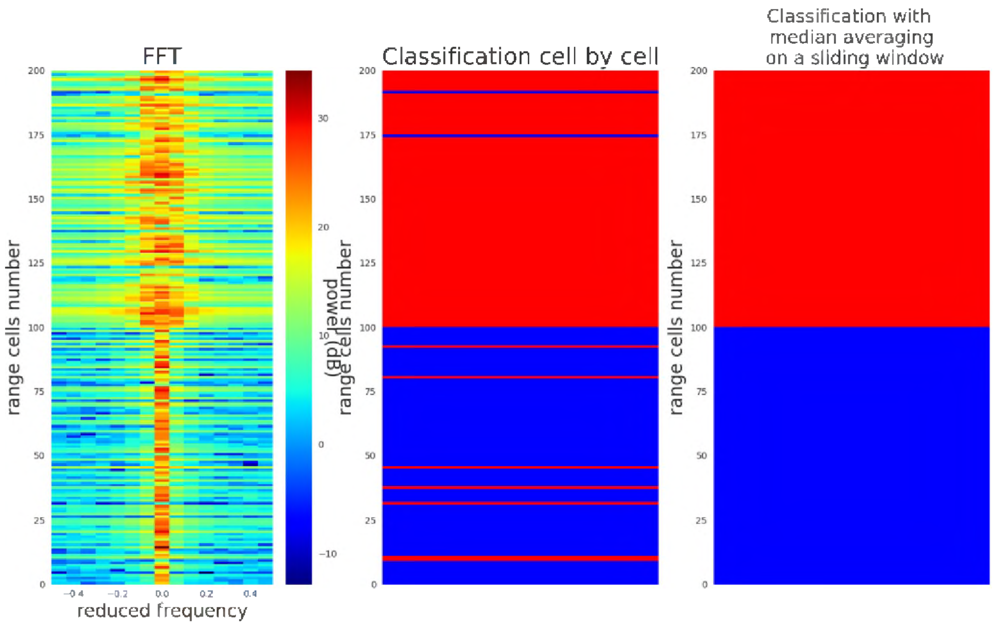

Figure 4 : Résultats de classification par l'algorithme de k-moyenne (k-means)

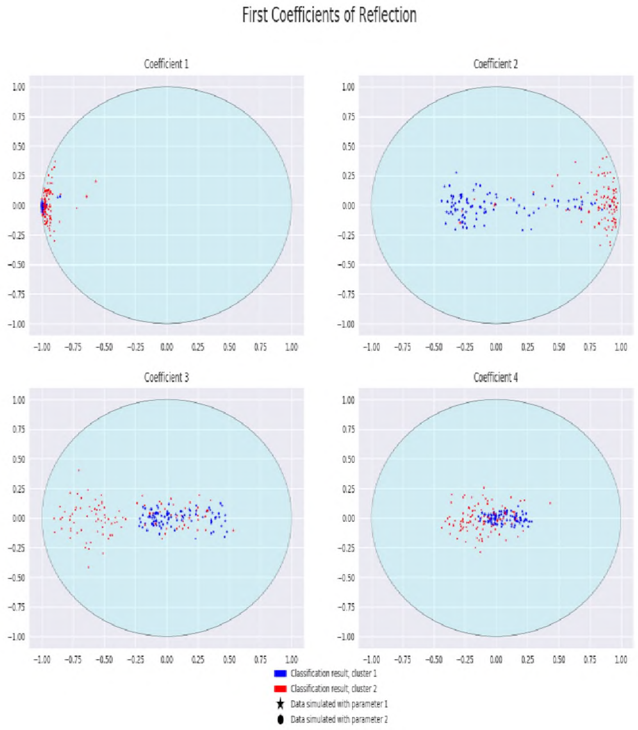

Figure 5 : résultats de classification sur les 4 premiers coefficients de réflexion dans le disque unité complexe de Poincaré (les points des 2 classes en bleau et en rouge)

Nous fixons le nombre de clusters k souhaités au début de l'algorithme. Nous initialisons l'algorithme en choisissant k points de façon aléatoire parmi l'ensemble des points à classifié. Ils représentent maintenant des barycentres de classes.

A chaque itération de l'algorithme :

- Associer à chaque point au cluster dont le barycentre est le plus proche. Pour cette étape, il faut disposer d'une distance explicite sur notre espace.

- Calculer le nouveau barycentre du cluster. Pour cette étape, il faut pouvoir approximer la position du barycentre d'un nuage de points, celui-ci étant défini comme le point X qui minimise la somme des distances au carré entre X et les points du nuage. Ce calcul n'est pas évident dans les espaces métriques non-euclidiens.

3.4.3 *Méthode de visualisation de la performance des algorithmes de classification*

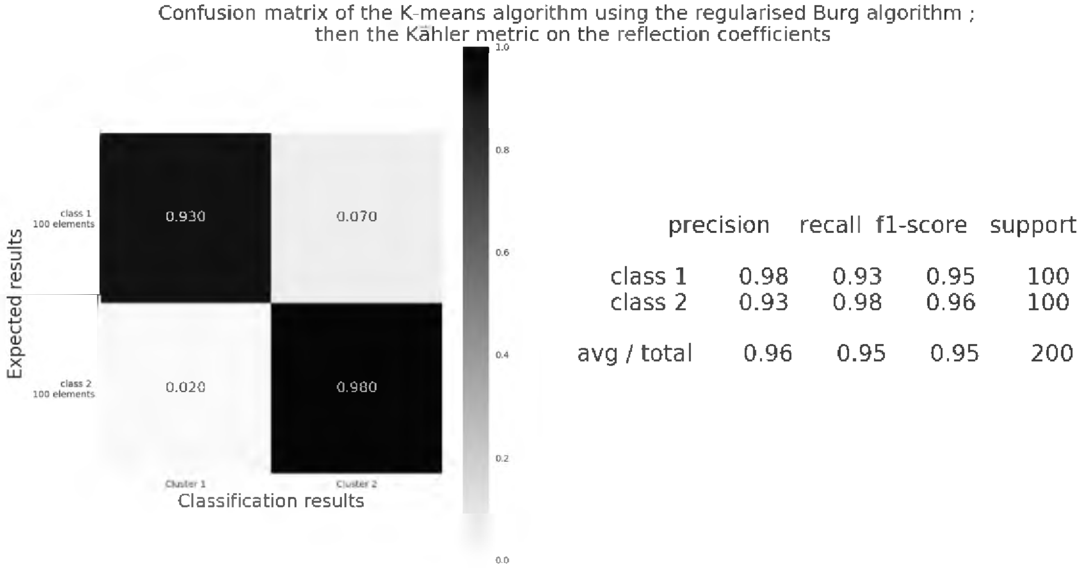

```
             precision    recall  f1-score   support

    class 1       0.98      0.93      0.95       100
    class 2       0.93      0.98      0.96       100

avg / total       0.96      0.95      0.95       200
```

Pour visualiser et pouvoir comparer la performance des algorithmes de classification non-supervisée, nous avons emprunté les méthodes usuelles de visualisation des algorithmes de classification supervisés : la matrice de confusion pour la visualisation et le f1-score (calculé à partir de la précision et du recall) pour le score. Puisque notre classification non supervisée ne donne pas de labels comme « paramètre de simulation P1 » ou « paramètre de simulation P2 » à nos clusters, nous testons toutes les permutions possibles pour trouver quel cluster correspond à quel jeu de données simulées en utilisant le paramètre Pi. Le score de la classification correspond au score de la meilleure permutation.

Références bibliographiques

[1] Fréchet,M.: Sur l'extension de certaines évaluations statistiques au cas de petits échantillons. Rev. l'Institut Int. Stat. 11(3/4), 182–205, 1943

[2] Rao, C.R.: Information and the accuracy attainable in the estimation of statistical parameters. Bull. Calcutta Math. Soc. 37, 81–89, 1945

[3] Balian, R.,The entropy-based quantum metric. Entropy 16, 3878–3888 (2014)

[4] Barbaresco, F., Le radar digital ou les structures géométriques élémentaires de l'information électromagnétique, exposé invité IHES (Institut des Hautes Etudes Scientifiques), 9 Mars 2017, vidéo : https://www.youtube.com/watch?v=cObbj06JlKE ; page IHES : https://www.ihes.fr/en/a-general-audience-conference-at-ihes-on-march-9th/

[5] Barbaresco, F., Symplectic and Poly-Symplectic Model of Souriau Lie-Groups Thermodynamics : Souriau-Fisher Metric & Geometric Structure of Information, TGS'17 "Topological & Geometrical Structure of Information", CIRM Luminy (Centre International de Recherche Mathématique), Aout 2017, vidéo : https://www.youtube.com/watch?v=VXxiMCn-tsE&feature=youtu.be

[6] Barbaresco F., Radar Micro-Doppler Signal Encoding in Siegel Unit Poly-Disk for Machine Learning in Fisher Metric Space, International Radar Symposium, Bonn, June 2018

[7] Barbaresco, F. Higher Order Geometric Theory of Information and Heat Based on Poly-Symplectic Geometry of Souriau Lie Groups Thermodynamics and Their Contextures: The Bedrock for Lie Group Machine Learning. Entropy 2018, 20, 840.

[8] Barbaresco, F. Jean-Louis Koszul and the elementary structures of Information Geometry. In Geometric Structures of Information; Nielsen, F., Ed.; Springer: Berlin, Germany, 2018.

[9] Chevallier, E.; Barbaresco, F.; Angulo, J. Probability density estimation on the hyperbolic space applied to radar processing. GSI'15; Springer, 2015; pp. 753–761.

[10] Decurninge, A.; Barbaresco, F. Robust Burg Estimation of Radar Scatter Matrix for Mixtures of Gaussian Stationary Autoregressive Vectors, IET Radar, Sonar & Navigation, Volume 11, Issue 1, January 2017, p. 78 – 89, 2016

[11] Chevallier, E.; Forget, T.; Barbaresco, F.; Angulo, J. Kernel Density Estimation on the Siegel Space with an Application to Radar Processing. Entropy 2016, 18, 396.

[12] Barbaresco, F. Information Geometry of Covariance Matrix: Cartan-Siegel Homogeneous Bounded Domains, Mostow/Berger Fibration and Fréchet Median. In Matrix Information Geometry; Bhatia, R., Nielsen, F., Eds.; Springer, 2012; pp. 199–256.

[13] Yann Cabanes, Frédéric Barbaresco, Marc Arnaudon, Jérémie Bigot, Non-supervised Machine Learning Algorithms for Radar Clutter High-Resolution Doppler Segmentation and Pathological Clutter Analysis, International Radar Symposium 2019

JS 19
APPROCHER LES DEUX INFINIS PAR
LES ONDES ELECTROMAGNETIQUES

Les ondes térahertz pour l'exploration de la matière à toutes les échelles
Terahertz waves for the exploration of matter at all scales

***Sophie Eliet*[1], *Gael Mouret*[2], *Olivier Pirali*[3], *Jean-François Lampin*[1]**

[1]*Institut d'Electronique de Microélectronique et de Nanotechnologie, UMR8520 CNRS, Université de Lille, Villeneuve d'Ascq, jean-francois.lamin@univ-lille.fr*
[2]*Laboratoire de Physico-Chimie de l'Atmosphère, Université du Littoral Côte d'Opale, EA4493 CNRS, Dunkerque*
[3]*Institut des Sciences Moléculaires d'Orsay, UMR8214 CNRS, Université Paris-Sud, Orsay*

Ondes Térahertz ; imagerie en champ proche ; spectroscopie ; radioastronomie
Terahertz waves ; near-field imagery ; spectroscopy ; radioastronomy

Abstract

The terahertz (THz) waves are electromagnetic waves whose frequency is located between the microwaves on the one hand and the infra-red on the other hand. The wavelengths are of the order of a fraction of a millimeter. In this range the interactions between matter and electromagnetic waves are very intense and we will see how they can be used to understand this matter at very small scales via near-field optical microscopy (scanning near-field optical microscopy or SNOM) and to understand also the universe at the largest scales via the THz (radio)astronomy.

Résumé

Les ondes térahertz (THz) sont des ondes électromagnétiques dont la fréquence est située entre les hyperfréquences d'une part et les infra-rouges d'autre part. Les longueurs d'onde sont de l'ordre d'une fraction de millimètre. Dans cette gamme les interactions entre matière et ondes électromagnétiques sont très intenses et nous verrons comment elles peuvent servir à comprendre cette matière aux très petites échelles via l'imagerie en champ proche (scanning near-field optical microscopy ou SNOM) et à comprendre aussi l'univers aux échelles les plus grandes via la (radio)astronomie THz.

Nanoantennes infrarouge et dispositifs nanophotoniques
Infrared nanoantenna and nanophotonics devices

Patrick Bouchon[1]***, Alice Fabas***[1]***, Baptiste Fix***[1]***, Hasnaa El Ouazzani***[1]***, Eslam El Shamy***[1]***, Julien Jaeck***[1]***, Mathilde Makhsiyan***[1]***, Arthur Salmon***[1]***, Léna Soun***[1]***, and Riad Haïdar***[1]

[1]*DOTA, ONERA, Université Paris-Saclay, F-91123 Palaiseau, France*

Mots-clefs: nanoantennes, absorption infrarouge, émission thermique, dispositifs nanophotoniques
Keywords: nanoantenna, infrared absorption, thermal emission, nanophotonics devices

---

Résumé:
La structuration de la matière à une échelle sub-longueur d'onde permet la conception de nanoantennes qui vont être capables de modifier la réponse optique (réflectivité, absorption) d'une surface avec une texturation d'une épaisseur inférieure au centième de la longueur d'onde. Ces nano-antennes peuvent aussi exalter les interactions lumière-matière dans leur voisinage champ proche. Une structure composée d'un empilement métal-isolant-métal va être le siège de résonances de type Fabry-Perot, de modes guidés ou de Helmholtz optique. Elles peuvent être mises à profit pour sculpter la réponse spectrale d'une surface en absorption et en émission infrarouge, avec une modulation spatiale de l'ordre de la longueur d'onde. Ces effets peuvent être utilisés dans des dispositifs de sources infrarouges, de convertisseurs thermiques ou non linéaires de longueurs d'onde ou bien pour exalter la signature infrarouge de molécules.

Abstract: The patterning of matter at a sub-wavelength scale allows the design of nanoantennas that will be able to modify the optical response (reflectivity, absorption) of a surface with a texturing thickness of less than one hundredth of the wavelength. These nano-antennas can also enhance light-matter interactions in their near-field neighbourhood. A structure composed of a metal-insulator-metal stack will be the seat of Fabry-Perot, guided modes or optical Helmholtz resonances. They can be used to shape the spectral response of a surface in absorption and infrared emission, with a spatial modulation at the wavelength scale. These effects can be used in various devices such as infrared sources, thermal or non-linear wavelength converters or to enhance the infrared signature of molecules.

1 Introduction

Les nanoantennes sont des structures sub-longueur d'onde capables de manipuler la lumière, soit en modifiant la réponse optique, soit en exaltant des interactions lumière-matière comme les effets non linéaires ou l'absorption infrarouge de molécules. Après avoir dressé un panorama des résonances présentes dans les structures de type métal-isolant-métal (MIM), et des couplages pouvant exister entre nanostructures voisines, je présenterai divers dispositifs nanophotoniques utilisant ces nanoantennes.

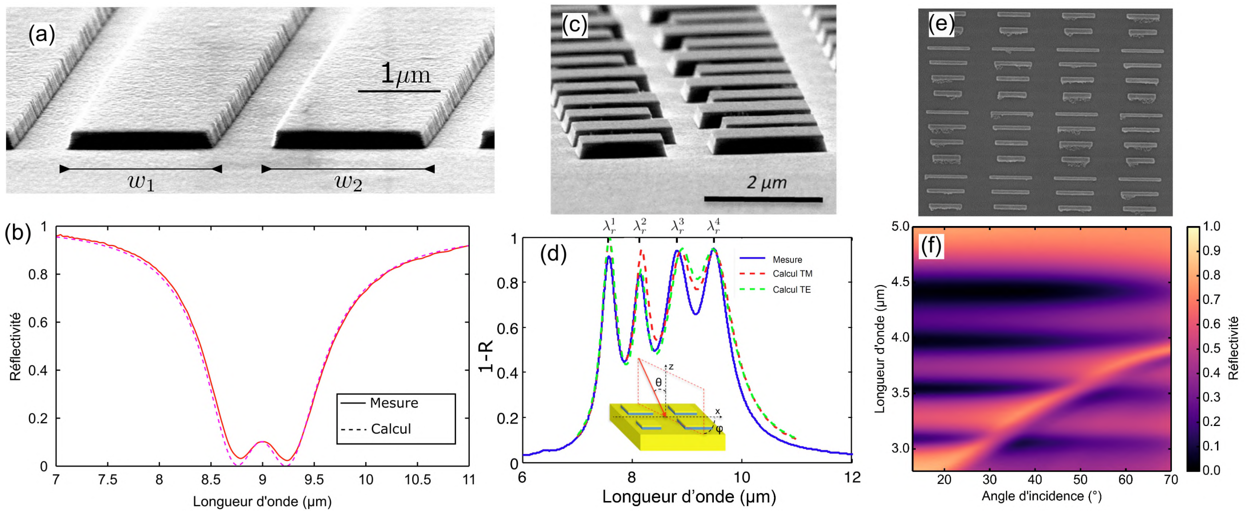

FIGURE *1* *Images MEB des structures (a) biMIM, (c) 4-MIM non polarisée et (e) 4 MIM polarisée. (b) Courbes de réflectivité expérimentale de la structure biMIM en polarisation TM avec un angle d'incidence de* 13° *mesurée (ligne pleine) et calculée (ligne pointillée). (d) Courbes de réflectivité expérimentale de la structure 4 MIM plots avec un angle d'incidence de* 13° *mesurée (ligne pleine) et calculée en polarisation TM et TE (lignes pointillées). (f) Diagramme de réflectivité expérimental de la structure à 4 MIM bâtonnets.*

2 Les nanoantennes

Les nanoantennes MIM sont composés d'une couche métallique continue, d'une couche diélectrique et d'une nanostructure métallique, qui va permettre la création d'une cavité optique dans lequel un mode gap-plasmon va résonner à une longueur d'onde déterminée par les dimensions latérales de la nanostructuration [1]. Cette résonance, équivalente à celle d'un résonateur de Fabry-Perot, donne lieu à une absorption quasi-totale de la lumière qui est indépendante de l'angle d'incidence. La nanoantenne a une section efficace d'absorption beaucoup plus grande que sa section géométrique.

Ces nanoantennes peuvent être combinées dans une même période sub-longueur d'onde, soit de manière indépendante, soit en étant couplées, créant un résonateur équivalent à une cavité Fabry-Perot à 3 miroirs [2]. Lorsqu'elles sont combinées de manière indépendantes, il est possible d'élargir la bande spectrale d'absorption comme montré sur la Figure 1 [3]. Paradoxalement, lorsqu'elles sont couplées, elles donnent naissance à une résonance présentant un facteur de qualité jusqu'à dix fois plus élevé.

Par ailleurs, ces résonateurs peuvent aussi être le siège de résonances de type Helmholtz optique, dont la principale caractéristique est une exaltation du champ électrique dans le volume chaud contenu entre deux nanostructurations [4]. Elles peuvent aussi être le siège de résonances de type modes guidés [5]. Toutes ces résonances peuvent être mises à profit pour sculpter la réponse spectrale d'une surface en absorption et en émission infrarouge, avec une possible modulation spatiale sur l'échelle d'une longueur d'onde.

3 Dispositifs nanophotoniques

Une application directe de ces résonateurs est leur utilisation comme sources infrarouge [6]. En effet, la loi de Kirchhoff stipule qu'une surface absorbante sera également émettrice avec les mêmes caractéristiques spectrales. On peut ainsi juxtaposer des sources infrarouge de caractéristiques spectrales différentes, et possiblement polarisées. Par ailleurs, en plaçant des antennes absorbantes à une longueur d'onde sur une face d'un substrat, et d'autres jouant le rôle d'émetteur thermique sur la face opposée, on conçoit un convertisseur de longueurs d'onde fonctionnant par transduction thermique. Ce composant peut être utilisé avec une caméra infrarouge pour réaliser un instrument d'imagerie capable de cibler les fréquences térahertz et millimétriques.

Enfin, ces nanoantennes concentrent le champ électrique dans leurs voisinages, menant à des exaltation de plusieurs ordres de grandeurs de l'intensité du champ. Cette propriété peut être utilisée pour exalter les signatures infrarouge d'absorption de molécules placée à proximité des nanoantennes pour des applications de capteurs optiques de molécules. Elle peut aussi être utilisée dans des scenarii de conversion non linéaire de fréquences. Dans ces applications, on tire également parti de la capacité de ces nanoantennes à présenter plusieurs résonances dont les exaltations sont colocalisées.

4 Références

[1] C. Koechlin, P. Bouchon, F. Pardo, J.-L. Pelouard, and R. Haïdar, "Analytical description of subwavelength plasmonic mim resonators and of their combination," *Optics Express*, vol. 21, no. 6, pp. 7025–7032, 2013.

[2] B. Fix, J. Jaeck, P. Bouchon, S. Héron, B. Vest, and R. Haïdar, "High-quality-factor double fabry–perot plasmonic nanoresonator," *Optics Letters*, vol. 42, no. 24, pp. 5062–5065, 2017.

[3] P. Bouchon, C. Koechlin, F. Pardo, R. Haïdar, and J. Pelouard, "Wideband omnidirectional infrared absorber with a patchwork of plasmonic nanoantennas," *Optics Letters*, vol. 37, no. 6, pp. 1038–1040, 2012.

[4] P. Chevalier, P. Bouchon, R. Haïdar, and F. Pardo, "Optical helmholtz resonators," *Applied Physics Letters*, vol. 105, no. 7, p. 071110, 2014.

[5] E. Sakat, G. Vincent, P. Ghenuche, N. Bardou, S. Collin, F. Pardo, J. Pelouard, and R. Haïdar, "Guided mode resonance in subwavelength metallodielectric free-standing grating for bandpass filtering," *Optics Letters*, vol. 36, no. 16, pp. 3054–3056, 2011.

[6] M. Makhsiyan, P. Bouchon, J. Jaeck, J.-L. Pelouard, and R. Haïdar, "Shaping the spatial and spectral emissivity at the diffraction limit," *Applied Physics Letters*, vol. 107, no. 25, p. 251103, 2015.

Antennas, propagation and information (Posters)

JS 19
APPROCHER LES DEUX INFINIS PAR LES ONDES ELECTROMAGNETIQUES

Interféromètre de mesure de phase atmosphérique pour l'observatoire NOEMA
Atmospheric Phase Monitoring Interferometer for the NOEMA Observatory

S. Mahieu[1], B. Pissard[1], M. Bremer[1], C. Risacher[1], R. Blundell[2], R. Kimberk[2], J. Test[2]

[1] Institut de Radio Astronomie Millimétrique, IRAM, 300 rue de la piscine, 38400 Saint Martin d'Hères, France.
[2] Harvard-Smithsonian Center for Astrophysics, 60 Garden Street, Cambridge, MA 02138, USA.

Interféromètre, phase atmosphérique, NOEMA.
Interferometer, Atmospheric phase, NOEMA.

Résumé/Abstract

L'IRAM adapte, en collaboration avec le Smithsonian Astrophysical Observatory (SAO), un système de contrôle de la phase atmosphérique, comme développé pour l'observatoire submillimétrique SMA, qui sera potentiellement utilisé à l'observatoire NOEMA (NOrthern Extended Millimeter Array).

IRAM is currently adapting, in collaboration with the Smithsonian Astrophysical Observatory (SAO), an atmospheric phase monitoring system as was developed for the Submillimeter Array (SMA) to be possibly used for the NOEMA (NOrthern Extended Millimeter Array) interferometer.

1 Introduction

In this paper, we present the proof-of-concept of an atmospheric phase monitoring system and show the first results obtained so far.

Millimeter wave astronomical interferometers combine signals received from cosmic radio sources that reach multiple antennas (soon twelve 15 meters antennas for the NOEMA case) to produce maps of the sky. Direction of the source and geometry of the array of antennas allows the signals to be combined with a predictable phase. Trouble is that signal propagation can be altered by atmospheric turbulences. Indeed, in the troposphere, water vapor plays a particularly important role in radio signals propagation, its refractivity being about 20 times greater in the radio range than in the near-infrared or optical regimes. The phase fluctuations in radio interferometers at millimeter and centimeter wavelengths are predominantly caused by fluctuations in the distribution of water vapor. Therefore, implementing such a phase monitor interferometer would provide us with a permanent monitoring system of the observing conditions for the NOEMA interferometer, located on the plateau de Bure, at 2550m above sea level in the French Alps. This system would make observations more efficient, by being able to choose the correct observing band right away and/or anticipate on whether to start or stop observing.

2 System description.

The atmospheric phase monitoring system demonstrator is based on a dual off- axis aluminium satellite dishes (Fuba DDA 110: 1090 x 991 mm^2) interferometer, that receive a broadband white noise-like Ku Band signal from a geostationary satellite and focus it to the center of the feed signal source. (see Figure 1)

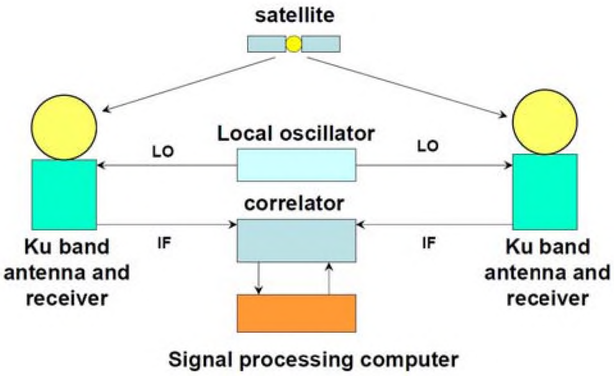

Figure 1: Phase Monitoring System Principle

The Low Noise Blocks (LNB) that down convert this signal to the Intermediate Frequency (IF) one (~1.2 GHz) are commercial satellite system receivers that have been modified to be fed with a common Local Oscillator (LO) signal through a SMA connector that integrates a spring loaded contact, once the original Dielectric Resonator Oscillator (DRO) is removed (see Figure 2).

Figure 2: Technomate Low Noise Block downconverter. Left: LO injection on the body, middle: LO circuit with Dielectric Resonator Oscillator, Right: SMA connector that integrates a spring loaded contact for LO signal injection.

The IF signals are then amplified, filtered and transported through optical fibres down to the rack that is located in the building where they are processed by a commercial analog correlator (IQ demodulation card) that produces the phase delays between pairs (only one so far) of antennas from the I & Q signals.

The data are then sampled at 10Hz and further processed by a LINUX pc that runs software which tracks the Walsh cycle and applies sign changes to remove offsets in Q and I signals. It determines the phase angle from arctan Q/I and calculates a least squares sine fit to the unwrapped phase, subtracts that from the unwrapped phase and then calculates the rms values from the residuals.

The Figure 3 below shows the schematic of the overall phase monitoring system, with two antennas.
This real-time statistical data measured in the direction of the satellite provides an estimate of the phase front distortion experienced at the same time by the NOEMA interferometer.

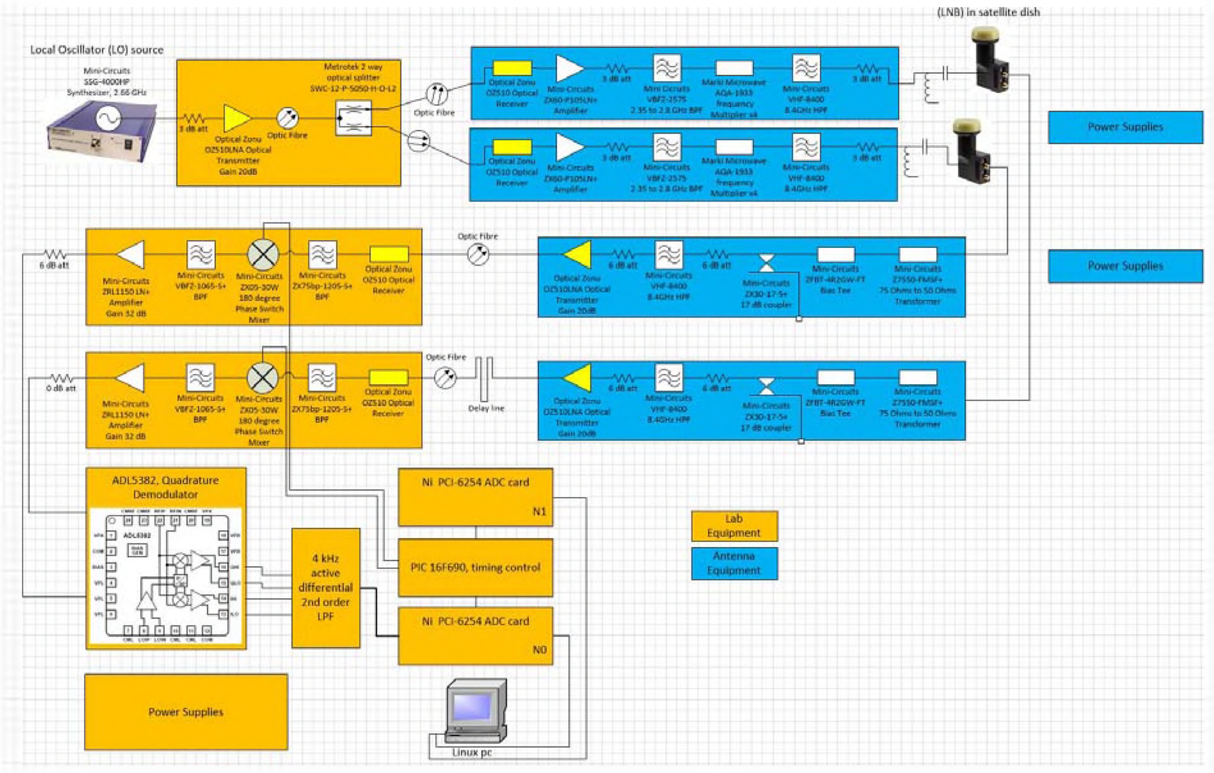

Figure 3: Dual Antennas Phase Monitoring System Schematic. Equipment highlighted in orange are located in the laboratory racks, while blue ones are situated in the antenna racks.

3 Phase Monitoring System Implementation

3.1 Improvements

During the development phase at the IRAM headquarters, located in St Martin d'Hères on the university campus, some optimizations were implemented in order to achieve the best possible results. The list is detailed below:

- Addition of strengthening aluminium tubes between parabola and LNB to ensure good mechanical stability
- Meticulous analysis and suppression of EMC related noise by addition of dedicated filtering on the DC lines, separation of IQ demodulation board and IF switch boards, use of low noise power supplies
- Use of a phase shifter to calibrate the IQ gain and offset errors
- Use of Mini-Circuits synthesizer for LO frequency generation
- First use of Technomate LNB, detailed study of effect of LO power fluctuation
- LO injection into LNB DRO amplifier input
- Use of Marki Microwave x4 frequency multiplier in LO circuit to reduce LO part count
- Use of Optical Zonu LNA transmitter to reduce IF and LO part count (fewer amps)
- Detailed study of phase shifter balance
- Implementation in the antenna racks of lightning protections

3.2 Rack Setup

Every box shown on Figure 3 materialises a mechanical enclosure that takes place either in a rack of electronic that is located in the laboratory or in a rack that is attached to the antenna pole. The Figure 4 shows the antennas on the roof of IRAM headquarters and laboratory rack of electronics.

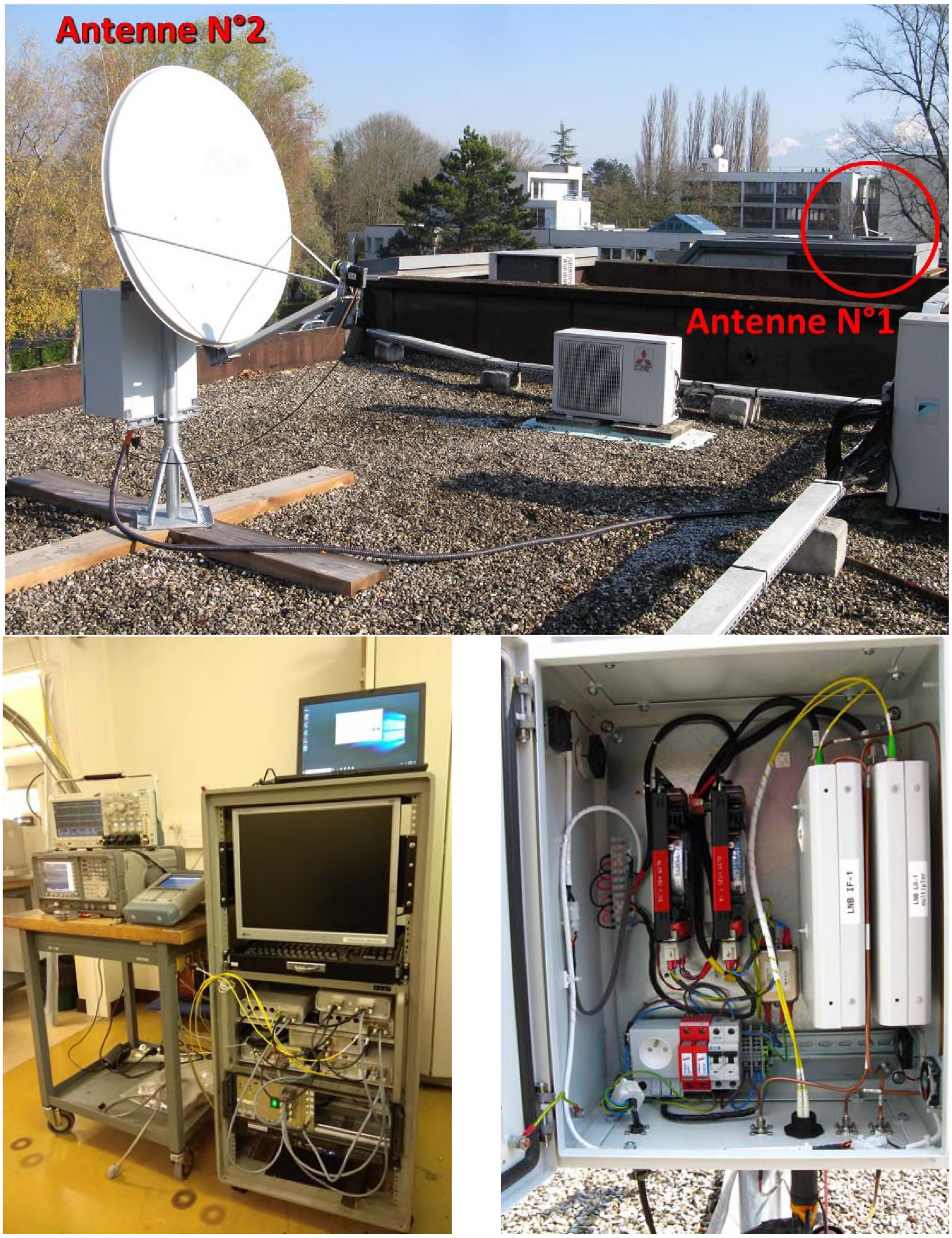

Figure 4: Top: Antennas on the IRAM headquarters roof in Grenoble. Bottom left) Indoor rack of electronics and control pc, Bottom right) Outdoor rack of electronics.

3.3 Data collection

After the initial tests carried out at the IRAM headquarters, where we were facing electromagnetic pollution and environmental limitation, the system was moved to Plateau de Bure in mid-October to make onsite observations before the coming of the winter: All-year operation of such a system requires a protective infrastructure (radomes or similar shielding) due to electronics vulnerability to the meteorological conditions of the site.

The goal of this experiment was to compare the measured satellite phase with the observed NOEMA interferometer phases. The two-element satellite interferometer operating at 11.85 GHz was installed on the Eastern NOEMA track, with the antennas pointing towards the south, with no NOEMA antennas in front (see Figure 5). The system spanned a baseline of 40 meters close to the E18 and E23 pads, and pointed to the geostationary ASTRA 3B satellite under an azimuth of -24.3° (with 0°=South, and negative numbers East) and an elevation of 35.7°.

Figure 5: One Atmospheric Phase Monitor Antenna on E18 pad, next to a 15 meters NOEMA Array antenna.

3.4 Data Analysis

The phase monitor system was installed and running on the plateau de Bure for a limited amount of time, before harsh winter weather condition occur and between two NOEMA interferometer configuration changes. During that period, two sets of data were collected, separated by a gap on the graph.

The measured fringes of the phase monitoring interferometer contain the traces of the satellite movement around its equilibrium point. A succession of second-order polynomial was fitted over several intervals, until the end of the recording where a final fit was made. The overlapping polynomials were then combined with a Gaussian weighting that dropped to 5% at the edges of each interval.

The result of this operation can be seen in Figure 6 left. For further analysis and comparison with NOEMA observations, the phase noise was converted from degrees phase to optical path microns. Phase noise was then studied over two timescales: 135 seconds corresponding to the duration of one NOEMA phase calibration, and 1 second for a consistency check of the phase information. Tropospheric water vapour being distributed in bubbles with a power-law size distribution; phase noise caused by turbulent water vapour is expected to rise according to a power law and level off at the outer edge of the turbulence, or at the length of the maximum baseline. From this behaviour one would expect a higher phase noise at 135 seconds than over a timescale of one second. The plot in Figure 6 right shows that the expected behaviour for tropospheric water vapour phase noise is fulfilled until about midnight UT on October 27 (passing from October 26th to 27th) but that there is a significant short-term phase noise contribution later. This noise must have a different reason than atmospheric water vapour, either instrumental (wind-induced vibrations) or due to external reasons like ionospheric activity.

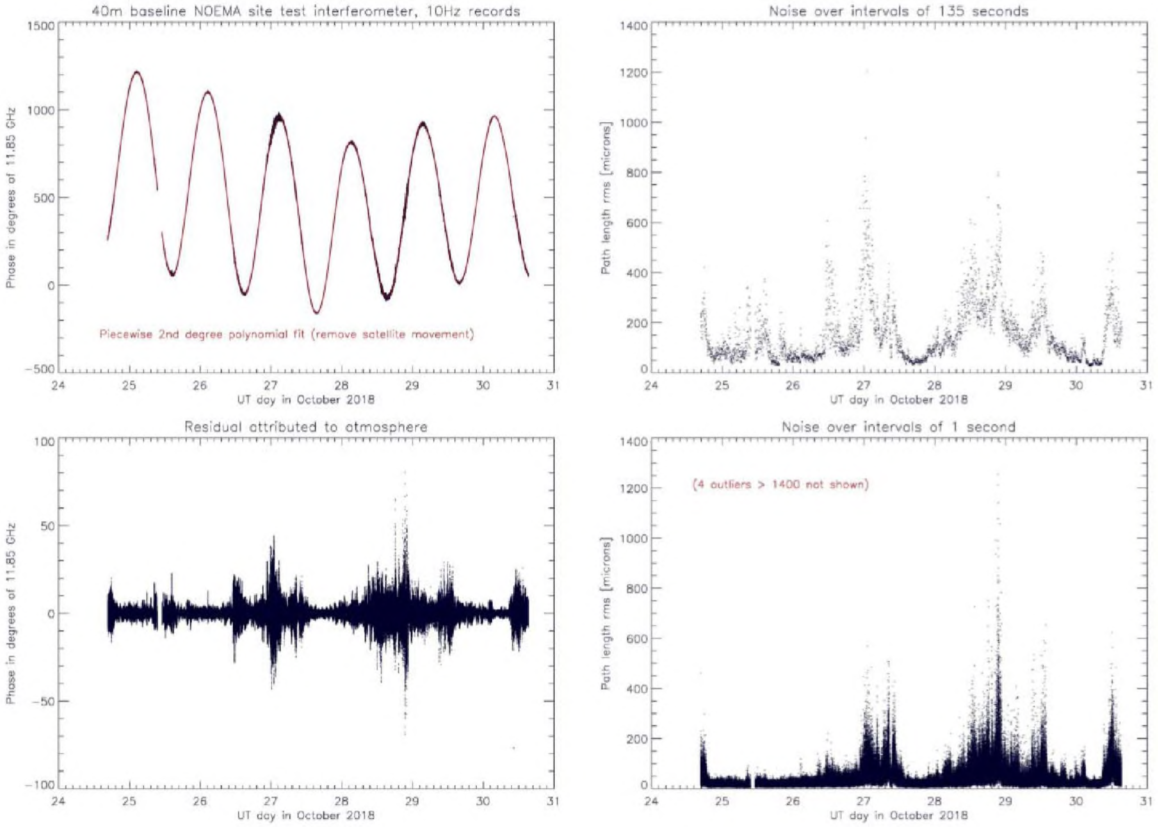

Figure 6: Left) Measured Satellite Interferometer Phase, sampling 10 Hz, Right) Phase Noise over intervals of 135 seconds and 1 second, in microns.

For comparison with NOEMA observations, archival interferometer data were retrieved and the calibrator phase noise for each 135 second phase calibrator observation calculated. The degrees phase were then converted to microns of optical path and sorted by baseline length. A linear fit in the log-log diagram of baseline length vs. noise was used to derive the optical path variations at 40 meters, i.e. the baseline length of the site test interferometer. The resulting superposition of satellite phase and observed phases is shown in Figure 7, together with the meteorological records of the NOEMA weather station. To confirm the correct time alignment between the data sets, the weather records of the NOEMA archived files are superimposed in green on the graphs.

Finally, observing conditions and antenna pointing information are compiled in Figure 8. It shows that the site test interferometer gives a reasonable optical path noise estimate under a variety of observing frequencies and observing directions, i.e. the fact that the satellite dishes always point to the same direction was not a fundamental problem in the monitoring of the all-sky observing conditions, at least not under the conditions during this test.

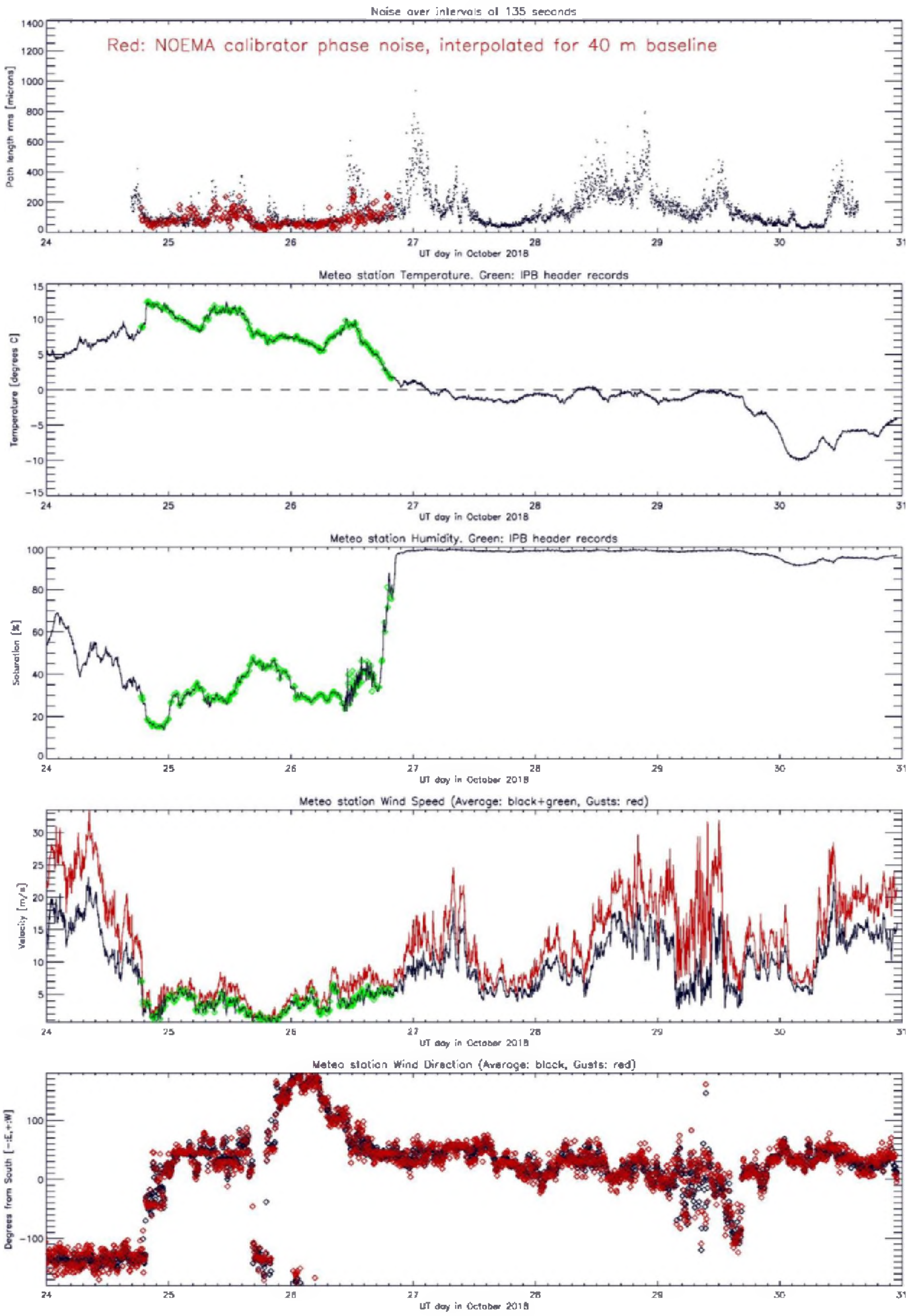

Figure 7: Phase Noise of Test Interferometer and NOEMA, with weather records.

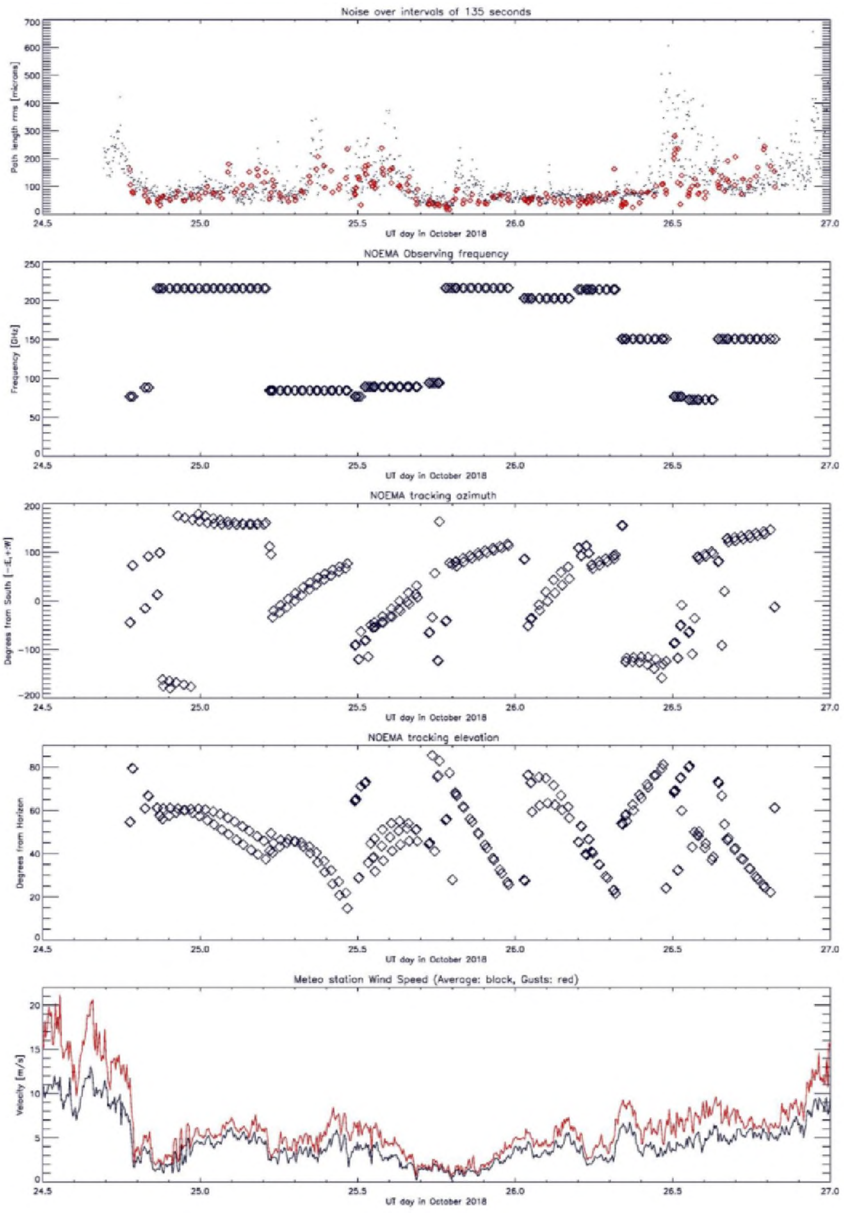

Figure 8: Phase Noise and NOEMA Tuning Frequency, Pointing Information and Wind.

4 Conclusion

This paper has described the phase monitoring system work that has been ongoing for the past two years at IRAM. It described in details the hardware that has been used, together with the first encouraging results that were obtained on the plateau de Bure. A new campaign of data collection will occur in the coming months. In order to make sure that the system is not affected by the environmental conditions, we plan, this time, to protect the antennas in some kind of shelter like radome or else.

Références bibliographiques

[1] Robert S. Kimberk & All “A Multi-Baseline 12 GHz Atmospheric Phase Interferometer with One Micron Path Length Sensitivity”, May. 2012.

Plan d'expérience optimal pour l'évaluation du couplage sur câbles soumis à des paramètres incertains
Optimal design of experiments for the assessment of cable coupling assuming uncertain parameters

***Yassir Karroum*[1]*, Imad Enneiymy*[1]*, and Sébastien Lalléchère*[2]**

[1] *ISIMA, Aubière, yassir@ykarroum.com, enneiymy.i@gmail.com*
[2] *Université Clermont Auvergne, Sigma Clermont, Institut Pascal, Clermont-Fd, sebastien.lallechere@uca.fr*

Mots-clefs: couplage radiofréquence, interférence électromanétique (IEM), propagation d'incertitudes (PU)
Keywords: radiofrequency coupling, electromagnetic interference (EMI), uncertainty propagation (UP)

Résumé:
Cette proposition vise à évaluer la distribution et les moments statistiques du courant induit au niveau de la terminaison d'une ligne située au-dessus d'un plan de masse, et soumise à une perturbation radiofréquence extérieure. Le problème revêt une importance majeure pour divers domaines d'applications en compatibilité électromagnétique (CEM). La volatilité des paramètres d'entrée nécessite des méthodes efficaces : cette contribution mettra en avant plus particulièrement une formulation analytique sur un problème CEM en parallèle avec une méthode de réduction d'ordre (MOR) et une technique de régression par apprentissage semi-supervisé (RAS), comparativement à la référence obtenue par la méthode de Monte-Carlo (MMC).

Abstract: This contribution aims to estimate the statistics and probability distribution of the current induced at the terminal of a cable above ground plane, illuminated by external radiofrequency stimulation. The problem is of paramount importance for various applications in electromagnetic compatibility (EMC). The volatility of input parameters requires efficient methods: a particular focus will be given in this proposal to analytical formulation, jointly with order reduction method (MOR in French) and semi-supervised learning regressor (RAS in French), both in comparison to classical Monte Carlo method (MMC in French).

1 Introduction

De nombreux systèmes électronqiues sont soumis à des stimulations radiofréquences (RF) pouvant entraîner le dysfonctionnement de ces derniers. C'est évidemment le cas pour des problématiques liées à la sensibilité de mesure en radiocommunication et astronomie. Ces dernières années, ce domaine s'est trouvé confronté à l'apparition de difficultées liées à la fois à la compatibilité électromagnétique (CEM) des systèmes [1, 2] et aux incertitudes entourant la mise en œuvre de programmes scientifiques d'envergures; e.g., le "square kilometer array (SKA)" [2]. Dans ce cadre, les études passées ont montré l'importance (devant la complexité des systèmes électroniques mis en jeu) de prendre en compte un nombre toujours croissant de paramètres entâchés d'incertitudes. Par exemple, le cas d'erreurs de montage sur des antennes est évoqué dans [3]. Ces problèmes entraînent la prise en compte d'un nombre conséquent de variables aléatoires (VAs) qui nécessite d'une part l'emploi de modèles (analytiques, numériques, expérimentaux) adaptés, mais également la définition de techniques stochastiques précises. La motivation de cette proposition concerne l'utilisation de méthodes originales permettant de réduire la complexité d'un problème générique de couplage entre une onde plane stochastique (incidence, polarisation, amplitude du champ électrique de perturbation aléatoires) et d'un système générique (ligne de transmission) elle-même soumise à des dérives (géométriques et électriques). En conséquence, la section 2 propose une description synthétique du problème posé. La section suivante donne des détails concernant les deux méthodes stochastiques choisies (respectivement méthode de réduction d'ordre MOR et régression par apprentissage semi-supervisé RAS). Une sélection de résultats numériques obtenus à partir des formalismes précédents est proposée dans la section 4 avec une confrontation aux données MMC. Enfin, La section 5 offre une synthèse et des perspectives à ces travaux.

2 Couplage radiofréquence en environnement incertain

L'exemple illustratif considéré ici concerne une ligne de transmission (longueur L, diamètre d, coefficient d'atténuation α) située à une hauteur h d'un plan de masse parfait. Le câble est chargée à ses deux extrémités par deux impédances Z_0 et Z_L, et il est soumis à un champ électrique perturbateur d'amplitude a_e issu d'une onde plane perturbatrice d'incidence (θ_p, ϕ_p) et de polarisation θ_e. En dehors de la fréquence de stimulation f, tous les paramètres précédents sont considérés comme des VAs, voir la Tab. 1. Un intérêt particulier est porté à l'amplitude du courant I en terminaison de ligne (i.e. au niveau de l'impédance Z_L). Il peut être exprimé pour une fréquence f (étude menée dans la suite entre 1 kHz et 20 MHz) en fonction des 10 VAs précédentes selon :

$$I(\mathbf{x}; f) = m(\theta_p, \phi_p, \theta_e, a_e, h, d, L, Z_0, Z_L, \alpha; f), \tag{1}$$

où $m(\mathbf{x}; f)$ est une fonction analytique dont l'expression exacte est donnée dans [4], avec $\mathbf{x} = [x_1, \ldots, x_{10}]^T$. On notera que la fréquence f est déterministe.

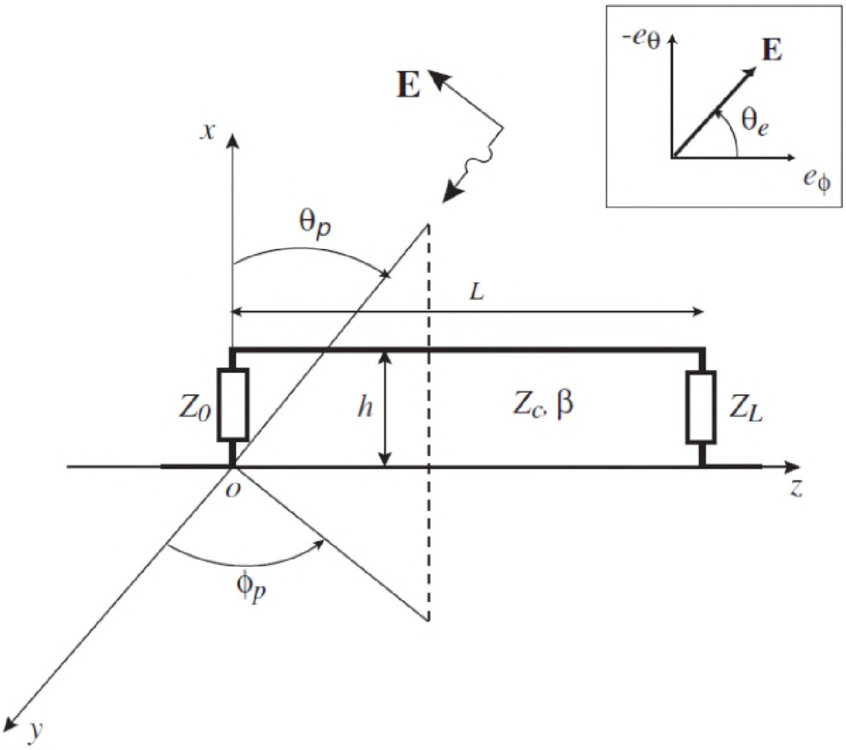

Figure 1 – *Position du problème : ligne de transmission au-dessus d'un plan de masse illuminée par une onde plane [4].*

Table 1 – *Statistiques (Moyenne Moy et coefficient de variation CV) et distributions (distrib., ℕ =normale) des VAs dans le cas test proposé.*

Var. aléa.	$x_1 =$ θ_p (rad)	$x_2 =$ ϕ_p (rad)	$x_3 =$ θ_e (rad)	$x_4 =$ E (V/m)	$x_5 =$ h (m)	$x_6 =$ d (m)	$x_7 =$ L (m)	$x_8 =$ Z_0 (Ω)	$x_9 =$ Z_L (Ω)	$x_{10} =$ α (-)
Moy	$\pi/4$	$\pi/4$	$\pi/4$	1	0.020	0.001	1	50	1000	0.001
CV	20%	20%	20%	5%	5%	5%	5%	5%	5%	5%
Distrib.	ℕ	ℕ	ℕ	ℕ	ℕ	ℕ	ℕ	ℕ	ℕ	ℕ

Si la prise en charge de la volatilité des paramètres exposés dans la Tab. 1 est directe avec la méthode de Monte-Carlo (MMC), la motivation de ces travaux repose sur l'utilisation de deux approches alternatives : méthode d'ordre réduit (MOR [5]) et régression par apprentissage semi-supervisé (RAS [6]). Les deux techniques précédentes font l'objet d'une présentation synthétique dans la section suivante.

3 Principes théoriques

Cette section décrit brièvement les fondements des deux grandes classes de méthodes proposées dans ces travaux pour l'extraction de plans d'expériences optimaux dans un contexte électromagnétique entâché par des incertitudes. Les codes sources développés sont librement accessibles depuis le dépôt github suivant : `https://github.com/ukarroum/optimal-experimental-design`.

3.1 Méthode d'Ordre Réduit (MOR)

La stratégie adoptée pour implémenter la technique MOR s'assimile à une approche de type "clustering" (plus précisément, une émanation de l'algorithme dit de *k-means*). L'algorithme de *k-means* permet de représenter un nombre important d'échantillons de départ (e.g. $n = 10^4, 10^5, \ldots$) à partir d'un nombre limité de points (e.g. ici $m = 10$, $m = 25$, ...). Les coordonnées de ces derniers (dans l'espace des paramètres d'entrée) déterminent les positions des "clusters" représentatifs de l'ensemble de points initiaux. Il peut arriver (en fonction de l'algorithme choisi) que les points sélectionnés de manière optimale (voir [5] pour une explication détaillée) ne fassent pas partie des points intialement définis (voir par exemple le traitement existant de la fontion *sklearn* sous *Python*). Les développements proposés dans le cadre de ces travaux visent à implémenter une version *ex nihilo* et modifiée de l'agorithme de *k-mean* sous *Python* permettant de choisir avec flexibilité : l'appartenance ou non des coordonnées des *clusters* au plan d'exépérience original, la fonction objectif à optimiser, ...
La réalisation de l'algorithme (voir Fig. 2) pour un nombre de *clusters* m donné permet la génération des m jeux de positions de points dans l'espace des entrées $\mathbf{x}_i = \left(x_i^1, x_i^2, \ldots, x_i^p\right)^T$ pour $i = 1, \ldots, m$ et p la dimension de l'espace de départ. Chacun des *clusters* est également caractérisé par son poids p_i dans l'ensemble des entrées du plan initial. Ainsi, le cacul des moments statistiques est obtenu de manière directe sur la base des grandeurs $\mathbf{x}_i$ et p_i. Pour l'illustration, on notera que la moyenne d'une grandeur I (courant dans la suite de cet exemple, pourra être obtenue selon

$$\langle I(\mathbf{s}, \mathbf{d}) \rangle = \sum_{i=1}^{m} p_i * I(\mathbf{x}_i, \mathbf{d}) \tag{2}$$

avec $\mathbf{s}$ et $\mathbf{d}$ respectivement les paramètres volatiles (stochastiques) et fixes (déterministes) du problèmes, et $\sum_{i=1}^{m} p_i = 1$. Comme évoqué précédemment, le critère d'optimisation de l'algorithme pourra être choisi en rapport avec les statistiques de l'ensemble des points de départ initiaux : moyenne, variance, densité de probabilité (PDF) par exemple. Historiquement, la technique MOR est plus utilisée dans le domaine de la simulation que pour les plans d'expérience optimaux (ce qui explique le nombre limité de ressources documentaires disponible dans ce contexte). L'algorithme développé est synthétisé dans la Fig. 2.

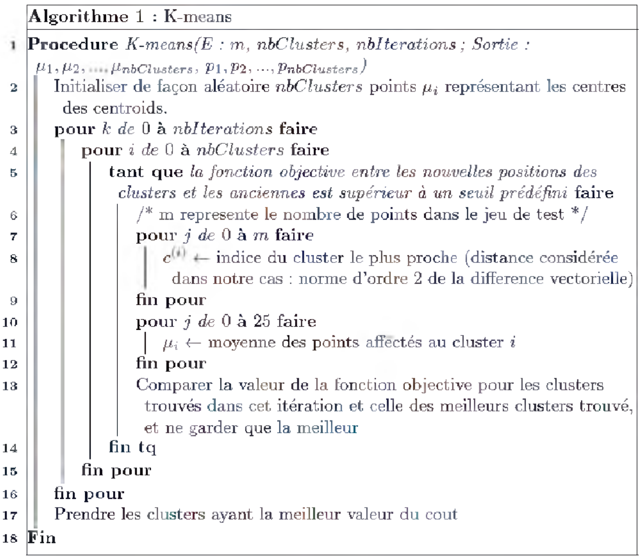

```
Algorithme 1 : K-means
Procedure K-means(E : m, nbClusters, nbIterations ; Sortie :
 $\mu_1, \mu_2, \ldots, \mu_{nbClusters}, p_1, p_2, \ldots, p_{nbClusters}$)
    Initialiser de façon aléatoire nbClusters points $\mu_i$ représentant les centres
     des centroids.
    pour k de 0 à nbIterations faire
        pour i de 0 à nbClusters faire
            tant que la fonction objective entre les nouvelles positions des
             clusters et les anciennes est supérieur à un seuil prédéfini faire
                /* m represente le nombre de points dans le jeu de test */
                pour j de 0 à m faire
                    $c^{(i)}$ ← indice du cluster le plus proche (distance considérée
                     dans notre cas : norme d'ordre 2 de la difference vectorielle)
                fin pour
                pour j de 0 à 25 faire
                    $\mu_i$ ← moyenne des points affectés au cluster i
                fin pour
                Comparer la valeur de la fonction objective pour les clusters
                 trouvés dans cet itération et celle des meilleurs clusters trouvé,
                 et ne garder que la meilleur
            fin tq
        fin pour
    fin pour
    Prendre les clusters ayant la meilleur valeur du cout
Fin
```

FIGURE *2 – Vue synthétique de l'algorithme MOR.*

3.2 Régression par Apprentissage semi-Supervisé (RAS)

L'apprentissage semi-supervisé permet d'aborder le problème précédent sous un angle différent. Ainsi, au lieu de chercher un nombre m réduit de points représentatifs du plan d'expérience initial, nous essayons à travers cette méthode d'inférer la fonctionnelle F représentative du modèle stochastique (i.e. à partir des réalisations aléatoires des paramètres d'entrée du modèle). Ceci peut être réalisé à partir d'une régression basée sur un nombre restreint (m également ici) de points. Une fois ce nouveau modèle (simple) déterminé, il est possible de pratiquer un nombre de réalisation substantiel pour extraire les moments statistiques nécessaires (moyenne par exemple). Les données choisies par cette méthode RAS (*active learning*) donnent une vision optimale de l'erreur commise sur le modèle, mais peuvent s'avérer moins représentatifs du plan d'expérience initial. Le processus global d'extraction est synthétisé dans la Fig. 3.

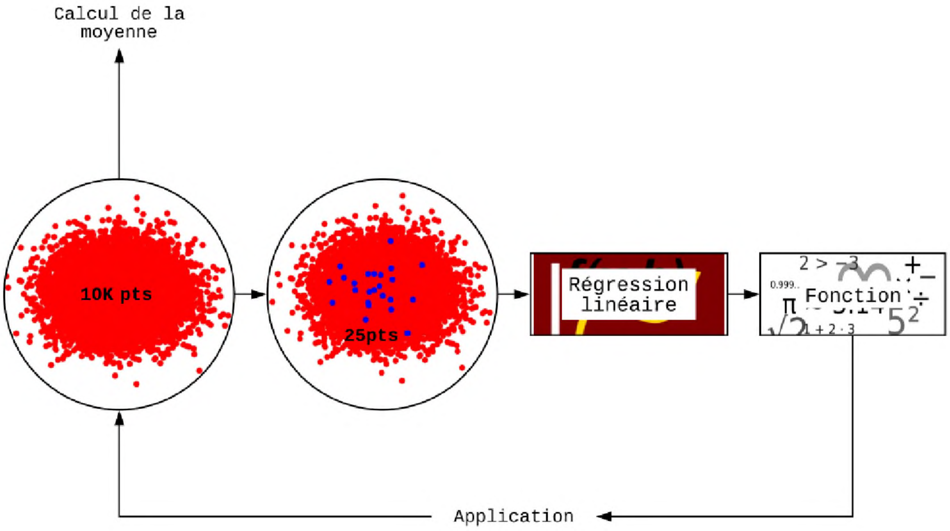

FIGURE 3 – *Diagramme de flux de l'algorithme RAS : illustration avec* $n = 10^4$ *points dans l'espace d'entrée,* $m = 25$ *points optimaux, régression linéaire, et détermination de la moyenne de l'observable choisi (dans la suite, moyenne du courant).*

Brièvement, on notera que différents critères d'optimalité ont été définis. Dans l'exemple présenté, le critère dit de "A-optimalité" est utilisé : cela consiste à choisir les points X' des points d'entrée qui minimiseront $trace([(X^T X)^{-1}])$. Pour le lecteur intéressé, les détails sont donnés dans le dépôt github : `https://github.com/ukarroum/optimal-experimental-design`.

L'algorithme décrit à travers les Figs 3 et 4 présente l'utilisation de techniques de régression "linéaires". Naturellement, les traitements proposés ont été généralisés pour des approches "non-linéaires" (à travers la génération de combinaisons). Ainsi, pour deux entrées x et y, on peut considérer différentes configurations de monômes :

- d'ordre 2 au maximum : x, y, x^2, y^2, xy ;
- d'ordre 3 au maximum : x^3, y^3, x^2y, xy^2, et ceux d'ordre 2 ;
- d'ordres plus élevés ...

Le pré-traitement précédent est automatisable pour différents ordres de manière automatique par la bibliothèque à condition de fixer cette information en début d'analyse.

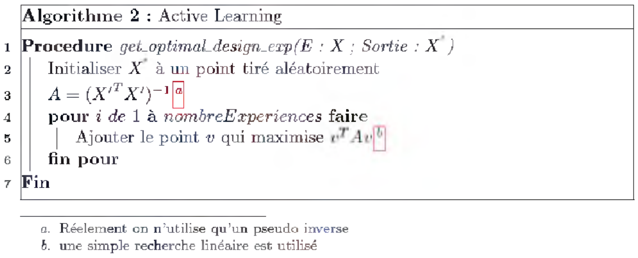

```
Algorithme 2 : Active Learning
Procedure get_optimal_design_exp(E : X ; Sortie : X')
    Initialiser X' à un point tiré aléatoirement
    $A = (X'^T X')^{-1}$ [a]
    pour i de 1 à nombreExperiences faire
        Ajouter le point v qui maximise $v^T A v$ [b]
    fin pour
Fin
```

---

[a] Réelement on n'utilise qu'un pseudo inverse

[b] une simple recherche linéaire est utilisé

FIGURE 4 – *Algorithme RAS : illustration de la fonction* get_optimal_design_exp.

4 Résultats numériques

L'utilisation de la relation (1) en tenant compte des incertitudes de la Tab. 1 conduit aux résultats des figures 5 et 6. Ainsi, on constate le très bon comportement du plan d'expérience MOR, permettant d'obtenir un très bon accord avec seulement 10 simulations, comparativement à 100000 réalisations MMC (Fig. 5). L'utilisation de la technique RAS à l'ordre 2 permet également d'obtenir des valeurs de courant moyen en accord avec MOR (25 simulations) et la référence MMC (fig. 6).

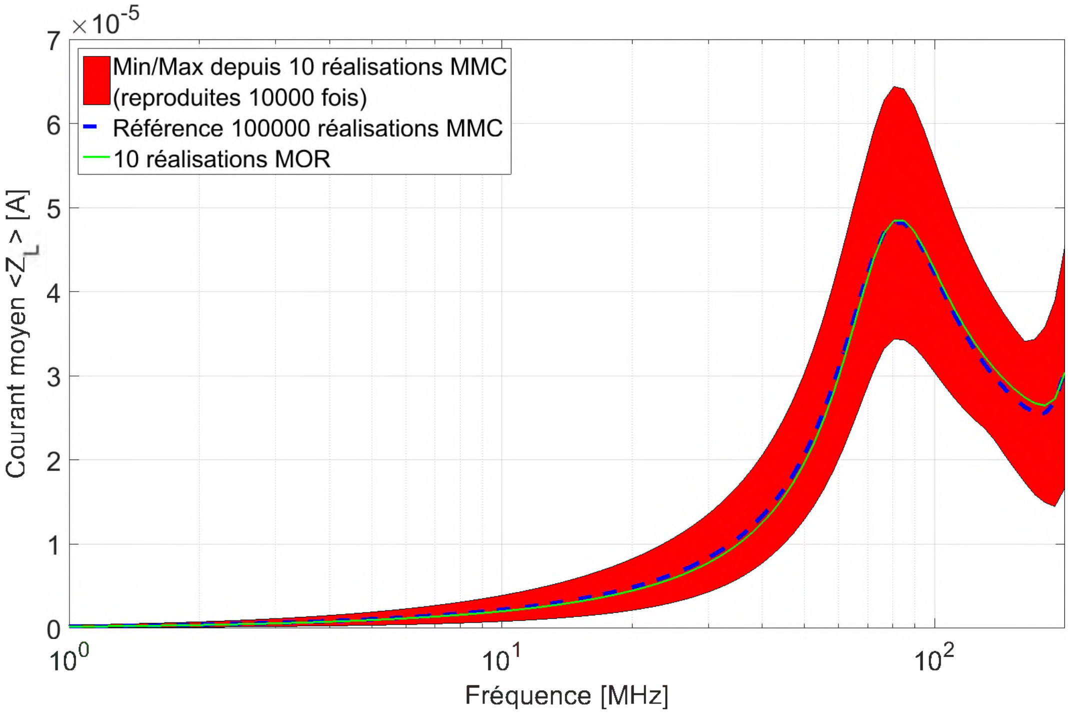

FIGURE *5 – Résultats obtenus par MOR (10 réalisations) et MMC (10^5 simulations).*

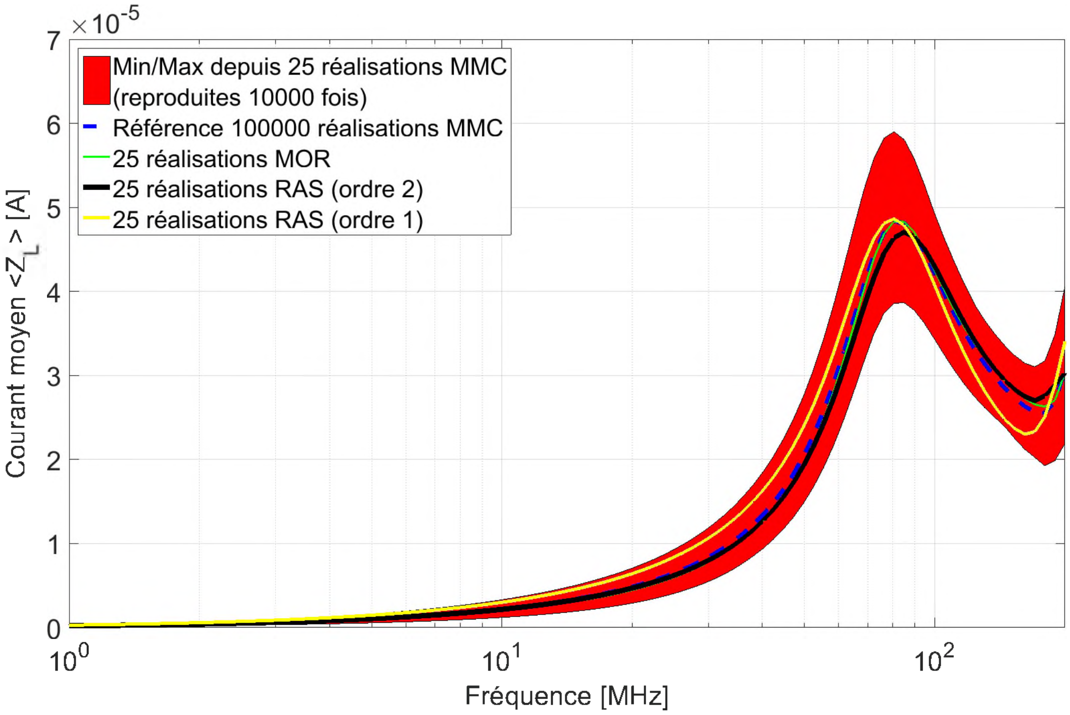

FIGURE *6 – Comparaison des techniques MOR et RAS (25 réalisations) vis-à-vis de la référence MMC.*

5 Conclusion

Cette proposition a permis d'illustrer l'intérêt de techniques originales d'apprentissage (respectivement MOR et RAS) pour la réduction de la complexité d'un problème de CEM soumis à des paramètres d'entrée incertains. L'avantage majeur de ces deux méthodes repose sur leur flexibilité quant au choix du nombre de réalisations nécessaires m pour la simulation, ceci en regard du nombre conséquent de simulations imposé la référence Monte-Carlo (MMC avec n réalisations et $n \gg m$). Les méthodes se révèlent prometeuses sur la base des résultats fournis concernant la détermination du courant moyen couplé sur une ligne de transmission. Des travaux complémentaires montrent actuellement le très bon comportement des méthodes, même pour l'extraction de quantiles élevés (e.g. maxima de courants).

6 Remerciements

Les auteurs tiennent à remercier :

- C. Duhamel, enseignant-chercheur à l'ISIMA, pour les conseils donnés durant la réalisation de ces travaux ;
- le rapporteur anonyme qui, sur la base du résumé proposé, a permis d'améliorer la qualité du papier final.

7 Références

[1] P. Yaya and C. Tourain, *"Impact of DORIS ground antennas environment on their radio signal quality"*, Advances in Space Research, vol. 45, pp. 1455–1469, 2010.

[2] T. Phiri, P. Wiid, and D. Davidson, *"Development and Validation of a Deterministic Propagation Model for MeerKAT"*, in proc. 2017 Int. Symp. on EMC – EMC Europe 2017, Angers, France, Sep. 2017.

[3] A. Young, D. De Villiers, and D. Davidson, *"Sensitivity of shaped offset Gregorian type reflector systems to mechanical mounting errors"*, in proc. Int. Conf. on Electromagnetics in Advanced Applications (ICEAA 2013), Turin, Italy, Sep. 2013.

[4] V. Rannou, F. Brouaye, M. Hélier, and W. Tabbara, *"Kriging the quantile : application to a simple transmission line model"*, Inverse Problems, vol. 18, no. 1, 2002.

[5] M. Grigoriu, *"Reduced order models for random functions. Applications to stochastic problems"*, Applied Mathematical Modelling, vol. 33, pp. 161–175, 2009.

[6] B. Settles, *"Active learning (Synthesis Lectures on Artificial Intelligence and Machine Learning)"*, Morgan & Claypool Publishers, 2012.

Author Index

AVEC LE SOUTIEN DE :

INSTITUT DE FRANCE
Académie des sciences

UNIVERSITÉ DE VERSAILLES
ST-QUENTIN-EN-YVELINES
université PARIS-SACLAY

cnrs
dépasser les frontières

TELECOM ParisTech

LATMOS

GDR ONDES

ANFR
AGENCE NATIONALE DES FRÉQUENCES

see

ROHDE&SCHWARZ

COMITÉ NATIONAL FRANÇAIS DE RADIOÉLECTRICITÉ SCIENTIFIQUE
UNION RADIO SCIENTIFIQUE INTERNATIONALE

Siège social : Académie des Sciences, 23 quai de Conti, Paris 6ème

Site Internet : http://www.ursi-france.org

Adresse postale : Alain Sibille, Secrétaire général d'URSI-France,
Télécom ParisTech, 46 rue Barrault, 75634 Paris Cedex 13
Téléphone : 01 45 81 70 60
Courriel : contact@ursi-france.org